University of Strathclyde
Electronic and Electrical Engineering Department

MODELLING AND OPTIMISATION OF THE DYNAMIC PERFORMANCE OF A REVERSIBLE SOLID OXIDE FUEL CELL SYSTEM FOR THE GRID INTEGRATION OF RENEWABLES

by

Jiancong Ren

A thesis presented in fulfilment of the requirements for the degree of Doctor of Philosophy

January 2013

Dedicated to my family

This thesis is the result of the author's original research. It has been composed by the author and has not been previously submitted for examination which has led to the award of a degree.

Signed : Date :

Acknowledgements

I would like to gratefully give my thanks to Prof. Graeme Burt at the University of Strathclyde for providing helpful guidance, support and resources for this research.

I would also like to express my gratitude to Dr. Andrew J Roscoe at the University of Strathclyde, who extensively helped me on the reversible SOFC computer model, and gave me many suggestions, encouragements and guidance. I would also like to thank all my colleagues at the research group, for their patient helps during my research.

I would like to especially thank Dr Stephen Gamble, who contributed his work in this collaborative research at the University of St. Andrews, for his supportive hard work and patient assistance during this research.

My parents and my wife Dr. Yushu Zhang deserve a great thank from me. I am so lucky and being loved and supported by them all the time.

I extend my gratitude to EPSRC who funded this research.

Abstract

Along with the increasing concerns on environmental issues, the penetration level of renewable energy is growing fast, e.g. wind, tide and solar energy. However the impact of renewable energy on the conventional power grid is increasing due to their intermittent characteristic of power supply. As a result conventional approaches of energy storage need to be improved or reconsidered. One way to increase the value of intermittent renewable energy is to use high efficiency reversible solid oxide fuel cell (RSOFC) system as an energy storage device.

A development of solid oxide fuel cell is being carried out at University of St. Andrews with focusses mainly on material selection and coating technology, etc. This RSOFC system aims to provide effective and flexible power delivery through advances in materials and fuel processing technology. The University of Strathclyde is also a partner of this collaborative research, and this thesis offers comprehensive modelling of this RSOFC system and optimisations proven by simulations to the original design proposed by the Fuel Cell group at University of St. Andrews.

The utilization of RSOFC systems within AC power networks requires power electronic inverters with appropriate controls to convert variable DC power into AC power. However it is commonly recognized that power electronic inverters have major impacts on the dynamic behaviour of the fuel cell system, and these effects are highly dependent on the inverter control algorithms. To investigate the performance and stability of the RSOFC system as an energy storage device within the AC power network this thesis also presents the modelling of the integrated system, along with three competing inverter control algorithms developed at the University of Strathclyde.

Conclusions include the fidelity of the RSOFC concept and the proposed design improvements proven by simulations. An overheating issue is discovered and solved by an innovative application of a phase-change heat store. This heat store is critical

in stabilizing the fuel cell system temperature and increasing the cycle efficiency. This thesis demonstrates that the direct deployment of certain control algorithms may not be appropriate under certain grid scenarios due to excess fuel cell current ripples. Simulations show that appropriate DC bus capacitors effectively reduce the ratio of fuel cell current ripple although potential system cost is implied. Finally it is found that the state of charge (SOC) can in fact have a more negative impact on system efficiency and safety operation than current ripple. The nominal operation range of state of charge is suggested to be constrained according to the ratings of the fuel cell system.

Table of Contents

List of Figures

List of Tables

List of Symbols

Roman Symbols

A	fuel cell effective area (m^2)
A_V	pressure vessel surface area (m^2)
CP_i	heat capacity of species ($Jkg^{-1}K^{-1}$)
$C_{area,surface}$	area specific capacitance (Fcm^{-2})
D	diffusion coefficient (m^2s^{-1})
$D_{H_2,m}$	ordinary diffusion coefficient, hydrogen
$D_{H_2O,m}$	ordinary diffusion coefficient, steam
D_{H_2,H_2O}	mutual diffusion coefficient, hydrogen and steam mixture
$E_{act,an}$	activation energy of the anode
$E_{act,cat}$	activation energy of the cathode
E_{stack}	RSOFC system energy generated or consumed (J)
F	Faraday's constant ($Cmol^{-1}$)
F_{max}	frequency maximum (Hz)
ΔG	the standard free energy of reaction ($kJmol^{-1}$)
$H_{fus,bronze}$	Enthalpy of fusion, bronze
ΔH	the standard enthalpy of reaction ($kJmol^{-1}$)
$i_{density}$	$i_{density}$
i_O	exchange current density (Acm^{-2})
J	Flux (mol^2s^{-1})
L_{an}	thickness of the layer between the outer surface and the reaction site (m)
L_V	pressure vessel dimensions: (m)
l	thickness of the insulation (m)
$L_{l,b}$	thickness of the layer between the concentration of gas in the bulk (m)
M	mass (kg)
M_{H_2,H_2O}	reduced mass of hydrogen and steam (g)
M_{gas}	molecular mass of gases ($gmol^{-1}$)
N_{gas}	moles of gas consumed per second per cell
N_{cell}	number of cells in the stack
n	number of electrons in the reaction

P_{H_2}	partial pressure of H_2 (Pa)
P_{O_2}	partial pressure of O_2 (Pa)
P_{H_2O}	partial pressure of H_2O (Pa)
P_{an}	total gas pressure anode (fuel electrode in fuel cell mode) (Pa)
Q	Electron charge (c)
p_e	heat generated/absorbed by the electrochemical reaction (W)
p_{ohm}	heat generated by the resistance components (W)
p_i	heat losses through insulation (W)
R_i	ohmic resistance of specie *i* (Ω)
R	Universal gas constant 8.314J/mol K
r	radius (m)
T	Temperature (K)
T_c	The temperature of the cold face of the insulation (K)
$T\Delta S$	the heat absorbed by the reaction ($kJmol^{-1}$)
V	Volume (m^3)
V_{nernst}	Nernst voltage (V)
$V_{standard}$	standard cell voltage (V)
X_i^r	mole fraction of species at reaction surface
X_i^b	mole fraction of species at bulk
X_i^l	Mole fraction at the limit of diffusion layer thickness
Z_{real}	real impedance (Ω)
Z_{img}	imaginary impedance (Ω)
ρ_i	resistivity (Ωm)

Greek Symbols

β	electron transfer coefficient
δ_i	current path length (m)
η	overpotential (V)
γ	pre-exponential coefficient
λ	thermal conductivity (Wm^{-1})
Φ	state-of-charge (%)
ρ	density (kgm^{-3})

ρ_i	temperature dependent resistivity(Ωm)
v	Volume

Subscripts

act	activation
an	anode
bronze,molten	molten bronze
bronze,solid	solid bronze
b	bulk
cat	cathode
diff	diffusion
h.s.	Heat store
inter	interconnect
l	gas on electrode surface
r	reaction site
sys	system
tot	total

Abbreviation

DC/AC VSC	DC/AC voltage sourced converter
FFT	Fast Fourier transformation
PEM	Proton exchange membrane fuel cells
PID	A proportional–integral–derivative controller
PLL	Phase lock loop
RSOFC	Reversible solid oxide fuel cell
SOC	State of charge
SPWM	Sinusoidal pulse-width modulation
SV-PWM	Space vector pulse-width modulation
THD	Total harmonic distortion

1 Introduction

1.1 Background

Conventional electric power generation systems in the world are based on fossil fuels (coal, oil and natural gas), nuclear power and hydropower. The demand for electrical energy is increasing and the growth is likely to rise by 76% by 2030 as reported in [1] [2]. However the whole world is facing the gradual exhaustion of fossil fuel supplies, and the volatility of fossil-fuel prices in a global market. Even nuclear power lacks the capability for a long-term solution [3]. In combination with recent trends in increasing energy consumption the questions about sustainability rise. It is predicted that the common large centralised generators with the tendency discussed above will become less dominant, in addition to that their poor efficiency due to large unrecovered heat losses. The renewable energies are achievable solutions to overcome this.

A sustainable energy source is one that is continually replenished, such as wind, wave, tidal and solar power. The UK has set a target of a 34% reduction in greenhouse gas emissions by 2020, from a 1990 baseline, and an 80% reduction target by 2050 [4]. Data collected in [5] shows that the share of renewable electricity almost matches renewable electricity generation growth as a percentage of the total consumption and the largest increase in generation is from wind and wave sources.

However, most of the renewable sources are highly intermittent and hard to predict, especially the wind power [6]. Besides, the power demand varies with time as well [8]. One example shown in Figure 1.1 demonstrates the imbalance between the grid power demand and wind power generation [9]. Therefore if the renewable sources are becoming a large part of the electricity network then it is inevitable that a great number of energy storage systems are required, for compensating the imbalances between the renewable power supply and customer demands. The pumped hydro storage is mainly used in the UK. However the entire capacity can provide up to

2788MW for only 5 hours then it drops to 1060MW, and finally runs out of water after 22 hours [10].

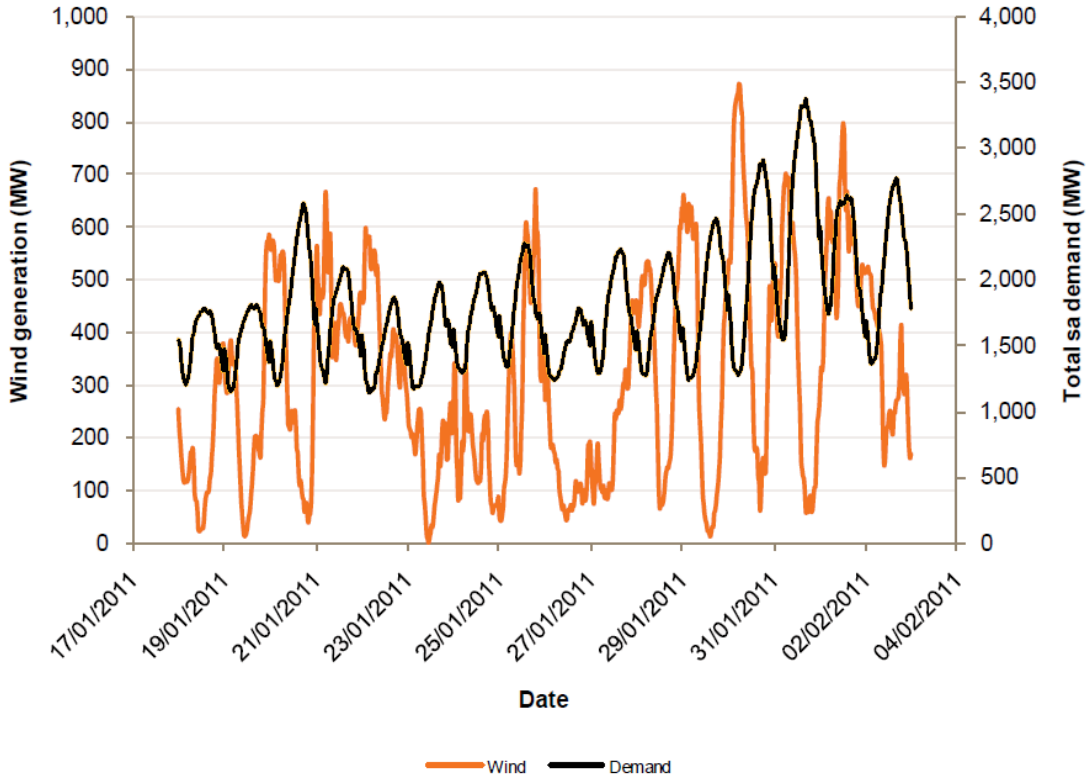

Figure 1.1 Wind generation and total power demand from January to February 2011 in south Australian [9]

Reversible solid oxide fuel cell (RSOFC) systems have high potential to be used as an energy storage device. This technology has high efficiency, low/zero emissions and is almost noiselessness (due to nonexistence of moving parts). The power levels can range from 2 kW to 50 MW [7]. Groups of cells can be interconnected within stacks in series/parallel to provide the desired voltage level. RSOFCs also produce extensive heat as a by-product of the exothermic electro-chemical reaction at high operating temperature; therefore they can be promising candidates in a combined heat and power (CHP) system. While recharging the RSOFCs in electrolysis mode the exceeded heat can be used to reduce the electricity input, if it is stored properly from the fuel cell - electrolyser cycle operation. In a reversible SOFC system, the available energy capacity is partially related to the power rating of the system because of the varying heat loss due to fuel cell ohmic components.

Table 1.1 Electrical energy storage methodologies under development

Storage	Cycle efficiency (%)	Benefits	Draw-backs
Compressed air	50-70 [8]	Large scale	Geology restraint
Pb-acid battery	70-80 [11]	Well developed	High maintenance; limited global supply
Pumped hydro	70-80 [12]	Large scale	Geology restraint
Redox flow cells	65-75 [11]	Reliability	Toxic chemicals
RSOFC	30-40 [13]	High part load efficiency	Cost and degradation

There are also other different types of energy storage systems currently available or under development, such as pumped hydro and compressed air which are compared in **Error! Reference source not found.**. The electrical cycle efficiency of reversible solid oxide fuel cell (RSOFC) is assumed with minimum of 30% - 40% under normal operating condition, without considering the heat storage, where the energy is stored as hydrogen only [13]. However, at the start of this research there was the hypothesis that much more efficiency can be obtained if the heat produced during power generating operation could be stored and re-absorbed during the electrolysis mode. However, work presented in this thesis shows that this benefit can be compromised when the cell is operated towards the higher end of its current rating, as more heat will be wasted into surroundings than can be recovered to generate electrical energy.

In conventional generations the generators operate at a fixed speed and grid frequency. However the voltage generated by fuel cells cannot be directly connected to the grid. Therefore power electronic inverters are normally required for the integration of fuel cell power to supply electricity to the grid, which converts DC to AC or vice versa. Power electronic technology therefore plays a vital role in

matching the requirements of fuel cell units to the grid connections, including frequency, voltage, control of active and reactive power, harmonic minimization etc. Power inverters are often used to provide optimum power quality to local sensitive loads within certain grid environments. However, it is commonly recognized that the power electronic inverters have major impacts on the dynamic behaviour of the fuel cell system, and the effects are highly dependent on the inverter control algorithms. It is inevitable that low frequency current ripples occur when implementing inverters, which can be serious to fuel cell performance and life span if not being carefully limited. In order to investigate the reliability of such operation, the development of the RSOFC system model will be described. After that, the investigations and analyses of the performance and stability of the RSOFC system to be used as an energy storage device within AC power system will be carried out, with comparisons of different effects on fuel cell from inverter control algorithms.

1.2 Research Motivations and Aims

The reversible solid oxide fuel cell system can be a valuable candidate as an energy storage solution to meet the intermittent renewable energy sources which is considered as a promising technology and attractive for research.

Although fuel cell systems provide promising benefits, a number of technical barriers still have to be considered and overcome, such as material durability, commercial viability, reliable interfacing with conventional utility grids and microgrids, etc. Therefore, the aims of the research in this thesis include designing and developing comprehensive and dynamic models of the RSOFC system which represents the fuel cell under development in St. Andrews University to be as realistic and practical as possible. The investigation is firstly to identify the performance and restraint of such RSOFC concept, and secondly provides valuable feedbacks and inferred improvements according to the simulations, e.g. stack geometry, dynamic temperature, cycle efficiency. A power conditioning unit is designed in accordance with the observed RSOFC characteristics. Therefore, three competing and effective inverter control strategies developed at University of Strathclyde for the integrated power system aiming to achieve high efficiency and reduced losses are to be examined and investigated under different grid conditions, e.g., stiff grid, weak grid,

microgrid, at varying disturbance. Dedicated case studies are conducted to identify the impacts on the fuel cell system and to estimate the validity of control algorithms under certain challenging scenarios.

1.3 Principle Contributions

A significantly comprehensive and dynamic model of the reversible solid oxide fuel cell (RSOFC) has been developed in Simulink/Matlab software. High fidelity has been obtained due to the dynamic sub-models of heat/temperature system, low and high activation polarisation, and the diffusion polarisation which is partly contributing to the Randles circuit (a well-known electrical equivalent circuit to represent fuel cell characteristics) [13].

The performance of the prototype RSOFC system design has been improved due to the feedbacks and inferred suggestions from simulations during the development of the fuel cell model. These include: a copper-tin compound of heat store which prevents over-heating and stabilise the system temperature, also restores the excess energy for cycle efficiency enhancement; the improved stack/vessel design considering both energy/hydrogen storage capability and heat transferring effects; fuel cell geometry and material are altered aiming at reducing the ohmic loss.

Some key parameters and cell geometry material selections are obtained according to the sensitivity analysis tests during the simulation, with the collaboration of the University of St. Andrews. A complete new derivation of the electron transfer coefficient which is crucial for the modelling of low and high activation polarisation for this specific RSOFC system is explained.

An AC power system model integrated with RSOFC system as an energy storage device has been developed and used for case studies. Three inverter control algorithms have been adapted within different grid conditions and disturbances to demonstrate their effects on both AC power quality and RSOFC system. Those case studies clarify the possibilities of certain control mode to be appropriately used for fuel cell system under different scenarios, and their trade-offs are discussed.

The analysis of effects on fuel cell current ripple induced at three control modes with the variations of AC voltage unbalance, THD, power factor and DC bus capacitance has been discussed. The RSOFC system is designed to have fuel cells connected both in parallel and series within a sealed stack vessel. The rated voltage of RSOFC system is proposed to be 450V. This is designed for allowing cell voltage drop due to the varying fuel cell state of charge (a percentage of remaining hydrogen partial pressure), and to connect to a 230V (+10%) AC busbar via an inverter. The benefits of adapting DC bus capacitance with different value to minimize the fuel cell current ripple has been described, and the conclusion suggests that at least 10 mF capacitor is required to provide a safe operation for RSOFC system (100kVA RSOFC rating with 450V at DC bus). The analysis of effects on fuel cell efficiency due to current ripple and state of charge (SOC) has been described as well.

1.4 Outline of Thesis

The research thesis constitutes of six chapters:

Chapter 1 briefly introduces the current energy issue world widely, and the (in growth displacement solutions of) renewable energies. The RSOFC is discussed as an promising energy stores for renewable generations and compared with other candidates. Also the aims and contributions delivered by this research are discussed.

Chapter 2 gives an overview and the literature review of the current scenarios of fuel cell/RSOFC technologies in different approaches and modelling profiles. This chapter also covers the backgrounds of power electronic inverter control algorithms.

Chapter 3 describes the significant mathematical modelling of a reversible solid oxide fuel cell system based on electro-chemical equations developed by the author in collaboration with Stephen Gamble at the University of St. Andrews. Nernst voltage and polarisations for a single cell are discussed and the derivations of certain sensitive parameters for this particular design are described. The important feedbacks from stack simulations are introduced which improves the original stack design to be more practical. This chapter also describes the impedance spectroscopy (IS) derived from the model of Randles circuit, which represents an equivalent electrical circuit of

RSOFC. Then the discussion is extended to a stack system with the modelling and simulations of temperature, partial pressure, state of charge (SOC) and thermal dynamic.

Chapter 4 demonstrates the simulations and investigations of the RSOFC system performance, including the effects of the state of charge, pressure and certain parameters on the fuel cell performance. Simulation results in this chapter also prove the design optimisations made in pressure, stack size, cell geometry and pre-exponential coefficient. The case studies examining the performance of the copper-tin heat store is finally described.

Chapter 5 describes three inverter control algorithms developed in Strathclyde University with an alternative PID power control approach for two of these control modes. Case studies of implementing these control algorithms on RSOFC system connected to stiff grid, weak grid and microgrid are described, including discussions of their effects on the DC/RSOFC side, e.g. DC bus voltage/current variation, power loss of ripple, RSOFC fuel consumption and efficiency. The suggestions of the inverter control applications, values of DC bus capacitance and an updated safe operation range for the state of charge are proposed based on the simulation results.

Chapter 6 concludes this research and also presents a future scope for the possible values of continuing the development of the RSOFC powered energy storage.

1.5 Publications

Conferences:

J. Ren, S. Gamble, A. J. Roscoe, and G. M. Burt, Modelling Interaction between Solid Oxide Fuel Cell, Inverters and AC Power Networks," in Universities' Power Engineering Conference (UPEC) 2009. INSPEC Accession Number: 11172197, Print ISBN: 978-1-4244-6823-2

J. Ren, S. Gamble, A. J. Roscoe, and G. M. Burt "Modelling a reversible solid oxide fuel cell to be used as a storage device within AC power networks," Power Electronics, Machines and Drives (PEMD 2010), 5th IET international conference, Publication Year: 2010, DOI: 10.1049/cp.2010.0119

J. Ren, S. Gamble, A. J. Roscoe, and G. M. Burt "Modelling a reversible solid oxide fuel cell to be used as a storage device within AC power networks," 4th World Hydrogen Technologies Convention, 2011, Glasgow, U.K.(WHTC 2011), Publication Year: 2011, Paper id:0059

Journal:

J. Ren, S. Gamble, A. J. Roscoe, and G. M. Burt "Modelling a reversible solid oxide fuel cell as a storage device within AC power networks," Fuel Cells: From Fundamentals To Systems. Published by WILEY-VCH Verlag GmbH & Co in July 2012, DOI: 10.1002/fuce.201100185

1.6 References for Chapter 1

[1] U. S. Department of Energy. (2009). International energy outlook 2009. [Online]. Available: *http:// www.eia.doe.gov/oiaf/ieo/index.html*, 2009

[2] World Nuclear Association. World energy needs and nuclear power 2009. [Online]. Available: *http://* www.worldnuclear.*org/inf/inf16.html*

[3] Department of Energy & Climate Change. (DTI). (2006). The energy challenge, energy review report 2006. [Online]. Available: http://www.berr.gov.uk/files/file31890.pdf

[4] Elizabeth II. *Climate Change Act 2008*, chapter 27, Act of Parliament, The Stationery Office.

[5] National Statistics, *Energy Trends*, Tech. Rep., Department of Energy and Climate Change, UK Government, 2010.

[6] J. Apt, "The spectrum of power from wind turbines," *J. Power Sources*, vol. 169, pp. 369–374, 2007.

[7] S. Rahman and K. Tam, "A feasibility study of photovoltaic-fuel cell hybrid energy system", *IEEE Trans. Energy Conversion,* vol. 3, no. 1, pp. 50−55**,** Mar. 1988.

[8] P. Denholm, G. L. Kulcinski, "Emissions and energy efficiency assessment of baseload wind energy systems" *J. Energy Convers. Manage*, vol. 45, no. 21532172, 2004

[9] Australian Energy Market Organization. (2010). South Australian Supply And Demand Outlook. [Online]. Available: http://www.aemo.com.au /Other/planning/SASDO2011/documents/SASDO2011%20pdf.pdf

[10] John Muir Trust. (2010). Analysis of UK wind power generation. [Online]. Available: http://www.jmt.org/assets/pdf/wind-report.pdf

[11] C. Ponce de León, A. Frías-Ferrer, J. González-García, D. A. Szánto, F. C. Walsh, "Redox flow cells for energy conversion," *J. Power Sources*, vol. 160, pp. 716–732, 2006.

[12] J. Kondoh, "Electrical energy storage systems for energy networks," *J. Energy Convers. Manage*, vol. 41, pp.1863 – 1874, 2000.

[13] P. Costamagna, "Modeling of solid oxide heat exchanger integrated stacks and simulation at high fuel utilization," *J. Electrochem*. Vol. 145, issue. 11, pp. 3995-4007, 1998.

2 Background and Literature Review

In this Chapter, the conventional perspectives and backgrounds of the fuel cells and power converters/inverters will be described. High temperature reversible solid oxide fuel cell (RSOFC) principle and operation are introduced upon a hydrogen based design with the superiorities highlighted. However the variations in SOFC design can lead to great performance diversities. Therefore, the existing designs and modelling of the solid oxide fuel cell system will be reviewed in this chapter, and the shortcomings that are exposed in these conventional approaches to the analysis and investigation of a RSOFC system will be discussed.

When utilizing the RSOFC system as an energy storage within a power network, the power electronic converter/inverters are required to convert the DC power source of RSOFC into AC power or vice versa. Two common types of power converter and output voltage modulation technologies will be described in this chapter, along with the fundamentals of inverter control algorithm. In addition the input current ripples which are induced from the implementation of inverter is discussed. Moreover, the key definitions, concepts and modelling of power electronic inverters used throughout this thesis are presented.

2.1 Solid Oxide Fuel Cell

2.1.1 SOFC Design and Operation Principles

The basic components of a typical fuel cell include two electrodes, an anode and a cathode where the reactions take place. An electrolyte is sandwiched between the anode and cathode which allows the oxygen ions to pass through from cathode to anode while blocking the electrons. It happens due to the tendency of charged particles migrating to regions of lower electrochemical energy. Meanwhile the electrical energy is produced when the electrons travel the external circuit. Heat is also one of the by-products, which makes fuel cells suitable for CHP (Combined Heat and Power) applications. The most commonly used fuel is hydrogen, and the oxidant is usually oxygen. The most common product of chemical reaction is water

which is produced either at the cathode or at the anode, depending on the type of fuel cell.

Polymer electrolyte membrane fuel cells (PEM) and solid oxide fuel cells (SOFC) are mostly studied for energy storage applications by reversible operation. PEM and SOFC produce electricity in fuel cell mode and store energy in hydrogen by electrolysis operation. SOFC is based on the concept of oxide ion migration through an oxygen ion conducting electrolyte from the oxidant electrode (cathode) to fuel electrode (anode) side. It operates at temperatures in the range of 600 – 1000 ℃ [1], which makes them highly efficient as well as fuel flexible. The electrolyte of SOFC is a dense solid that involves ceramic materials like Yttrium-stabilized Zircon (YSZ) dioxide whose function is to prevent electrons from crossing over while allowing passage to the charged oxygen ions. However, the reversible SOFC in this study are operated upon the hydrogen gas only, as it allows Ni-YSZ electrodes to be used. Figure 2.1 shows an operating SOFC and solid oxide electrolysis cell (SOEC).

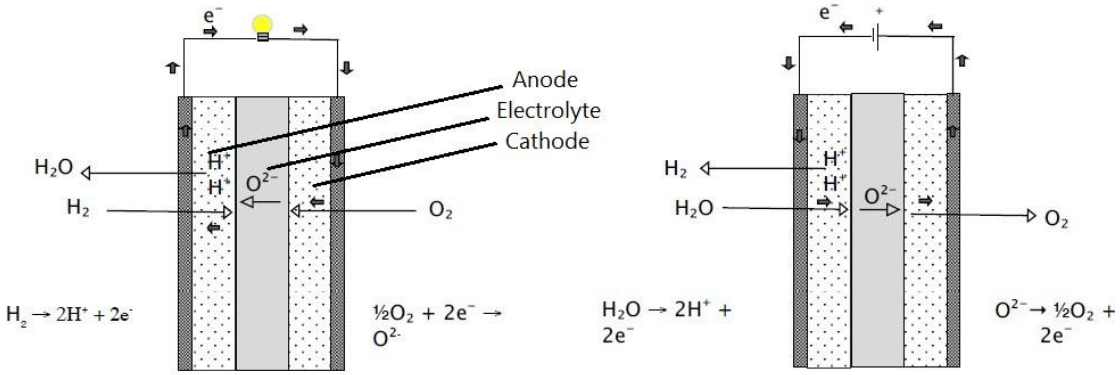

(a) (b)

Figure 2.1 Principles of SOFC operation in (a) fuel cell mode and (b) electrolysis mode [1]

The electrochemical reaction carried out at the cathode is molecular oxygen reacts with the electrons supplied from external circuit to produce oxide ions in the SOFC system that only hydrogen and oxygen are used. The oxygen ions migrate through the solid electrolyte to the anode where they combine with the hydrogen molecule to produce water. The electrons flow through the externally connected circuit to reach

the cathode, doing electrical work and producing electrical energy in this process. Water is produced at the anode on recombination of oxygen ions and electrons with hydrogen, as opposed to the PEM where water is produced at the cathode. The high temperature of the SOFC enables the capability of using hydrogen as the fuel as well as hydrocarbon-based gases. In addition, The SOFC shows a high tolerance to fuel impurities such as natural gas. The SOFC permits internal reforming, and also uses less expensive catalysts for the dissociation of the oxidant.

The reversible SOFC is more suitable for energy storage than the PEM fuel cell. First of all a voltage step occurs in the PEM-FC when switching from fuel cell mode to electrolysis mode [2], however this does not appear in the reversible SOFC Secondly the heat produced from the reversible SOFC can be massive. The chemical reactions which are involved in the production of electricity inside typical hydrogen fuelled SOFC are as follows [3] [4]:

At anode (fuel electrode):

$$2H_2 + 2O^{2-} \rightarrow 2H_2O + 4e^- \qquad (2.1)$$

At cathode (oxygen/air electrode):

$$O_2 + 4e^- \rightarrow 2O^{2-} \qquad (2.2)$$

Overall cell reaction:

$$H_2 + \frac{1}{2}O_2 \rightarrow H_2O + heat \qquad (2.3)$$

Equation (2.4) is the overall reaction in electrolysis mode.

$$2H_2O + heat \rightarrow 2H_2 + O_2 \qquad (2.4)$$

While each fuel cell has advantages and fields of application, the main reasons why the SOFC has been given precedence over other fuel cells are as follows:

- The SOFC technology is best suited for Distributed Generation application because they provide higher system efficiency and higher power density.
- SOFCs are suitable for stationary power applications with step load changes.
- The design of SOFCs is simpler than a fuel cell based on liquid electrolytes.
- The exhaust heat in case of SOFCs can be utilized for co-generation application in industries.
- Since an SOFC operates at a high temperature (600 ℃ to 1000 ℃), it has high reactant activities which helps in reduction of activation polarisation (a fuel cell voltage drop mainly occurs at low fuel cell current), thus increasing the cell efficiency.
- SOFCs are flexible in the choice of fuel such as carbon-based fuels, like natural gas.

2.1.2 Concepts of Gibbs Free Energy and Reversible Energy Storage

The reversible SOFC can store energy by reserving the heat produced by the exothermic fuel cell reaction of Equation (2.3) in the system and then recycling to the endothermic electrolysis reaction of Equation (2.4). This is a major improvement compared to only storing the energy in the chemical form of hydrogen. The cycle efficiency can only be around 30% if the heat is discarded.

It is very important to understand the concept of Gibbs free energy while developing the RSOFC model. The Gibbs free energy can be defined as the energy available to do the external work, e.g. the electrical power output, etc., neglecting any work done by changes in the pressure and/or volume of the reactants and products of the fuel cell. The external work is also referred to as the electrical work done. Therefore if considering fuel cells operating as a electrolyser, then more efficiency can be obtained if less extra heat is supplied by other means of sources for the endothermic reaction of Equation (2.4), and this can be achieved by storing the heat which is generated from the exothermic reaction of Equation (2.3).They are related according to Equation (2.5).

$$\Delta H = \Delta G + T\Delta S \qquad (2.5)$$

$T\Delta S$ is the heat absorbed by the reaction, ΔG is the standard free energy of reaction - the amount of energy available in electrical work, and ΔH is the standard enthalpy of reaction, which is the total energy change of the reaction. The standard voltage of the reaction is related to the standard free energy of reaction by Equation (2.6). Where E is the fuel cell voltage (volt), F is the Faraday's constant (96487 C/mol) and n is normally given the value of 2 (as 2 electrons are transferred for one molecular of hydrogen reacted).

$$\Delta G = -nFE \qquad (2.6)$$

Therefore, as the temperature of the fuel cell reaction increases, more heat is produced but less electricity. However, the electrolysis reaction requires less electricity to produce hydrogen, and more heat, at higher temperatures. By defining the fuel cell efficiency as the ratio of electrical power to the heat enthalpy released/stored in hydrogen, then this means that the electrical to chemical conversion efficiency can exceed 100% in electrolysis mode (where heat is disregarded in the efficiency calculation), if a massive amount of heat is not provided by input electric power but from a heat store.

2.1.3 SOFC Geometries

There are two main SOFC geometries of planar and tubular generally being used for reversible SOFCs, as shown in Figure 2.2. The planar geometry is harder to seal, but provides a high volumetric power density. In the design shown in Figure 2.2 (a), several cells are connected in series, which increases the voltage obtained from a single substrate.

The tubular design shown in Figure 2.2 (b) is used by Siemens-Westinghouse, and has an interconnect running along the cell. Although the tubular geometry is easier to seal, it generally has longer current paths than the planar cell, which cause more ohmic losses in the cell. However sealing is more serious for the planar cell when the

pressure increases. This is because any leaks cause hydrogen and oxygen to mix and combust and producing heat rapidly in tandem. This enlarges the hole and causes a bigger leak, so this process will be faster if the pressure is higher [5]. Therefore, it is the tubular geometry chosen by the University of St. Andrews for this research.

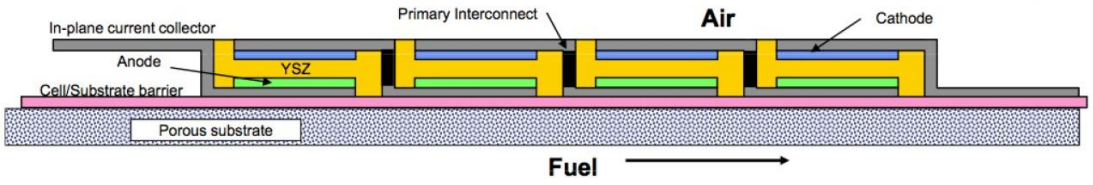

(a)

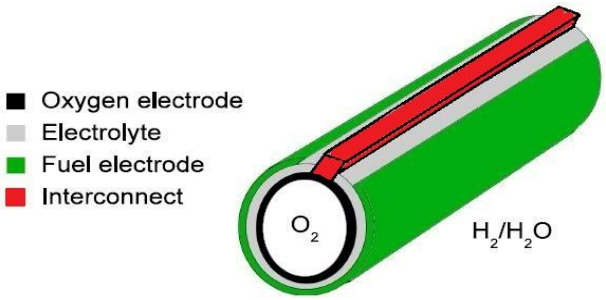

(b)

Figure 2.2 SOFC geometries: a) planar geometry of a Rolls-Royce Fuel Cell Systems cell. ©2009 Rolls-Royce Fuel Cell Systems (US) inc. and is used by permission. All rights reserved. [6], and b) Tubular SOFC geometry, designed by Siemens Westinghouse [7].

For both designs the air flow rate and pressure ratio are the most important parameters to the system performance, but these parameters have less impact on the tubular system than the planar design. The research in Ref. [8] compares the performances of these two common SOFC geometries, in a gas turbine hybrid cycle. The main difference between the planar and the tubular system for the gas turbine cycle is the internal pre-heating of the air in the tubular system, permitting a lower air inlet temperature. The reduced amount of high-temperature heat in the pre-heating section allows for a higher-pressure ratio at acceptable turbine inlet temperatures. The tubular system's ability to be operated at lower air excess ratio lowers the exhaust gas losses and increases the afterburner temperature, improving

the effectiveness of the cycle. These effects compensate for the lower efficiency of the tubular fuel cell stack, which is caused by its higher ohmic resistivity. Also, for planar cells the double layer capacitance can be much bigger in the equivalent Randles circuit [9] ， while for tubular cells the capacitance is dominated by the surface diffusion capacitance which can be much smaller. [9] [10] [11].

Other fuel cell geometry features involve the material/component selection for supporting the cell within the stack system. A SOFC consists of a cathode, an electrolyte, and an anode as the main component as shown in Figure 2.2 (a) and (b). In order to install the cell then two basic designs have been explored in conventional developments; the electrolyte-supported and the electrode-supported geometries [12]. The selection of the support/substrate can be a determining factor in developing a high-performance SOFC. In electrolyte-supported cells the ohmic contribution is large due to high electrolyte resistivity. For this reason, such cells are being developed for operation at ~1000 ℃ where the electrolyte resistivity is low, typically ~20 Ωcm [13]. In cathode-supported cells an additional layer of YSZ is deposited on a porous LSM cathode [13]. The same applies for the anode-supported cells. Ref [14] concludes the better way for enhancing the cell performance is to apply the electrode-supported geometry rather than electrolyte supported. Ref [15] has made a much more detailed sensitivity test based on the thickness of fuel cell components. The study shows that the performance of an anode-supported cell is superior to that of an electrolyte-supported cell or a cathode-supported cell for the same materials used, having the same electrode kinetics with the same operational constraints. The study in [15] also reveals that a cathode-supported cell is no better than an anode-supported cell for high performance fuel cell design even under elevated pressure conditions at the cathode compartment to compensate for the serious cathode concentration over potential loss. Results from literature show the sensitivity of cell voltage due to the change of electrolyte thickness is the highest, compared with that due to cathode and anode. Reducing all three component thicknesses causes, in general, reduced sensitivity strength with an improved operating current density range. However improvements in performance can be obtained if none of the electrodes or electrolyte is designed to be a support component, as described in [16], which shows the diffusion polarisation can be much smaller than that due to the great reduction of electrode thicknesses.

2.1.4 SOFC Modelling

A detailed SOFC model can be made from a huge numbers of equations and sub-models integrated together, especially for a stack system model which represents the specific features of the partial pressure and heat transfer calculations. To overcome the extreme complexity of modelling, some researchers choose to make simplifications by developing the model into individual sections and sequencing the models as a multi-dimension system, as demonstrated in Ref. [16] and [17]. This approach of simplicity can be useful under certain considerations because it helps speed up simulations and avoids unnecessary calculations. Therefore it explains why in Ref. [17] the separated models between the electrochemical equations and the thermal dynamic equations are not simulated at the same time. However the results can be very limited because a huge amount of variables can be affecting the fuel cell performance at the same time, e.g. the stack temperature, pressure, reactant concentration, etc. This results in the simulation data of thermal behaviour in [17] has to be obtained before being applied to the next dimension of electrochemical model.

It is also possible to simplify the detailed model by applying an electrical equivalent circuit to represent all the polarisations of activation, diffusion and ohmic resistance. The researchers normally build the model this way when a prototype of fuel cell is available and accessible in the research, Ref. [14] and [18]. The equivalent circuit can be obtained by having impedance spectrum (IS) test on the real cell at a preliminary temperature and pressure condition, or by frequency response analysis (FRA) technique. The benefit of IS leads to a simplified fuel cell model with an acceptable accuracy. However, without the appropriate modelling of multi-parameter dependent electrochemical behaviours and the heat transfer/balance modelling of the system, the IS based simplified model is very limited to the same temperature, gas flow rate and pressure at which the real fuel cell is examined.

It is normally inevitable that particular assumptions are needed to be made for the development of fuel cell system model. Researchers apply the assumptions according to their specific focuses on simulations. Some are due to the limitations of available devices/techniques or valuable data which is classified as commercially sensitive.

The assumptions are normally catalogued in fuel cell geometry [15] [19] [20], Nernst voltage and polarisations [17], heat transfer and balance [8] [9], etc. Some assumptions can be treated as minor when neglecting some of the least affecting factors. However making a tricky assumption can be terrible on representing the performance of a real fuel cell, which has to be carefully acknowledged. One bad example can be found in [21] that a demo model of a fuel cell from Matlab/Simulink® is applied but neglecting the physical geometries of the fuel cell system. The approach in [21] can be very risky because the performance of the fuel cell is highly dependent on the cell geometry, which is a determining factor in both ohmic resistance and diffusion polarisation.

2.1.4.1 SOFC Time Response / Time Constant

The response time, or the relaxation time of the fuel cell to any operating condition or load change is always one of the research topics. Many factors influencing the fuel cell performance can be attributed to the time constant due to step change, like temperature, gas flow, activation and diffusion polarisations. Therefore, it is difficult to model all aspects but ignoring some. In a SOFC model, it is typical to ignore the response time of activation polarisation since high operating temperatures experience little activation polarisation [22]. According to Ref [23] the activation polarisation actually responses fast to the current step change. Therefore for a high temperature SOFC it is rational to neglect the time constant of activation polarisation for simplicity.

Another contribution to the fuel cell response time is the moisture issue. Ref [25] examines the effects on PEM to load changes and one of the reasons for the slow response is the water management issue. The PEM fuel cell system reported in [24] operates at low temperature of about 150 ℃ and is controlled by the rate at which the fuel is fed to it, and has a starting up time constant of 90 seconds. The reported response time to load changes in [24] is as high as 60 seconds. This is because PEM fuel cells produce liquid water instead of steam due to the low temperature operation, and in fact water is required to hydrate the anode in order to help the fuel cell function properly. However step changes in load can cause a dehydration of the anode, which takes about a minute to come back to normal performance. Solid oxide

fuel cells have a different design on materials therefore none of this particular problem exists, which makes SOFCs relative fast response power sources.

The computational fluid dynamic (CFD) code is highly useful in determining the response of the reactants to the load and operating condition changes. The researches which applied CFD code modelling in [19] [20] [25] show that the time constant of the output voltage to step-load changes is highly related to the effect of the temperature dynamics, which is also described in [10] as strongly related to the solid cell structure, the design parameters of the cell (such as the solid material properties: the thermal conductivity, heat capacity and the density). This relaxation process is closely related to the transient temperature distribution within the fuel cell system, since the internal cell resistances are greatly temperature dependent. This arises because the load change in the system changes the amount of resistive losses in the fuel cell, which causes temperature fluctuations in the system. The time taken for the system to reach a thermal equilibrium is the cause of the time constants seen in system performance. However this effect will not be seen if isothermal system is assumed as in [8] [9] and in this research, where all heat produced is assumed to be distributed throughout the system immediately, therefore no time effect due to heat convection and temperature fluctuations is counted for. The only way to see these transient effects would be to use a heat transfer model, or do the computational fluid dynamic (CFD) code modelling of the system, which would greatly increase its complexity. So without this extra modelling it is difficult to predict how long or how significant the transient effects would be. Without the help of a CFD model the relaxation frequency is found higher in the simulated data compared to the experimental data as reported in [23], which means the electrode process is faster in simulations than it is found in the experiments.

Ref [19] [20] also found that the temperature and species dynamics (atoms, molecules or ions subjected to a chemical process) are important for slow transients. Their proposed models confirm that these dynamics can be neglected for fast transients. Results from [22] indicate two time-scale behaviours in the voltage and current. The immediate change is a consequence of the direct dependence of the voltage and current on the cell resistance. The cell-tube temperature response is

significantly slower and has a time constant of about 35s, as the cell tube has a high heat capacity and mass.

2.1.4.2 Heat Transfer and Temperature Modelling

The modelling of heat transfer and temperature dynamic can be difficult and complex, especially for the gas flow involved system with pre-heated inlet gases at none-uniformed temperature. As discussed above, the CFD code modelling can be critical in the heat transfer simulation because both solid components and gas fluids determine the heat convection and radiation behaviours within the stack system. However it is not common in the literature that both influences were considered or simulated, but being made according to the authors' own emphasis and assumptions. Examples in [16] [19] [20] all have an assumption of uniform gas distribution among cells, since there is a small deviation of the gas distribution among the cells. There is no heat transfer among cells and each cell has the same temperature based on the uniform gas distribution assumption. Campanari [16] also made an assumption of uniformed heat generation, with which the heat exchange by radiation within the stack is ignored. Kourosh [19] also presumed a system with the pre-heated inlet gas at the system temperature. However the benefit from the contribution of [16] can be from the application of the CFD code modelling. The applied CFD code modelling in [16] helps to detail the heat exchange model on the inlet flow at different temperatures and the heat losses to the outside of the system due to exhaust gases, which provides a more comprehensive simulation of thermodynamics of gases.

The lack of CFD can lead to inaccuracy in the gas dynamics modelling. However the heat transfer and the radiation effects among cell components still can be modelled as described in [8]. The main contribution from [8] is the heat transfer modelling to both planar and tubular geometries, with the assumptions that the respective temperatures in the anode, electrolyte and cathode layer are regarded as uniform in each specific control volume and the effect of interconnect and circumferential heat conduction is not considered. The modelling of the heat transfer within the fuel cell system can be done by treating the cell components as thermal resistances as thermal lumped parameter which has been successfully used in motors and generators. In [8], the heat conduction is calculated in two dimensions in the planar model, and the heat

flow in the stacking direction is neglected. The tubular model features heat conduction in axial direction as well as radiation between the concentric tubes, and even the radiation between the solid and the injector tube is modelled. Ref [8] shows that the tubular geometry has higher temperature differences than planar between the solid and the injector tube.

2.1.4.3 Calculation of the Efficiency

The efficiency of a fuel cell system is a determining factor. It is inevitable that the pre-heat process for the inlet flow will lower the total cycle efficiency. To enhance the cycle efficiency therefore the concept of combined heat and power (CHP) can be applied to fuel cells and this is traditionally improved either by increasing the steam/gas temperature at the inlet of the steam/gas turbine, or by reducing the discharge temperature at the steam/gas turbine exit [15].

However with different fuel cell designs or concepts, the calculation of efficiency can be altered. Almost all authors in literature consider the fuel cell efficiency as a ratio of the external work (electrical power work) versus the energy enthalpy of the inlet fuel gas. In [26] a different definition is given by only considering the efficiency of the fuel cell as being based on the amount of electrical work that can be extracted from Gibb's free energy ΔG in Equation (2.5). However, ΔG is less than the total fuel energy content ΔH because of the existence of heat energy. Therefore by applying the calculation methodology in [26] the fuel cell efficiency is higher and the electrolysis efficiency is lower. However the overall cycle efficiency can still be the same if considering a recycle operation with the heat $T\,\Delta S$ is reserved.

Another important concept that has to be carefully considered is related to the fuel utilization (FU). In [11] the efficiency is examined by introducing a variation of current ripple. In this concept the highest efficiency can be obtained only when the excess fuel (the wasted fuel that being exhausted) is zero. However this may cause a decrease in the fuel gas partial pressure and lowers the Nernst voltage and the resultant power output. So a trade-off has to be considered, as [17] pointed out that none-zero excess fuel is necessary for an optimal fuel cell operation. It is also found in [11] that a higher magnitude of ripple current forces fuel cells to decrease the

operating fuel utilization (FU), hence, lowers the stack efficiency. And it is highlighted in [18] the power loss caused by ripple currents can be as high as 10%, especially at the frequency twice of the fundamental of electrical power system.

2.2 Requirements of the Integration of Fuel cell and AC Power System

Visions of future power systems contain a high penetration of power electronic inverters that are used to convert power from DC to AC or vice versa. Simple examples are generators interface where the power flow is unidirectional, such as those required to connect a DC source of fuel cell to an AC power distribution network. More complex bi-directional examples are required to connect DC electrical storage devices to the AC distribution network, as in the case of supercapacitor, reversible fuel cell, or vehicle-to-grid storage systems.

Power electronic converters can be catalogued into voltage source converters and current source converters. For fuel cell applications, VSCs are mostly being used. In this section, the background of converter topologies and the relative control fundamentals will be described. Finally the aggregation of VSC induced input current ripple on fuel cell will be described.

2.2.1 Power Electronic Converters

A voltage source converter uses self-commutated devices such as the insulated gate bipolar transistor (IGBT) as its main switching device. It normally uses IGBTs at switching frequency around 2kHz. The adoption of IGBTs in fuel cells for grid integration normally uses the high frequency Pulse Width Modulation (PWM). This results in fast dynamics response and the independent control of active and reactive power. Furthermore, the use of a 1kHz ~ 2kHz switching frequency is sufficient to separate the harmonics from the power frequency, therefore only small size ac filters are needed to mitigated the high order harmonics. Two main inverter topologies currently used for grid integrating of fuel cell. These are two-level inverter and H-bridge with isolated DC source inverter [27].

2.2.1.1 Conventional Two-level Inverter

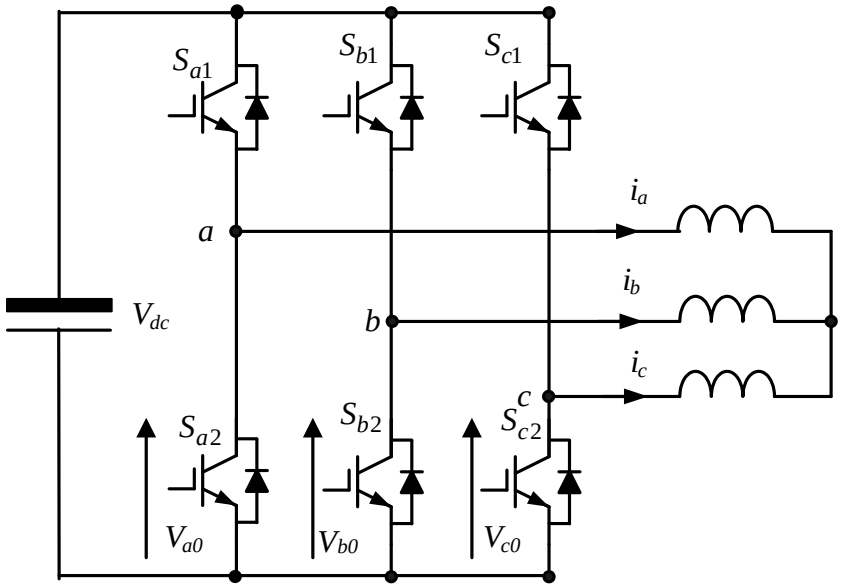

Figure 2.3 Two-level inverter circuit [28]

This type of inverter has been widely used in the power electronic industry and renewable energy applications over decades, the two series switches in each leg (e.g. Sa_1 and S_{b2}) are complementary switch pairs, when one switch is turned on /off, the other switch must be off/on. Each phase can produce two voltage output level $+V_{dc}$ or $-V_{dc}$, and line-to-line output voltage will have three-levels.

2.2.1.2 Cascaded H-bridge Inverter

The cascaded H-bridge inverter is based on the series connection of H-bridge cells to achieve multi-level output of voltage. The cascaded H-bridge multi-level inverter requires a number of isolated dc sources to support each H-bridge cell which is suitable for fuel cell application as shown in Figure 2.4 [28]. Each power modular is capable of producing an output voltage of $+V_{dc}$, 0, or $-V_{dc}$ by connecting the dc source to the output terminals in different combinations of the four switches. The two series switches in each leg and module (e.g. S_1 and S_3) are complementary switch pairs, means when one switch is turned on /off, and the other switch must be off/on.

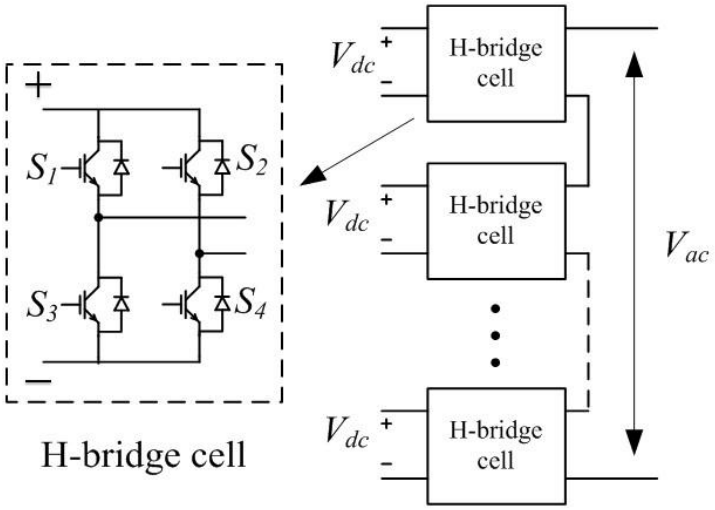

Figure 2.4 cascaded H-bridge with electrical isolated DC sources converter [29]

Table 2.1 Switching states combinations of one cell of Cascaded H-bridge Inverter.

Switching state	Device switching status (Phase A)				Terminal voltage V_{ac}
	S_1	S_2	S_3	S_4	
1	On	Off	Off	On	$+V_{dc}$
0	Off	Off	On	On	0
	On	On	Off	Off	
-1	Off	On	On	Off	$-V_{dc}$

The operating status of the switches can be represented by switching states shown in **Error! Reference source not found.**. Switching state '1' denotes that the two switches S_1 and S_4 are on and the inverter terminal voltage V_{ac} is $+V_{dc}$, whereas '-1' indicates that the two switches S_2 and S_3 conduct, leading to $V_{ac} = V_{dc}$. Switching state '0' determines that either the upper two switches S_1 and S_2 or the lower two switches S_3 and S_4 are on or off.

The cascaded H-bridge converter has been proposed for photovoltaic grid integration [30]. Also, it is suitable for fuel cell grid integration applications due to the fact that each H-bridge module can be supplied by a series connection of fuel cells and can

generate the multi-level output voltage with high voltage qualities and current with lower THD, compared to the conventional Two-level inverter.

2.2.2 Pulse Width Modulation (PWM)

For any pulse width modulation (PWM) scheme, a primary objective is to calculate the duty cycles for the converter switches to output the desired voltage and current. Secondly, it is used to determine the most effective way of arranging the switching processes to minimize undesired THD and switching losses, etc. [31]. The mostly used PWM schemes for VSC are the carrier-based Sinusoidal Pulse Width Modulation (SPWM) and the Space Vector Pulse Width Modulation (SV-PWM).

2.2.2.1 Carrier-based SPWM

The carrier-based SPWM technique controls each phase leg of the converter individually. Comparisons between one or more carrier signals and the modulating signal determine the on/off action for the switches, and the width of each pulse generated is in proportion to the amplitude of a reference wave evaluated at the pulse centre [32], as shown in Figure 2.5. Figure 2.6 shows the line-to-line voltage, three-phase current and the frequency spectrums of a conventional two-level inverter based on 400kV DC voltage, 0.85 modulation index and 1500Hz modulation frequency using SPWM.

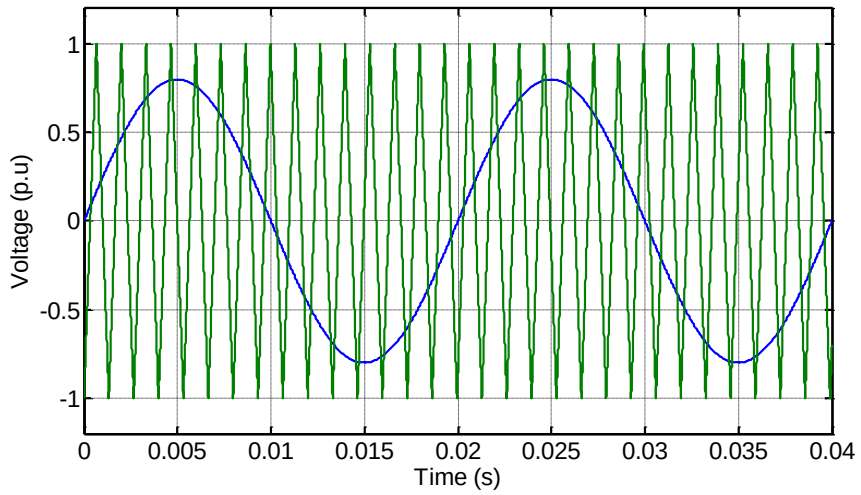

Figure 2.5 Two cycles of PWM signals generation for two-level converter (*M=0.85*, f_c*=1500Hz*).

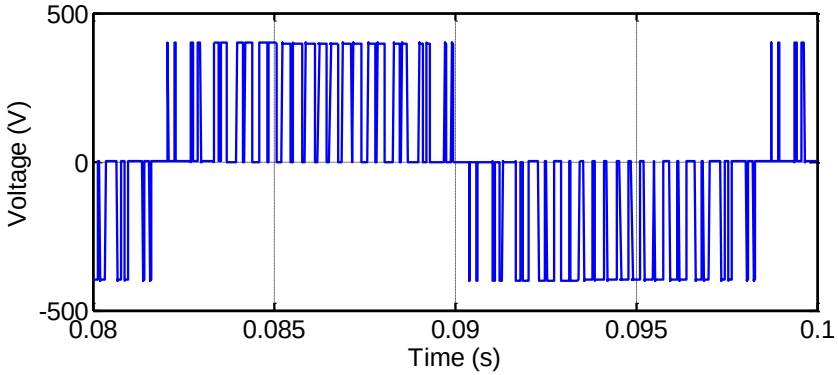

(a)

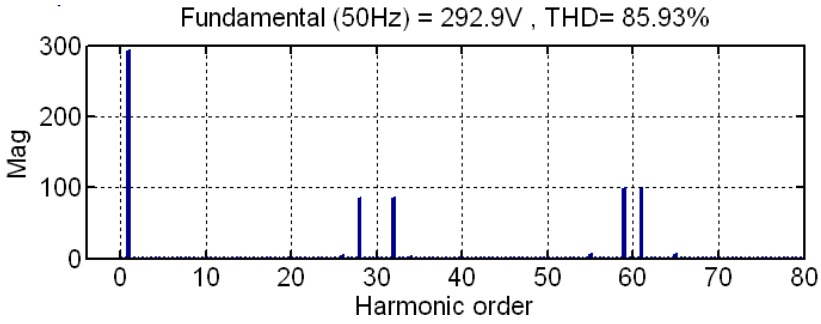

(b)

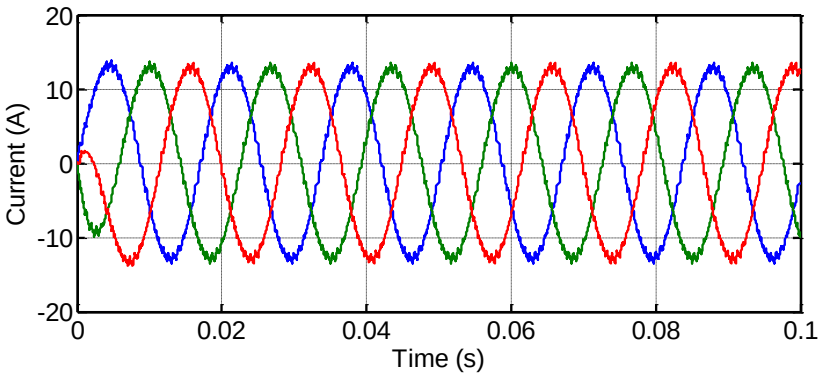

(c)

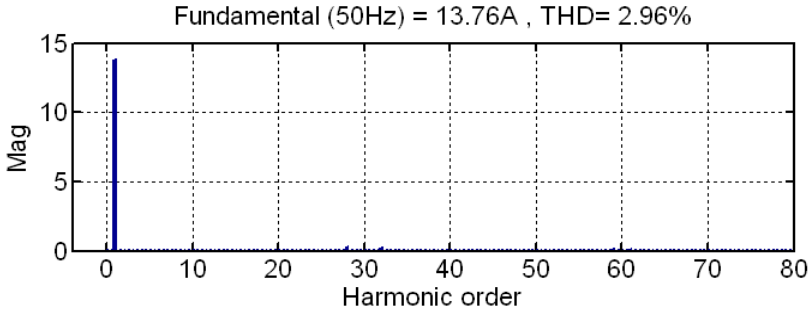

(d)

Figure 2.6 Line-to-line voltage, three phase current and their spectrum of a two-level inverter (*M=0.85, V_{dc}=400V.f_c=1500Hz*).

2.2.2.2 Space Vector PWM (SV-PWM)

The SV-PWM is normally applied within a three-phase system. Compared to the carrier-based PWM, the SV-PWM treats the three inverter phases as a single unit. The SV-PWM is a digital modulating technique with the objective to generate PWM based voltages equal to a reference voltage vector on average [33]. The diagram of space vectors for a two-level inverter is shown in Figure 2.7. The vertex of each triangle represents a space vector. To explain the space vectors, an example of vector $V^* = 100$ indicates the three phase voltage as: $V_a = V_{dc}, V_b = 0$ and $V_c = 0$, etc, (where V_a, V_b, and V_c are the phase voltages), and V^* can be derived as: $V^* = V_a + V_b e^{j\frac{2\pi}{3}} + V_c e^{-j\frac{2\pi}{3}}$, with the coordinates described in Appendix A, the magnitude and phase angle are $V_{ref} = \sqrt{V_\alpha^2 + V_\beta^2}$ and $\theta = arctan\frac{V_\beta}{V_\alpha}$, respectively:

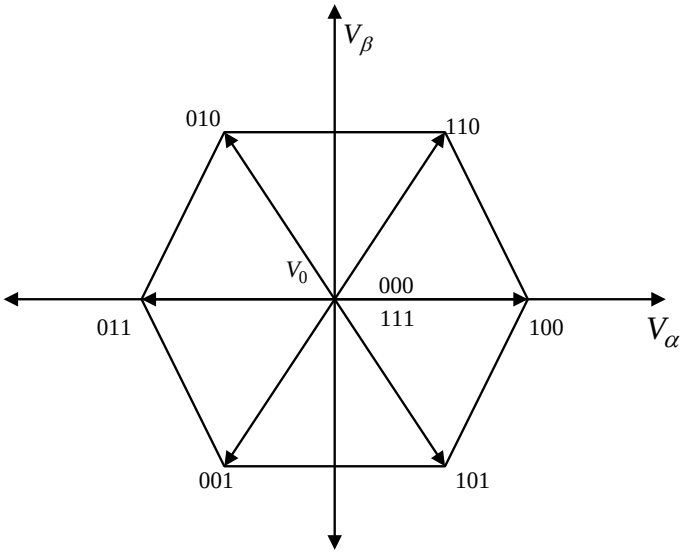

Figure 2.7 Space vector diagram for a two-level inverter.

Figure 2.8 shows the line-to-line voltage, three-phase current and their spectrum simulation results of a conventional two-level inverter based on 400V DC voltage, 0.85 modulation index and 1500Hz modulation frequency using SV-PWM.

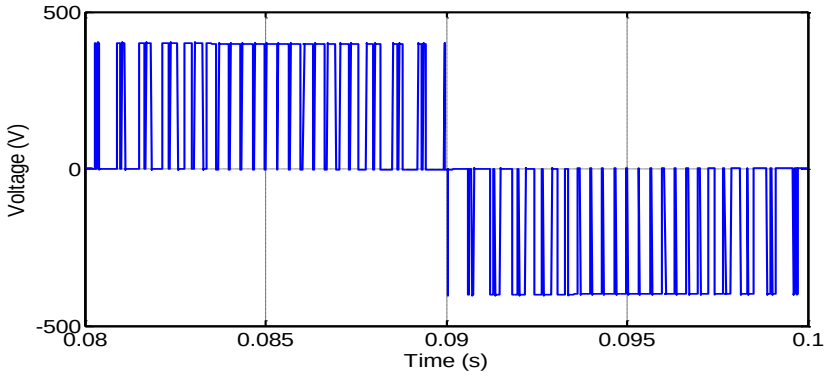

(a)

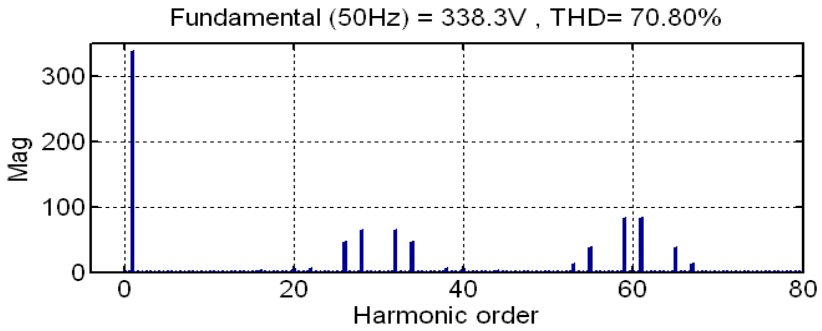

(b)

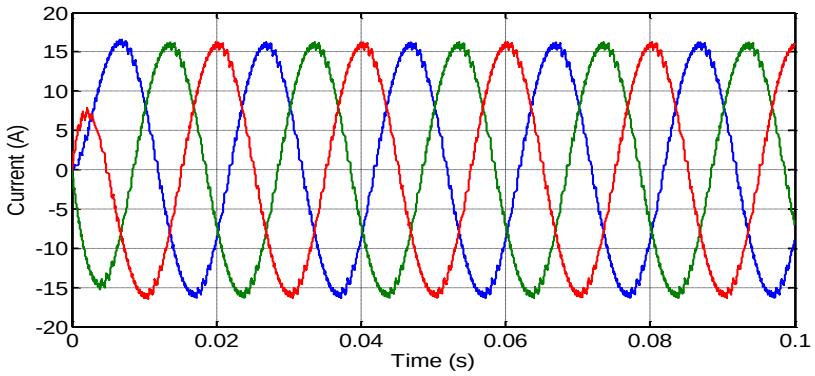

(c)

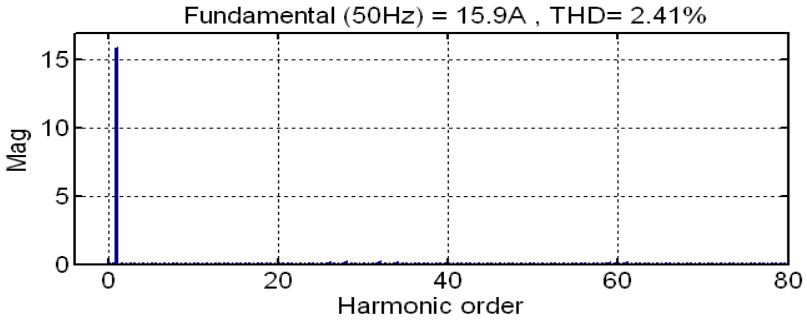

(d)

Figure 2.8 Line-to-line voltage, three phase current and their spectrum of a two-level inverter (*M=0.85, V_{dc}=400V.f_c=1500Hz*).

Compared to the SPWM, the SV-PWM offers dc-link efficiency as high as 15.47%, thus higher fundamental component of three-phase current. The total harmonic distortion (THD) of the three-phase output current using SV-PWM is lower compared to what due to SPWM (2.96% with SPWM, 2.41% with SVPWM). Moreover, the SV-PWM has advantages in digital implementation, thus is employed in this research.

2.2.3 Effects of the Fuel Cell Input Current Ripple Induced by Power Converters/Inverters

An inverter load applied to a fuel cell has several transient features [8]. There is a current ripples related to the frequency of the fundamental output waveform e.g., 100 Hz ripple for a 50 Hz single-phase output for certain inverter topologies. In addition, there may be a high frequency ripples related to a DC/AC VSC switching frequency and the carrier frequency at a PWM output stage [17]. Such ripple currents may shorten fuel cell life span and worsen the fuel efficiency due to the hysteresis effect [34]. The hysteresis effect is experienced in Ref [35] on a PEM cell system and it does not occur around 1Hz because the double layer capacitance has enough time to fully charge and discharge. And it has no effect around 10kHz either because the capacitor does not have enough time to charge or discharge. However, a “hysteresis” appears around 100Hz due to the double layer impedance dipole.

The most obvious impact of high ratio of ripples is its tendency to reduce the fuel cell output capacity. The fuel cell controller also may trip under instantaneous over-current condition [34]. However short-term studies in [17] with negligible diffusion limits and at fuel and air utilizations below 70% and 20% respectively show that a PEM fuel cell can withstand significant load changes without noticeable degradation. Even so, to ensure a minimal impact on performance of the fuel cell, as well as its durability, fuel cell developers would prefer to specify as little ripple as possible, e.g., below 2% of the theoretical fuel cell current [36]. Since the reactant utilization is known to impact the mechanical nature of a fuel cell, it is suggested in [18] that the varying reactant conditions surrounding the cell (due to ripple current) govern, at

least in part, the life time of the cells. Both the magnitude and frequency of the ripple current is important.

Fuel cells have an internal impedance that is variant to the current frequency. The internal impedance has a larger magnitude at low frequencies (< 1 kHz). The presence of low frequency current ripple has side effects as additional heating, and more importantly, a reduction in the output power, thus diminishing the power availability and power conversion efficiency of the system [37].

2.2.3.1 Generation and Propagation of Low Frequency Current Ripples

The generation and propagation of the 100Hz low frequency ripple in case of the single phase inverter can be explained by using energy conservation law. The voltage and current of the inverter are given in Equation (2.7) and (2.8) respectively.

$$v_o(t) = V_m \cos(\omega t + \theta) \tag{2.7}$$

$$i_o(t) = I_m \cos(\omega t + \varphi) \tag{2.8}$$

where θ and φ represent phase angles of voltage and current. The frequencies of the output voltage and current are the same as ω, so that the output power has double the frequency (i.e. 2ω) This can be derived as in Equation (2.9).

$$P_{out}(t) = \frac{V_m I_m}{2}\{\cos(2\omega t + \theta + \varphi) - \cos(\theta - \varphi)\} \tag{2.9}$$

The powers at DC link and at output should be identical by means of the energy conservation law as Equation (2.10), neglecting the inverter loss.

$$V_d(t) I_d^*(t) = v_o(t) i_o(t) \tag{2.10}$$

The frequency and shape of the DC link current ($I_d^*(t)$) has the same as the counterparts of the output power and it can be calculated as Equation (2.11) [38]

because that the DC link voltage is regulated by the control of the converter output voltage.

$$I_d^*(t) = \frac{V_m I_m}{2V_d}\cos(2\omega t + \theta + \varphi) - \frac{V_m I_m}{2V_d}\cos(\theta - \varphi) \qquad (2.11)$$

2.2.3.2 Harmonic Analysis of Converter and Inverter

A fuel cell current of the converter appears as a pulsating waveforms as shown in Figure 2.9 (a). Generally a film capacitor is used to filter high frequency ripple components and the output current of the filter becomes more continuous in shape as shown in Figure 2.9 (b). By Fourier analysis, this continuous waveform can be expressed as Equation (2.12) [38].

$$f(t) = a_o + \frac{8A}{\pi^2 n^2}\sum_{n=1}^{N} sin\frac{n\pi}{2}\sin n\omega_0 t \qquad (2.12)$$

where *n=odd numbers*, ω_0 is the fundamental frequency, a_o is the DC base magnitude.

The fuel cell current consists of a fundamental frequency component and odd-multiple components of switching frequency. Therefore, it does not affect the generation of low frequency ripple components. The Fourier coefficient B_n is derived as Equation (2.13) and the harmonics in the output current waveform appears as sidebands, centred around twice the frequency modulation index, $2\,m_f$ and its multiple is given as in Equation (2.14) [39].

$$B_n = \sum_{m=1}^{2p} \frac{4\mathrm{A}}{n\pi} sin\frac{n\delta_m}{2}\left[\sin n\left(\alpha_m + \frac{3\delta_m}{4}\right) - \sin n\left(\pi + \alpha_m + \frac{\delta_m}{4}\right)\right] \qquad (2.13)$$

where δ_m is the width of m^{th} pulse, and α_m is the phase angle of the m^{th} pulse,

$$f_n = [j(2m_f) \pm k] \times f_c \qquad (2.14)$$

where, n (=1,3,5…, m_f) is frequency modulation index. Therefore, the high frequency ripple due to switching frequency does not affect the low frequency ripple.

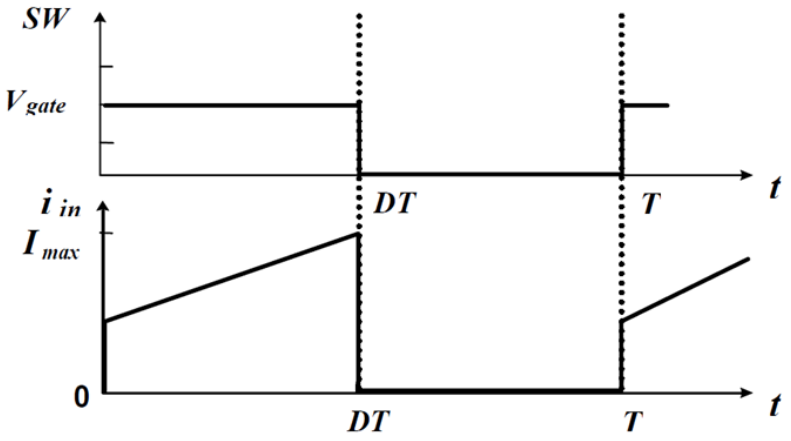

(a) Without filter

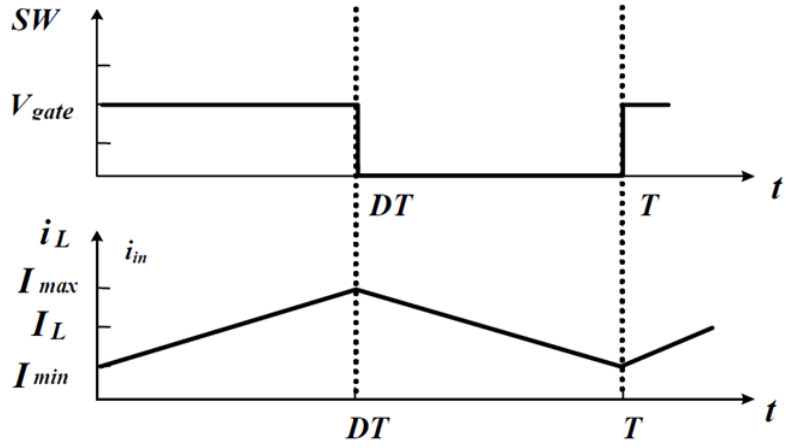

(b) With filter

Figure 2.9 Fuel cell current of the full bridge converter [38]

It is also proven in the literature that the high frequency current ripple can be totally ignored. Ref [34] [40] [41] highlighted that the PWM switching noise can be easily filtered by a high-frequency dc bus capacitor. In [35] it has been shown that even a fuel cell stack offers possibilities to filter high frequency current harmonics by the

intermediary of its double layer capacitor. The ageing tests in [42] show only a slight effect of high frequency current oscillations produced by the electrical interactions of a DC/DC converter on the reduction of the PEMFC stack performances. Therefore, it can be concluded that the power converter will be able to impose a high frequency current ripple on the delivered FC current without altering the lifetime of the stack. And a National Energy Technology Laboratory (NETL) study [43] reports that the ripple frequencies above 400 Hz have only minor impact on the fuel cell operation.

2.3 Conclusions

This chapter has presented a comprehensive literature review on aspects of determining factors of the system design to the performance of SOFC. The analysis of previous work provides perspectives on the conventional approaches as a useful tool for learning and facilitating in the new scopes. However the literature also provides a huge number of specifications, assumptions and methodologies that lead to diverse results. Those diversities need to be carefully discussed and revised with the specific perspective of the investigation of a reversible fuel cell system proposed in this research, which whose design differs in many aspects to that of conventional fuel cell systems. This opens an opportunity to reconsider or modify existing methodologies.

The electrical effect of implementing inverters on RSOFC system, mainly the induced input current ripple, is introduced using energy conservation law. A strong background in the fundamental knowledge of power electronic converter design and output modulation derivations provides is necessary in the investigation of integrated RSOFC system into power grid.

2.4 References for Chapter 2

[1] Private communication with Dr. Stephen Gamble, in the University of St. Andrews, UK

[2] M. Mogensen, S. H. Jensen, A. Hauch, I. Chorkendorff, T. Jacobsen "Recycling CO2 into Sustainable Hydrocarbon Fuels: Electrolysis of CO2 and H2O," in *7th European Solid Oxide Fuel Cell Forum*, European Fuel Cell Forum, Lucerne, pp. 301–311.

[3] K. Sedghisigarchi and A. Feliachi, "Dynamic and transient analysis of power distribution systems with fuel cells-Part I: Fuel cell Dynamic model," *IEEE Trans. Energy Conversion,* vol. 19, no. 2, pp. 423−428. Jun. 2004

[4] D. J. Hall and R. G. Colclaser, "Transient modeling and simulation of tubular oxide fuel cell," *IEEE Trans. Energy Conversion,* vol. 14, no. 3, pp. 749 –752. Dec. 1999

[5] Department of Energy & Climate Change. (DTI). (2006). The energy challenge, energy review report 2006. [Online]. Available: http://www.berr.gov.uk/files/file31890.pdf

[6] U. S. Department of Energy. (2009). International energy outlook 2009. [Online]. Available: *http:// www.eia.doe.gov/oiaf/ieo/index.html*, 2009

[7] S. C. Singhal, "Advances in solid oxide fuel cell technology," *J. Solid State Ionics*, vol. 135, pp. 305–313, 2000.

[8] S.Christoph, T., Bjørn; S. Steinar; "Finite-volume modeling and hybrid-cycle performance of planar and tubular solid oxide fuel cells" *J. Power Sources*, vol. 141 (2Mar, 2005.

[9] Y. Shia, N. Caia, C. Lia, C. Baoa, E. Croisetb, "Simulation of Electrochemical Impedance Spectra of Solid Oxide Fuel Cells Using Transient Physical Models," *J. Electrochem. Soc,* vol. 155, issue. 3, .2008

[10] E. Achenbach, "Response of a solid oxide fuel cell to load change," *J. Power Sources*. vol. 57, issues 1–2, pp. 105–109, Sept 1995.

[11] K. Sanjaya, "Effects of Electrical Feedbacks on Planar Solid Oxide Fuel Cell," *J. Fuel. Cell. Science & Technology*, vol.4, pp. 154-166, 2007.

[12] N.Q. Minh, J. Am. Ceram. "Solid oxide fuel cell technology—features and applications," *J. Solid State Ionics,* pp. 76-563, 2004,.

[13] S.C. Singhal, in: "The role of electrode microstructure on activation and

concentration polarizations in solid oxide fuel cells," in *1997 Joint International Meeting*, the Electrochemical Society and the International Society of Electrochemistry, Paris, France, August 31–September 5, 1997, p. 2498.

[14] A. V Virkar, J. Chen, C. W Tanner, JJ. Kim, "The role of electrode microstructure on activation and concentration polarizations in solid oxide fuel cells," *J. Solid State Ionics*, vol.131, issues 1–2, pp. 189–198, June 2000.

[15] S.H Chan, K.A Khor, Z.T Xia, "A complete polarization model of a solid oxide fuel cell and its sensitivity to the change of cell component thickness,", *J.Power Sources,* vol. 93, Issues 1–2, pp. 130–140, Feb 2001.

[16] S. Campanari, P. Iora, "Definition and sensitivity analysis of a finite volume SOFC model for a tubular cell geometry," *J. Power Sources*, vol. 132, Issues 1–2, pp. 113–126, May 2004

[17] R. S. Gemmen, "Analysis for the effect of inverter ripple current on fuel cell operating condition," *J. Fluids Eng.*, vol. 125, no. 3, pp. 576–585, 2003.

[18] W.Choi, P. Enjeti, "Development of an equivalent circuit model of a fuel cell to evaluate the effects of inverter ripple current," , J. *Power Sources*, vol. 158, pp. 1324–1332, 2006

[19] K. Sedghisigarchi, A. Feliachi, *"*Dynamic and transient analysis of power distribution systems with fuel cells—Part I: fuel-cell dynamic model," *IEEE Trans. Energy Conversion*, vol. 19, NO. 2, June 2004

[20] K. Sedghisigarchi, A. Feliachi, "Dynamic and transient analysis of power distribution systems with fuel cells—Part II: fuel-cell power system," IEEE Trans. Energy Conversion, vol. 19, NO. 2, June 2004

[21] A. Gebregergis, P. Pillay, *"*The Development of Solid Oxide Fuel Cell (SOFC) Emulator,*"* in 2007 *Power Electronics Specialists Conference*, Clarkson Univ. Potsdam, Potsdam Pillay, P. June 2007, pp. 1232-1238

[22] S. Ahmad Hajimolana and Masoud Soroush,*"*Dynamic Behavior and Control of a Tubular Solid-Oxide Fuel Cell System,*" in 2009 American Control Conference,* Dept. of Chem. Eng., Azad Univ. of Shahrud, Shahrud, Iran Soroush, M. June 2009, pp. 2660-2665

[23] A. Bieberle, L.J. Gauckler, "State-space modeling of the anodic SOFC system Ni, H2–H2OjYSZ," J. *Solid State Ionics*, vol. 146, pp. 23 – 41, 2002

[24] P.T. Krein, “Low cost inverter suitable for medium-power fuel cell sources,” in *2002 Power Electronics Specialists Conference*,. pesc 02. IEEE 33rd Annual, vol. 1, pp. 321- 326

[25] P. Kazempoora, F. Ommia, V. Dorerb, “Response of a planar solid oxide fuel cell to step load and inlet flow temperature changes,” *J. Power Sources*, vol. 196, Issue 21, pp. 8948–8954, Nov 2011.

[26] S. Samuelsen, “Dynamic analyses of regenerative fuel cell power for potential use in renewable residential applications,” *J. Hydrogen Energy*, pp. 994-1009, 2002.

[27] J. Wang, F. Z. Peng, J. Anderson, A. Joseph, and R. Buffenbarger, ”Low cost fuel cell inverter system for residential power generation,” in *Applied Power Electronics Conference and Exposition, 2004. APEC '04. Nineteenth Annual IEEE*, Vol.1, 2004, pp. 367-373.

[28] R. Seyezhai and B. L. Mathur, “Hybrid cascaded H- bridge multilevel inverter for fuel cell power conditioning systems,” in *Universities Power Engineering Conference, 2008. UPEC 2008. 43rd International*, the University of Padova, Italy, 2008, pp. 1-5.

[29] L. Yi-Hung and L. Ching-Ming, “Newly-constructed single-phase multistring multilevel inverter for fuel-cell microgrid,” in *Power Electronics and ECCE Asia (ICPE & ECCE), 2011 IEEE 8th International Conference on*, 2011, pp. 1440-1444.

[30] S. J. Lee, H. S. Bae, and B. H. Cho, “Modeling and control of the single-phase photovoltaic grid-connected cascaded H-bridge multilevel inverter,” in *Energy Conversion Congress and Exposition, 2009. ECCE 2009. IEEE*, 2009, pp. 43-47.

[31] T. A. l. D.G. Holmes, *Pulse Width Modulation for Power Converters: Principle and Practice*, Wiley-Interscience IEEE, 2003.

[32] S. R. Bowes and L. Yen-Shin, “The relationship between space-vector modulation and regular-sampled PWM,”*, IEEE Trans. Industrial Electronics,* vol. 44, pp. 670-679, 1997.

[33] M. A. A. Younis, N. A. Rahim, and S. Mekhilef, "Fuel Cell Model for Three-Phase Inverter," in *Power and Energy Conference, 2006. PECon '06. IEEE International*, 2006, pp. 399-404.

[34] C. Liu, J. Lai, “Low Frequency Current Ripple Reduction Technique With Active Control in a Fuel Cell Power System With Inverter Load”, *IEEE Trans. Power Electronics*, pp. 1429 - 14362007

[35] G Fontes , "Interactions between fuel cells and power converters influence of current harmonics on a fuel cell stack", in Power Electronics Specialists Conference, 2004. PESC 04. 2004 IEEE 35th Annual, 4729- 4735 Vol.6, June 2004

[36] G. Allen, ‘‘Equipment Design and Interface Specifications for 10 kW Inverter,’’ Inverter specification data provided by Fuel Cell Technologies, Ltd. for the Future Energy Inverter Competition.

[37] L. Palma. "An active power filter for low frequency ripple current reduction in fuel cell applications", in *Power Electronics Electrical Drives Automation and Motion (SPEEDAM)*, 2010 International Symposium on, 1308- 1313 , 2010

[38] J, Kim, H, Kang, “Analysis of Low Frequency Current Ripples of Fuel Cell Systems based on a Residential Loads Modeling”, in *Proceeding of International Conference on Electrical Machines and Systems 2007*, Oct. 8~11, Seoul, Korea

[39] Muhammad H. Rashid, *Power Electronics Circuits, Devices and Applications, 3rd ed*. PRENTICE HALL, 2004, pp.576-585.

[40] B. Ozpineci, "TRADE STUDY ON AGGREGATION OF MULTIPLE 10-KW SOLID OXIDE FUEL CELL POWER MODULES", in *Applied Power Electronics Conference and Exposition Annual IEEE Conference* – APEC, Oak Ridge National Laboratory, pp. 133-141, 2011

[41] EG&G Technical Services, Inc. *Fuel Cell Handbook (Seventh Edition),* U.S. Department of Energy Office of Fossil Energy National Energy Technology Laboratory November 2004

[42] Wahdame, B. "Impact of power converter current ripple on the durability of a fuel cell stack", in *Industrial Electronics, 2008*. ISIE 2008. IEEE International Symposium on, 1495- 1500, 2008

[43] R. S. Gemmen, “Analysis for the effect of inverter ripple current on fuel cell operating condition,” *J. Fluids Eng.*, vol. 125, no. 3, pp. 576–585, 2003.

3 Development of a Comprehensive Model of the Reversible Solid Oxide Fuel Cell System as an Innovative Energy Storage

3.1 Introduction

This Chapter describes the computer modelling of the reversible solid oxide fuel cell (RSOFC) system as shown in Figure 3.1 which is based on the electro-chemical equations that will be introduced in the following. The RSOFC stack system model involves the electrical properties of Nernst voltage and cell polarisations in both fuel cell and electrolysis modes. The stack modelling also features the configuration of cells connection, as well as the temperature, partial pressure, state of charge (SOC) and heat capacity based thermal dynamic, as shown in Figure 3.1.

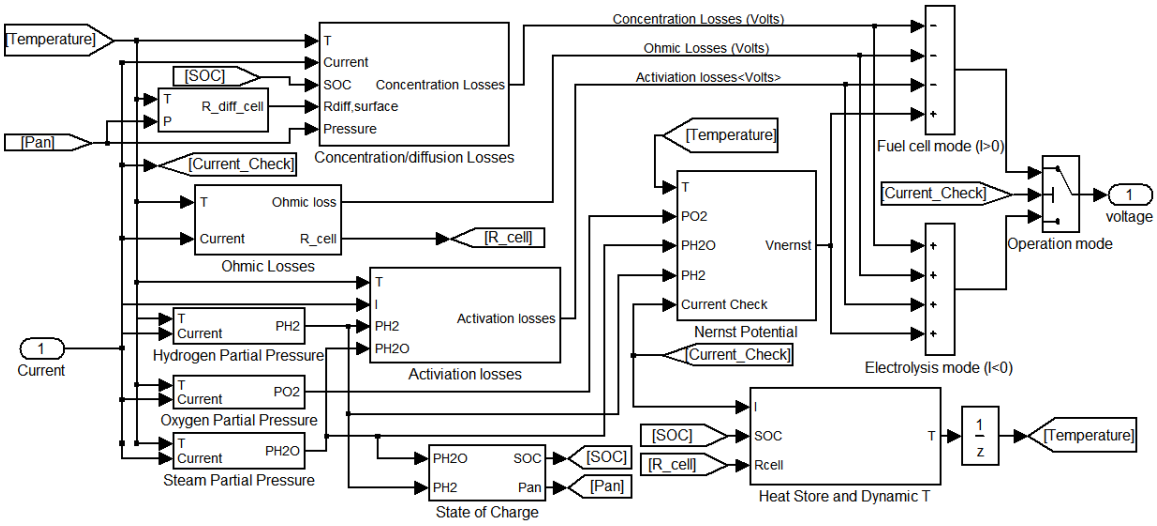

Figure 3.1 Matlab/Simulink model of a single fuel cell

It is essential that the model developed in this thesis delivers a comprehensive representation of the RSOFC system proposed by the University of St. Andrews. Therefore the model is required to be highly detailed with multiple sub-models to be integrated with the specific settings of geometry for both the cell and stack system. It has been introduced in Chapter 2 that both tubular and planar cell geometry can be considered and in this research it is the tubular cell being developed at the University

of St. Andrews. Therefore it is important that the research at the University of Strathclyde provides a comprehensive tubular cell modelling to investigate the performance and accordingly introduce modification for possible improvement.

One unique design of this fuel cell is related to an individual support component within the cell, rather than the generalised approach which use the electrolyte or electrodes as the support. This design greatly reduces the thickness of the electrolyte and electrodes and in tandem lowers the diffusion polarisation. However it leads to higher cell resistance. Therefore it is essential to analyse the resultant diffusion polarisation under such a design.

In previous works, most researchers develop fuel cell models as equivalent circuits to represent the polarisations of activation, diffusion and ohmic resistance, for the purpose of simplicity. In fact these variations are highly dependent on the cell/stack geometry which in fact is a determining factor in temperature variation, in turn, influence the system performance. Therefore it is important that all effects of stack parameters on fuel cell performance are fully modelled. In addition, critical shortcomings in the original design proposed by the University of St. Andrews are discovered by the help of the stack model, which also provides the simulations for the design enhancements in the purpose of performance improvements.

During the investigation two issues about the stack performance have been found. One is the inadequate hydrogen storage capacity, and another is the overheating issue. To overcome the first one, the stack geometry and the pressurisation level are improved according to the simulations results. In addition, a novel application of a copper-tin based heat store system is proposed and described in this chapter which is used to stabilize the system temperature by phase change.

3.1.1 Previous Modelling and Research Works

Many examples of models describing SOFC system can be found in literatures. The SOFC can use a wide range of fuel, for example both H_2 and CH_4 are utilized in [1] and [2]. However in this research only hydrogen is used. The difference in applied fuel gases can distinguish many characteristics from one type of fuel cell to others.

Most importantly the derivation of electron-transfer coefficient can be significant different, which is a key parameter in determining low and high polarisation, and this is described in Section 3.3.4.

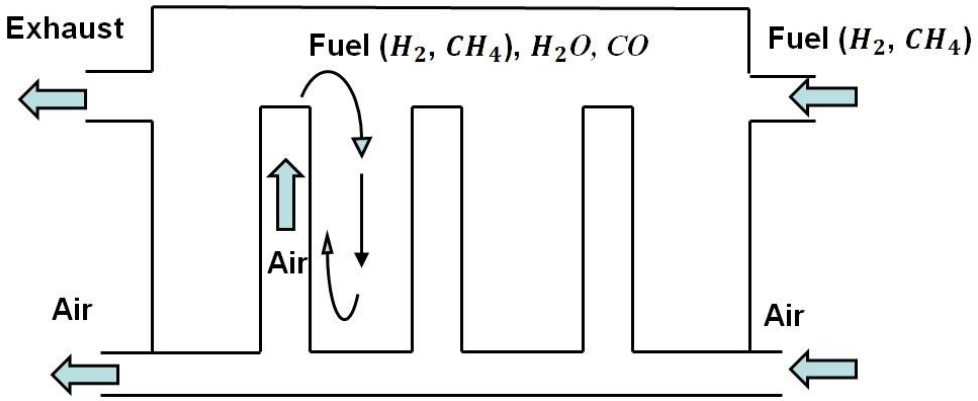

(a)

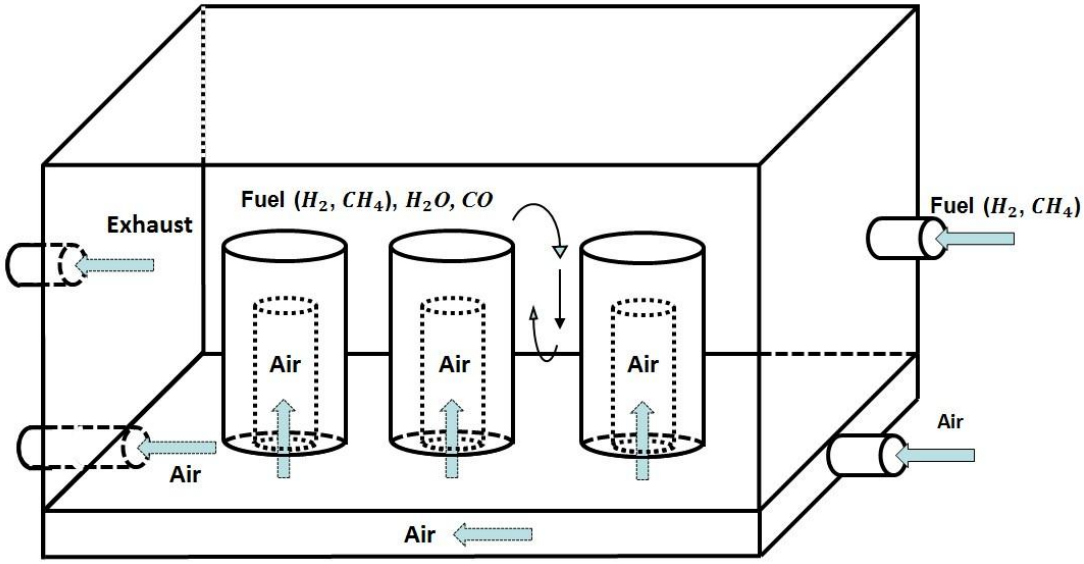

(b)

Figure 3.2 Generic SOFC system design of fuel utilization: (a) the vertical section, (b) the space diagram

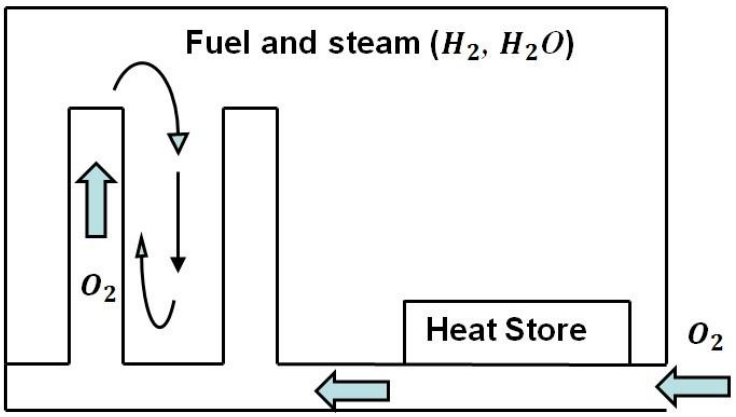

(a)

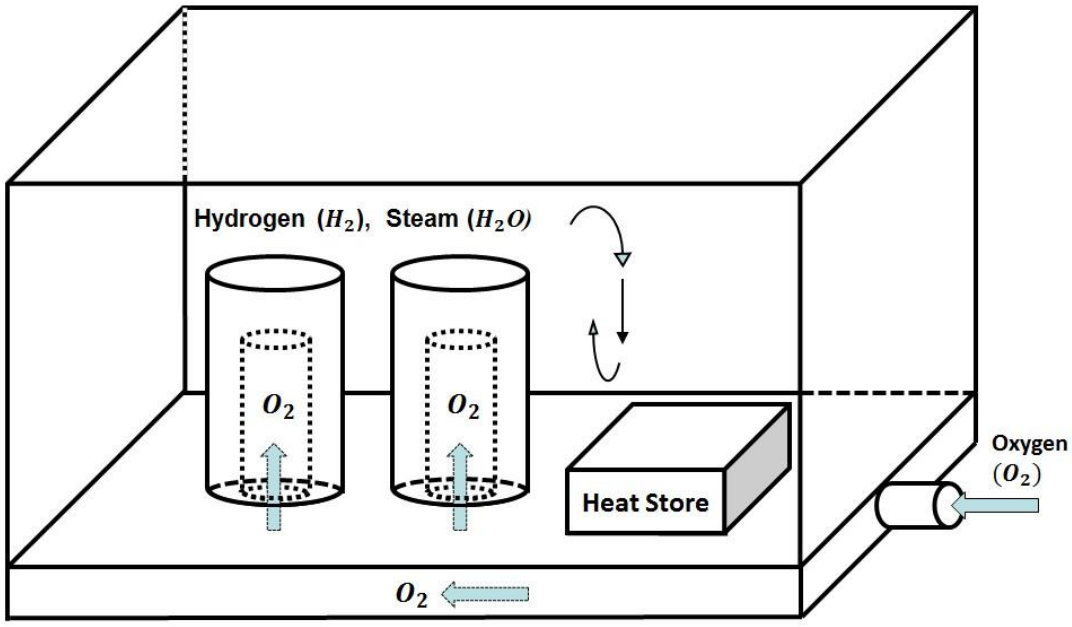

(b)

Figure 3.3 The RSOFC stack system fuel utilization: (a) the vertical section, (b) the space diagram

Most designs of SOFC system found in literatures have controlled reactant inlets as shown in Figure 3.2. Examples in [1] [2] [3] [4] and [5] use the input fuel flow to control the cell performance by altering the reactants partial pressures. Higher flow rate leads to more reactions happening on electrodes, so more power is produced. However in this generic fuel cell design it is inevitable that some of the input fuel is not consumed but wasted by exhaust. To implement the fuel cell concept as a

reversible energy storage, the RSOFC system in this research is designed by the University of St. Andrews with no fuel gas inlets or exhaust as shown in Figure 3.3. This is the most distinguished difference compared to the generalized fuel cell designs. The proposed RSOFC stack system only has oxygen pumped into the inner tube of the cells which are attached onto a insulation platform. The heat store is used to partially reserve the heat energy.

For the heat dynamic modelling, in Ref. [3] [6] [7] they proposed SOFC systems neglecting the heat storage capability of the fuel gases and oxidant gas, so the fidelities of their models could be limited due to the simplifications on the thermal behaviours and overestimating the fuel cell heat capacity. In [8] it is interesting to know that the diffusion over-potential is not counted within the model. In [9] and [10] it is also suggested that the electrochemical kinetics is mainly limited to the activation polarisation/over-potential.

The SOFC normally operates at high temperature which may require heat extraction strategy. However the sealing material tested in [11] can be used in system insulation to maintain the temperature and minimise the effect of time constant due to step changes. Ref. [12] indicates the issue of slow time constant during load changes due to the low operating temperature and the water management issue in PEM cells (cell surface water prevents reactant exchanging). The PEM system requires hydration of the anode in order to function properly. However the SOFC does not have this requirement [13].. Therefore the determination of relaxation time/time constant normally requires the CFD codes modelling as discussed in Chapter 2 [1]. In [10] the lumped parameter modeling is applied. By this way the calculation of heat transfer is determined similarly as using an equivalent electrical circuit. However either the CFD modeling or lumped parameter modeling is not considered in this thesis due to the lack of available sources.

3.2 Summary of the Features of RSOFC System and the Modelling

3.2.1 RSOFC Modelling Protocols

The RSOFC system is a mathematical model developed in the Simulink/Matlab environment. To achieve the reversible operations some of the structures consist of several sets of sub-model in parallel representing the electro-chemical characteristics for both operation modes (fuel cell mode and electrolysis mode). The modelled monitors are demanded during the development due to the introduction of the innovative heat store which features different molten stages. The other requirements of such a model include:

(a) System modelling which enables fast responses in dynamic simulations.

(b) Justifications of the thermal balance.

(c) Capability of connecting to AC power network models in Matlab/Simulink (from SimPower package).

3.2.2 RSOFC Material and Geometry

The RSOFC requires materials to be heat resistant and stable in oxidizing and these can be the ceramic ionic conductor of Yttrium stabilized Zirconia (YSZ). YSZ has been very deeply studied, and is known to be stable, fairly unreactive with other perovskites. The thickness of the active layers is always a challenging topic in cell design. Thin active layers could minimize gas diffusion polarisation losses [14] but are inevitably weak in mechanical stress. Therefore the SOFC is usually supported by a thick layer, which can be one of the active layers, usually the fuel electrode, electrolyte, or oxygen electrode. It may also be an inactive porous ceramic support e.g. the Rolls-Royce Fuel Cell Systems planar cell, or a metallic interconnect support [15]. From the survey of literature, a design for a reversible SOFC is proposed from University of St. Andrews. The geometry of an individual cell is a tube, and the illustration in Figure 3.4 [16] It is formed of a ceramic support tube which is the individual cell shown in Figure 3.3, with a interconnect on top, then anode,

electrolyte, and cathode layers (in fuel cell mode). Hydrogen constantly presents at the anode side and reacts with oxygen ions which pass through the cathode, electrolyte and anode to form water (steam). **Error! Reference source not found.** shows the different manufacturing methods proposed for each of the components. The detailed geometry and dimension are proposed by the University of St. Andrews in **Error! Reference source not found.**.

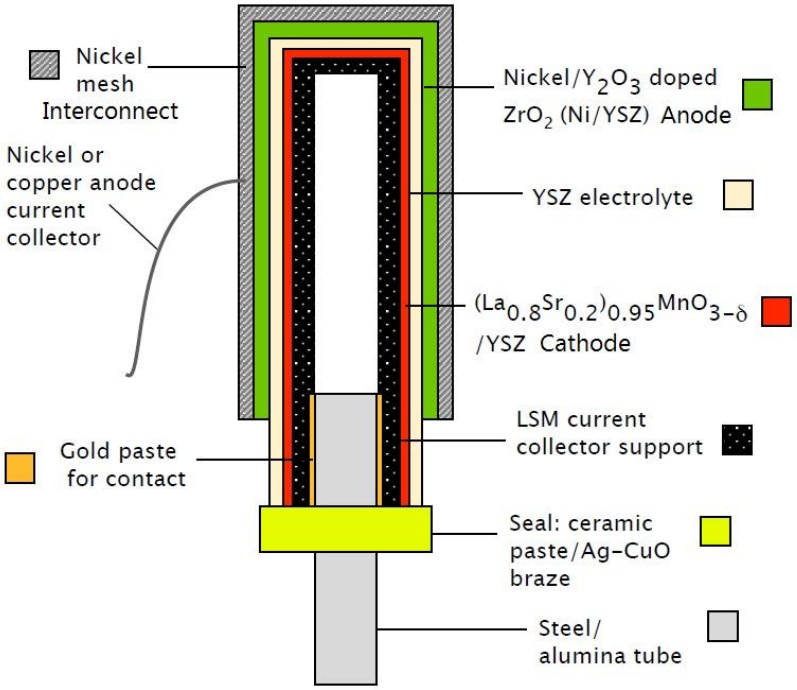

Figure 3.4 A schematic of the proposed tubular reversible SOFC (not to scale) [16]

Table 3.1 Proposed materials and manufacturing methods for the tubular reversible SOFC [16]

Component	Material	Manufacturing method
Support	$(La_{0.8}Sr_{0.2})_{0.95}MnO_{3-\delta}$	extrusion
Oxygen electrode	$(La_{0.8}Sr_{0.2})_{0.95}MnO_{3-\delta}$/8YSZ	painting/YSZ dip-coat
Electrolyte	8YSZ	dip-coat/painting ink
Fuel electrode	NiO-8YSZ	painting ink
Electrode current collector	Ni mesh/Ag paste	mesh wound/painting
Seal/interconnect	Cu-Ag braze or ceramic paste	brazing or painting

Table 3.2 RSOFC geometry [16]

	Inner radius (m)	Outer radius (m)	Current path length (m)	Current path area (m^2)
Support	0. 007	0.01	0.075	0.00016022
Cathode	0.01	0.01002	2×10^{-5}	0.006283
Electrolyte	0.01002	0.01004	2×10^{-5}	0.006283
Anode	0.01004	0.01006	2×10^{-5}	0.006283
Interconnect	0.01006	0.01036	0.05	0.19132×10^{-5}

3.2.3 ROSFC Stack Geometry, Isolation and the Heat Assumptions

The RSOFC stack vessel is assumed to be a cube shape as shown in Figure 3.3. The total system volume is $4\ m^3$. A high-performance micro-porous insulation is used to insulate the vessel e.g. products from Microtherm®. The thickness of the isolation is proposed to be 0.15 m around all the vessel walls. Values of thermal conductivity are

taken from the Microtherm® official documents [11]. As shown in Figure 3.3 the cells are connected and sealed in a pressured vessel and the gases are always present at a stabilized pressure. Advantages of this design include:

(a) The issues of sulphur poisoning are entirely avoided, (sulphur reacts with nickel in the anode is a problem with a constant fuel input, and an exhaust). As there is no constant flow of fuel into the system.

(b) Pre-heated gases need to be pumped into the system in the ordinary fuel cell concepts. In this RSOFC system the gases (mostly the hydrogen and steam) are always present in the vessel and already at the cell operation temperature, which saves energy. The required excess fuel which is necessary on enhancing the fuel cell performance is not a concern any more either according to the literature review from Chapter 2.

(c) The stack is not influenced by a thermal gradient as it is the case in a constant flow system with fuel cooled by incoming gases (if the pre-heating process is not implemented or not equalized), which reduces performance. The thermal gradients across the stack also cause stresses in it.

The heat balance modelling of the fuel cell stack considers several parts, such as the enthalpy of the electrochemical reactions, heat generated by resistance components and heat losses to surroundings, versus the heat capacitance of the fuel cell stack system. As mentioned before, this SOFC design does not involve a fuel gas inlet controlled system, so pre-heat or heat loss due to the gas flow is not considered. Therefore the heat transfer between cells and the surrounding by inlet/exhaust gases are neglected. For simplicity the following assumptions were made.

(a) The system operate at uniform temperature: i.e. any heat produced is instantaneously distributed through the system, and any heat consumed cools the whole system.

(b) The external walls of the system are evenly insulated

(c) There is no leakage of gas in the system across the reversible cell electrolytes, so all heat generated comes from the electrochemical oxidation of hydrogen rather than combustion. This is also fairly accurate for the proposed pressurized system. The RSOFC would not be used in a real system if they were leaky.

In a real system, the cells will be hotter than surroundings while operating in fuel cell mode, and will lose heat by conduction, convection and radiation. Therefore with the assumptions above the model may underestimate the temperature variation and hence poorly model the performance of the cells. However there is a way to make the distribution of the heat around the system insignificant by pressurizing the system with a relative high value. Therefore the density of the gases is significantly higher and this could improve the thermal conductivity of reactants.

The model may also underestimate the effect of current step changes due to load variation. It has been demonstrated for a dynamic model of a planar SOFC that load changes cause an overshoot or undershoot of the cell voltage, which takes time to come back to the new steady-state value [17]. This may be due to fuel depletion/enrichment at the electrode interface or the time required reaching a new equilibrium temperature. With the assumptions above, the transit/instantaneous heat gradient leads to a uniformed temperature being shared within the whole system. Therefore the temperature increased at reaction sites/electrodes might be small. In addition, if the current is stepped up, the real cell would heat up faster than the modeled cell because the stack would not dissipate heat instantaneously to its surroundings. Furthermore, different parts of the cell would be at different temperatures, the parts with most electrical resistance would be the hottest. This leads to variations in cell performance over its surface. In addition, the external walls of the system would also not be at an even temperature, so heat loss would vary from one part of the wall to another. It has been shown for a tubular fuel cell stack that a simple model of convective and radiative heat transfer is sufficient to predict the performance of the whole cell, but if the local variations are taken into account, a more complex model is necessary with the computational fluid dynamic (CFD) code [17]. However in this model it is assumed with instantaneous heat transfer, so these mechanisms are not modeled at all. If the model were to be developed further then great improvements can be achieved from using a CFD model of the system, or

lumped parameter modelling.

3.2.4 Fuel Cell Stack Pressure and State of Charge (SOC)

In this research a different parameter of state of charge (SOC) is discussed due to the specific design of a pressurized and sealed vessel, rather than the gas flow rate or fuel utilization (FU). The SOC is the mole percentage of hydrogen in the hydrogen-steam mixture within the stack volume (outside the cell tubes in Figure 3.3) as calculated by Equation (3.1). The gases on the anode side (fuel cell mode) are hydrogen and steam. For every molecule of hydrogen consumed/produced in operation, a molecule of steam is exchanged. Therefore, the total number of moles of gases on the fuel side is independent of the state of charge, which means the pressure at anode ($P_{hydrogen} + P_{steam}$) holds a constant value. To simplify the modelling simplified it is rational to assume that the pressure of oxygen is always the same at the anode. However in a real RSOFC system, there would have to be a mechanism to balance the oxygen pressure against the pressure of the fuel gases, by pumping or removing oxygen to the system, otherwise the cells could be damaged.

$$State\ of\ Charge\ (\%) = \frac{P_{hydrogen}}{P_{hydrogen} + P_{steam}} \times 100 \qquad (3.1)$$

There are maximum and minimum operation limits of the state of charge. The fuel electrode could become oxidized and expand to damage at very low hydrogen concentrations. This has been observed to cause cracking and mechanical failure in the cell during electrolysis [3]. At very high concentrations of hydrogen (nearly 100% of SOC) there will be very little steam in the system, which will reduce the performance in the electrolysis mode. It will also cause greater diffusion polarisation and lower exchange current density, hence greater activation polarisation. Therefore, the safe operating range of the state of charge is first assumed by the University of St. Andrews, that the lower limit is 5% and the upper limit is 95%. However a new SOC safety range is updated and suggested in Chapter 5 during this research.

3.3 RSOFC Modelling

3.3.1 Key Novelties and Contributions from RSOFC Modelling to the Original Design

This research involved many cycles of design proposal, simulation tests, re-design and verifications, for the purpose of improving the fuel cell stack with a more practical capability and realistic performance. Some of these key values are outlined as following.

- **Derivation of Key Parameters**

The sub-models of activation and concentration loss are fully comprehensive and described in Section 3.3.4. As a result it is found that the electro-transfer coefficient β cannot be simply assumed with a generic value used by most literatures. This coefficient is realized as being critical in the activation loss model to check whether the polarisation is in a low or high condition. Thus an appropriate value of β has to be determined otherwise the simulation will be highly unstable. It is also found that β is only related to the involved electro-chemical reactions and should not be given a generic value for all fuel cell designs. In this Chapter an entirely new derivation methodology of β for simulations of activation polarisation is proposed.

Similar to β, the pre-exponential coefficient is also found to be uncertain according to Ref. [1]. Therefore a sensitivity test is processed for determining a proper value as well.

- **Copper-tin Bronze Based Internal Heat Storage System**

In order to store the fuel gas and increase the cycle efficiency then the proposed stack is designed as a pressurized vessel by University of St. Andrews. However with this feature, the simulations show that the system temperature can increase rapidly without the help of gas inlet and exhaust which in tandem cool the system down by exchanging heat with the surrounding environment, especially when fuel cells are at

high power density. To prevent overheating firstly the stack dimension is improved but the result is still far from satisfactory. A suggestion of adding a heat storage equipment was requested from the author according to the simulations, then the best solution so far is an extra copper-tin based internal heat storage system from St. Andrews which can prevent overheating to the original system design. This heat store starts to melt when the temperature reaches 1010 ^{O}C, the temperature will not go up again until the heat store is totally molten [18] [19]. This protects the system from rapid overheating and also reserves energy of heat in the form of the bronze phase change.

- **Improvements of Stack Geometry due to Simulation Feedbacks**

The pressure of the stack system was set to 5 bar and the volume was 2 m^3 in the original design. These are improved to 70 bar and $4m^3$ according to the simulation feedbacks in two purposes. The first one is to compensate the issue of rapid temperature increase as discussed above. This is because higher volume and pressure massively increase the heat capability of gases. The second benefit comes from the increased hydrogen/energy capability of a stack system which is proven by simulation results, this enables greatly extended operation terms for the proposed RSOFC system as a high power density energy storage.

3.3.2 RSOFC Output Voltage (V_{cell})

The enthalpy of the chemical reaction in fuel cell mode is exothermic and the fuel cell outputs power. The endothermic electrolysis reaction absorbs heat and current flows into fuel cell. Therefore the proposed RSOFC system stores electrical energy and heat into fuel gas (hydrogen) by running in electrolysis mode, and then converts the hydrogen back to electrical energy and heat when needed, by running in fuel cell mode. The terminal voltage V_{cell} of a single fuel cell is a combination of Nernst potential and other polarisations/losses, and it is different between fuel cell mode and electrolysis mode. V_{cell} equals to the Nernst potential minus all the other losses in fuel cell mode and this is described in Equation (3.2). However in electrolysis mode V_{cell} equals to the sum of them as shown in Equation (3.3)

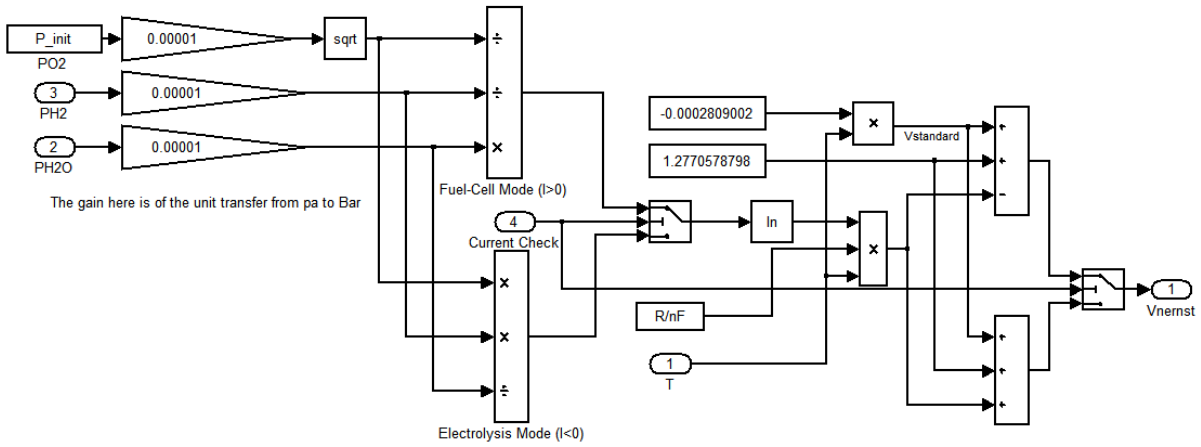

Figure 3.5 Nernst voltage block in Simulink

$$V_{cell,fuel\ cell} = V_{nernst} - V_{ohmic} - V_{activation} - V_{concentration} \tag{3.2}$$

$$V_{cell,electrolysis} = V_{nernst} + V_{ohmic} + V_{activation} + V_{concentration} \tag{3.3}$$

The fuel cell current is monitored all the time to help to switch the operation between two modes in simulations. A positive current in the model means the fuel cell is outputting power and operating in fuel cell mode, otherwise in electrolysis mode. An example of such logic monitoring block is shown in Figure 3.5. Similar designs are widely used in the rest of the modelling, e.g. the activation polarisation block which monitors the activation status and switches polarisations between either high or low condition.

3.3.3 The Nernst Voltage (V_{nernst})

The Nernst potential or the open circuit voltage is the cell potential without considering any losses within the cell. The electrochemical reaction involved in fuel cell is shown in Equation (3.4). In order to calculate the Nernst potential in fuel cell mode then Equation (3.5) is used. Where P_i (bar) is the partial pressure of the gases, and also the temperature of the system (K), the molar gas constant R which has a value of $8.314472 \mathrm{J} mol^{-1} K^{-1}$; Faraday's constant F which has a value of $96485.339\ \mathrm{C} mol^{-1}$; n, the number of electrons per molecule of reactant, which in

this case is equal to 2 because of hydrogen is the only fuel.

$$H_{2(g)} + \frac{1}{2} O_{2(g)} \rightarrow H_2O_{(g)} \tag{3.4}$$

$$V_{nernst,fuel\ cell} = V_{standard} - \frac{RT}{nF} ln \frac{P_{H_2O}}{P_{H_2} {P_{O_2}}^{1/2}} \tag{3.5}$$

$V_{standard}$ is the standard potential for the electro-chemical reaction and it depends on the concentration of reactants (hydrogen and oxygen) and product (steam) and also the temperature (T) at which the reaction takes place. Where T is the system temperature in Kelvin (K). In some of the literature like [7], [20], [21] the standard potential $V_{standard}$ is set to a fixed value. Ref. [1], [8] and [22] propose an equation to determine $V_{standard}$ and this approach is applied in this research. It can be calculated by considering the free energy of reaction, ΔG^o (Gibbs free energy) using Equation (3.6).

$$\Delta G^o = -2FV_{standard} \tag{3.6}$$

Values for ΔG^o at different temperatures can be obtained from the literature e.g. [23][24]. As ΔG^o is positive for the electrolysis reaction which is non-spontaneous, V_{Nernst} and $V_{standard}$ are therefore negative for the electrolysis reaction. However, for the ease of calculation in this model, they are converted to positive values, and the equations in the model reflect this. Therefore, when values of ΔG^o are inserted into Equation (3.5), then Equation (3.7) [16] can be generated and it is valid for both fuel cell mode and electrolysis mode (which is shown here after being multiplied by -1 to give positive $V_{standard}$ values).

$$V_{standard} = (-0.0002809002T + 1.2770578798) \tag{3.7}$$

In electrolysis mode, the reaction equation is given by Equation (3.8), and the electrolysis Nernst Voltage is determined by Equation (3.9).

$$H_2O_{(g)} \rightarrow H_{2(g)} + \frac{1}{2}O_{2(g)} \tag{3.8}$$

$$V_{nernst,electrolysis} = V_{standard} + \frac{RT}{nF} ln \frac{P_{H_2} {P_{O_2}}^{1/2}}{P_{H_2O}} \tag{3.9}$$

3.3.4 Activation Polarisation (V_{act})

The electrochemical reactions requires overcoming an energy barrier called the "activation energy" and results in activation or charge-transfer polarisation, which is due to the transfer of charges between the electronic and the ionic conductors. The activation polarisation may be regarded as the extra potential necessary to overcome the energy barrier of the rate-determining step of the reaction to a value such that the electrode reaction proceeds at a desired rate. The Butler-Volmer Equation (3.10) can accurately represent the relationship between activation polarisation and current density at high and low polarisation conditions, and is assumed to be the same for fuel cell and electrolysis mode [1] [10]. The approach taken here is from [1].

$$i_{density} = i_o \left\{ exp\left(\beta \frac{nFV_{act}}{RT}\right) - exp\left[-(1-\beta)\frac{nFV_{act}}{RT}\right]\right\} \tag{3.10}$$

where β is the transfer coefficient and its value is usually set to 0.5 [10]. However it is found in this research that the simulation is difficult if β is set to this generic value. The appropriate value of is derived as 0.3465 for this specific RSOFC design and its derivation is presented in section 3.4.3.1. The exchange current density i_O can be calculated by using Equation (3.11) and (3.12) for both anode and cathode respectively [1]. It is the forward and reverse electrode reaction rate at the equilibrium potential [25]. A high exchange current density means that a high electrochemical reaction rate and good fuel cell performance can be expected.

$$i_{o,an} = \gamma_{an} \left(\frac{P(H_2)}{P(H_2 + H_2O)}\right)\left(\frac{P(H_{2O})}{P(H_2 + H_2O)}\right)^m ex\square\left(-\frac{E_{act,an}}{RT}\right) \tag{3.11}$$

$$i_{o,cat} = \gamma_{cat}\left(\frac{P(O_2)}{P(O_2)}\right) exp\left(-\frac{E_{act,cat}}{RT}\right) \quad (3.12)$$

where γ_{an} and γ_{cat} are the pre-exponential coefficient. The sensitivity analysis in [1] and [26] were performed by varying the pre-exponential coefficient in a relatively wide range from 1×10^8 to $1 \times 10^{10}\ Am^{-2}$. Similar sensitivity test can also be found in Ref. [27] [28]. Due to the particularly wide dispersion of values found for these parameters, it is important to consider the effect of different assumptions on their values. In this case the pre-exponential coefficients γ_{an} and γ_{cat} both have a value of $7 \times 10^8 Am^{-2}$, for the cathode (oxygen electrode) and the anode (fuel electrode), respectively. These values were chosen as they were within the range of values reported, determined by experiment on fuel cells [29]. $E_{act,an}$ is the activation energy of the fuel electrode, which is 110000 $Jmol^{-1}$, and $E_{act,cat}$ is the activation energy of the oxygen electrode, which is 120000 $Jmol^{-1}$ [30][31]. P_i stands for the partial pressure of component *i* (Pa). The dimensionless coefficient *m* has a value of 1.

The Butler-Volmer Equation (3.10) can be approximated in low polarisation and high polarisation conditions. The term $\beta \frac{nF\eta_{act}}{RT}$ in Equation (3.10) could be much smaller in low polarisation so the exponential term in Equation (3.11) can be expanded as a Taylor series and yields the linear Equation (3.13) [1]; and at high polarisation, the first exponential term in Equation (3.10) will be much greater than the second term and yields the well-known Tafel equation as Equation (3.14) [1]. Very often, the Tafel equation or the linear current versus voltage relationship is used to replace the Butler-Volmer equation in the calculation of activation over-potential. In these equations $i_{density}$ stands for the fuel cell current density.

$$V_{act,low} = \frac{RTi_{density}}{nFi_o} \quad (3.13)$$

$$V_{act,high} = \frac{RT}{nF\beta} ln\left(\frac{i_{density}}{i_o}\right) \quad (3.14)$$

To determine whether the polarisation is low or high in simulations then Equation (3.15) is used. If the term $\frac{F\eta_{act}}{nRT}$ is less than 1 then Equation (3.13) is applied in simulations for deriving activation polarisation; and if greater than 1, Equation (3.14) is used. The blocks of activation polarisations on anode and cathode are built separately in the model. As mentioned with Figure 3.5 before, in Figure 3.6 (which is also very similar for the block of activation loss on cathode) the polarisation status check block features the function of Equation (3.15) and monitors the status of activation polarisation on anode and helps the model to output the specific results from the streams of "Low activation" or "High activation".

$$\frac{FV_{act}}{nRT} < 1 \tag{3.15}$$

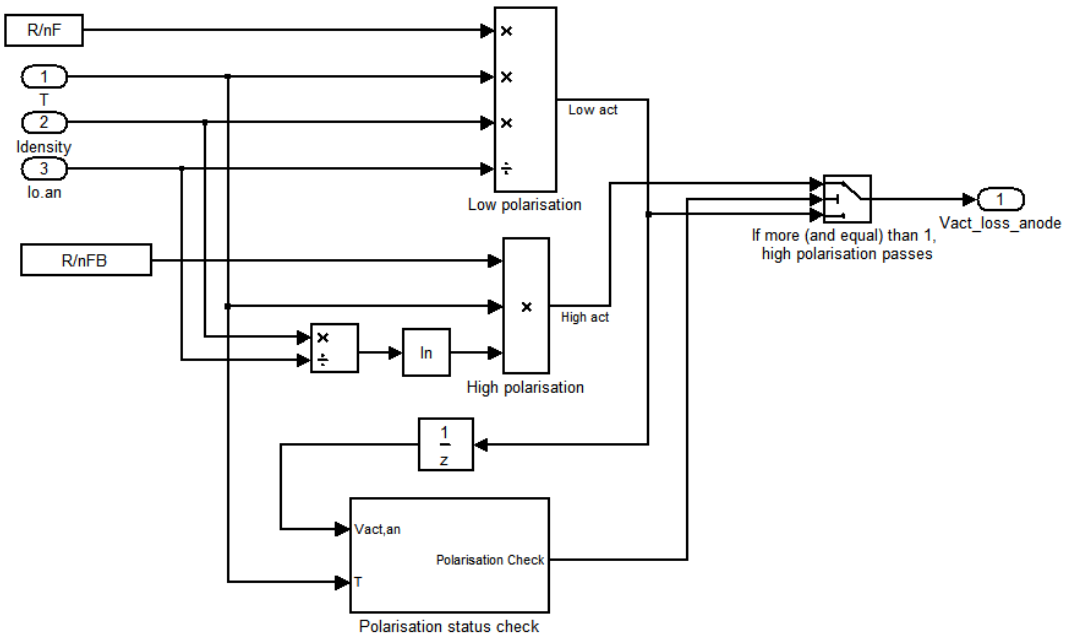

Figure 3.6 Block diagram for calculating the Activation loss on anode

3.3.4.1 The Derivation of Electron Transfer Coefficient and the Effects if Being Set Inappropriately

The settings of the electron transfer coefficient and pre-exponential coefficient are crucial to this fuel cell modelling because the activation variation is highly dependent

on them, in tandem the RSOFC performance. The value of β is chosen to keep the continuity of Equations (3.13) and (3.14) according to [10]. In simulations there is a "status switching point" on the curve of activation polarization. (at which the linear dependence of activation polarisation on current at low currents, changes to non-linear, Tafel type one at higher currents as shown in Figure 3.7.)

While building the sub-model of activation polarisation two approaches were taken to monitor the activation status. In the first approach the polarisation status check block in Figure 3.6 was used to monitor both Equation (3.13) and (3.14). However adapting an inappropriate setting of electron transfer coefficient will cause a sawtooth or stepped waveform region on the V_{act} curve around the "status switching point". Figure 3.7 below shows these effects. In this way the only method to find an appropriate value of β is by trial and error through repeated estimation using simulation and refinements. **Error! Reference source not found.** and Figure 3.8 are showing the trends of variations of electron transfer coefficient β. However it is not practical in a long term simulation because **Error! Reference source not found.** and Figure 3.8 show the appropriate value of β varies with temperature, pressure and state of charge at this approach. It is very complicated to be mapped corresponding to the model's statuses, not to mention that this approach has not been proved correct yet.

The second approach is to monitor Equation (3.13) and check if Equation (3.15) is satisfied equalling or to be lower than 1. In this approach it has been found that β is independent of everything but the natural of electrochemical reactions. At the switching point, Equation (3.15) becomes 1. Therefore V_{act} at the switching point can be calculated as a function of temperature. This value is then substituted into Equation (3.13) to find the value of $i_{density}$ at the switching point. Below the switching point, Equation (3.13) is used to calculate V_{act}. The values of $i_{density}$ and η_{act} at the switching point are substituted into Equation (3.13) to find β. This process can be visualised as plotting V_{act} below the switching point, and then the value of β is set such that the high polarisation curve of η_{act} maps onto the low polarisation values smoothly with no step at the switching point. The derivation methodology of β is shown below.

When Equation (3.15) equals to 1,

$$V_{act} = \frac{nRT}{F} \tag{3.16}$$

then both values of low and high activation polarisation are equalling to each other at this "status switching point", therefore Equations (3.13) and (3.14) share the same value of V_{act}, substituting Equation (3.16) into (3.13) yields

$$\frac{i_{density}}{i_o} = 4 \tag{3.17}$$

Then β can be found by substituting Equation (3.17) into (3.14)

$$\beta = \frac{1}{n^2} ln(\frac{i_{density}}{i_o}) \tag{3.18}$$

where *n* is the number of electrons in the reaction and in this specific design *n* is 2, therefore the value of β is 0.3465.

Table 3.3 Appropriate Values of Electron Transfer Coefficient in the first switch monitoring approach

SOC (%)/	β at 1073K (5bar)	β at 1173K (5bar)	β at 1273K (5bar)
10	0.2535	0.2385	0.2280
20	0.3145	0.3055	0.3
30	0.3340	0.3290	0.3235
40	0.3400	0.3365	0.3320
50	0.3423	0.3383	0.3343
60	0.3400	0.3360	0.3320
70	0.3340	0.3280	0.3225
80	0.3145	0.3055	0.2970
90	0.2435	0.2285	0.2165

It is interesting to know that in [1] the reported fuel cell design involves the reforming reactions shown in Equation (3.19) which generate H_2 and CO from the methane and steam contained in the fuel flow. The value of β is set to -0.35 for the model used in [1]. However it is a shame that they didn't show the derivation of this coefficient. Finally a conclusion is drawn that the electron-transfer coefficient should be carefully derived corresponding to the specific reactions involved within the fuel cells.

$$CH_4 + H_2O = 3H_2 + CO \tag{3.19}$$

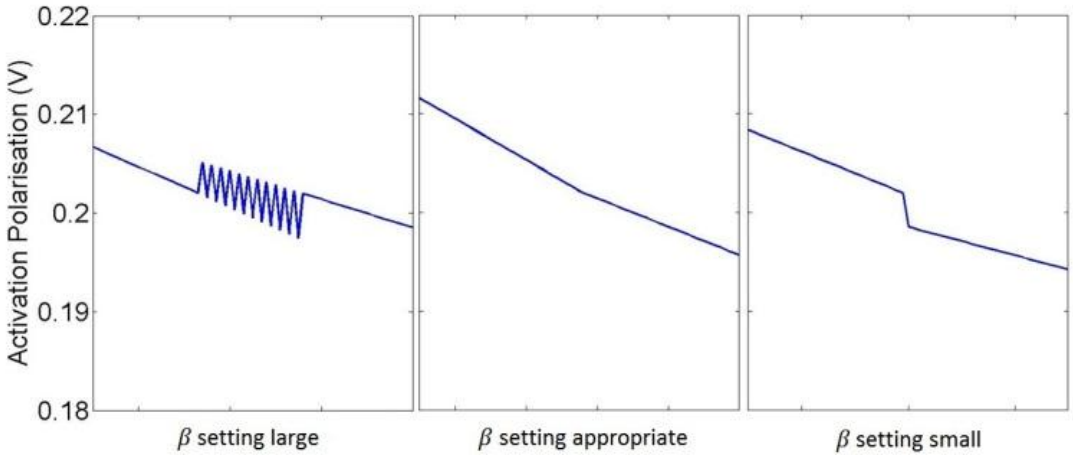

Figure 3.7 Activation polarisation waveforms using appropriate (middle), low (right) and large (left) values of β at the "status changing point"

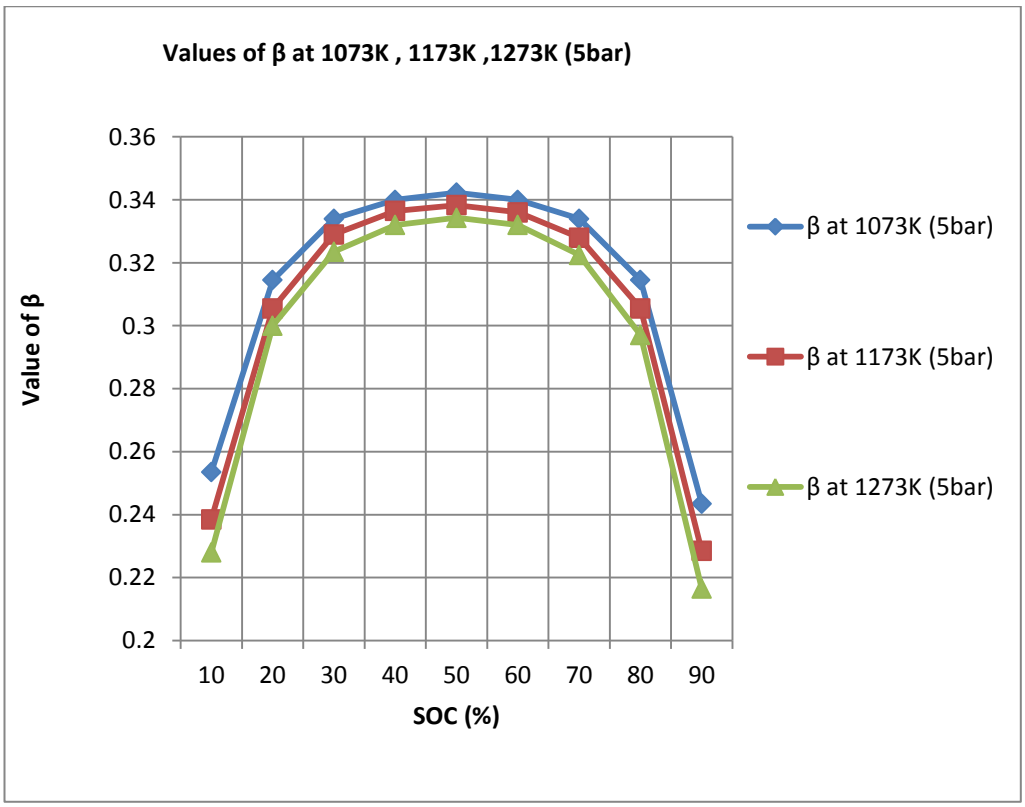

Figure 3.8 Appropriate Values of Electron Transfer Coefficient in the first switch monitoring approach

3.3.4.2 Effects of the Pre-exponential Coefficient

It was also found that the pre-exponential coefficient, which is an empirical value used in the equations to calculate the exchange current density, can be strongly affecting to the cell performance in simulation. The pre-exponential coefficient has been described as depending on cell temperature, reactants (hydrogen and oxygen) and product (steam) concentrations [32]. Figure 3.9 shows the effect on V_{act} of varying the pre-exponential coefficients, γ_{an} and γ_{cat} by simulation.

It can be seen the pre-exponential coefficient has a major impact on the activation energy as previously observed in [1]. When it is increased from $7 \times 10^8\ Am^{-2}$ to $1 \times 10^9\ Am^{-2}$, the simulation data shows cell power increases by 19 % (at 900 ^{o}C, 95% state of charge, with a cell current of 40.8 A). It also affects the position of the "status switching point" between the low and high activation polarisation as shown

in Figure 3.9 and pointed by the red arrows. At low γ values the switch to a high polarisation regime occurs at a lower current, and vice versa.. It is expected that at high currents, the potential of the cell is quite different to the standard potential, so the cell should be in the high polarisation region where it displays Tafel type behavior [10]. In this research the pre-exponential coefficient is set to $7 \times 10^8\ Am^{-2}$ according to the predictions from the University of St. Andrews for both anode and cathode.

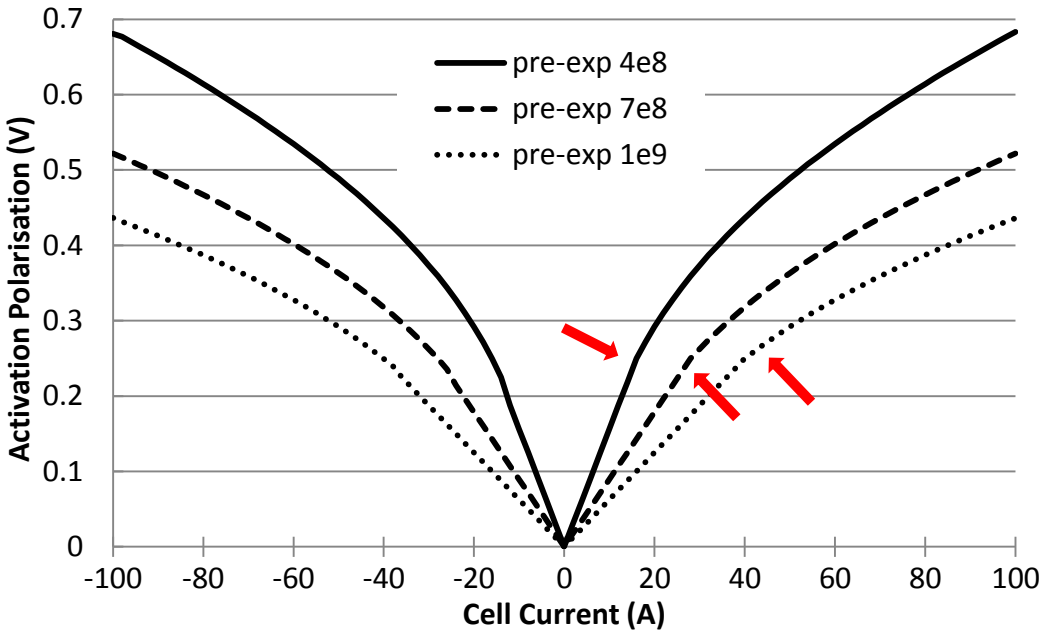

Figure 3.9 Activation energy in the RSOFC, at 1283K (900 ^{o}C), 70 bar pressure, 95% state of charge, for three values of pre-exponential coefficient for both γ_{an} and γ_{cat}: $4 \times 10^8 Am^{-2}$, $7 \times 10^8 Am^{-2}$ and $1 \times 10^9 Am^{-2}$

3.3.5 Diffusion Polarisation (V_{diff})

As the fuel cell operates the gases have to diffuse through the gas-filled pores of the electrode in order to reach the reaction sites. At the anode the hydrogen is consumed in the fuel cell mode so the concentration of hydrogen at the reactive surface of the anode decreases, leading to a diffusion gradient from the bulk concentration to the reactive surface of the anode, so as the partial pressure of hydrogen. This is vice-versa to the steam concentration at the anode. Figure 3.10 shows the diffusions of hydrogen and steam in the anode from the bulk concentrations to their concentrations at the reactive surface (provided by University of St. Andrews). In electrolysis mode, at the state of charge < 50%, the two curves would be swapped around. Area 1 shows the diffusion gradient within the anode pores (molecular diffusion), area 2 shows a diffusion gradient above the anode (bulk diffusion), and area 3 shows the bulk concentrations of hydrogen and steam. Differences in gas concentration with respect to distance from the electrolyte have been exaggerated for clarity.

Diffusion through the porous material is typically described by either Fickian diffusion or Knudsen diffusion, which are two possible types of diffusion mechanism. The Fickian (or called molecular) diffusion occurs when the pore diameter of the material is large in comparison to the mean free path of the gas molecules, which is also referred as the ordinary modelling method. Knudsen diffusion uses the assumption that the mean free path of the molecules (i.e. the average distance between intermolecular collisions in the gas) is greater than the pore diameter. This means that the molecules are more likely to hit the pore walls and this diffusion model is valid for very small pores and at low gas pressure. However in this research the ordinary model is used by the University of St. Andrews with a molecular diffusion coefficient as shown in Equation (3.20) and (3.21) for both fuel cell and electrolysis modes [1]. The superscript b represents the bulk gas, and r the gas at the anode reactive sites [1] [33]. To calculate the parameters of specie concentrations of the hydrogen and steam at the reactive surface and bulks, the equations in Appendix B are required.

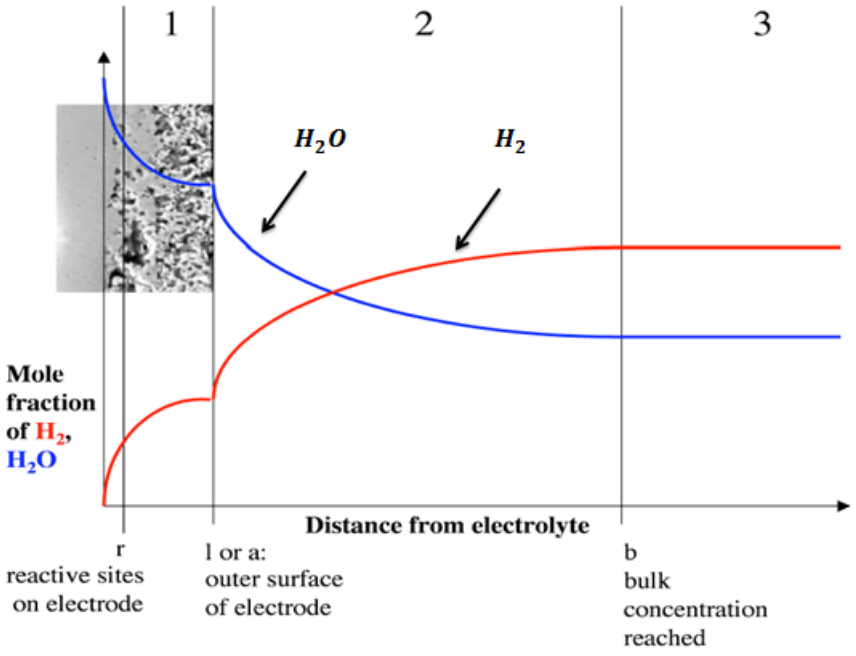

Figure 3.10 Concentration of hydrogen and steam within and above the anode during operation in fuel cell mode, for a state of charge > 50% [16]

$$V_{diff,fuelcell} = \frac{RT}{2F} ln\left(\frac{X_{H_2}^b X_{H_2O}^r}{X_{H_2O}^b X_{H_2}^r}\right) + \frac{RT}{4F} ln\left(\frac{X_{O_2}^b}{X_{O_2}^r}\right) \quad (3.20)$$

$$V_{diff,electrolysis} = \frac{RT}{2F} ln\left(\frac{X_{H_2O}^b X_{H_2}^r}{X_{H_2}^b X_{H_2O}^r}\right) + \frac{RT}{4F} ln\left(\frac{X_{O_2}^b}{X_{O_2}^r}\right) \quad (3.21)$$

The first and second terms of Equation (3.20) and (3.21) particularly represents the diffusion losses contributed by anode and cathode as shown in Equation (3.22).

$$\eta_{diff} = \eta_{diff,an} + \eta_{diff,cat} \quad (3.22)$$

Figure 3.11 shows the block diagram of diffusion polarisation according to Equation (3.20) and (3.21). The modelling of diffusion polarisation also involves two sets of blocks for both fuel cell mode and electrolysis mode. The diffusion on cathode

$\eta_{diff,cat}$ is replaced by a surface diffusion resistance $R_{diff,cell}$ and this will be described in the follow.

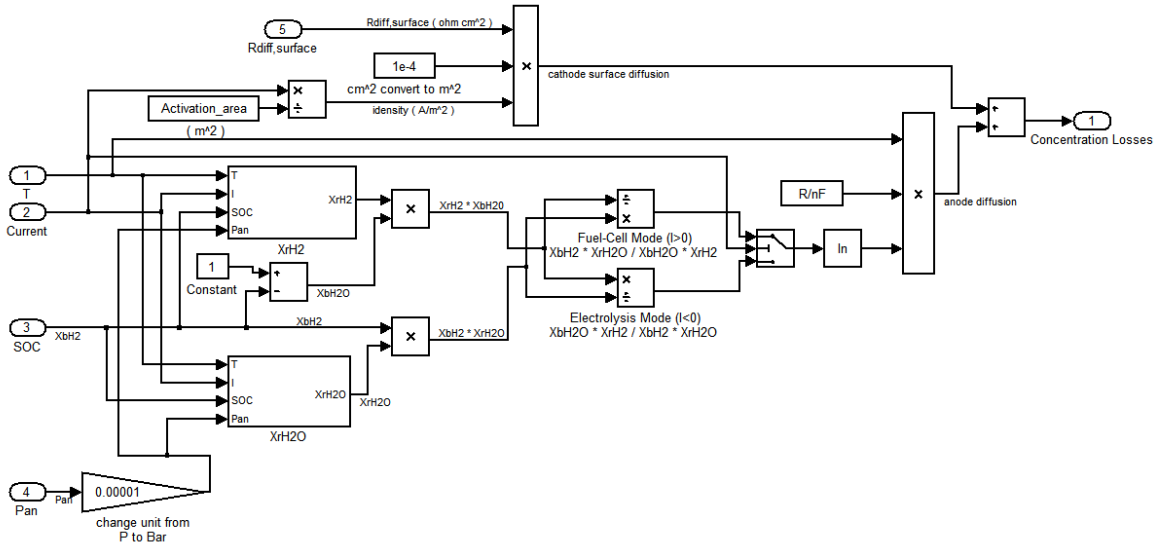

Figure 3.11 Block diagram of diffusion polarisation

3.3.5.1 Diffusion at the Cathode and the Cathode Surface Resistance $R_{diff,cell}$

As it has been previously introduced there is only oxygen on the cathode side, therefore, the concentration of oxygen in the bulk is the same as the concentration at the surface and also the reactive sites of the cathode. As the molar fraction of the oxygen is 1, hence the logarithm terms in Equation (3.20) and (3.21) for the cathode are zero ($ln(1) = 0$). Therefore a zero bulk diffusion polarisation for the oxygen can be assumed in this model.

There exists another diffusion polarisation from the surface diffusion of the oxygen species on the electrodes which is normally neglected by most literatures. This can be considered as part of the cathode diffusion resistance as described in Ref. [38]. Since the diffusion polarisation on cathode is ignored in this proposed RSOFC system, the diffusion resistance contributed from the surface diffusion of the oxygen is considered as dominant in $\eta_{diff,cat}$. Semi-empirical equations for the oxygen surface diffusion were obtained by analyzing the data from studies of symmetrical

half cells of the LSM-YSZ oxygen electrode in the University of St. Andrews [19]. The results showed that the dominant process was a surface diffusion process, rather than mass transport of oxygen gas through the electrode microstructure. The area specific diffusion resistance of the oxygen electrode surface $R_{diff,surface}$ (Ωcm^2) can be modelled by Equation (3.23), this applies to both electrolysis and fuel cell mode. Equation (3.23) was plotted as a function of temperature and pressure by using the software program Mathematica (Wolfram) [16]. As $R_{diff,surface}$ has units of Ωcm^2, and the current density has units of Am^{-2}, a conversion factor of 1×10^{-4} is also used to ensure the area units are the same. The equation is valid in the approximate range 1 bar - 70 bar pressure, and 750 ^{o}C - 1050 ^{o}C. The value of $R_{diff,surface}$ versus system temperature and pressure is simulated and plotted in Figure 3.12 and it is obvious that its dependence on both temperature and pressure is more significant at lower ranges. Studies have also shown that the trend of decreasing resistance with increasing pressure continues to nearly 100 bar for LSM-YSZ composite electrodes [39].

$$R_{diff,surface} = 2.45311 \times 10^{-5} \exp\left(\frac{8.85338 \times 10^{3}}{T}\right) P^{-0.532569} \qquad (3.23)$$

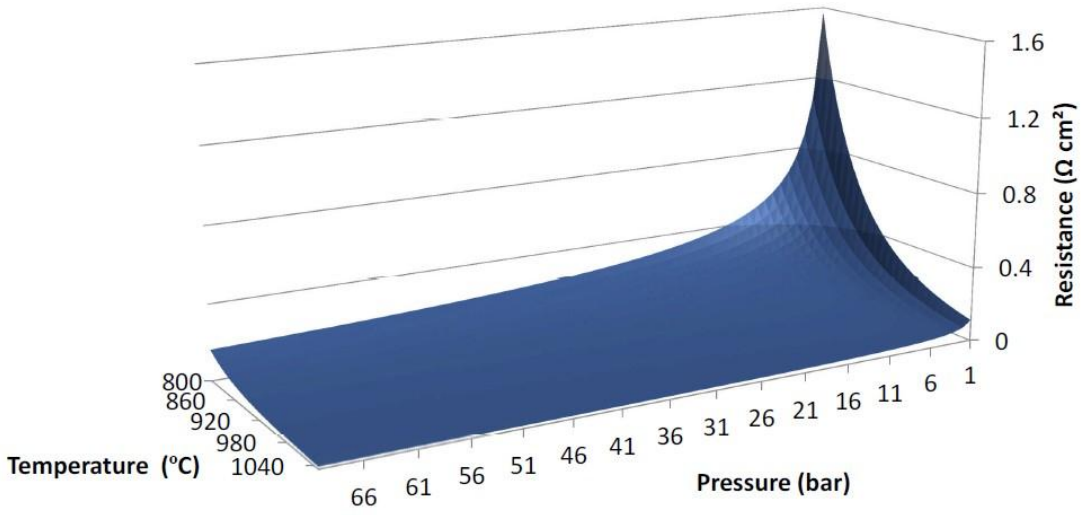

Figure 3.12 $R_{diff,surface}$ as a function of temperature and pressure.

In order to calculate the diffusion resistance for a whole cell $R_{diff,cell}$ (Ω), the value

of $R_{diff,surface}$ (Ωcm^2) calculated in Equation (3.23) must be converted to (Ωm^2), and normalised by the cell area A (m^2). This is accomplished with Equation (3.24).

$$R_{diff,cell} = \frac{1 \times 10^{-4} R_{diff,surface}}{A} \tag{3.24}$$

The summit frequency F_{max}(Hz) (at which the cell impedance response the largest value) of the diffusion resistance arc $R_{diff,surface}$ (Ωcm^2) can be modeled by Equation (3.25). The data for this equation was obtained by experiment at the University of St. Andrews, and was then plotted to give a three-dimension surface of temperature, pressure and area-specific polarisation resistance. The surface was modeled using Mathematica software (Wolfram) and an empirical equation for F_{max} calculated as a function of system pressure and temperature.

$$F_{max} = 1.5809 \times 10^{10} \exp\left(\frac{-.1.98253 \times 10^4}{T}\right) P^{0.807662} \tag{3.25}$$

As the diffusion resistance $R_{diff,surface}$ and the summit frequency F_{max} are known, the area specific capacitance $C_{area,surface}$ (Fcm^{-2}) of the process as a function of temperature and pressure can be calculated using Equation (3.26) [16].

$$C_{area,surface} = \frac{1}{R_{diff,surface} 2\pi F_{max}} \tag{3.26}$$

In order to calculate the diffusion capacitance for a whole cell C_{cell} (*F*), then Equation (3.27) [16] is used.

$$C_{cell} = 1 \times 10^4 C_{area,specific} \tag{3.27}$$

Now the surface diffusion polarisation and the capacitance can be calculated for a cell at any temperature and pressure in the range of 1 bar - 70 bar pressure, and 750 ^{o}C - 1050 ^{o}C, the polarisation behavior can be partly determined using a Randles cell - a resistor and capacitor in parallel, as shown in Figure 3.13 [31].

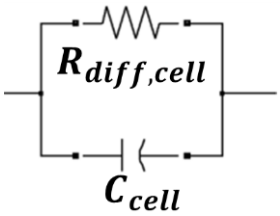

Figure 3.13 Randles cell for modelling the surface diffusion polarisation resistance $R_{diff,cell}$, in parallel with a capacitor C_{cell}.

Therefore the total diffusion polarisation at both operation modes which are given in Equation (3.20) and (3.21) can be simplified to Equation (3.28) and (3.29) by replace the cathode diffusion polarisation by the surface diffusion resistance.

$$V_{diff,fuelcell} = \frac{RT}{2F} ln\left(\frac{X_{H_2}^b X_{H_2O}^r}{X_{H_2O}^b X_{H_2}^r}\right) + 1 \times 10^{-4} R_{diff,cell} i_{density} \qquad (3.28)$$

$$V_{diff,electrolysis} = \frac{RT}{2F} ln\left(\frac{X_{H_2O}^b X_{H_2}^r}{X_{H_2}^b X_{H_2O}^r}\right) + 1 \times 10^{-4} R_{diff,cell} i_{density} \qquad (3.29)$$

Under constant DC current, the capacitance for $R_{diff,cell}$ in Randles circuit will charge up in a short period of time and remain fully charged. Then, the circuit behaves as a pure ohmic resistor. Figure 3.14 shows the simulation results of the voltage drops associated with $R_{diff,cell}$, as a function of cell temperature and current density. It can be seen that temperature is a more significant factor than the current density.

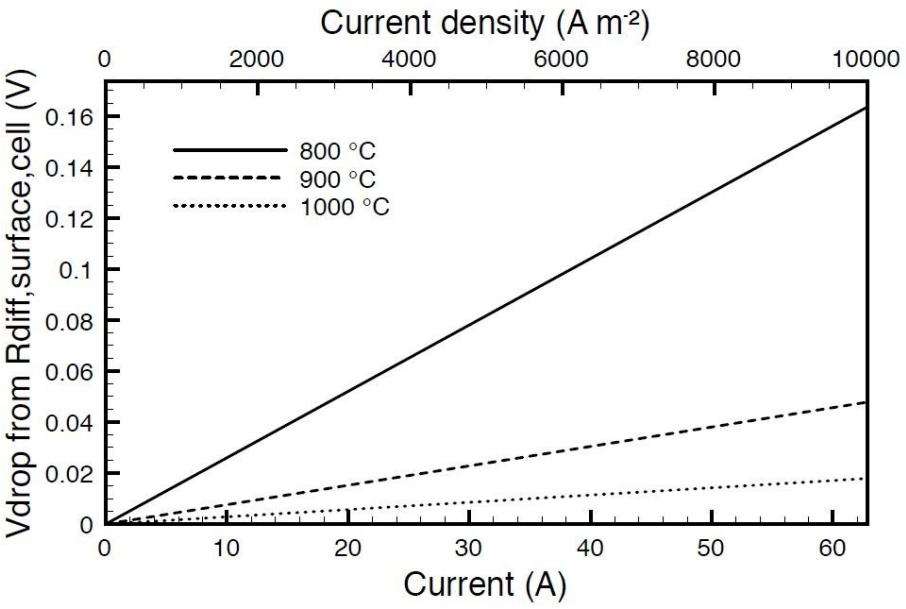

Figure 3.14 Voltage drop from $R_{diff,cell}$ at 70 bar pressure, 50% state of charge as a function of cell current and current density at 800 ^{o}C, 900 ^{o}C and 1000 ^{o}C.

3.3.6 RSOFC Resistance (R_{cell})

The total ohmic resistance of a fuel cell R_{cell} is the sum of the component resistances, namely the anode, electrolyte, cathode, and interconnect [40]. Ref [14] demonstrates the resistance sensitivity tests for both electrolyte-supported and anode-supported geometries and proved that the anode-supported design is superior to the electrolyte-supported design as that the main contribution to the ohmic polarisation is from the electrolyte. The derivation of the resistance of each involved component requires a clear understanding of the current flow path, which is related to the geometry of a single cell as demonstrated in Figure 3.15, which is drawn by the author. Current flows along the support first which is 0.1m long. However, it is assumed that the average current path of the support is 0.075 m, because the path starts to go horizontally when current reaches and enters the oxygen electrode. The current then flows through the thicknesses of oxygen electrode, electrolyte and fuel electrode which are 2×10^{-5} m, and then on average, halfway along the length of the interconnect, 0.05 m. The current path area for the support tube is the cross sectional area, which is calculated from Equation (3.30) according to Figure 3.15 and using the dimensions in table 1. To minimize the resistance of the support then the

material of LSC ($La_{0.8}Sr_{0.2}CoO_{3-\delta}$) is chosen according to simulations and Ref [8]. The current path area of interconnect is calculated by the Equation (3.31), which can be determined by Figure 3.15. It is assumed that each strand of the mesh is square, and has thickness and width of $3x10^{-4}$ m, and that they are spaced $6x10^{-4}$ m apart, surrounding the tube. Therefore, it can be assumed that the current path area of the mesh is 1/3 of the area of a solid layer of the same thickness.

$$A = \pi(r_{outer}^2 - r_{inner}^2) \tag{3.30}$$

$$A = \frac{\pi(r_{outer}^2 - r_{inner}^2)}{3} \tag{3.31}$$

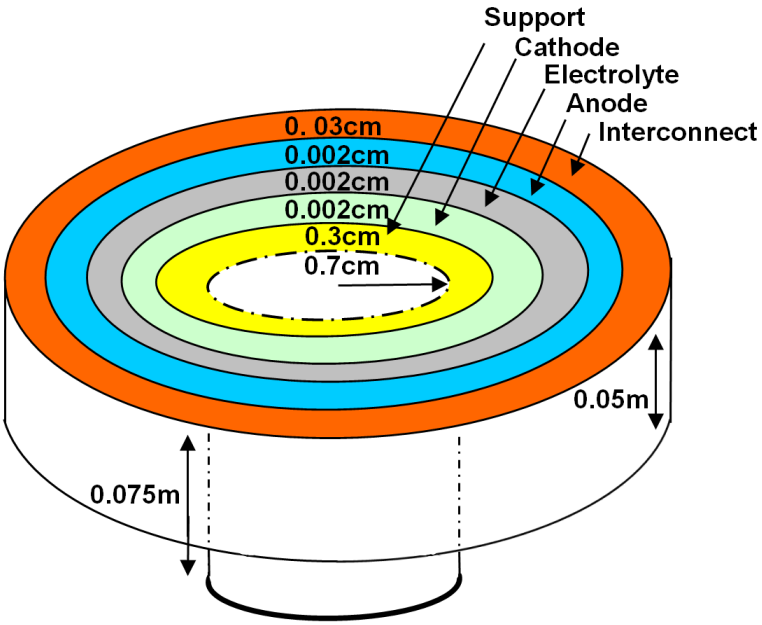

Figure 3.15 Geometry of a single RSOFC (not to scale)

The cathode, electrolyte and anode current path area is the surface area of each on the tube, which is calculated from Equation (3.32) where *r* is the inner radius in m, and *l* is the length of the tube, 0.1 m.

$$A = 2\pi rl \tag{3.32}$$

The cell connection is a single nickel wire, the same material as the interconnect, and its area is calculated using the Equation (3.33):

$$A = \pi r^2 \tag{3.33}$$

For each component, the ohmic resistance may be calculated using Equation (3.34).

$$R_i = \frac{\rho_i \delta_i}{A_i} \tag{3.34}$$

where R_i is the ohmic resistance of the ith component, ρ_i is the temperature dependent resistivity of the ith component in Ωm, δ_i is the current path length (m) and A_i is the area of the section where the current flows. The resistivity ρ_i is temperature dependent, according to Equation (3.35) and (3.36) for the anode and cathode.

$$\rho_{anode} = 2.98 \times 10^{-5} exp \frac{-1392}{T} \tag{3.35}$$

$$\rho_{cathode} = 8.11 \times 10^{-5} exp \frac{600}{T} \tag{3.36}$$

Similar equations for the support tube can also be written. The supporting material can either be LSM or LSC, where LSC is $La_{0.8}Sr_{0.2}CoO_{3-\delta}$. If the support is LSM, Equation (3.37) may be used, and if LSC, Equation (3.38) should be used. These equations were calculated by fitting a linear trend line to literature data [10]. The conductivity of LSC is slightly less than 10 times that of LSM, and it is a metallic conductor, so the conductivity should decrease slowly with increasing temperature.

$$\rho_{support-LSM} = 4.055 \times 10^{-5} exp \frac{600}{T} \tag{3.37}$$

$$\rho_{support-LSC} = \frac{\exp(\frac{-316.1}{T} - 2.8719)}{100} \tag{3.38}$$

The resistivity of the electrolyte in Ωm can be calculated from Equation (3.39). This equation was calculated by fitting data from [36].

$$\rho_{electrolyte} = \frac{\exp(\frac{4062.9}{T} - 2.2.4332)}{100} \tag{3.39}$$

The resistivity of the interconnect, which is assumed to be nickel metal increases directly proportionally with temperature, according to the Equation (3.40). The same Equation (3.40) can be used to model the resistivity of the cell connection.

$$\rho_{interconnect} = 6 \times 10^{-10} \times T - 1 \times 10^{-7} \tag{3.40}$$

Equation (3.41) represents the total ohmic resistance for one single cell. The total resistance of a stack system is determined according to the numbers of cells connected in series and parallel within a stack.

$$R_{cell} = (R_{support} + R_{cathode} + R_{anode} + R_{electrolyte} + R_{cellconnection} + R_{interconnect}) \tag{3.41}$$

Figure 3.16 shows a logarithmic plot of the ohmic resistance of each component of a single RSOFC cell, from the simulation in this research. The cell resistance is dominated by the resistance of the support. This is because it acts as a distributor for the current over the electrode surface, and has lower conductivity than the nickel interconnect, which distributes current on the fuel electrode side. The next highest resistance comes from the interconnect and cell connection. The electrolyte resistance is also large at lower temperatures. The anode and cathode resistances are both very small because they are very thin and the current path is determined by their thickness.

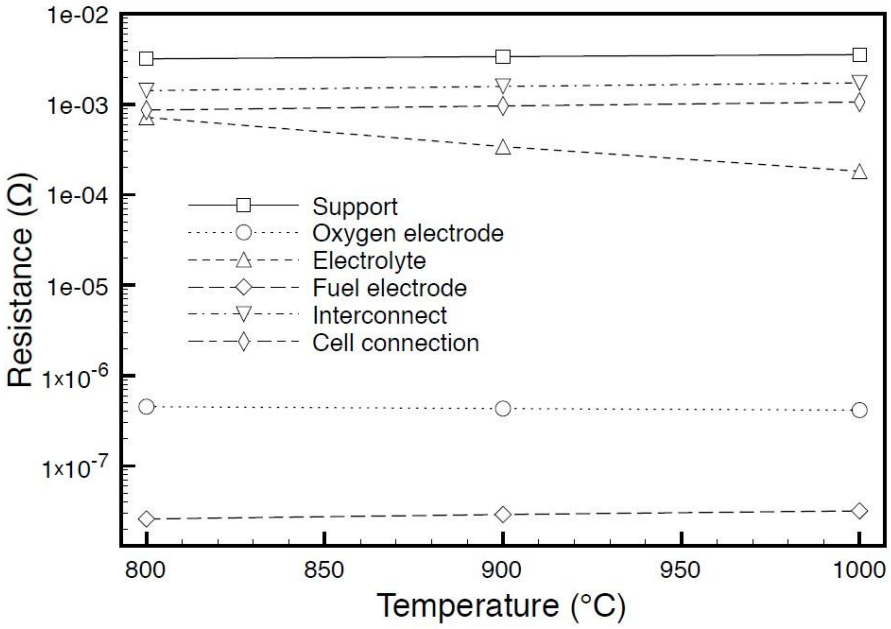

Figure 3.16 Fuel cell resistance of each component of a single RSOFC, on a logarithmic scale, at 800 ^{o}C, 900 ^{o}C and 1000 ^{o}C.

3.4 Randles Circuit and AC Impedance Spectroscopy Modelling

Model selection using electrochemical impedance spectroscopy is an empirical process and the model should correspond to the best possible fit or representation of the system. The Randles cell is one of the simplest models represented in electrical impedance spectroscopy (IS) tests [41]. In this model the impedance of a single RSOFC is simulated by the electrical equivalent circuit shown in Figure 3.17. The model takes part of the performance of a single cell, and allows the prediction of the performance of a stack system. The polarisations due to activation and diffusion are treated as voltage drops on resistance.

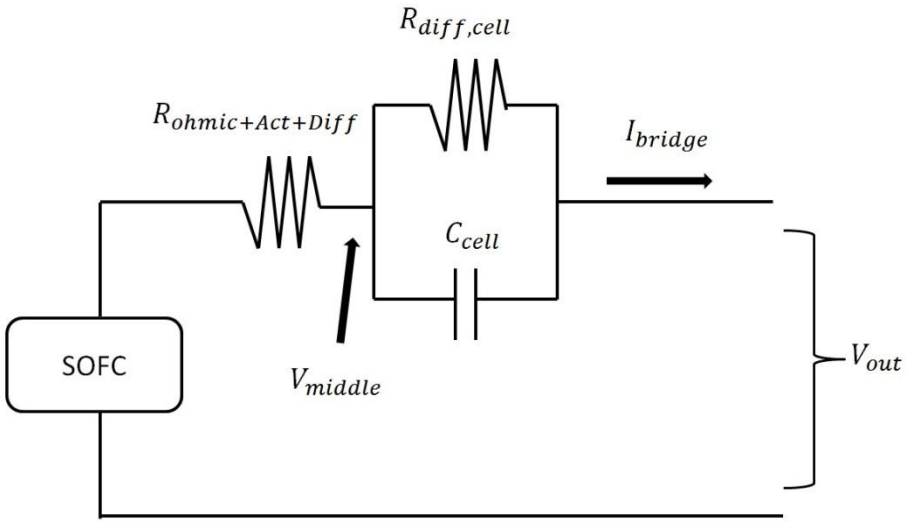

Figure 3.17 Randles electrical equivalent circuit for modelling a single RSOFC and impedance spectroscopy

The following impedance spectroscopy simulations are on a single cell based on 90 frequencies at the range from 0.05 Hz to 1 MHz, with the settings of 50% state of charge. The Randles cell model is a separate part within the RSOFC model as shown in Figure 3.18 and Figure 3.19. The impedance spectroscopy simulation requires the values of Nernst voltage, the total ohmic losses, $R_{diff,cell}$, and C_{cell} to be supplied by the RSOFC model as shown in Figure 3.17. To generate the impedance spectroscopy simulation, the RSOFC model and the Randles cell model are executed at the same time, which is carried out by a dedicated routine. The whole system is subjected to a simulated current waveform consisting a larger DC bias (20 A) and a smaller AC current (10 mA) which is swept across the frequency range mentioned earlier. In the model this is achieved by using the state space functions as shown in Appendix C rather than using electrical components in SimPower (a Matlab/Simulink package) for the simplicity and fast simulation.

Figure 3.18 shows the mathematical model which represents the circuit diagram shown in Figure 3.17 based on the state-space equations in Appendix C. It is noticed that this model is simulated in discrete-time based settings and tested in the steady-state condition, therefore the initial voltage V_c of C_{cell} is set to an estimated value of $R_{diff,cell}$ times bridge current in the cycle delay block. Figure 3.19 is showing the part of the Fourier analysis blocks which is linked to the model in Figure 3.18. The

discrete Fourier blocks is the key to measure the magnitude and phase of the fuel cell terminal voltage and current, and then followed by phase operators to derive the value of impedance. Due to the use of the discrete Fourier analysis, the sample time T_s and simulation length are critical for optimizing both the speed and fidelity of the simulations. T_s is defined and coordinated at each spectrum frequency to ensure at least 20 samples can be captured per cycle. So the minimum sampling time T_s is set to 1/F/20 (where F is the frequency) and can be calculated by Equation (3.42).

$$T_s \ll \frac{I \times R_{diff,cell} C_{cell}}{I} = R_{diff,cell} C_{cell} \tag{3.42}$$

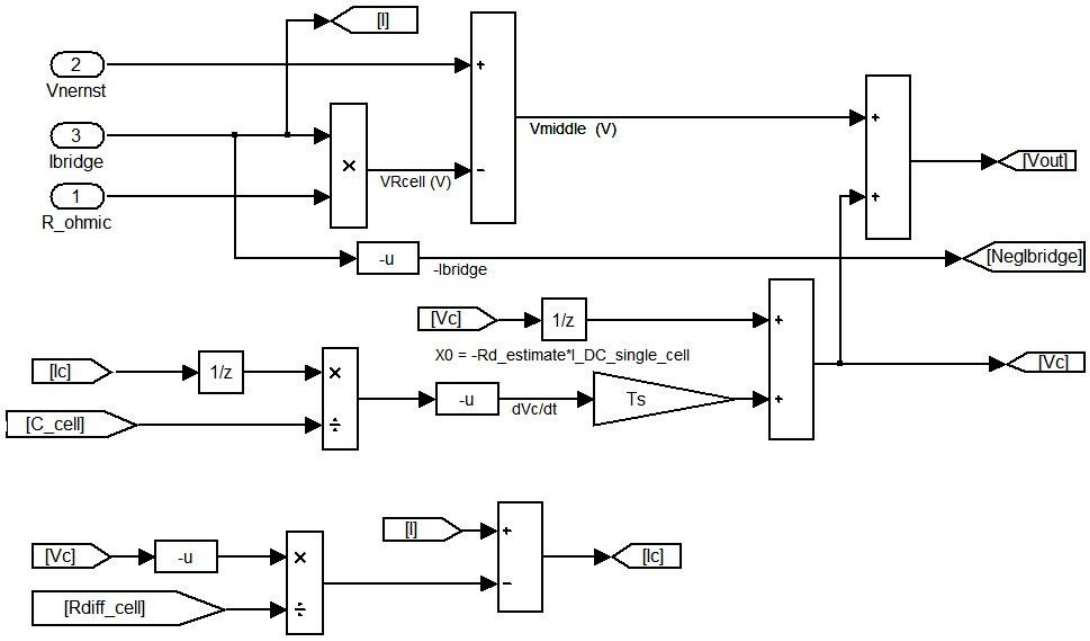

Figure 3.18 Block diagram of mathematically represented state-space functions

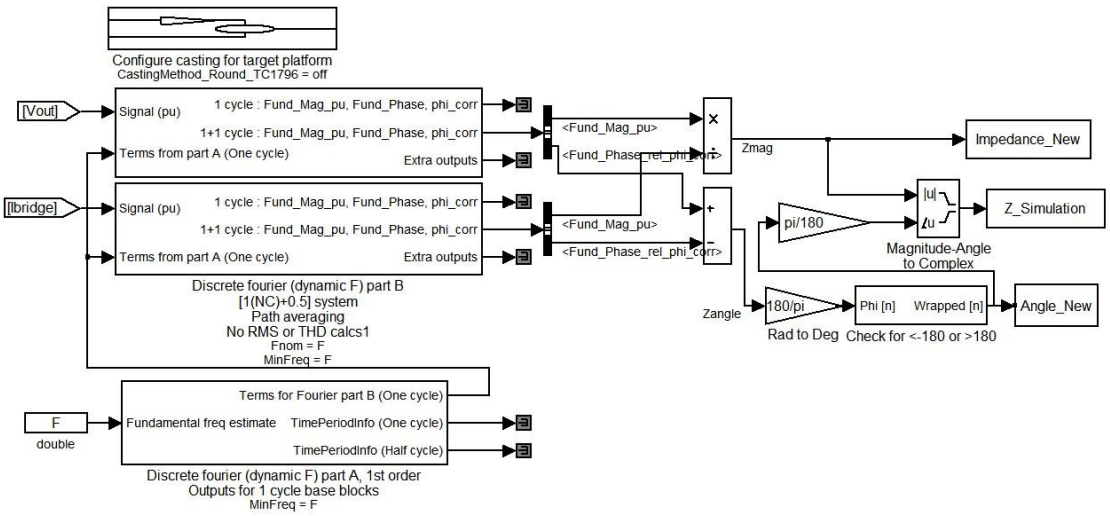

Figure 3.19 Block diagram of Discrete Fourier analysis of SOFC impedance

The impedance spectrums in Figure 3.20 are simulated at four selected scenarios with different temperature and pressure (all at 50% state-of-charge). In the Randles circuit in Figure 3.17 R_{ohmic} is temperature dependent, meanwhile $R_{diff,cell}$ and C_{cell} are pressure dependent, thus the effects of temperature and pressure on the impedance are demonstrated in Figure 3.20 (with arcs demonstrating impedance spectrums from high to low as left to right). The surface diffusion resistance $R_{diff,cell}$ is the part under the impedance arc. The real part of the impedance is greater at higher temperature. This is because it is dominated by the resistive contribution of R_{cell}. Figure 3.20 also shows a quite significant effect of pressurisation. Higher system pressure leads to a large decrease in surface diffusion resistance $R_{diff,cell}$, as seen between 5 bar and 70 bar of pressure. The impedance spectroscopy tests again prove the performance enhancement (by higher pressurisation) by lowering the total cell impedance as shown in Figure 3.20.

However the impedance spectrum shown here does not take into account of the time constant from activation polarisation impedance which can be treated as other equivalent capacitances. Therefore, $R_{diff,cell}$ and its associated capacitance dominates the polarisation resistance and capacitances in these simulation. One way of improving the IS simulations in the future is by taking experimental measurements on a reversible SOFC to compare and validate the predicted impedance spectra. By doing this, the arcs of impedance may contain more than one convex curve. Another

way of improving this can be a CFD code modelling to find the response time due to any ripples, as discussed in Chapter 2.

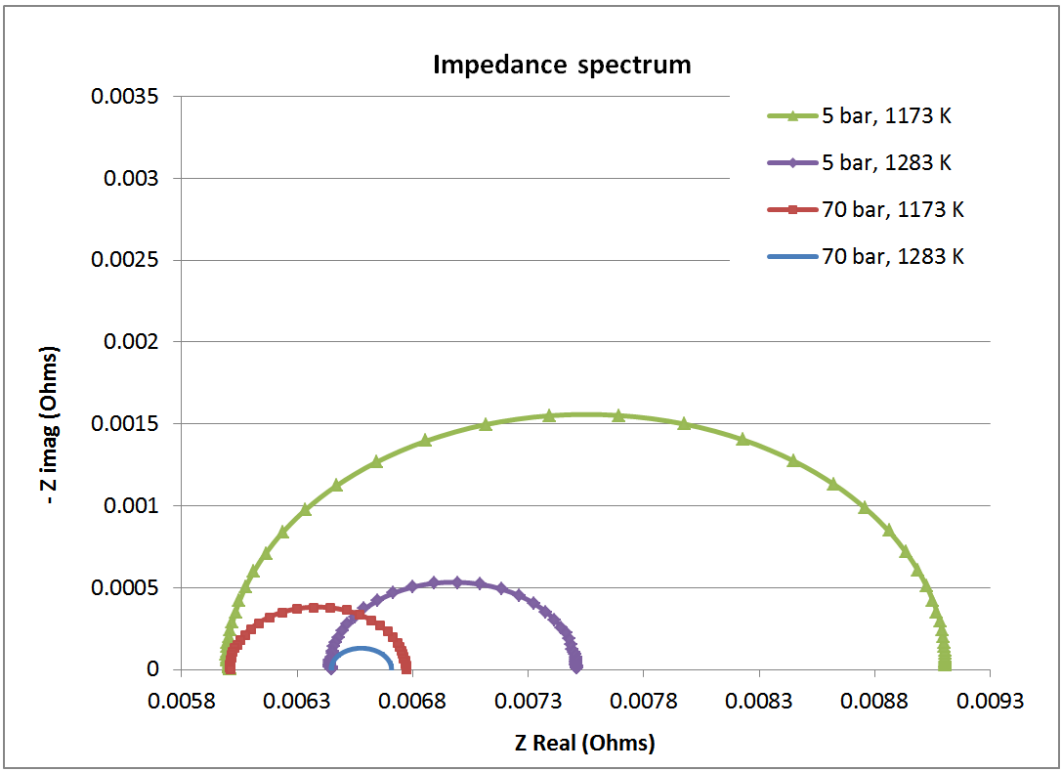

Figure 3.20 Impedance Spectroscopy Simulation of a single reversible SOFC

3.5 RSOFC Stack Modelling

3.5.1 Gas Partial Pressure and Fuel Storage

The derivation of the partial pressure of hydrogen and steam is based on their total moles of gas N_i in the system. It can be calculated from the classic ideal gas law (the equation of state) Equation (3.43) [42], where *P* is the pressure in Pascal, *v* is volume in m^3, *R* the molar gas constant and *T* the temperature.

$$N_i = \frac{Pv}{RT} \tag{3.43}$$

For subsequent changes in temperature, Equation (3.43) can be rearranged to Equation (3.44) in order to calculate the system pressure. This equation only applies to the combined hydrogen and steam pressure, and does not apply to the oxygen pressure which is assumed equal to the pressure on the anode side (fuel cell mode).

$$P = \frac{N_i RT}{v} \tag{3.44}$$

In the model, the real time partial pressures of hydrogen and steam are determined by using a discrete time integrator with an initial pressure value and the determined pressure changing rate which is dependent on the current density and number of cells in the stack. The volume of the cell v_{cell} can be calculated from the cell dimensions given in Table (3.2). Using the Equation (3.45) where r_{inner} is the inner radius of the tubular cell, and r_{outer} is the outer radius of the tubular cell, and *l* is the cell length, then v_{cell} can be calculated. A diagram of a single cell geometry is shown in Figure 3.15.

$$v_{cell} = \pi(r_{outer}^2 - r_{inner}^2)l \tag{3.45}$$

The volume of the solid parts of the system v_e is assumed to be the sum of volume of the total fuel cells and the total interconnect volume (v_{inter}) according to Equation (3.46) (v_{inter} is decided to be 0.00001 m^3 by the University of St. Andrews), and N_{cell} is the number of cells in a stack. Figure 3.3 and Figure 3.15 shows the volume

relationships between cell components and the stack system.

$$v_e = N_{cell}(v_{cell} + v_{inter}) \tag{3.46}$$

The volume of the heat store $v_{h.s}$ is separated from the system volume, and can be calculated from Equation (3.47), where the mass of the heat store is divided by its density $\rho_{h.s}$, which is 7890 kgm^{-3}. [18].

$$v_{h.s} = \frac{M_{h.s}}{\rho_{h.s}} \tag{3.47}$$

Then the volume of hydrogen and steam in the system is calculated by Equation (3.48).

$$v_{H_2,H_2O} = v_{stack} - v_e - v_{h.s} \tag{3.48}$$

Therefore to derive the partial pressure changing rate dependent on current then the gas consume rate is required. For a single cell the charge transferred is

$$Q = it \tag{3.49}$$

where *i* is the current in a single cell. and *F* is the Faraday's constant [1].

$$N_i = \frac{Q}{2F} \tag{3.50}$$

Where N_i is the mole number of gas species, so the gas consumption rate (mol$A^{-1}s^{-1}$) equals

$$\frac{dN_i}{dt} = \frac{i}{2F} \tag{3.51}$$

Then substitute Equation (3.51) into (3.44) yields:

$$\frac{dP}{dt} = \frac{i}{2F}\frac{RT}{v_{H_2,H_2O}} \tag{3.52}$$

For a whole stack, the total partial pressure changing rate is multiplied by the number of cells N_{cell}. According to Equation (3.1) and (3.43), the fuel storage can be determined when both SOC and partial pressure are known, hence the total electrochemical energy capacity too.

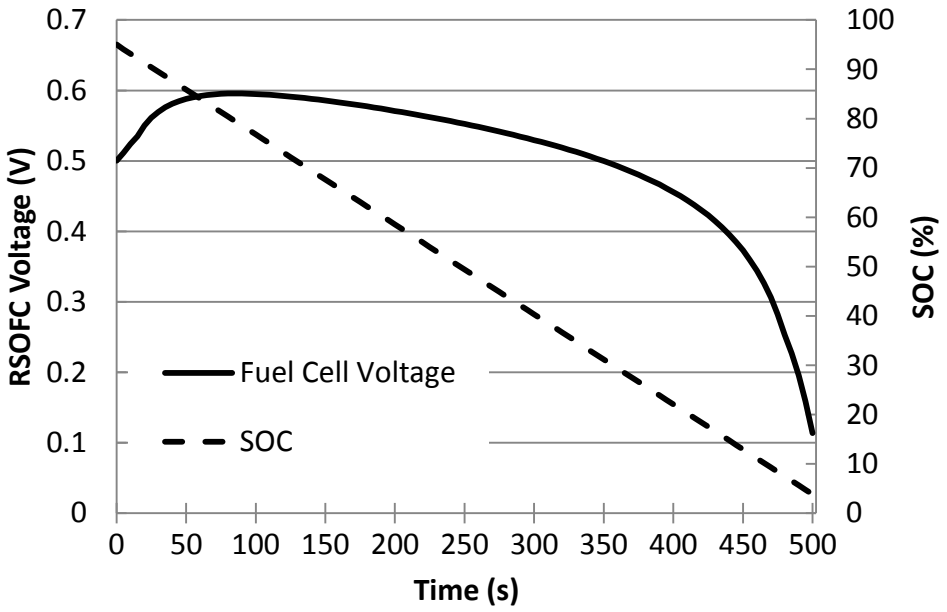

Figure 3.21 SOC from 95% to 5% and cell voltage versus time at 40.8A and 1283K, 5bar and $2m^3$

The energy storage capacity of the system is obviously limited by the amount of hydrogen that can be stored in the system. Figure 3.21 shows that in the original design with pressure of 5 bar and volume of 2 m^3 the fuel hydrogen can be run out in less than 9 min at 40.8A (rated power output at 1283K). In order to overcome this limitation, the system pressure could be increased with high volumetric storage density. Also the system volume could be increased. However, in the first case, a higher pressure would need a stronger and more expensive vessel. In the second case, a larger surface area means more heat would be lost through the walls which potentially reduces the electrical efficiency of the system.

According to the literature research by University of St. Andrews, the LSM-YSZ electrodes used in this research are able to stand for the variation of pressure from 1 bar to 100 bar, as shown in ref [43]. Therefore the enhanced stack geometry is updated to 70 bar of pressure and 4 $m^3$of volume. This proposal will be discussed with simulation demonstration in Chapter 4, as the operation time being extended to 3.75 hours at the rated power. Also, in this way the entropy of the gases in the system can be reduced, so every mole of hydrogen that is consumed produces less heat, and more energy is available to be converted into electricity, which boosts the electrical conversion efficiency.

3.5.2 Heat Balances and Capacities

It is introduced that this RSOFC model assumes an isothermal system in which all the heat produced is immediately distributed throughout the stack. In this way the transient response of the fuel cell at rapid current change due to the thermal capacitance is ignored. Because the fuel cell system has a large thermal mass, changes in temperature will not be as great or fast as current because it takes time to heat up and cool down. The only way to see these transient effects would be using a heat transfer model, which may conducted using a CFD modelling of the system. The relaxation time in the RSOFC system greatly depends on the geometry of the system, so without this extra modelling, it is difficult to predict how significant it would be. As a result the following modelling of the heat balance of such isothermal system mainly counts for the relationships among heat generation/absorption, heat loss, heat capacity of components and species and heat storage function.

The rate of transient temperature variation can be determined by dividing the heat output by the stack heat capacity. This is shown by Equation (3.53) for both fuel-cell mode and electrolysis mode and it is only valid if the bronze is in a solid state ($M_{h.s.}CP_{solid.bronze}$). Equation (8) in [12] is referred and modified by adding the heat capacity of the heat store $M_{h.s.}CP_{solid.bronze}$ at the denominator, which yields Equation (3.53).

$$\frac{dT}{dt} = \frac{q_e + q_{ohm} - q_i}{M_{stack}CP_{stack} + M_{h.s.}CP_{solid.bronze} + M_{gases}CP_{gases}} \tag{3.53}$$

As can be seen from Equation (3.53) both the stack and the gases are part of the heat capacity. $M_{stack}CP_{stack}$ represents the heat capacity of the whole stack including every single cell and other connecting materials; and $M_{gases}CP_{gases}$ is for the gases within the vessels. Figure 3.22 shows the heat balance block diagram for both operation modes, at where the block of q_e is the heat generated by the electrochemical reaction per second in fuel cell mode. It is noticed that q_e is negative in electrolysis mode which is due to the endothermic property of electrochemical reaction. The block of q_{ohm} is the heat produced by the ohmic losses per second, and q_i is the heat loss through the insulation per second.

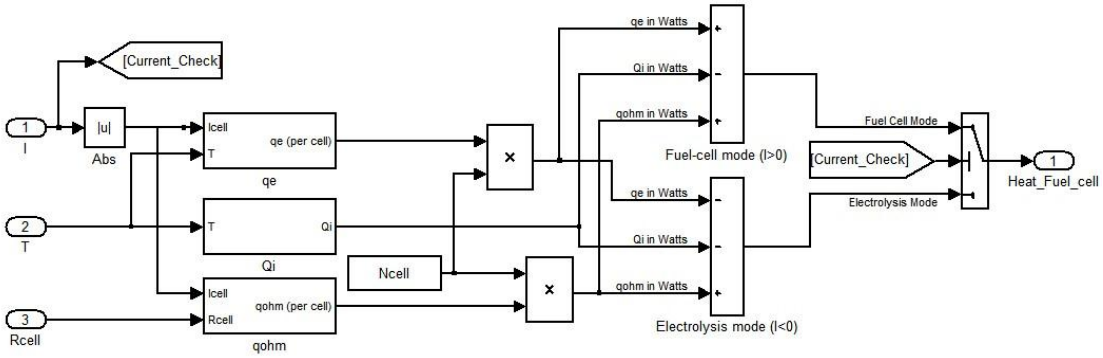

Figure 3.22 Block diagram of fuel cell stack heat balance

3.5.2.1 Heat Capacity of the Heat Store

According to the simulation tests the original RSOFC stack system requires a great amount of thermal mass in order to store heat and increase the operation time of the system as introduced in Section **Error! Reference source not found.**. The maximum reversible energy storage capability of the system depends on two factors: the amount of heat that can be stored and the amount of chemical energy that can be stored in the form of hydrogen (which is described in Section 3.5.1). A test in the fuel cell mode with the starting parameters of 95% SOC, 1073K (800 ^{o}C), 70 bar of pressure is presented here. The system temperature and electrical power output are recorded as a function of time, at a constant current of 40.8 A per cell, or a current density of 6494 Am^{-2} as shown in Figure 3.23 and Figure 3.25.

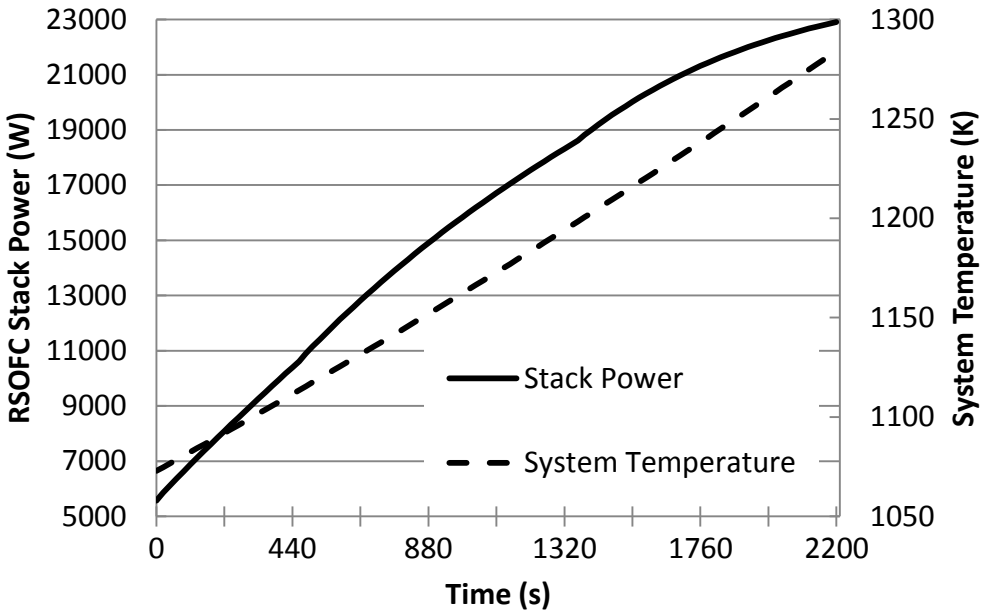

Figure 3.23 Electrical power output and system temperature over time, at a current of 40.8 A per cell, starting conditions 95% state of charge, 1073K (800 ^{o}C), showing the time until the system temperature reaches 1283K (1010 ^{o}C), with no heat store

The proposed system is designed with the maximum temperature of 1283K (1010 ^{o}C) by the University of St. Andrews to avoid any damage to the RSOFC. It can be seen from Figure 3.23 that without a heat store device the system temperature increases fast and reaches 1283K (1010 ^{o}C) after ~37 min (~2200 seconds). Therefore the system is quickly overheated and no longer able to produce electrical energy but shut down, or must be switched to electrolysis mode to be cool down. The rapid rise in temperature is due to the low heat capacity of the system. Figure 3.24 shows the heat capacities of different system components. The gases provide 73.4% of the total heat capacity, with the stack contributes 26.6%. Although the gases have a low heat capacity at atmospheric pressure, their volumetric heat capacity at 70 bar is considerably greater.

During this research it has always been found that the temperature/heat control is a big challenge for a high performance RSOFC system. According to the results from Figure 3.23 it is a fact that the heat capacity of the system has to be increased and

must be able to reversibly store more energy for a longer operation period. One way to achieve this would be to increase the pressure and the volume of the system, as the same solution for the lack of fuel cell storage capacity discussed in Section 3.5.1. However, increasing the system volume will result in higher heat losses to surroundings, and increasing the pressure of the stack would add costs. However after all overheating is still inevitable. At the University of Strathclyde a design improvement was requested: a heat absorption/dispatching device which is actually able to hold the temperature. At the University of St. Andrews a proposal of adding a solid mass to the system was eventually considered.

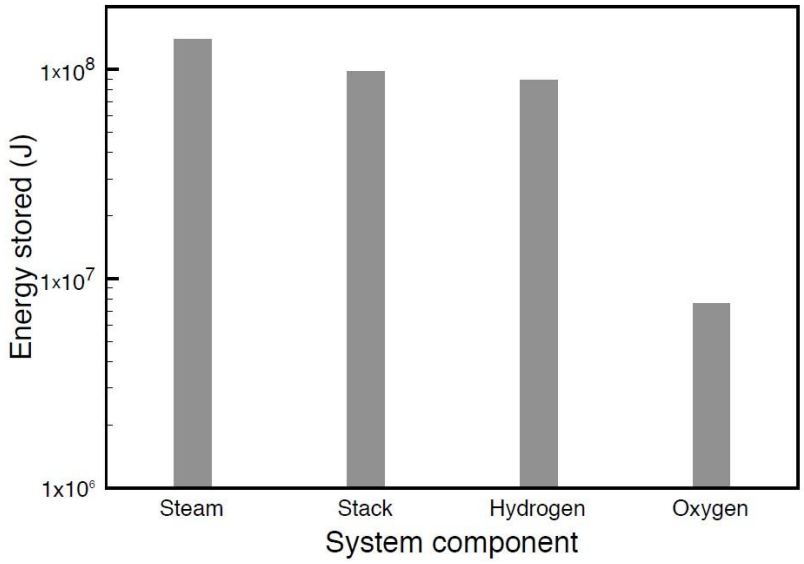

Figure 3.24 Logarithmic plot of heat stored by each system component (The stack includes the cells and bases)

A much greater volumetric density of heat storage is obtained by the use of a suitable phase change material, in which a phase transformation between solid to liquid occurs at a particular temperature. As shown in Equation (3.53), $M_{h.s}CP_{solid.bronze}$ represents the heat capacity of the solid heat store which is made of a type of bronze, a copper-tin alloy, 11% tin by mass or 6.21 mole% tin [18] [19]. The heat store is described in three stages: below, at and above the melting point. It melts at 1283.15K (1010.15 ^{O}C). The bronze acts as a thermal mass, storing heat as the temperature increases. When it melts, it stores heat equivalent to the enthalpy of fusion (latent heat of melting). It still acts as a thermal mass above the melting point. The heat is stored when it heats up, and will be released in electrolysis mode.

Firstly, for temperatures below the melting temperature, i.e. <1010 ^{O}C (1283 K), as the bronze is mostly copper then the heat capacity of copper is used as a function of temperature to model the bronze heat capacity. The mass of the heat store is $M_{h.s}$ (kg). Equation (3.54) calculates the heat capacity of the bronze below the melting point, $CP_{solid.bronze}$ $Jkg^{-1}K^{-1}$, as a function of temperature (K) [18] [19]. This equation is valid only at T < 1010 ^{O}C (1283K).

$$CP_{solid.bronze} = 0.1594T + 293.09 \qquad (3.54)$$

Secondly, if the system temperature rises up to 1010 ^{O}C the bronze begins to melt with the heat store state of charge Φ (%) starting to increase from zero (where Φ is the proportion of bronze which is molten), then Equation (3.55) should be used to calculate the addition energy (J) stored by the heat store when it completely melts, where $H_{fus.bronze}$ is the enthalpy of fusion for the bronze, which is $3.4 \times 10^{5} Jkg^{-1}$.

$$E_{h.s.} = H_{fus.bronze} M_{h.s.} \qquad (3.55)$$

Thirdly, when all the metal has melted (Φ =100%) then the temperature of the system begins to rise again. At temperatures > 1010 ^{O}C, the heat capacity of the molten bronze, $CP_{melton.bronze}$ is constant with temperature because the bronze is a liquid, and it has a value of 490 $Jkg^{-1}K^{-1}$.

Figure 3.25 shows the same simulation as in Figure 3.23 but with 500kg heat store. The obvious difference is that it takes more than 98 min (~5880 seconds) for the temperature to reach the limit. Furthermore the significant benefit will be keeping the temperature steady for a reasonably long time and further case studies are demonstrated in Chapter 4. To avoid a total melt down of the heat store as well as the system, it is suggested to apply the mass of heat store according to the fuel gas storage and power output strategy. For example, the fuel gas consumption should be no faster than melting down rate of heat store or vice versa.

Figure 3.26 shows the amount of energy stored by each system component. The heat

stored by the phase change of the heat store represents 31.3% of the total stored heat which can be used in electrolysis mode at 1010 ℃. Therefore, by adding a 500 kg heat store, the heat storage capacity of the system has significantly increased. The remaining heat is mostly stored by the system gases. The modelling of the heat store as being logically designed with 3 molten stages is described in Appendix D.

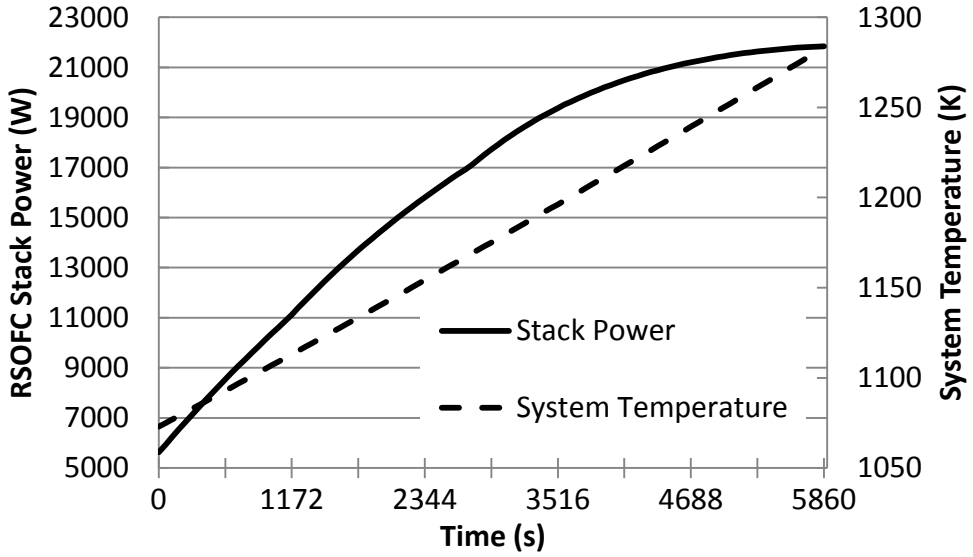

Figure 3.25 Electrical power output and system temperature over time, at a current of 40.8 A per cell, starting conditions 95% state of charge, 1073K (800 ^{o}C), showing the time until the system temperature reaches 1283K (1010 ^{o}C) with 500kg heat store

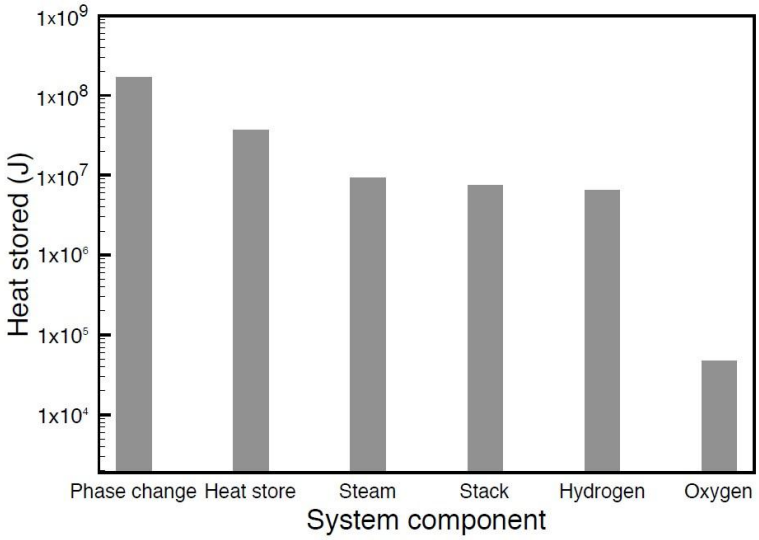

Figure 3.26 Logarithmic plot of heat stored by each system component including the amount can be stored by the copper-tin heat store and its phase change (The stack includes the cells and bases)

3.5.2.2 Heat Capacity of the RSOFC Stack

The heat capacities, volumes and masses of various parts of the system are calculated in order to determine the heat capacity of the system. CP_{stack} is the specific heat capacity of the stack and equals 400 $Jkg^{-1}K^{-1}$ [1]. The total stack mass is calculated from Equation (3.56) where M_{stack} is the mass of the stack in kg, and ρ_{cell} is the density of a cell, which is 6000 kgm^{-3}. There is also a solid ceramic interconnect plate connecting the cells, of density 6000 kgm^{-3} [1] as well, and volume 0.00001 m^3 per cell, which are represented by ρ_{inter} and v_{inter} respectively in Equation (3.56).

$$M_{stack} = N_{cell}(\rho_{cell}v_{cell} + \rho_{inter}v_{inter}) \qquad (3.56)$$

Where v_{cell} is represented by Equation (3.45) and v_{inter} takes the same value as in Equation (3.46).

3.5.2.3 Heat Capacity of the System Gases

The heat capacity of the gases in the system makes a significant contribution to the heat capacity of the system. **Error! Reference source not found.** shows the molar heat capacities of the gases used in the reversible cell system. Hydrogen stands out as having a very high gravimetric heat capacity. However, the heat capacity per mole is similar to the other gases.

Table 3.4 Heat capacities of the gases in the reversible cell system, at 400 K and 1 bar pressure [18].

Gas	Heat Capacity $(Jkg^{-1}K^{-1})$	Heat Capacity $(Jmol^{-1}K^{-1})$
Hydrogen	14380	29.05
Steam	1990	35.85
Oxygen	1249	39.97

The heat capacity $(Jkg^{-1}K^{-1})$ of the gases in the system at 70 bar, as a function of temperature is calculated by the following equations. The gravimetric heat capacity of the gases increases slightly with pressure, but their volumetric heat capacity significantly increases as they become denser with increasing pressure. The data for these equations was taken from the NIST standard reference database [44].

$$CP_{H_2} = 1.50216T + 13491 \quad (3.57)$$

$$CP_{O_2} = 0.144437T + 951.593 \quad (3.58)$$

$$CP_{H_2O} = 0.182118T + 2207.90 \quad (3.59)$$

The volume of hydrogen and steam in the system V_{H_2,H_2O} (m^3) is calculated by Equation (3.48), where the total system volume is 4 m^3. The total moles of hydrogen

and steam in the system N_{H_2,H_2O} can then be calculated by Equation (3.43). The moles of hydrogen may be calculated from N_{H_2,H_2O} using Equation (3.60) by multiplying the state of charge, and it is similar for determining oxygen as Equation (3.61), where Φ is the state of charge.

$$N_{H_2} = N_{H_2,H_2O}\,\Phi \tag{3.60}$$

$$N_{H_2O} = N_{H_2,H_2O}\,(1-\Phi) \tag{3.61}$$

The total mass (kg) of hydrogen is calculated by Equation (3.62), and the total mass of steam (kg) by Equation (3.63) [45] [46].

$$M_{H_2} = 0.00202 N_{H_2} \tag{3.62}$$

$$M_{H_2O} = 0.01801 N_{H_2O} \tag{3.63}$$

The number of moles of oxygen in the system can be calculated using Equation (3.43), except the volume is replaced by the volume of oxygen in the system v_{O_2}. This is calculated from the internal volume of each cell, multiplied by the number of cells, according to Equation (3.64). Then, the mass of oxygen (kg) in the system is calculated from Equation (3.65).

$$v_{O_2} = 0.1\pi r_{cell}^2 N_{cell} \tag{3.64}$$

$$M_{O_2} = 0.0320 N_{O_2} \tag{3.65}$$

The total heat capacity (JK^{-1}) of the gases in the system $H_{c,gases}$ may be calculated from Equation (3.66), where the heat capacity of each gas is multiplied by the mass of the gas (kg), and these heat capacities are added together. For instance, at 1000 ◦C, the total heat capacity of the system gases is 1324 kJK^{-1}.

$$H_{c,gases} = M_{gases} CP_{gases} = M_{H_2} CP_{H_2} + M_{H_2O} CP_{H_2O} + M_{O_2} CP_{O_2} \tag{3.66}$$

3.5.2.4 Heat Generated/Absorbed from Electrochemical Reaction

In the fuel cell mode, the system produces heat and electricity and consumes hydrogen. In electrolysis mode, the system consumes heat and electricity, storing the energy in the form of hydrogen. This heat input due to the reaction enthalpy change is p_e (Watts); in fuel cell mode, the reaction is exothermic, whereas in the electrolysis mode the reaction is endothermic. Besides the energy stored in chemical form, there is also energy existing in the form of heat within the stack, and this heat energy changes dynamically with time. The heat produced by the fuel cell reaction can be calculated from the current density and area of the reversible cell stack by using the following equations. The cell current can be related to the charge flowing per unit time (Equation (3.49)) and converted into moles of hydrogen consumed per second M_{H_2} using the Equation (3.51) [46]. These equations are suitable for both fuel-cell mode and electrolysis mode.

$$p_e = N_{cell} M_{H_2} (42.3241T - 4473.97) \tag{3.67}$$

The rate of moles of hydrogen consumed to heat generated per unit time p_e (W) for the whole system by the reaction depends on the fuel cell temperature and number of cells according to the Equation (3.67) [49].

3.5.2.5 Ohmic Heat Production

The resistance of the fuel cell components produces heat at a rate p_{ohm} (Watts) in both fuel cell mode and electrolysis mode.

$$p_{ohm} = N_{cell} i^2 R_{ohmic} \tag{3.68}$$

3.5.2.6 Heat Losses to Surroundings

The heat loss rate p_i (to surroundings) depends on the temperature difference between the stack and the surroundings, and the thermal conductivity and surface area of the vessel. This heat loss q_i could be ignored only if the vessel was assumed

to be perfectly insulated. therefore the dimensions of the vessel L_V may be calculated from Equation (3.69) where the volume v is 4 m^3, and the surface area A_V in m^2 from Equation (3.70).

$$L_v = \sqrt[3]{v} \tag{3.69}$$

$$A_V = 6L_V^2 \tag{3.70}$$

The thermal conductivity of the insulation changes with temperature according to Equation (3.71), where $a = 2.54132 \times 10^{-8}, b = 1.93343 \times 10^{-5}, c = 0.0257471$ [11].

$$\lambda = aT^2 - bT + c \tag{3.71}$$

The temperature of the cold face of the insulation T_c, on the outside of the system, is calculated from the semi-empirical Equation (3.72) [11], as a function of the temperature of the hot face of the insulation. The hot face temperature is assumed to be the same as the system temperature, therefore in this equation it is represented as T.

$$T_c = 0.0225455T + 279.627 \tag{3.72}$$

The heat flow through the walls q_i (Watts) may then be calculated from Equation (3.73) [11].

$$p_i = A_V \left[\left(\frac{a}{3l}T^3 - \frac{b}{2l}T^2 + \frac{c}{l}T\right) - \left(\frac{a}{3l}T_c^3 - \frac{b}{2l}T_c^2 + \frac{c}{l}T_c\right)\right] \tag{3.73}$$

3.6 RSOFC System Efficiency

3.6.1 Efficiency in Fuel Cell Mode

In order to calculate the electrical conversion efficiency in fuel cell mode, the energy content or enthalpy of the fuel, W_{fuel} (W) must be determined by using Equation (3.74) [44]. In this equation N_{H_2} is the moles of hydrogen consumed per second per

cell, from Equation (3.51), the enthalpy of the fuel W_{fuel} is calculated based on the hydrogen lower heating value (LHV), i.e. when the steam is not condensed, because this is the case within the RSOFC system [45]. Equation (3.75) shows the total electrical power output from the stack when running in fuel cell mode.

$$W_{fuel} = N_{cell} N_{H_2} (4.76042\mathrm{T} + 243825) \qquad (3.74)$$

$$W_{stack} = V_{stack} I_{stack} \qquad (3.75)$$

Then the percentage electrical conversion efficiency $E_{electrical,fuel\,cell}$ may be calculated from Equation (3.76).

$$E_{electrical,fuel\,cell} = \frac{W_{stack}}{W_{fuel}} \times 100\% \qquad (3.76)$$

3.6.2 Efficiency in Electrolysis Mode

In electrolysis mode, Equation (3.74) can be used to calculate the energy stored in the fuel. The percentage electrical conversion efficiency of the system over one second in electrolysis mode $E_{electrical,electrolysis}$ is defined in Equation (3.77) as the energy in the fuel created by electrolysis, W_{fuel}, divided by the energy input, which is the electrical energy W_{stack} used for electrolysis. By defining the fuel cell efficiency as the ratio of electrical power to the heat enthalpy released/stored in hydrogen, then this means that at low currents the electrical to chemical conversion efficiency can exceed 100% in electrolysis mode (where heat is disregarded in the efficiency calculation), if a massive amount of heat is not provided by input electric power but from a heat store , because some of the energy demand comes from heat in the system which is absorbed during the electrolysis. However, it does not exceed 100% at moderate or large cell currents, because of the ohmic losses in the cell increase faster with increasing current than the heat absorbed.

$$E_{electrical,electrolysis} = \frac{W_{fuel}}{W_{stack}} \times 100\% \qquad (3.77)$$

3.7 Conclusions

In this Chapter, the electro-chemical equations based modelling of a reversible solid oxide fuel cell system (RSOFC) are described. From literature survey and previous works it is realised that most models used for predicting the performance of the SOFC system are not appropriate to be directly applied for this research. This is because the RSOFC system proposed in this thesis has a pressurised vessel which stores fuel gas (hydrogen) within the sealed stack and no gas inlet or exhaust is involved. Therefore a unique model is required to represent the performances of Nernst voltage and cell polarisations which are highly distinctive to this specific stack geometry and the relative operating conditions, e.g. thermal dynamics, species partial pressures and the state of charge (SOC). It was decided to create a complete polarisation model in University of Strathclyde rather than applying a generalized SOFC model, e.g. demos can be from the Matlab/Simulink model library.

In this Chapter, the RSOFC electrical properties of Nernst voltage and polarisations are discussed first, and then the dimension of the modelling is extended to a stack with the considerations of the cell connection topology. Other influencing variables such as temperature, partial pressure, state of charge (SOC) and thermal dynamic (heat store status) are described as part of stack modelling. Simulations of the performance of a stack system are studied and discussed to provide important feedbacks to the proposed design, in turn, improving the fuel cell stack with an enhanced practical capability and realistic performance. A Randles circuit which represents an equivalent electrical circuit of RSOFC is derived and implemented for impedance spectroscopy (IS) simulation.

It is found that the temperature can increase rapidly in s the original design proposed by the University of St. Andrews, especially at high density power outputs. Overheating will lead to irreversible mechanical damage to cell and this is hard to avoid due to the specific design of the sealed and pressurised vessel from which the massive heat exchange between gas fluids and external environment is not possible. To prevent overheating firstly the stack geometry and pressurization were improved

which helps with a slight gain of enhancement. Another suggestion of adding a heat storage equipment was proposed by the author, and then a novel application of a copper-tin based internal heat storage device is proposed by the University of St. Andrews. This heat store prevents overheating by phase change. It starts to melt when the temperature reaches 1010 ^{O}C and the system temperature remains constant until the heat store is totally melt down. It is suggested that the heat store should be calibrated with the fuel storage to avoid being totally molten, to prevent further damage.

Multiple positive feedbacks can be obtained by improving pressurisation and system volume from 5 bar and 2 m^3 as for the original design, to the updated settings of 70 bar and $4m^3$. First of all, the entropy of the gases in the system is reduced, so every mole of hydrogen that is consumed produces less heat. Secondly, it is obvious that the hydrogen/energy stock capability of the system can be increased. Therefore more energy stored in hydrogen is available to be converted into electricity, which significantly enhances the operation time at the rated power. Higher volume and pressure level also increase the heat capability of gases massively according to the simulations, which can partly compensate the overheating issue, and boost the electrical conversion efficiency.

In activation polarisation modelling it is found that the electro-transfer coefficient β cannot be simply assumed with a generic value used by most authors reported in literature, but to be derived for this specific RSOFC design. This coefficient is critical in activation loss model to check whether the polarisation is in low or high condition so β has to be found with an appropriate value, otherwise simulation will be highly unstable. It is also found during this research that β is only related to the involved electro-chemical reactions, and it is not suggested to be the same value for all fuel cell designs. In this thesis a new derivation methodology of β is proposed and this mostly cannot be found from literatures, which is highly possible to name this work a high valued contribution.

3.8 References for Chapter 3

[1] S.Campanari, P.Iora, "Definition and sensitivity of a finite volume SOFC model for a tubular geometry," *J. Power Sources*, vol. 132, pp. 113–126, (2004).

[2] J.H. Lee, T.R. Lalk, "Modeling fuel cell stack systems," *J. Power Source*, vol. 73, pp.229–241, June 1998.

[3] K. Sedghisigarchi, A. Feliachi, "Dynamic and transient analysis of power distribution systems with fuel cells—Part I: fuel-cell dynamic model," *IEEE Trans. Energy Conversion*, vol. 19, NO. 2, June 2004

[4] S. Ahmad Hajimolana and Masoud Soroush, "Dynamic Behavior and Control of a Tubular Solid-Oxide Fuel Cell System," *in 2009 American Control Conference,* Dept. of Chem. Eng., Azad Univ. of Shahrud, Shahrud, Iran
Soroush, M. June 2009, pp. 2660-2665

[5] W. Choi, Jo.W. P. Enjeti, "Development of an equivalent circuit model of a fuel cell to evaluate the effects of inverter ripple current," , J. *Power Sources*, vol. 158, pp. 1324–1332, 2006

[6] A. Dicks and J. Larminie, *Fuel Cell Systems Explained, 2nd Edition* John Wiley and Sons Inc, ISBN: 0-470-84857-X

[7] A. Gebregergis, P. Pillay, "The Development of Solid Oxide Fuel Cell (SOFC) Emulator," in 2007 *Power Electronics Specialists Conference*, Clarkson Univ. Potsdam, Potsdam Pillay, P. June 2007, pp. 1232-1238

[8] S.H Chan, K.A Khor, Z.T Xia, "A complete polarization model of a solid oxide fuel cell and its sensitivity to the change of cell component thickness,", *J.Power Sources,* vol. 93, Issues 1–2, pp. 130–140, Feb 2001.

[9] A. Petric, P. Huang, "Evaluation of La–Sr–Co–Fe–O perovskites for solid oxide fuel cells and gas separation membranes,", , *J. Solid State Ionics*, vol. 135, pp. 719–725, 2000

[10] S. Christoph, S. Steinar; "Finite-volume modeling and hybrid-cycle performance of planar and tubular solid oxide fuel cells," *J. Power Sources*, vol. 141, Mar, 2005.

[11] Microtherm®, Specs of High Temperature Microporous insulation. [online]. Available:

http://www.microthermgroup.com/high/EXEN/site/downloads-overview.aspx?k=63&l=8

[12] X. Yuan, H. Wang, "AC impedance technique in PEM fuel cell diagnosis—A review," *International J. Hydrogen Energy*, vol. 32, Issue 17, pp. 4365–4380, December 2007

[13] Y. Wang, C.Wang, "Dynamics of polymer electrolyte fuel cells undergoing load changes," *J. Electrochimica Acta,* vol. 51, Issue 19, pp. 3924–3933, May 2006]

[14] V. Virkar, J. Chen, C. W. Tanner, "The role of electrode microstructure on activation and concentration polarizations in solid oxide fuel cells", , *J. Solid State Ionics*, vol. 131, pp. 189–198, 2000.

[15] M. Ni, M. K. H. Leung, D. Y. C. Leung, "A review on reforming bio-ethanol for hydrogen production," *Int. J. Hydrogen Energy*, vol. 32, pp. 2305–2313, 2007

[16] Private communication with Dr. Stephen Gamble, in University of St. Andrews, UK

[17] D. Sánchez, A. Muñoz, T. Sánchez, "An assessment on convective and radiative heat transfer modelling in tubular solid oxide fuel cells," *J. Power Sources*, vol. 169, pp. 25–34, 2007

[18] J. Mahmoudi, H. Fredriksson, "Thermal analysis of copper-tin alloys during rapid solidification," *J. Mater. Sci*, vol. 35, pp. 4977–4987, 2000

[19] N. Saunders, A. P. Miodownik, "The Cu-Sn (copper-tin) system", *J. Phase Equil*, vol. 11, pp. 278–287, 1990.

[20] S. Yerramalla, A. Davar, "Modeling and simulation of the dynamic behavior of a polymer electrolyte membrane fuel cell," *J. Power Sources*, vol. 169, pp. 177–189, 2003

[21] F. Jurado, "Modeling SOFC plants on the distribution system using identification algorithms," *J. Power Sources*, vol.129, pp. 205–215, April 2004

[22] Anon, *Fuel cell handbook, 5th , ed*, US Department of Energy, October 2000

[23] J.W. Gibbs, "A Method of Geometrical Representation of the Thermodynamic Properties of Substances by Means of Surfaces,"

Transactions of the Connecticut Academy of Arts and Sciences, Dec. 1873, pp. 382-404 (quotation on p. 400)

[24] Müller, Ingo (2007). *A History of Thermodynamics - the Doctrine of Energy and Entropy*. Springer. ISBN 978-3-540-46226-2

[25] H. Mahcene, H. Ben Moussa, "Losses effect on solid oxide fuel cell stack performance," *J. Fuel Cells*, vol.117, pp. 218–236, 2004

[26] P.-W. Li, M. K. Chyu, "Simulation of the chemical/electrochemical reactions and heat/mass transfer for a tubular SOFC in a stack," *J. Power Sources*, vol. 124, pp. 487–498, 2003

[27] J. Larminie and A. Dicks, *Fuel Cell Systems Explained*, Wiley, 2nd edn., 2003

[28] A.L. Hines, R.N. Maddox, *Mass Transfer: Fundamentals and Applications*, Prentice-Hall, Englewood Cliffs, NJ, 1985

[29] P. Iora, "Definition and sensitivity analysis of a finite volume SOFC model for a tubular cell geometry," *J. Power Sources*, vol. 132, Issues 1–2, pp. 113–126, May 2004

[30] A. Selimovic, "Modelling of solid oxide fuel cells applied to the analysis of integrated systems with gas turbines," PhD Thesis, Lund University, Sweden, 2002.

[31] P. Costamagna, K. Honegger, "Modeling of solid oxide heat exchanger integrated stacks and simulation at high fuel utilization," *J. Electrochem. Soc.* vol. 145 (11) pp. 3995–4007, 1998.

[32] D. A. Noren, M. A. Hoffman, "Clarifying the Butler–Volmer equation and related approximations for calculating activation losses in solid oxide fuel cell models," *J. Power Sources*, vol. 152, pp. 175–181, 2005

[33] C. J. Hatziadoniu, A. A. Lobo, F. Pourboghrat, M. Daneshdoost, "A Simplified Dynamic Model of Grid-Connected Fuel-Cell Generators" *IEEE Trans. Power Delivery,* , vol. 17, Issue 2, pp. 467 – 473, Apr 2002

[34] R. H. Perry, D. W. Green, *Perry's Chemical Engineer's Handbook 7th ed*., of Chemical Engineering Series, McGraw-Hill, 1997

[35] B. E. Pauling, J. M. Prausnitz, J. P. O'Connell, *Properties of Gases and Liquids 5th ed*., of The Properties of Gases and Liquids, McGraw Hill, 2001

[36] S. Campanari, P. Iora, "Definition and sensitivity analysis of a finite

volume SOFC model for a tubular cell geometry," *J. Power Sources*, vol. 132, Issues 1–2, pp. 113–126, May 2004

[37] Mason, E.A, *Gas transport in porous media : the dusty-gas model / E.A. Mason and A.P. Malinauskas*, ISBN: 0444421904, Elsevier Scientific, 1983

[38] P.Li, M, K, Chyu, "Simulation of the chemical/electrochemical reactions and heat/mass transfer for a tubular SOFC in a stack," *J. Power Sources*, vol. 124, Issue 2, pp. 487–498, November 2003.

[39] E. C. Thomsen, G. W. Coffey, L. R. Pederson, and O. A. Marina, "Performance of lanthanum strontium manganite electrodes at high pressure," *J. Power Sources*, vol. 191,pp. 217–224, February 2009

[40] I. EGG Technical Services, *Fuel Cell Handbook*, U.S. Department of Energy, 2004

[41] P. Costamagna, K. Honegger, "Modeling of solid oxide heat exchanger integratedstacks and simulation at high fuel utilization," *J. Electrochem. Soc*. vol. 145 (11), pp. 3995–4007, 1998

[42] Clapeyron, E. (1834). "Mémoire sur la puissance motrice de la chaleur". Journal de l'École Polytechnique XIV: 153–90. (French) Facsimile at the Bibliothèque nationale de France (pp. 153–90).

[43] A. Atkinson, S. A. Baron, N. P. Brandon, "AC impedance spectra arising from mixed ionic electronic solid electrolytes," *J. Electrochem. Soc.* vol. 151, pp. 186–193, 2004.

[44] NIST, NIST Chemistry WebBook, last accessed 01/08/2011

[45] Palmer, D. "*Hydrogen in the Universe*" NASA. Retrieved 2008-02-05. (13 September 1997)

[46] G. J. Leigh, "Principles of chemical nomenclature: a guide to IUPAC recommendations", pp. 99. Blackwell Science Ltd, UK.ISBN 0-86542-685-6 *et*,1998

[47] P Kazempoora, Fathollah Ommia, "Response of a planar solid oxide fuel cell to step load and inlet flow temperature changes," *J. Power Sources,* vol. 196, Issue 21, pp. 8948–8954, November 2011

[48] R. H. Perry and D. W. Green. *Perry's Chemical Engineer's Handbook. Chemical Engineering Series. McGraw-Hill, 7th edition*, 1997

[49] J. Ren, S. Gamble, A. J. Roscoe, and G. M. Burt, "Modelling a reversible

solid oxide fuel cell to be used as a storage device within AC power networks*",* in *Power Electronics, Machines and Drives (PEMD 2010),* 5th IET international conference, Publication Year: 2010, DOI: 10.1049/cp.2010.0119

[50] W. He, "Dynamic Simulations of Molten-Carbonate Fuel-Cell Systems," PhD dissertation, Mechanical Maritime and Materials Engineering, The Netherlands: Delft Univ. Press, Dec. 2000

4 Investigation into the Dynamic Performance of RSOFC System

4.1 Introduction

In this chapter the dynamic performance of the RSOFC system will be investigated in detail. Simulations which support the updated system design for performance improvements are demonstrated. Case studies of discharge - recharge cycle operations are fully discussed to examine the fidelity of the copper-tin heat store proposed in this research. The cycle efficiencies at different operating current magnitudes are also listed and discussed.

4.2 Effects of Temperature, Pressurization and State of Charge on RSOFC Performance

4.2.1 Nernst Voltage

The Nernst voltage is dependent on three factors: temperature, species (gas) partial pressure and SOC according to Equation (3.5) and (3.9) in Chapter 3, whose variation as a function of these variables is shown in Figure 4.1. The Nernst voltage is greater at higher system pressure and SOC, but decreases with the increase of the system temperature. Among all three parameters the SOC causes the highest impact, as about 25% of deviation exists in V_{Nernst} between 5% to 95% of SOC. It can be seen that the voltage drop due to lower SOC leads to less power output. Therefore to maintain a high power output it is suggested for the RSOFC system not to be operated at particularly low SOCs.

Higher temperature leads to a reduction in V_{Nernst} as well; however this deviation is much smaller. In fact the kinetics of the other electro-chemical reactions of activation and diffusion can be improved with higher temperature and pressurisation, and these are shown in Section 4.2.2 and 4.2.3. Therefore the enhancement from higher temperature on overall cell performance is possible and this is demonstrated in Section 4.2.5.

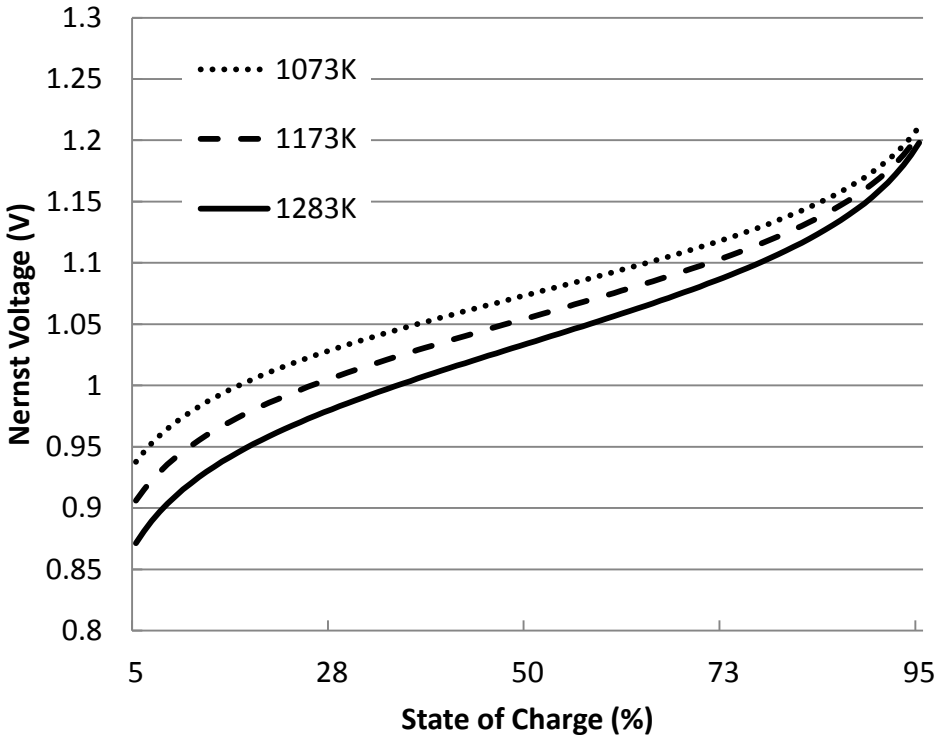

(a)

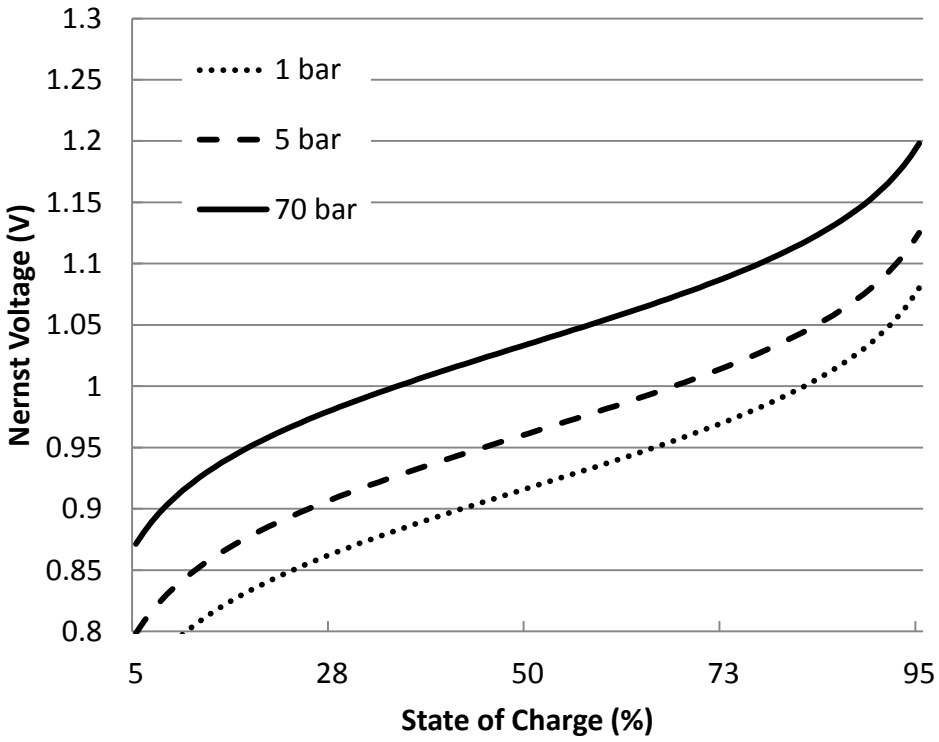

(b)

Figure 4.1 Nernst voltage of a single RSOFC against SOC: a) at 70 bar pressure, b) at 1283K （900 ^{o}C）

4.2.2 Activation Polarisation

The activation polarisation is dependent on temperature and the magnitude of current according to both Equation (3.13) and (3.14) in Chapter 3, and it is obvious as shown in Figure 4.2 in both fuel cell (positive current in figures) and electrolysis (negative current in figures) modes.

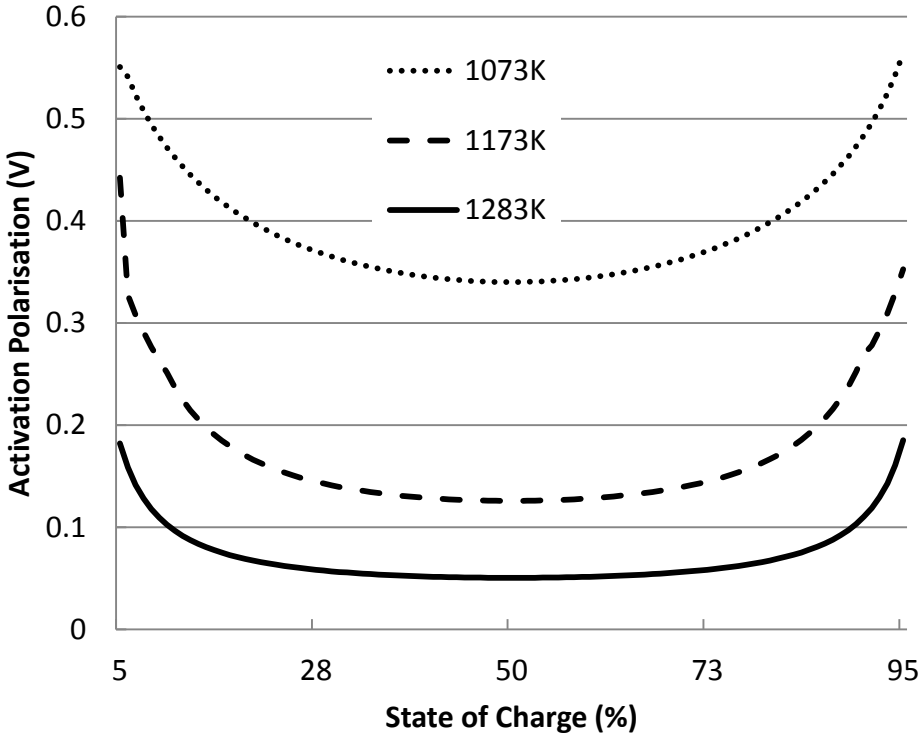

Figure 4.3 shows higher temperature significantly lowers the activation polarisation and this is because the charges are more active during the transport between the ionic conductors, which lowers the "energy barrier" in electrochemical reactions. It is also interesting to know that even both Equation (3.13) and (3.14) do not show the relationship between the activation polarisation and SOC, however it increases greatly at extremely low and high SOC. This is because both low hydrogen and high steam concentration require a higher energy boost to overcome the extra potential for electrode reactions. At low or high SOCs where the concentration of hydrogen and steam is more imbalanced in the system, the exchange current density is lower, increasing activation losses.

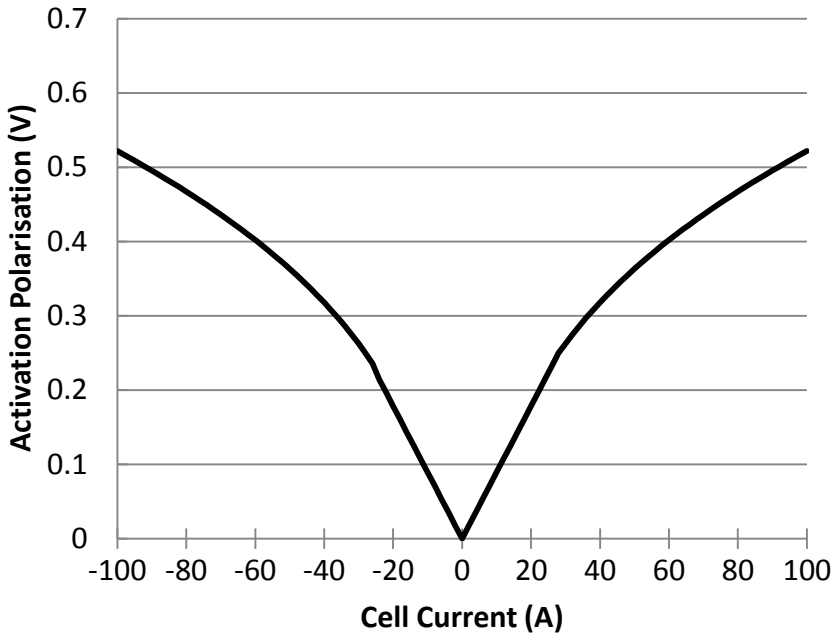

Figure 4.2 Activation polarisation VS current of a single RSOFC (70 bar, 1283K, 95% SOC)

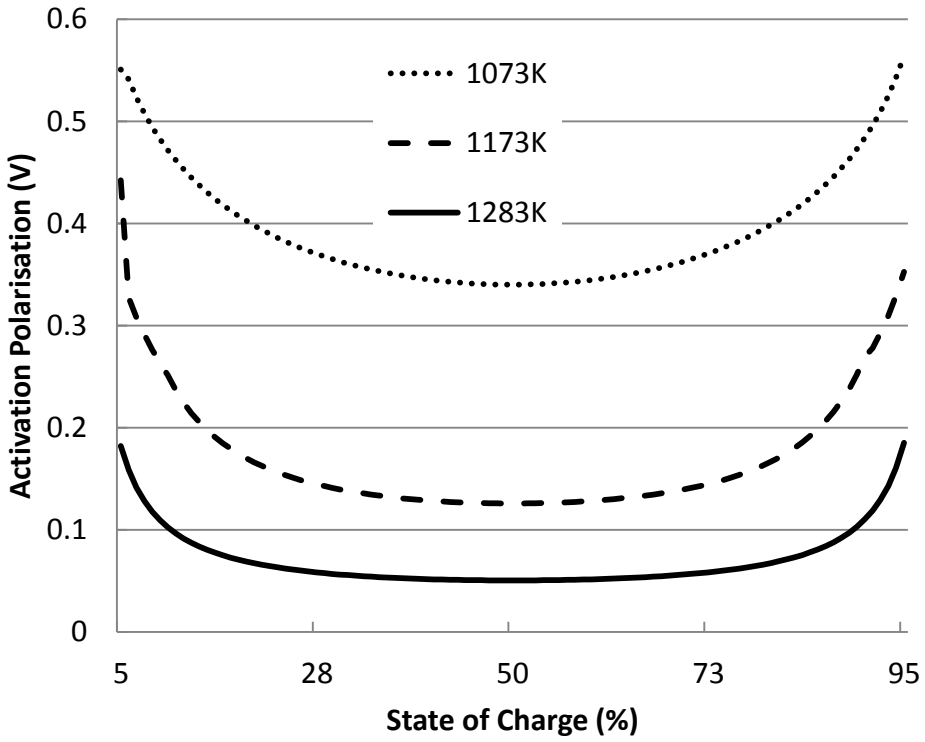

Figure 4.3 Activation polarisation VS temperature of a single RSOFC (70 bar, 20.4A)

4.2.3 Diffusion Polarisation

The diffusion polarisation increases with the magnitude of current and this is shown in Figure 4.4. Figure 4.5 shows the effects on the diffusion polarisation by varying the system pressure and temperature. It is obvious that higher pressurisation and temperature lower the diffusion polarisation and these can be significant. At 1 bar of system pressure the diffusion varies greatly with temperature. However at 70 bar the diffusion loss is significantly reduced and the temperature affects much less. This again proves the significant improvement that can be obtained at 70 bar compared to the original design of 5 bar of system pressure. This is because at higher pressure the concentrations of gases are higher, then the reactants can more easily pass through the pores of the electrode. Higher temperature also plays a role in enhancing the overall performance as discussed before. In fact diffusion polarisation is also dependent on SOC, but the variation is extremely small so it is not discussed here.

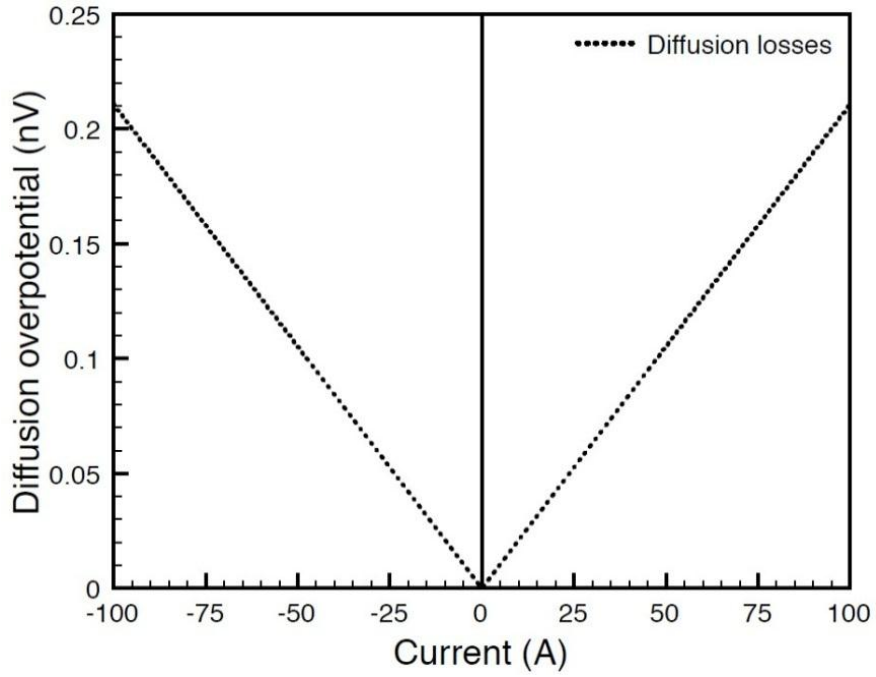

Figure 4.4 Diffusion losses at the fuel electrode as a function of RSOFC current, at 1173K (900 ^{o}C), 70 bar pressure, and 50% state of charge. Negative currents represent electrolysis mode, and positive currents fuel cell mode.

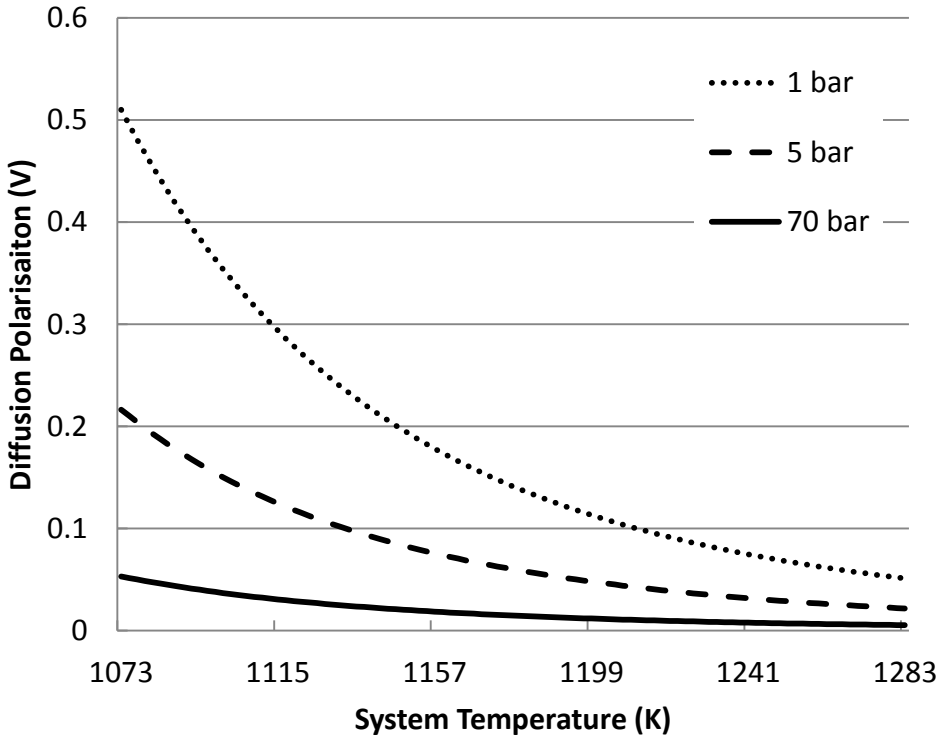

Figure 4.5 Diffusion Polarisation against temperature (90% SOC, 20.4A)

4.2.4 Voltage Drop on Electrical Resistance

At high system pressure and temperature the activation and diffusion polarisation decease significantly, however the overall fuel cell performance can still be compromised by the ohmic losses, especially at high current density and which is even worse at high temperature as shown in Figure 4.6. The resistance depends on the materials used, e.g. the electrolyte has a lower electrical conductivity than other ceramic materials as the nickel metal on the fuel electrode side of the cell. The ohmic losses are also a function of the length of the current paths in the cell design. If these were shortened by redesigning the cell geometry, the ohmic losses would be reduced. In addition it is suggested that cells should be connected in parallel with reasonable designing considerations to lower the overall resistance of a stack system.

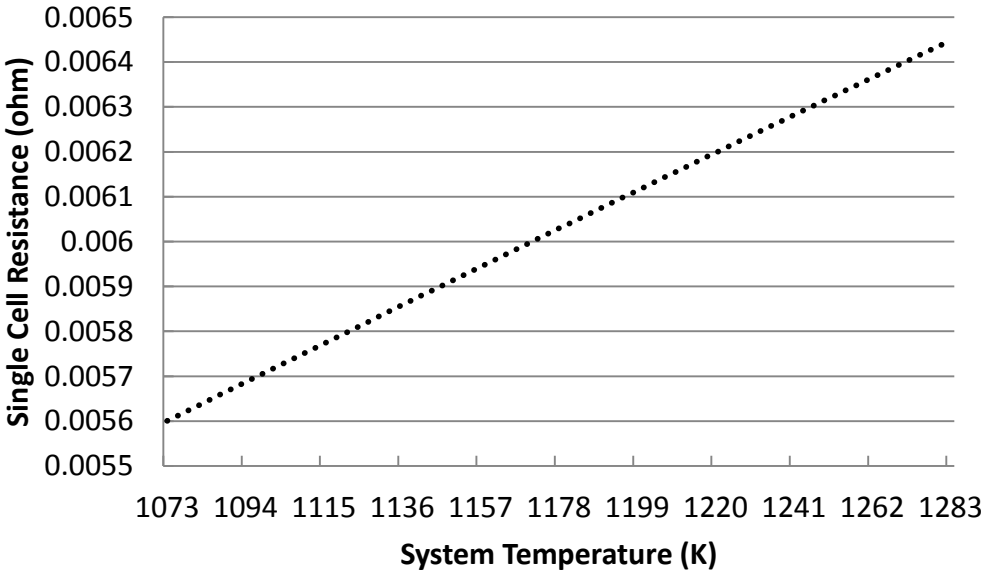

Figure 4.6 Resistance of a single cell against temperature

4.2.5 Effects of Temperature, Pressurization and State of Charge on Fuel Cell Terminal Voltage

Figure 4.7 shows the simulated terminal voltage of a single RSOFC with varying currents. The fuel cell operates in electrolysis mode when the current is negative, which means the current is flowing into the fuel cell. In fuel cell mode the current is positive and the SOFC outputs power to the network. According to Equation (3.3) in Chapter 3, the cell voltage is the Nernst potential plus all of the voltages drops in electrolysis mode, therefore as the current density increases the cell voltage is increased as well as the power input (recharging rate), which can be much more than the power output in fuel cell mode. Temperature has a large impact on the maximum power which can be enhanced from 11.7W at 1073K (800 ^{o}C), to 21 W at 1173K (900 ^{o}C), to ~29.3 W at 1283K (1010 ^{o}C) in fuel cell mode as shown in Figure 4.7 (b). However the temperature has a negative impact in electrolysis mode by reducing the recharging power input from 265 W at 1073K (800 ^{o}C) to ~190 W at 1283K (1010 ^{o}C) at -100 A of current.

Figure 4.8 shows the performances under three different pressure conditions. An increase in output power is achieved at higher pressure due to greater Nernst voltage and reduced diffusion loss (18.3W at 1bar, 23.1 W at 5bar), ~29.3 W at 70 bar and 1283K (1010 ^{o}C) 50% of SOC). Figure 4.9 also shows the RSOFC performance at three SOC values at 1283K (1010 ^{o}C). Normally as the state of charge increases, the Nernst voltage of the cell increases as shown in Figure 4.1, and so the cell performance improves. The worst performance in fuel cell mode happens at the lowest state of charge, and the worst performance in electrolysis mode is at the highest state of charge.

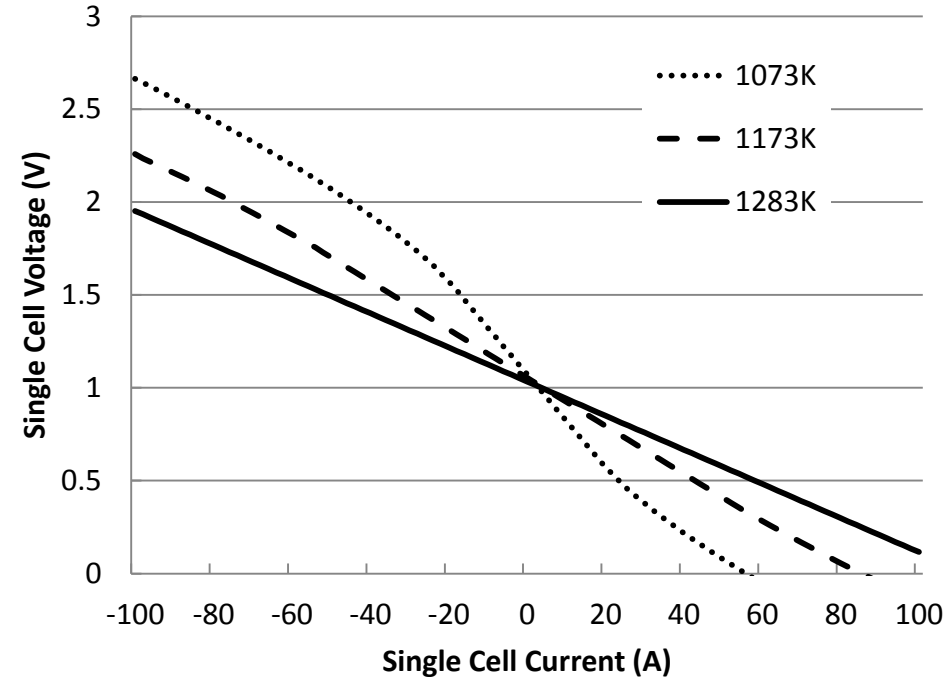

(a)

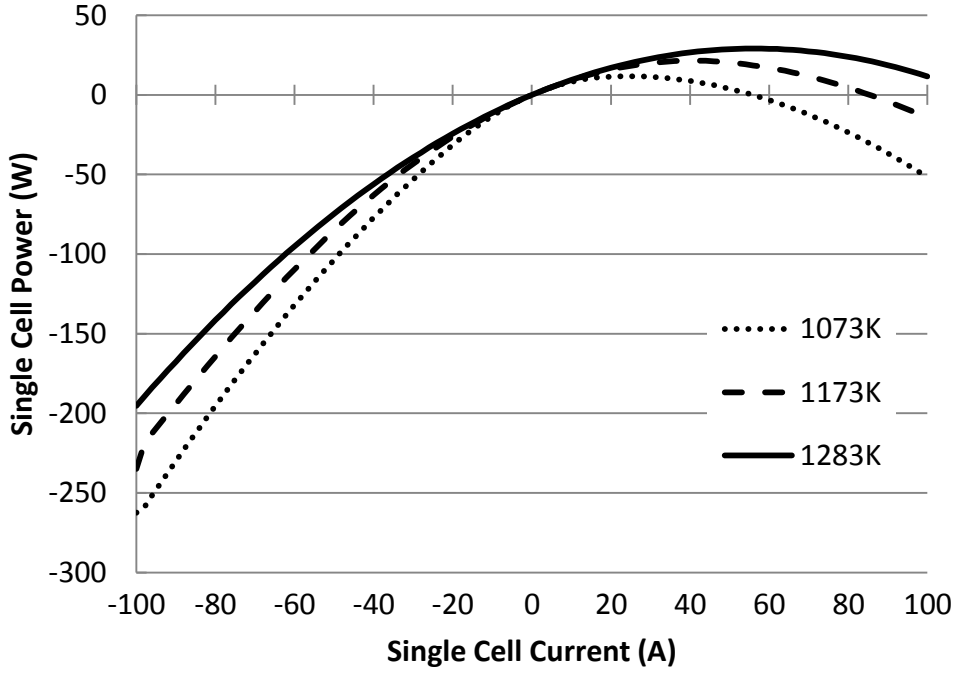

(b)

Figure 4.7 RSOFC voltage at 1073K, 1173K and 1283K (800 ^{o}C, 900 ^{o}C and 1010 ^{o}C) for a single reversible SOFC, at 50% SOC, 70 bar pressure: a) V-I curves, b) P-I curves

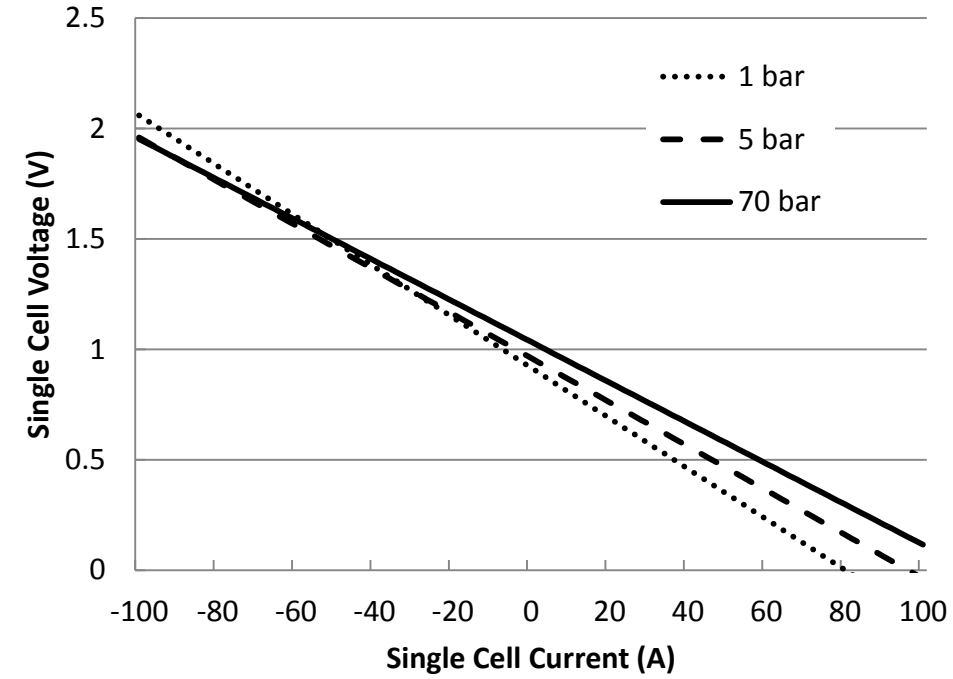

(a)

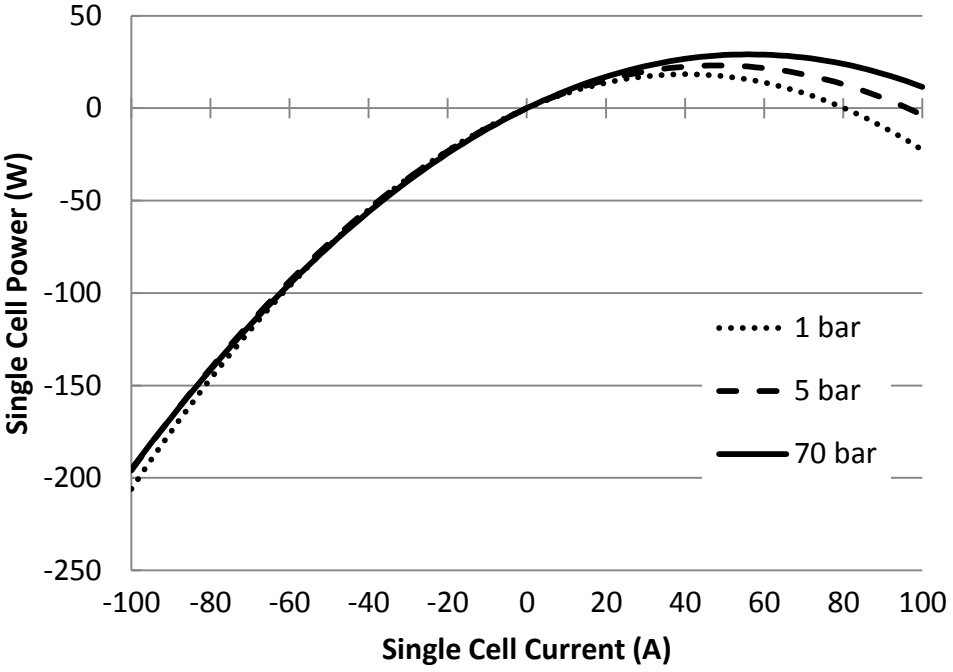

(b)

Figure 4.8 RSOFC performance at 1 bar, 5 bar, and 70 bar, at 50% state of charge and 1283K (1010 ^{o}C): a) V-I curves, b) P-I curves, for a single reversible SOFC.

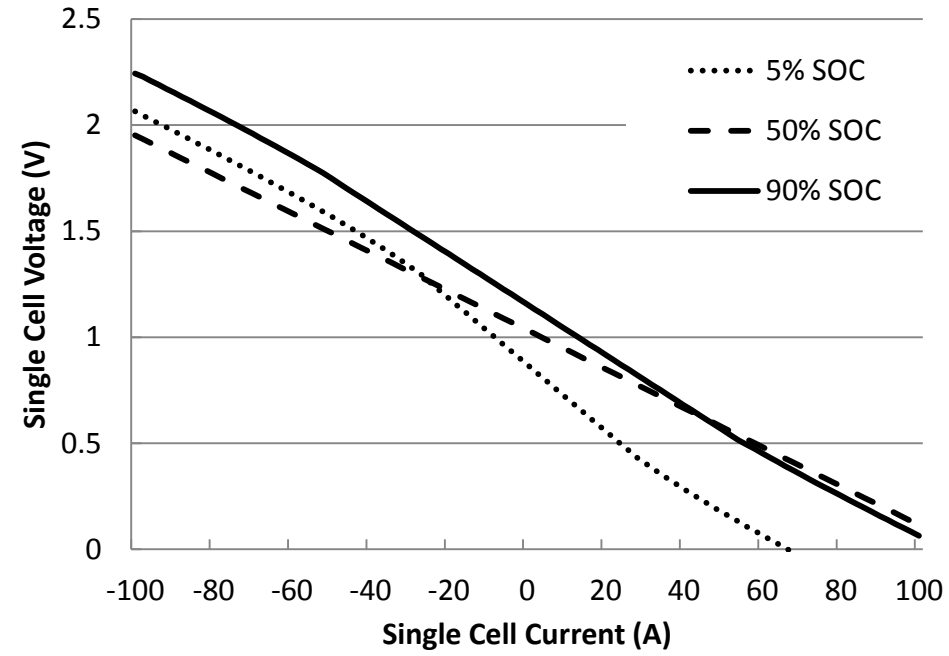

(a)

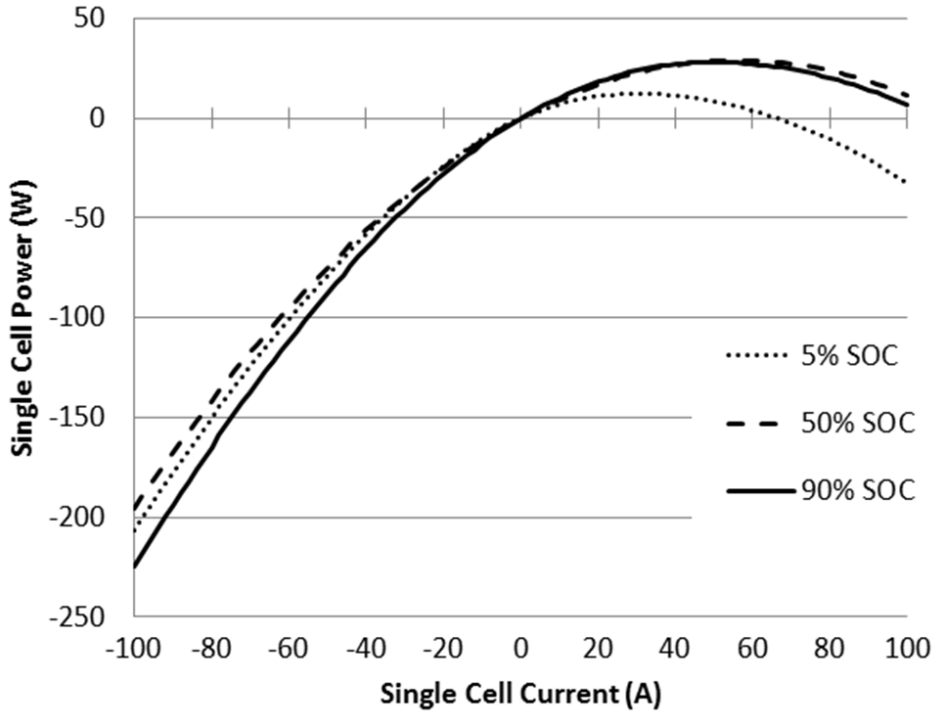

(b)

Figure 4.9 RSOFC performance at various states of charge, 5%, 50% and 90%, at 70 bar pressure and 1283K (1010 ^{o}C): a) V-I curves, and b) W-I curves, for a single reversible SOFC.

The traditionally normalized VI curve of RSOFC is much like the one at 1073K in Figure 4.7 (a) and the one at 5% of SOC in Figure 4.9 (a). Both curves have the concave area at high current density and convex area at low current density. This is because at low current density the VI shape is dominated by activation loss and at high current the diffusion loss shapes it with more effort. The nominal fuel cells with fuel inlet (with low pump pressure at which the partial pressure of fuel gas can be treated as low SOC) and lower system temperature always observe a VI curve with the convex and concave sections. However in this research the system is at high system pressure and mostly does not operate at low SOC such as 5% therefore the VI curve is close to a straight line. This RSOFC design also involves more resistance components than is simplified in some literatures, such as the independent support, interconnect and cell connections. The benefit of designing the cell geometry this way is to minimise the thickness of the electrode layers in order to lower activation and concentration losses. Figure 4.8 shows the simulation results under 1283K of temperature, at which although the activation and diffusion polarisations are decreased significantly but the resistance is even higher, according to the discussions in Section 4.2.2, 4.2.3 and 4.2.4. Therefore the resistance components dominate the voltage drop as shown in Figure 4.8 (a). So this is another reason that the V-I curve is more like a straight line rather than curved with obvious activation and concentration polarisation contributions.

4.3 RSOFC Stack System Performance

4.3.1 Heat Performance and System Efficiency

Figure 4.10 shows the net heat production/consumption by a single RSOFC as a function of current as described in Section 3.6 in Chapter 3. In fuel cell mode, heat is produced from both the ohmic resistance and exothermic electro-chemical reactions, so the temperature can rise rapidly with current. In electrolysis mode, the endothermic electro-chemical reactions contribute heat reduction and this offsets the resistance heat production. Therefore, at low currents where the ohmic losses are low, there is a range of current within which the negative net heat production occurs. This can be seen where the heat balance curve is below the x-axis.

The electrical efficiency is directly determined by the fuel cell current density as shown in Figure 4.10. Higher current leads to higher resistance heat production so the efficiency is decreasing in fuel cell mode with increasing current. Therefore, the best way to maximize electrical storage efficiency is to run the system at relatively lower currents. It can also be influenced by other operating parameter/conditions, e.g. system temperature and pressure. The point of maximum electrical efficiency will not correspond to the point of maximum output power in both modes, as discussed in the previous chapters. The electrical conversion efficiencies in both modes are defined by Equation (3.76) and (3.77) in Chapter 3. It is suggested that the cells should be connected in parallel as much possible within the stack to make the system current being shared by several paths of cells, which increases the efficiency.

Figure 4.11 shows the heat loss through the walls of the system as a function of system temperature. The heat loss from the system increases by 40% when the system temperature increases from 1073K (800 ^{o}C) to 1283K (1010 ^{o}C). However this part of heat loss is small compared to the maximum electrical power output of the RSOFC system in fuel cell mode, e.g. at 1283K (1010 ^{o}C) the heat loss is 2.1 kW, and the maximum electrical power output is 23.6 kW (800 cells).

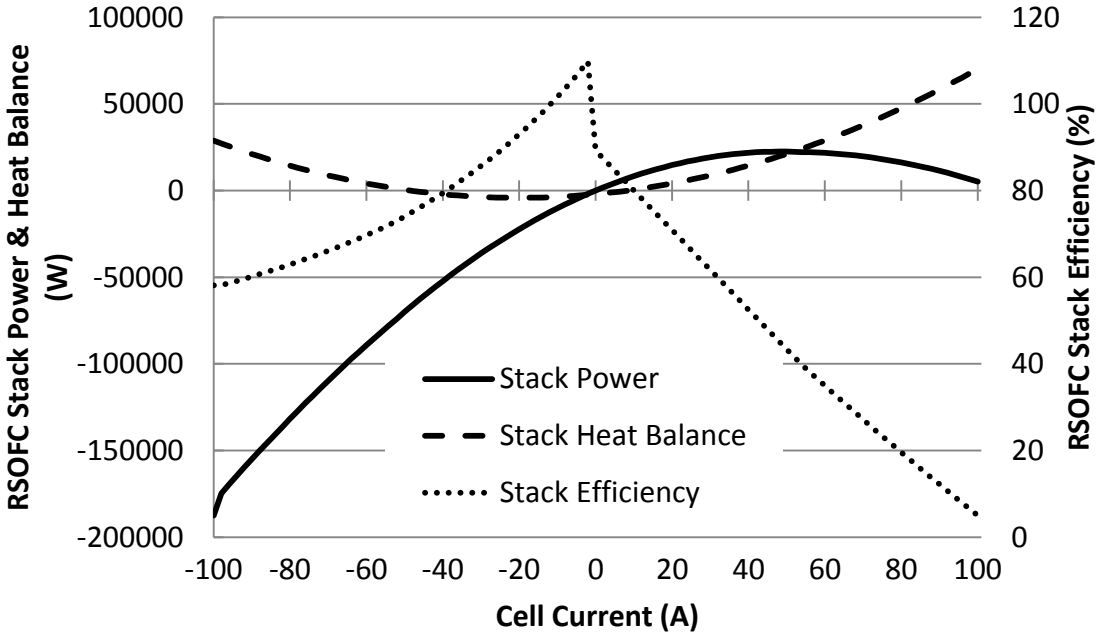

Figure 4.10 Net electrical power (W) and heat consumption/production (W) by the RSOFC as a function of current (at 1283K (1010 ^{o}C) 70 bar of pressure, and 90% SOC)

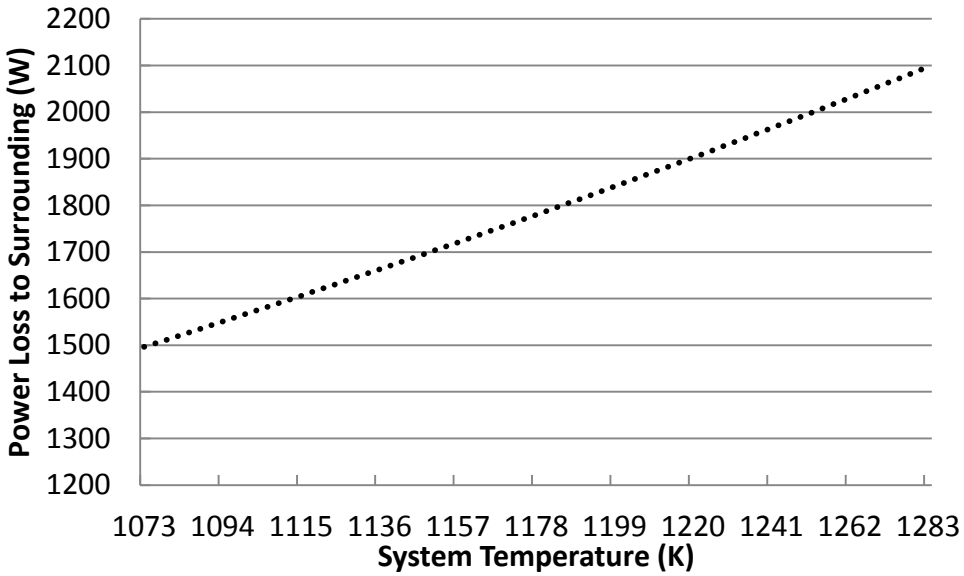

Figure 4.11 Heat loss through the isolation of the RSOFC system to the surroundings as a function of system temperature.

4.3.2 Case Studies of Discharge-Recharge Cycles

4.3.2.1 Heat Performance of RSOFC System during Cycle Operations

Energy is stored in the RSOFC system into two forms: chemical energy in hydrogen, and the heat energy in the thermal mass of the stack, system gases and the heat store. This Section shows case studies of a complete cycle operations which focus on discharging and recharging the ROSFC system towards to its limits, to verify the proposed copper-tin heat store introduced in Chapter 3 (within the RSOFC stack having 800 cells). The protocol is to start the operation in fuel cell mode first from 95% of SOC and 1073K ($800\,^{O}C$) at a constant current density until 5% SOC is reached, then reverse the operation in electrolysis mode until the SOC raises back to 95% at the same recharging current density. The mass of heat store is set to 500 kg in the following case studies.

Figure 4.12 (a) shows a cycle operation running at 20.4 A/-20.4 A per cell (half rated current at 1283K) and Figure 4.12 (b) is at 40.8 A/-40.8 A (rated current at 1283K) per cell. The graphs show the heat produced/consumed by the electro-chemical reactions, ohmic losses, the heat lost to the surrounding, and the net heat balance which actually is the energy being stored in heat store at the steady state temperature of 1283K. In electrolysis mode the net heat can be negative which indicates a heat energy release from the heat store.

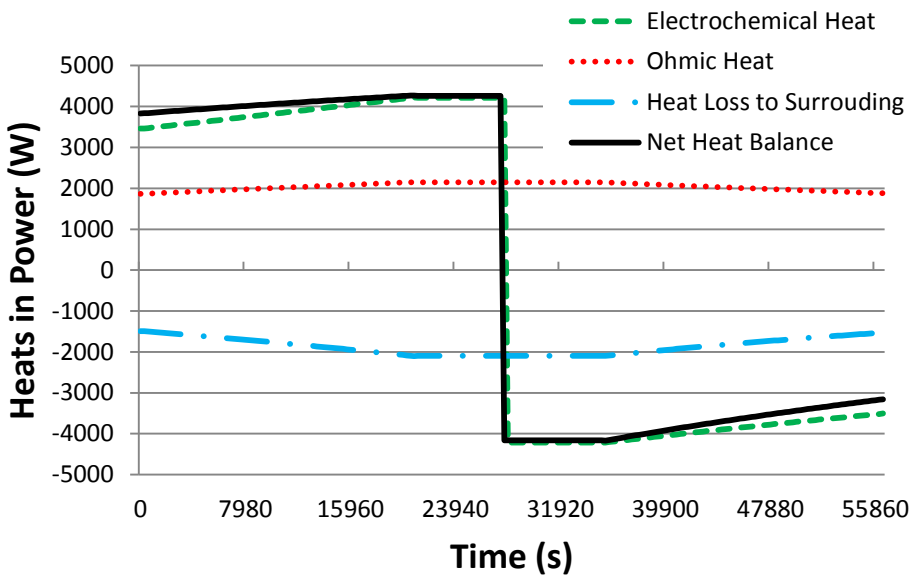

(a)

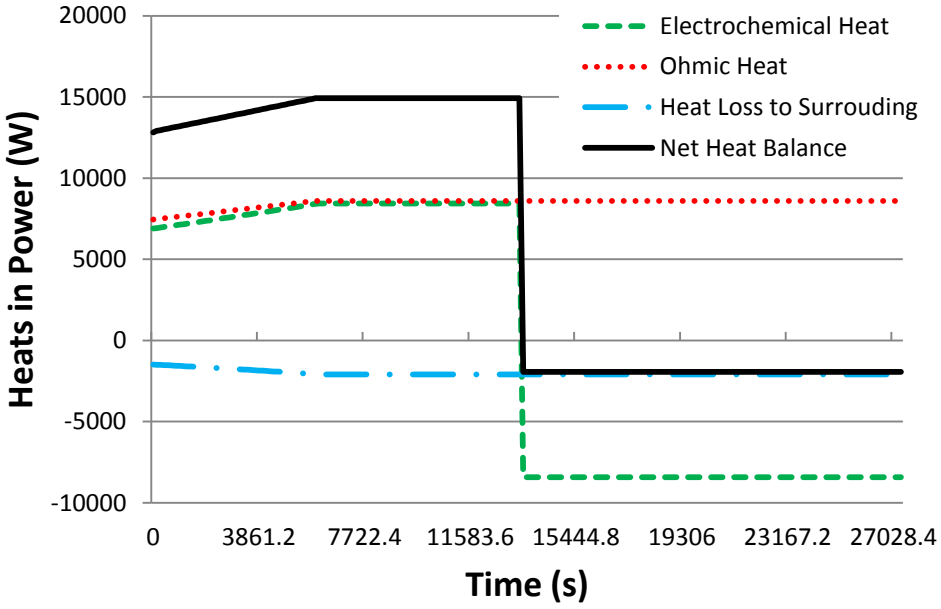

(b)

Figure 4.12 Stacked heat flows and heat balance in the reversible. The cycle in graph : a) 20.4 A per cell, or 3247 Am^{-2} in fuel cell mode, and -20.4 A, or -3247 Am^{-2} in electrolysis mode, b) 40.8 A per cell, or 6494 Am^{-2} for fuel cell mode, and -40.8 A per cell, or -6494 Am^{-2} in electrolysis mode.

It can be seen from Figure 4.12 that the heat production is much greater at the rated current (40.8 A per cell) than at the half rated current (20.4 A). At the half rated current the heat production from ohmic components nearly equals to the heat loss to surroundings during the cycle operation, which results in that the magnitudes of positive and negative net heats are very close between the fuel cell mode and electrolysis mode. Therefore the SOC and heat store can almost be recovered during a cycle operation with same operation periods in both modes.

At the rated current much more heat is generated from both the ohmic resistance and the exothermic reactions in fuel cell mode, therefore the temperature raises rapidly. During the electrolysis mode the heat produced by ohmic components and the heat absorbed by electrolysis almost cancel each other. Under this situation the net heat only counts for the heat loss to surroundings. Therefore the net heats between both modes are very unbalanced and there exists an excess energy not being recycled, which leads to a hidden risk of overheating. The safest operation current is found to be 8.3A at which the RSOFC system reaches a thermal-neutral state that the system temperature is constant because of zero net heat. Actually in cycle operations at low rated current (less than half rated current) the system temperature can cool down below the optimised range and the heat store is not even necessary.

With the features and results discovered above, it is difficult to allocate an optimised amount of heat store to satisfy all possible conditions. Figure 4.13 shows the system temperature, state of charge and heat store molten ratio during the same cases. In both cycles, the system temperature rapidly increases to 1283K (1010 ^{O}C) then remains constant as the heat store starts to melt down (phase change of the copper-tin compound). Figure 4.13 shows that in the half rated and the rated current operations, more than 80% and 30% of heat store amount (500kg) is considered as wasted as the none-molten segments until the fuel is nearly exhausted. To guarantee an overheating protection in a fully discharged operation, the amount of heat store has to be coordinated with the operating power rating, as well as the fuel cell hydrogen storage capability. In this proposed design of the vessel with 70 bar and 4 m^3 geometry, it is suggested that at least 390 kg of heat store is required for the rated power output operation, and at least 200 kg for the operation at half rated fuel cell current.

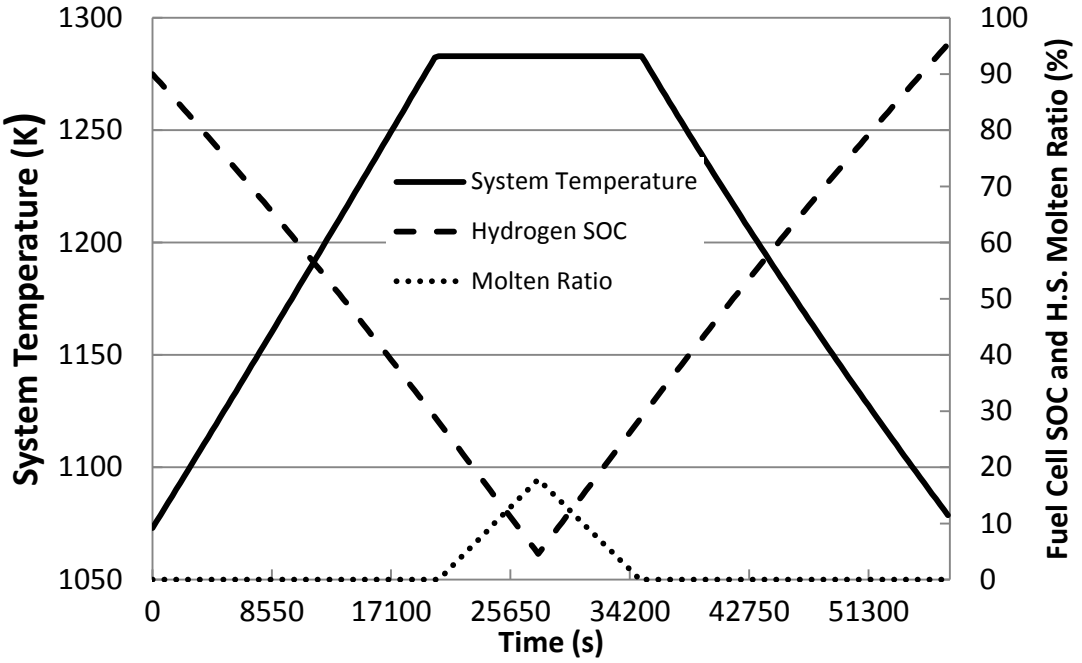

(a)

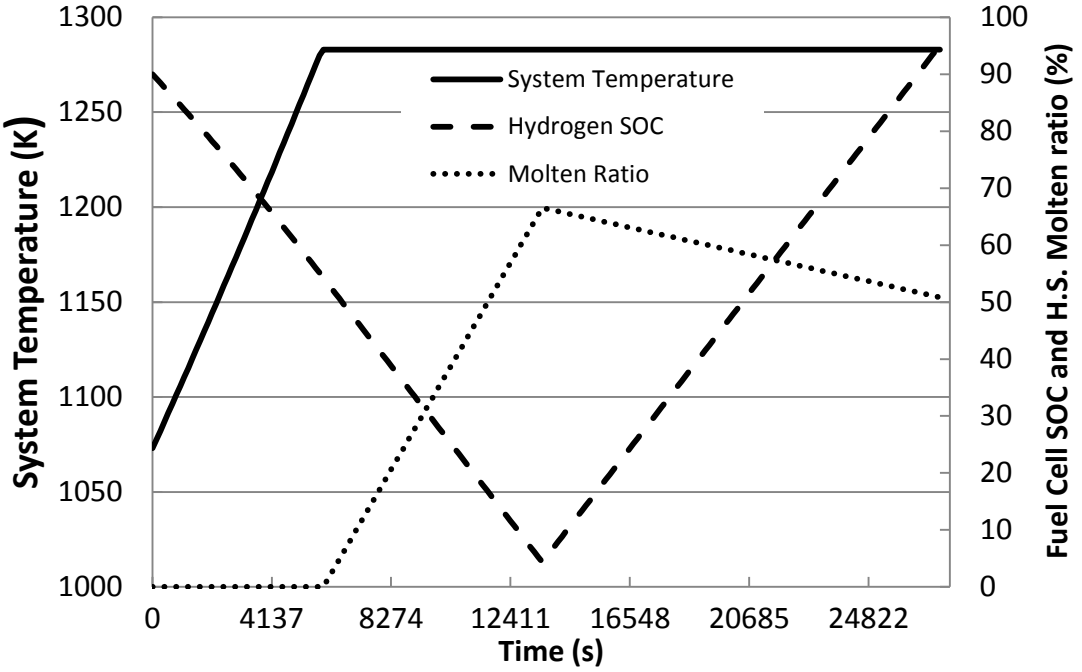

(b)

Figure 4.13 System temperature, state of charge and heat store molten ratio over the RSOFC cycles: a) at 20.4 A per cell, or 3247 Am^{-2} in fuel cell mode, then -20.4 A per cell, or -3247 Am^{-2} in electrolysis mode, b) at 40.8 A per cell, or 6490 Am^{-2} in fuel cell mode, then -40.8 A per cell, or -6490 Am^{-2} in electrolysis mode

However, this RSOFC system is proposed as an energy storage integrated within the power system to buffer the imbalances between the system demand and renewable power generation as introduced in Chapter 1. Therefore it is not required to be a complete fuel exhaustion operation all the time, the ROSFC system may be operated in cycles without approaching to the SOC limits. It can be seen from Figure 4.13 (a) that in the cycle operation at 20.4 A, the system temperature almost returns to the starting value. Therefore, multiple cycles could be run at this current without overheating or cooling the system, as long as the operation time in both fuel cell mode and electrolysis mode are equal. However, for the rated current cycle shown in Figure 4.13 (b) ~50% of the heat store is still molten at the end, therefore this means an excess energy remains as unreleased heat in the heat store. This is because not all of the heat reserved by heat store is absorbed by the endothermic electrolysis reaction during the electrolysis operation, as illustrated by the net heat shown in Figure 4.12 (b). It is the fact that at the rated current the heat store melts 7.9 times faster than it turns back into solid, so as long as the cycle operations are being taken equally then the overall heat store molten ratio will be gradually increasing. Therefore the concern of overheating remains at high rated power cycle operations even with relatively big amount of heat store.

In respect of continuous cycle operations without further CHP schemes to remove the excess heat then the half rated fuel cell current is recommended and the heat store can be of 200kg to guarantee an overheating protection. In regard to the operation at rated fuel cell current, the amount of heat store has to be increased and this depends on the length of operation required. However it is suggested that in this research at least 500 kg of heat store is required. During the simulation tests it is also found that the lowest net heat occurs at -20 A of fuel cell current. However even for the most effective cooling operation the time is still required to be 3 times longer or even more to reset the system temperature back to the start of the cycle. Therefore if high rated current operation is required for a certain period of time then the ROSFC system is suggested to be recovered in electrolysis mode at current of -20 A combined with non-operation periods off to cool the RSOFC system down before it is back online.

4.3.2.2 RSOFC System Efficiencies

The electrical conversion efficiencies are also recorded and plotted in Figure 4.14, during the same case studies discussed in the previous section. The system efficiency is greater in electrolysis mode than in fuel cell mode. It also demonstrates that it is possible to recover heat energy stored in the system from the fuel cell cycle, and convert it to chemical energy in hydrogen by electrolysis. It shows the electrical efficiency reaches a maximum of 112% at about 8 hours during the cycle at 20.4 A per cell in electrolysis mode. This is possible because part of the heat energy generated in fuel cell mode is reserved and being absorbed during the production of hydrogen in electrolysis mode, e.g. 1 W of electrical energy, and 0.12 W of heat energy are required to produce an amount of hydrogen gas with an enthalpy of 1.12 W.

When the system is at 40.8 A per cell as shown in Figure 4.12 (b), the heat generated in the system exceeds the heat absorbed by the endothermic electrochemical reaction in electrolysis mode. Therefore more energy produced into hydrogen comes from the electric power, and some is even wasted on ohmic losses. In such a situation the system cannot recover all of the heat generated in the fuel cell cycle, so the electrical conversion efficiency never exceeds 100% in electrolysis mode.

The electrical cycle efficiency for a cycle operation is different from the definition of electrical conversion efficiency as described in Chapter 3. The cycle efficiency is calculated from Equation (4.1), by dividing the total electrical energy in fuel cell mode $E_{stack,fuel\,cell}$ (J) by the total energy consumption $E_{stack,electrolysis}$ in electrolysis mode.

$$\varphi_{electrical,cycle} = \frac{E_{stack,fuel\,cell}}{E_{stack,electrolysis}} \times 100\% \qquad (4.1)$$

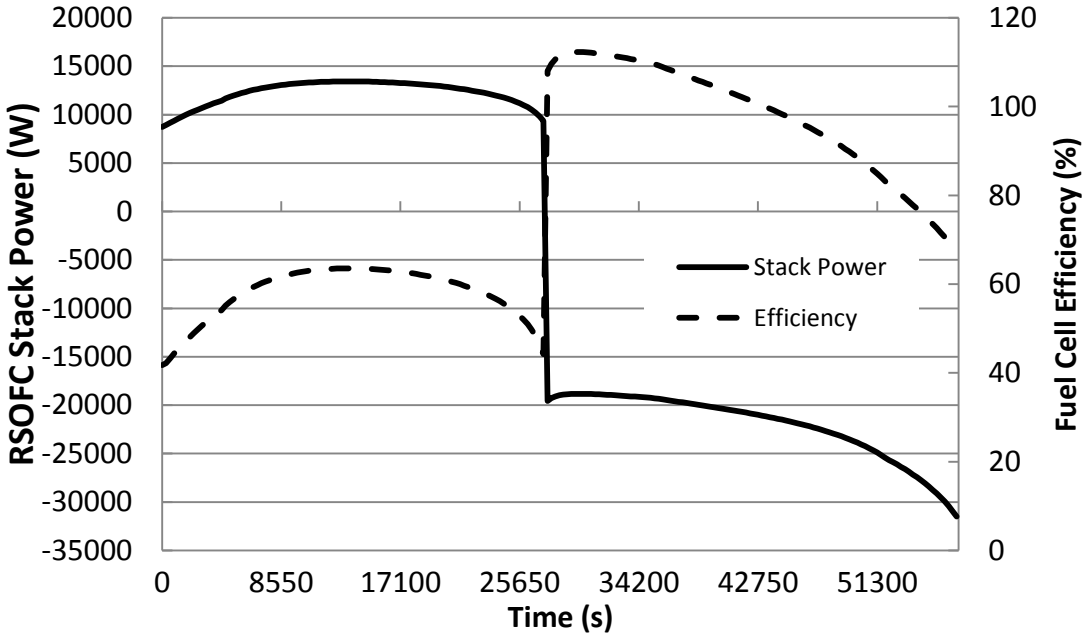

(a)

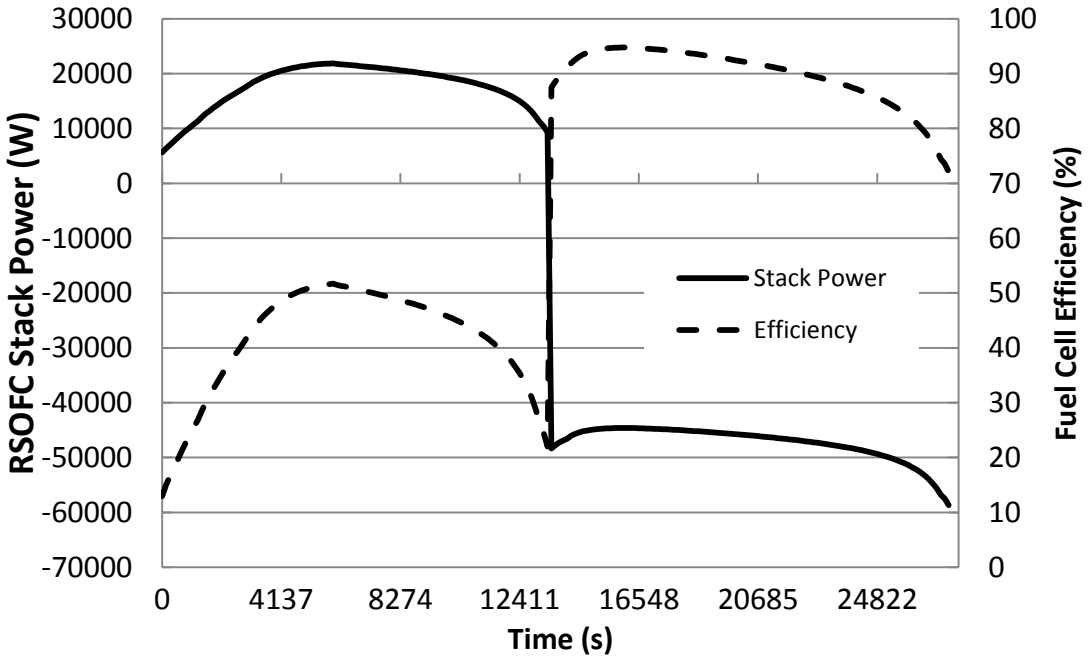

(b)

Figure 4.14 Electrical conversion efficiency and system temperature during the RSOFC cycle: a) at 20.4 A per cell, or 3247 Am^{-2} in fuel cell mode, then -20.4 A per cell, or -3247 Am^{-2} in electrolysis mode, b) at 40.8 A per cell, or 6490 Am^{-2} in fuel cell mode, then -40.8 A per cell, or -6490 Am^{-2} in electrolysis mode.

It is apparent that the system is more efficient at storing and releasing electricity at lower cell currents as discussed above, as shown inTable 4.1. The best electrical cycle efficiency of 64.4% is obtained at a current of 20.4 A per cell. This can be explained by considering Figure 4.12. Furthermore, the RSOFC cycle has a longer operation time at lower currents due to the low rate of fuel usage/production. However when more heat is lost to the surrounding (through the isolation) then the system could cool below its optimal temperature range of 1173K-1283K during the electrolysis mode, which reduces the efficiency as well. This is why the cycle at a magnitude of 10.2 A has a much lower efficiency than cycles at higher currents as shown in **Error! Reference source not found.**.

The electrical cycle efficiency can also be boosted by the additional heat store and this depends on the operation power rating, for example, at the rated power 1.1% more of cycle efficiency can be obtained compared to the case of not using the heat store. However lower power rating leads to less heat energy being stored in the heat store phase-change for the electrolysis mode, so only 0.2% of cycle efficiency can be boosted at half rated power operation. However, this benefit from the heat store can be compromised at high current rating, as more heat is produced through losses than can be usefully utilised to generate electrical energy, which lead to a greater drop in cycle efficiency than can be boosted.

The electrical cycle efficiency also depends on other parameters, such as the value of the pre-exponential coefficient in the activation energy calculation. The choice of the value of the pre-exponential coefficient also slightly influences the cycle efficiency in the simulations. Different values of pre-exponential coefficient are used in RSOFC models. When a coefficient of 1×10^9 Am^{-2} was used in this model, the electrical cycle efficiency increased to 67.9% at 20.4 A per cell, showing that the cycle electrical efficiency is not very sensitive to this parameter. The efficiencies measured are similar to or slightly lower than the electrical cycle efficiency of redox flow cells, which ranges from 65% - 75% [1]. **Error! Reference source not found.** compares five different cycles, with different parameters for each.

Table 4.1 Electrical efficiency during a RSOFC cycle at 70 bar, in the range 95% to 5% to 95% state of charge, at two different values of cell current and pre-exponential coefficients.

Cell current (A)	Current density (Am^{-2})	Pre-exponential coefficient (Am^{-2})	Electrical cycle efficiency (%)
10.2	1623	7×10^8	36.3
20.4	3247	7×10^8	64.4
30.6	4870	7×10^8	53.0
40.8	6494	7×10^8	42.0
20.4	3247	1×10^9	67.9

In order to improve the cycle efficiency the cell resistance should be lowered by optimising the fabrication and geometry of the cell, and the insulation of the system should be improved, to achieve a lower loss from the resistance and to the surroundings.

The energy storage capacity could also be potentially limited by the cycle length. If the system was operating at a lower power level, the cycle time might be longer. In this case, the total heat lost through the walls would be greater, so in electrolysis mode, the system might cool below the optimum temperature range of operation and have to be switched into fuel cell mode to heat it up again, otherwise the efficiency would be greatly reduced. Therefore from the optimum operation point of view it is required that an operation current at which the system runs at maximum cycle efficiency should be determined. And in this research 20.4A of current is such a suggestion.

4.4 Conclusions

The investigations and discussions in this Chapter focus on the performances of both the single cell and stack system. Case studies are interpreted with two scenarios (full and half rated currents). The simulation results prove the fidelity of the improved stack design on enhanced volume and pressurization settings. The case studies also validated the copper-tin heat store system proposed from this research. With this design the RSOFC system provides both high valued power density and energy restore functionality.

The pressurization provides a major cell performance improvement. When the system is pressurized from 1 bar to 70 bar, the Nernst voltage increases by 11.5 % from 0.924 V to 1.035 V (at 50% state of charge, 900 ℃), and the diffusion polarisation significantly decreases by more than 50%, leading to a significant ~18.6% boost in cell terminal voltage. Large volume and high pressure both massively increase the heat capability of gases. It is found in the simulations that steam, hydrogen and oxygen under 70 bar of pressure and 4 m^3 of volume of pressure contribute a heat capacity equivalent to ~18% of the 500 kg heat store, which partly compensate the overheating issue as well. It is obvious that the hydrogen/energy stock capability of the system also can be increased from higher volume and pressure, which leads to improved operation time. It is proved that the hydrogen/energy storage capability of the system is significantly increased by 28 times more than the original design.

The activation and diffusion polarisation could be significantly decreased at high system pressure and temperature, however the overall fuel cell performance can still be compromised by the ohmic losses and the large resistance comes from the cell support. This is because at high power output with high current density the voltage drop on the components resistance can be much higher than the activation and diffusion polarisations, which is even worse at high temperature. In addition it is suggested that cells should be connected in parallel with reasonable designing considerations to lower the overall resistance of a stack system.

The second biggest voltage drop comes from the activation polarisation. In addition,

the SOC determines in increase in the activation loss, especially at conditions of extreme low or high states of charge. This is because when concentrations of hydrogen and steam are much more unbalanced in the stack then the exchange current density will be much lower which increases the activation losses.

A heat storage device is proven to be required by the simulation tests because in the original design the system temperature can rise rapidly especially at high density of power output. A heat store having a mass of 500 kg increases the operation time by 7.5 times longer (from 1/2 hour to 3 and 3/4 hours) at maximum power output without overheating, for a stack consisting 800 cells with cubed shape and size of 4 $m^3$and 70 bar of pressure. During the operation this has to be carefully monitored and controlled because the system temperature will go up again if the copper-tin compound is completely molten. However it can be difficult to allocate an optimised amount of heat store. In case studies of fully discharged operations with 500kg of heat store, that about 30% of heat store are un-molten segments at the rated and half rated current. It is suggested that at least 390 kg of heat store is required for the rated power operation, and at least 200 kg for the half rated power operation. Therefore to guarantee an overheating protection, the amount of heat store needs to be designed in coordination with the power rating, as well as the fuel cell hydrogen storage capability.

The proposed RSOFC system in this research is used to buffer the imbalances of the supply of renewable power generations and demands of the power grids. Therefore the ROSFC system is not required with fully discharged or recharged cycle operations at all the time but frequently being operated in cycles without approaching the SOC limits. It is found that multiple cycles can be achieved at half rated current without overheating or cooling the system with 200kg of heat store, as long as the operation periods in both fuel cell mode and electrolysis mode are equal. However at the rated current the heat store melts 7.9 times faster in fuel cell mode than it cools into solid in electrolysis mode, so the overall molten heat store is highly possible to gradually increase. Therefore the concern of overheating remains at cycle operations at high rated power. Two steps can be considered in regard to the overheating protection at high rated current. First of all the amount of heat store has to be designed large enough according to the length and numbers of cycle operation

required. Secondly, the system can be effectively cooled down during the electrolysis operation and the most efficient condition is found at -20 A of fuel cell current. Therefore the RSOFC system operates at -20 A is recommended in electrolysis mode combined with no operation periods for further cooling effect.

The heat store also provides an enhancement on the cycle efficiency by reserving the energy of heat in phase change and minimizing the net heat loss during a cycle operation. The additional 500 kg of heat store could reserve up to 31.3% more heat energy to be used in electrolysis mode, so at the rated power the cycle efficiency can be increased by 1.1% compared to the case without the heat store (at 1010 ℃). However at half rated power operation only 0.2% of cycle efficiency can be boosted. It is because this boost depends on the power level, which means lower power rating leads to less heat energy to be reserved for the electrolysis mode. However this benefit can also be compromised when the cell is operated towards the higher ends of its current rating as more heat is produced through losses than can be usefully utilised to generate electrical energy, which lead to a greater drop in efficiency than can be boosted.

4.5 References for Chapter 4

[1] C. Ponce de León, A. Frías-Ferrer, J. González-García, D. A. Szánto, F. C. Walsh, "Redox flow cells for energy conversion," *J. Power Sources*, vol. 160, pp. 716–732, 2006.

[2] S. Rahman and K. Tam, "A feasibility study of photovoltaic-fuel cell hybrid energy system", *IEEE Trans. Energy Conversion,* vol. 3, no. 1, pp. 50−55**,** Mar. 1988.

[3] M. W. Ellis, M. R. V. Spakovsky, and D. J. Nelson, "Fuel cell systems: efficient, flexible energy conversion for the 21st century", *Proceedings of the IEEE*, Vol.89, No.12, Dec.2001 pp.1808-1818.

5 Analysis of Effects of Electrical Feedbacks and Power Electronic Inverter Controls on RSOFC system

5.1 Introduction

In order to connect the DC source of the fuel cell to the AC power system, extra help from the power electronic inverter is required, which is bi-directional in power flow and flexible in control modes. Some specialized inverter applications are designed to provide optimum power quality to local sensitive loads which may be limited to certain grid environments; however the resultant DC ripple may reach an undesirable level.

An important parameter of the power electronic converter/inverter for fuel cells is the level of ripple current that can be induced. Ref. [1] [2] [3] [4] reported that ripple currents may shorten fuel cell life span and worsen the fuel efficiency due to the hysteresis effect. The reported frequency tests in [5] indicate that the biggest hysteresis effect occurs at 100Hz on PEM fuel cells, and this effect can be ignored at frequencies around 1Hz and 10 kHz. Randall [6] shows that the ripple imposed by an inverter from unsteady loads can have significant impact within fuel cell diffusion layers. It is also found in [6] that higher ripple ratio and lower ripple frequency both lead to more decrease in oxygen concentration. It is suggested in [7] that the varying reactant conditions surrounding the cell due to ripple current decrease the reactant utilization which is known to impact the mechanical nature of a fuel cell. A more prospective effect is reported in [6] that if not enough excess fuel is supplied to support the voltage potential across the entire cell due to ripple current, then internal damages to the cell can result, such as oxidation of the cell materials. Wahdame [8] found that low frequency ripple current can speed up the degradation of fuel cell electrodes, even if the effect is relatively small. Another obviously important impact is that it tends to reduce the fuel cell output capacity, and the fuel cell controller trips under instantaneous over-current conditions [3]. It is also inevitable that the presence of low frequency current ripple has a side effect of additional heating, and more importantly, diminishing the power availability as shown in Figure 5.1 [9].

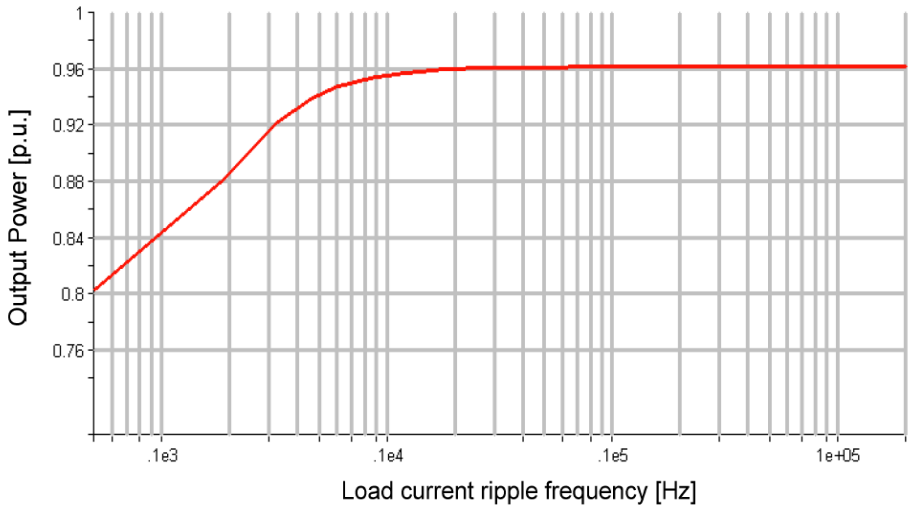

Figure 5.1 Fuel cell output power versus ripple frequency [9] (3183A/m^2, 40% of ripple current)

Many authors in literature can be found proposing different approaches to minimize or eliminate the fuel cell input ripple. The ripple cancellation methodologies from [9] [10] [11] are very similar using the DC-DC boost converter and integrated inner control loops. It is suggested in [4] [12] [13] that a DC-DC boost converter with the concept of pulse DC link can reduce the DC capacitance for smoothing the ripples. Changrong [3] and Chen [12] examined the ripple current reduction capability of passive energy storage components supported by simulations and experiments. However most of them only focus on the ripple induced by converter switching and rectifying operations, therefore these researches are limited to the inverter hardware specifications.

To minimise the influences of ripples on fuel cell stability and durability there is also a desire to reduce the power flow ripple and this can be critical when the RSOFC system plays a role as an energy storage in the case of bi-directional power flow. Current ripples are affected by the AC power disturbances, such as the voltage unbalance and harmonics. These lead to different levels of power flow ripples, which in turn, influence the input current ripples. This is because the response of inverter to the AC power perturbations are highly dependent on the control algorithm [14] [15], and this can vary case by case with different approaches and aims. Therefore the

research of such responses under the variations of integrated grid scenarios and disturbance needs to be conducted.

In particular, there is a trade-off between DC bus ripple and AC power quality while implementing the power electronic inverters. Therefore complex algorithms of inverter control are demanded to balance the benefits on both DC and AC links. In the University of Strathclyde Department of Electronic and Electrical Engineering four competing control schemes for inverter are developed and presented in [16]. Three of them are examined in this chapter. In [16] the trade-offs between these controls are demonstrated in both simulation and laboratory. In this chapter the research is extended to examine the control algorithms in terms of introducing side effects on the RSOFC system when it operates as a variable DC voltage source rather than a constant DC source implemented in [16]. Case studies are followed as the analysis of the perturbations of inverter outputs at point of common coupling (PCC) to examine both the behaviours and influences of controls on RSOFC system under different grid scenarios.

5.2 Effects of Current Ripple on the Performance of the Proposed RSOFC system

5.2.1 Current Ripple Specifications

To ensure a minimal impact on the performance of fuel cells, as well as the durability, fuel cell developers would prefer to specify the minimum possible ripple. However no specification standard for fuel cell ripple tolerance has been agreed. There are even different suggestions as to the limitation of the ripple ratio for inverters. Randall and Ozpineci suggest to ensure negligible inverter ripple impacts on fuel cell then the frequencies of inverter induced ripple need to be above 120 Hz, or have ripple factors less than 4% [6] [10]. Allen [17] suggests it should be below 2% of the theoretical fuel cell current without giving a specific frequency range. It is suggested in [18] that the ripple current needs to be limited to less than 10%. Ballard Nexa specifies a limit of 24.7% rms (35% peak-to-peak ripple) for 120 Hz ripple current for their manufactured product [19]. In [20] a ripple limit of 15% of its rated current for all fuel cells, and a limit of 10% is specified for 60Hz ripple current are proposed, and

this is agreed with the maximum ripple specification highlighted in [11] as shown in Figure 5.2.

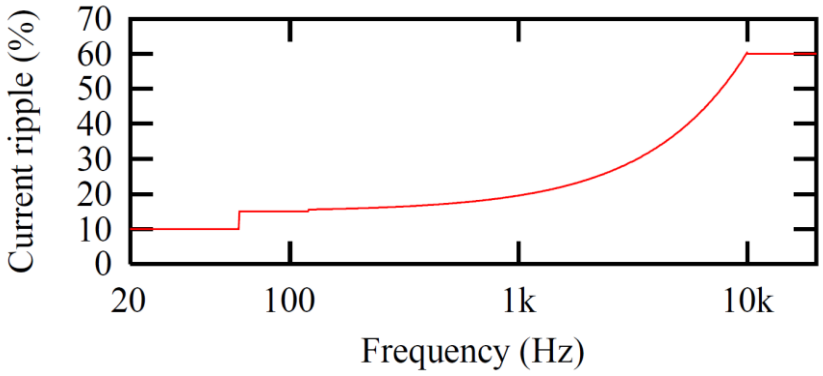

Figure 5.2 Fuel cell maximum input current ripple specification (to the rated current) [11]

The low frequency current ripple components (e.g. a 100Hz pulsating current in the UK) are from both the rectification effect through the inverter switches and the variations in instantaneous power drawn from fuel cell as described in Chapter 2. However as discussed in Chapter 2 that without an appropriate CFD code (which is used to determine the relaxation time of the polarisation performances related to the effect of temperature and reactant fluid dynamics) it is not possible to model the diffusion response of reactant gases on electrode surface due to low frequency current ripple [24], therefore it is difficult to visualise the effects of different specifications in simulations.

Fuel cells may also need to face high frequency ripples drawn from power converter high frequency switching operations. However this is the least of fuel cell designer's concerns. It should be noted that high frequency components at the converter output can be easily filtered via a small capacitive filter [1] [2] [3]. The output filter connected to the inverter also helps to generate high quality sinusoidal AC waveforms suitable for the load. To filter the ripple more effectively, a larger capacitor might be required [10].

The time constant/response of fuel cell can be far different from high frequency ripples [17], therefore the electrochemical performance should not be affected as much as by the low frequency ripple [21] either. A National Energy Technology Laboratory (NETL) study in [22] reports that the ripple frequencies above 400 Hz have a minor impact on the fuel cell operation. Wahdame [8] shows an ageing test for PEMFC in stationary conditions for more than 1000 hours and only a slight effect of high frequency current oscillations produced by the electrical interactions of a DC/DC converter on the reduction of the PEMFC stack performances. Therefore, it can be concluded that the power converter will be able to impose a high frequency current ripple on the delivered fuel cell current without altering the lifetime of the stack. It is also interesting to know that in [23] the fuel cell stack system is proven to be capable of filtering high frequency current harmonics by the intermediary of its double layer capacitor.

However most of these specifications are found for PEM and other kinds of fuel cells and it is not convenient to find test reports/manufacturing specifications of ripple related damage/degradation on SOFCs. Considering the SOFC is superior in electrode/electrolyte material and the proposed system in this research does not suffer the same water management issue as low temperature fuel cells (which leads to a relaxation time on fuel cell performance to load change), it is rational to refer the specification in Figure 5.2 for this RSOFC system as a worst case.

5.2.2 Effects of Current Ripple on RSOFC System Temperature, SOC varying rate and Fuel Consumption

Higher ripple ratio does make difference in temperature and fuel consumption rate due to higher current RMS value. Figure 5.3, Figure 5.4 and Figure 5.5 below show the influences brought by current density and ripple ratio on the RSOFC system. It has been discussed in Chapter 4 that higher current density leads to more consumption of fuel and more heat generated by electro-chemical reaction and ohmic resistance. The following results clearly show that although the temperature increases faster when higher ripple ratio occurs at high current density, however the dominating factor is still the current density. Similar trends can be observed in SOC and fuel consumption. The recorded simulation data shows than the maximum

variations of SOC changing rate and fuel consumption are 1.28% and 5.6% and these may be major drawbacks if a long-term operation is considered.

Speaking of temperature, if the current ripple is not well limited then the temperature can increase up to 6.4% faster than none existence of ripple, which in tandem shortens the time for the fuel cell system to reach the heat store threshold. Under such condition the RSOFC system has to be switched off or operated in electrolysis mode in order to cool down. The same issue may happen when the remaining fuel gas/SOC is low at a certain condition. Therefore even without knowing how current ripple affects the microstructure or reactant behaviour at reaction site it is clear that the RSOFC system will be benefited from limiting the current ripple over long operation times.

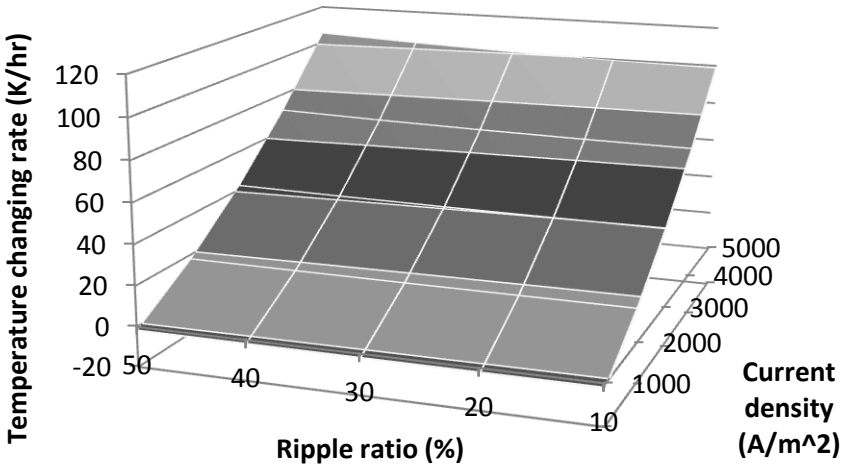

Figure 5.3 RSOFC system temperature changing rate versus power ripple and current density

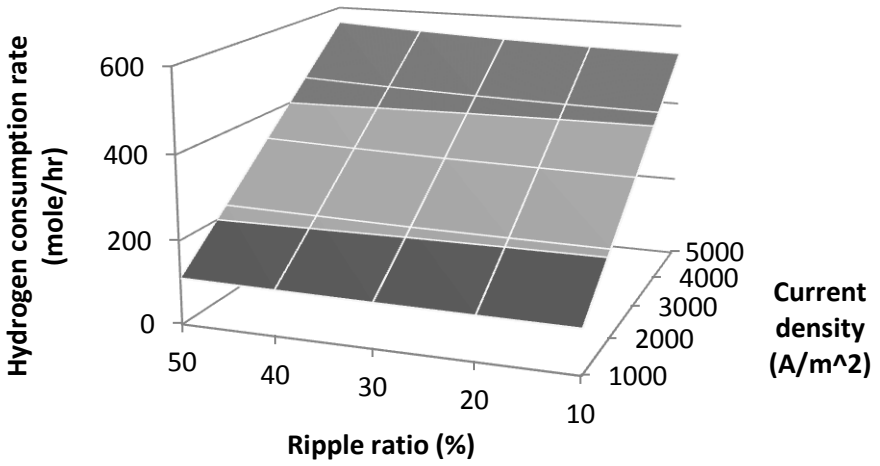

Figure 5.4 RSOFC system hydrogen consumption rate versus power ripple and current density

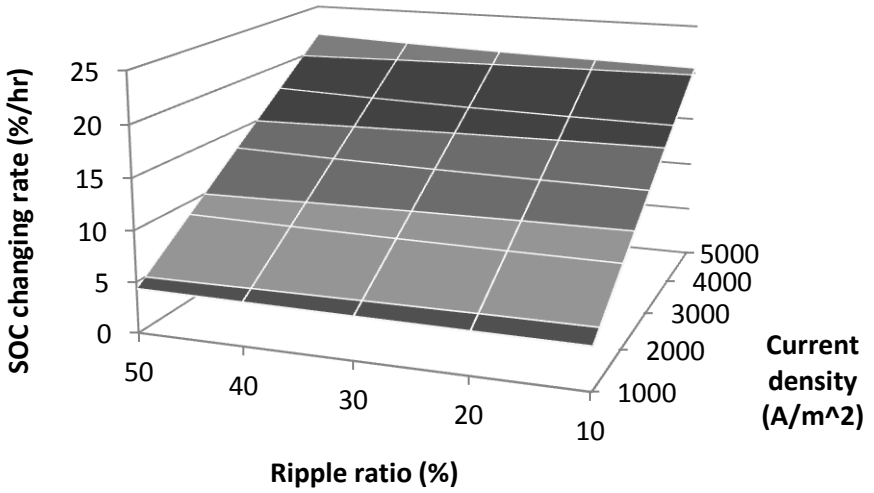

Figure 5.5 SOFC system SOC changing rate versus power ripple and current density

5.2.3 Effects of SOC and Current Ripple on RSOFC Efficiency

In this section, the effects of fuel cell current ripple and SOC on the efficiency of the RSOFC stack system are examined. Most applications of the fuel cell system demand high efficiency. This is always one of the primary goals. It is mentioned in [1] that ripple currents can contribute up to 10% reduction in the available output power and this is partly due to the increase in excess fuel (a decrease in fuel utilization). To make maximum efficiency operation in the traditional fuel cell concepts which have gas flow and pump controls, the fuel cell operates at zero excess fuel. However, it is already well understood that a minimal amount of excess fuel is necessary to ensure a stable output voltage [6]. However because pure hydrogen fuel cells have a potential for zero or near zero excess fuel, so this concern can be ignored with this proposed pressurized vessel in this research which keeps constant attendance of fuel (hydrogen) gas at the reaction site. This feature covers the necessity of excess fuel as the traditional pumped fuel cells. As a result, with no reactant inlet system the calculation of fuel cell efficiency only counts the amount of reacted fuel rather than the fuel utilization. Therefore the decrease in efficiency at 20% of current ripple can only be as a small drop as ~0.1%, which is shown in Figure 5.6.

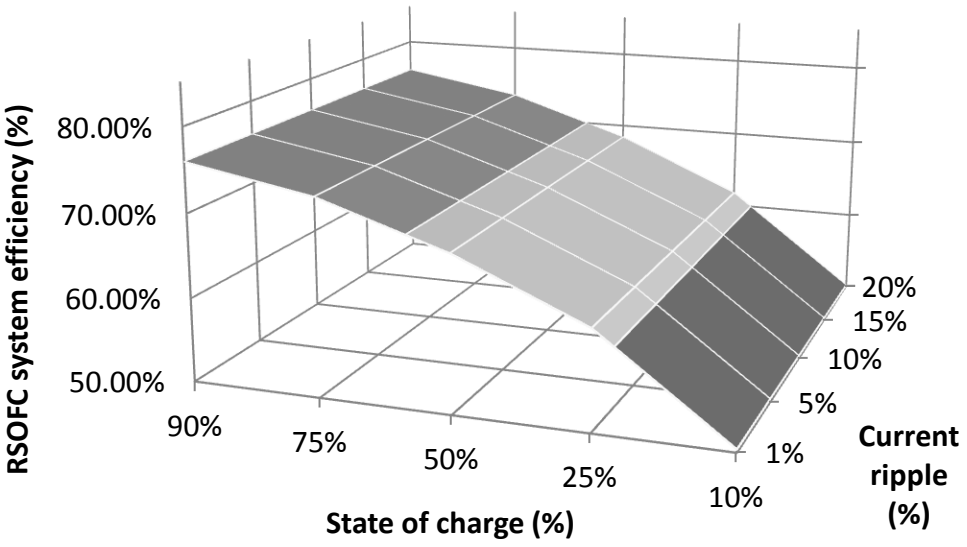

Figure 5.6 Effects of SOC and Current Ripple on RSOFC Efficiency

The simulation shown in Figure 5.6 is carried out at half RSOFC rated current (at 1283 K). It demonstrates that as long as the fuel cell system is under operation for long term, the decrease in SOC leads to a significant trend of decline in efficiency. This is much more of concern than the efficiency loss caused by current ripple which is actually barely observed from the Figure 5.6. Figure 4.9 in Chapter 4 has shown that under certain system temperature and pressure, the maximum output power of a fuel cell varies with state of charge. This is because the fuel cell voltage decreases with lower SOC, as shown in Figure 4.1 in Chapter 4. Therefore in order to maintain a constant fundamental power output, the fuel cell has to draw more current to compensate the drop in the terminal voltage, and this is only possible to happen before the fuel cell reaches the rated power according to the varying SOC. Higher current density definitely causes more loss and decreases the efficiency. However the decline of efficiency is partly contributed by the ohmic loss into heat which can be reserved by the copper-tin heat store and still can be used in electrolysis mode. Therefore trade-offs have to be considered from the aspect of cycle efficiency for the low SOC operation.

It is also found during the simulation that although the SOC limits proposed before are set to 5%~95% by University of St. Andrews, however it is highly possible that the fuel cell system will be unstable at the rated power output all of the time. This is because the decreasing SOC shifts the maximum power output to a lower point, which means at a lower SOC the fuel cell system is not capable of outputting the same rated power. In simulations this will cause the fuel cell generating significant high currents, which may lead to damage in a real fuel cell. Therefore it is recommended to avoid operating the RSOFC system at the rated power as much as possible. For the operation limitation of state of charge, 20% as the lower limit is suggested in this thesis.

5.3 Implemented Inverter Controls and the Effects of Electrical Feedbacks on the RSOFC system

In this section, firstly three inverter control algorithms will be briefly described, and then a case study will be shown in addition. The three control modes are simply referred as Ripple Minimization, Current Drive and Voltage Drive in the following texts. However during the simulation a small improvement of adding a power PID controller has been made to the original Ripple Minimization and Current Drive as in [16], the diagrams of original control algorithms are shown in Appendix E.

The investigation focuses on the effects on RSOFC system while implementing the three competing inverter controls for the grid integration at the presence of certain perturbations and electrical feedbacks. After the descriptions of the control methodologies, two groups of simulation results will demonstrate how the unbalance, THD, power factor and DC bus capacitor impact the fuel cell current ripple, followed by a frequency spectrum analysis.

5.3.1 Introduction of Inverter Controls Algorithms

5.3.1.1 Control A: Ripple Minimization

In this control algorithm the derivations of targeting *dq* components are under the basic instantaneous *PQ* theory which is described in Appendix F. However only the positive sequence of V_{dq}^{p} is applied here to allow power-flow ripple minimization under conditions of unbalance, harmonic content and non-zero Q^* (reactive power set point). High-bandwidth controllers is then required such that control capability is enough for unfiltered measurements of V_{dq}^{p} for the calculation of desired currents I_{dq}^{p*}. Controllers with bandwidth at least 3 times the fundamental frequency are used [10]. However the use of unfiltered measurements of V_{dq}^{p} and high-bandwidth controllers lead to the I_{dq}^{p*} containing harmonic contents. Note that V_0 and I_0 play no part in this equation, since the zero sequence components of current and voltage are not physically possible or defined for a 3-wire inverter as introduced in Chapter 2. The derivation of reference I_{dq}^{p*} can be given by Equation 5.1 [16]:

$$\begin{bmatrix} I_d^{P*} \\ I_q^{P*} \end{bmatrix} = \begin{bmatrix} V_d^P & V_q^P \\ V_q^P & -V_d^P \end{bmatrix}^{-1} \begin{bmatrix} P^* \\ Q^* \end{bmatrix} \quad (5.1)$$

P^* and Q^* are the desired (per-unit) power outputs, V_d^P and V_q^P are the (positive sequence) measured voltages from the PLL, I_d^{P*} & I_q^{P*} are the target (pu) currents, then:

$$\begin{bmatrix} I_d^{P*} \\ I_q^{P*} \end{bmatrix} = \frac{1}{\left[(V_d^P)^2 + \left(V_q^P\right)^2\right]} \begin{bmatrix} V_d^P & V_q^P \\ V_q^P & -V_d^P \end{bmatrix} \begin{bmatrix} P^* \\ Q^* \end{bmatrix} \quad (5.2)$$

The choice of reference values of P^* and Q^* in Equation (5.2) is made from the conventional droop controllers to account for DC bus voltage requirements [26] [27] The following relationship describes voltage E_{dq}^p at PCC required to generate the current I_{dq}^{p*} through the primary inductor with assumed per-unit impedance $(R_L + jX_L)$ according to Appendix G:

$$E_{dq}^p = V_{dq}^p + (R_L + jX_L)I_{dq}^{p*} + \frac{X_L}{\omega}\frac{dI_{dq}^{p*}}{dt} \quad (5.3)$$

These terms can all be implemented within the PI controller as feed-forward terms, with a dynamic value of ω provided by the PLL. For practical implementation the conventional form of the high-bandwidth controller is to measure the actual current I_{dq}^p and compare them with the target current I_{dq}^{p*}, and then apply a high-bandwidth PID controller to control the inverter bridge drive voltages E_{dq}^p. In this way because the control system has a finite switching frequency then the PID controllers only need to make adjustments due to hardware component variations from assumed values. The diagram of the methodology of Ripple Minimization control is shown in Figure 5.7.

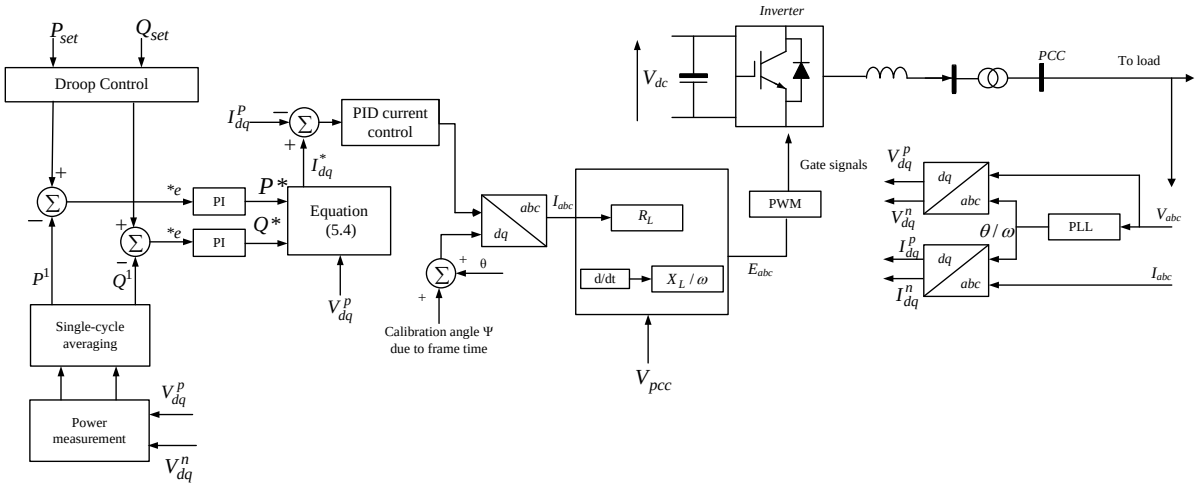

Figure 5.7 Diagram of Ripple Minimization control

5.3.1.2 Control B: Current Drive

This control scheme is designed for outputting balanced sinusoidal current regardless of the minimization of power-flow ripple, although the resultant ripple is found to be relatively small. Modifying the filtered positive components of V_{dq}^{P1} in Equation (5.2) into Equation (5.4) then yields the algorithm for desired reference I_{dq}^{p*} for this control scheme as follow:

$$\begin{bmatrix} I_d^{P*} \\ I_q^{P*} \end{bmatrix} = \frac{1}{\left|V_d^{P1} + jV_q^{P1}\right|} \begin{bmatrix} 1 & 0 \\ 0 & -1 \end{bmatrix} \begin{bmatrix} P^* \\ Q^* \end{bmatrix} \qquad (5.4)$$

Compared to Equation (5.2), this scheme uses a similar high-bandwidth controller. However better performance of balanced, sinusoidal currents on all three phase can be obtained from simulations by feeding forward the filtered fundamental positive sequence terms of V_d^{P1} and V_q^{P1}, and replace the unfiltered V_{dq}^{p} in Equation (5.2). Therefore the differential feed-forward term in Equation (5.3) is not required since I_{dq}^{p*} is counted from filtered measurements of positive-sequence fundamental component V_{dq}^{P1} and will be invariant against unbalance and harmonics on the PCC voltage in Equation (5.4). The diagram of the methodology of Current Drive control is shown in Figure 5.8.

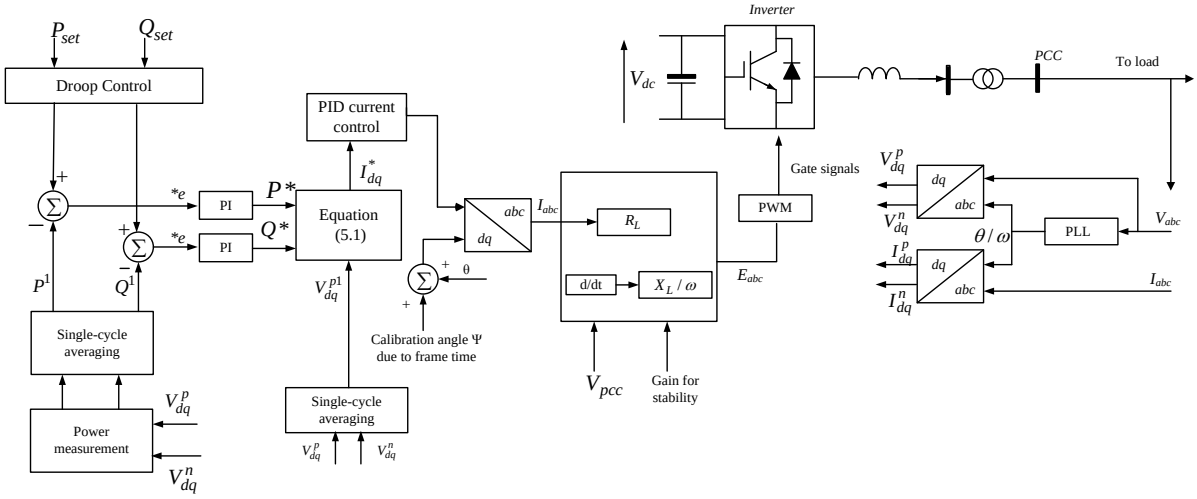

Figure 5.8 Diagram of Current Drive control

5.3.1.3 Control C: Voltage Drive

The inverter can be operated such that the bridge synthesizes a balanced sinusoidal voltage set by using low-bandwidth PI controllers to set a relatively constant value of E_{dq}^{p}. This is shown in Figure 5.9. The use of the filtered fundamental-only values means that additional low-bandwidth low-gain controllers are required to control DC currents. This control mode is intending to mitigate both unbalance and harmonics on the voltages at the PCC while the power-flow ripple can be significant. However under the presence of voltage with certain unbalance at PCC this control is limited by the link inductor ($j\omega L + R$) with typical 10% per-unit of X_L, and it can causes 10 times the power ripple to flow to a perturbed grid.

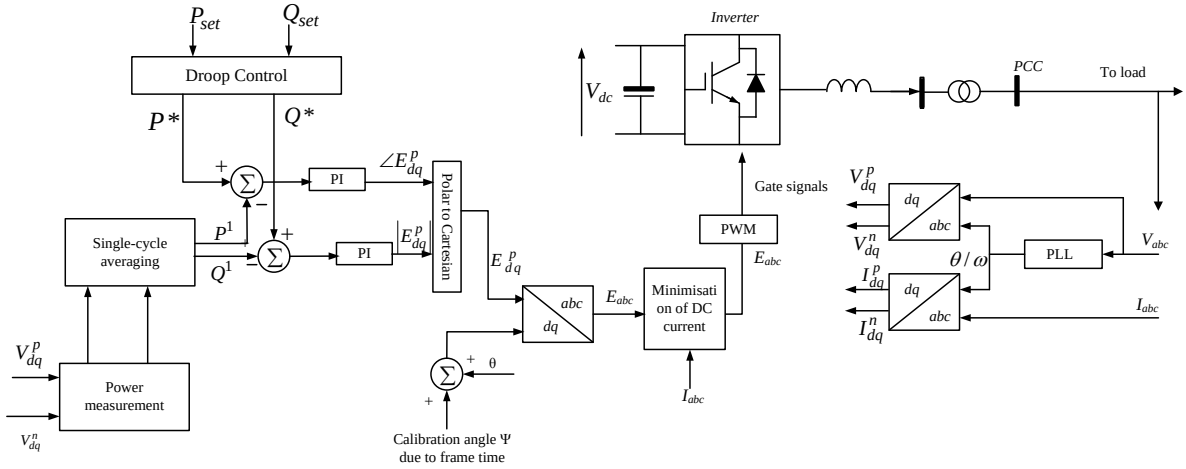

Figure 5.9 Diagram of Voltage Drive control

At the point of inverter output voltage, assuming the PLL is locked and the voltage drive is balanced sinusoidal, and that the resistive impedance of the inductor is small:

$$\begin{bmatrix} V_a \\ V_b \\ V_c \end{bmatrix}_{drive} = \begin{bmatrix} sin(\omega t) & cos(\omega t) \\ sin\left(\omega t - \frac{2\pi}{3}\right) & cos\left(\omega t - \frac{2\pi}{3}\right) \\ sin\left(\omega t + \frac{2\pi}{3}\right) & cos\left(\omega t + \frac{2\pi}{3}\right) \end{bmatrix} \begin{bmatrix} 1 + QL_{pu} + PR_{pu} \\ PL_{pu} - QR_{pu} \end{bmatrix} \tag{5.5}$$

Where L_{pu} and R_{pu} are the per-unit reactance and resistance of the inductor, and P & Q are the per-unit active and reactive power flows.

5.3.2 Effects of Electrical feedbacks on RSOFC system

5.3.2.1 Introduction of Simulation Setups and Algorithms

The three control schemes described in [16] have been tested in laboratory with a constant DC source via an inverter and low voltage transformer coupled to an AC power network. The results clearly show the trade-offs of these controls in aspects of AC power quality. More interests placed in this research are extended to the field of DC/RSOFC side at the scenario that RSOFC system connected to power grid via high voltage (HV) transformer, as to understand the different impacts due to three control algorithms on the RSOFC system under different grid disturbances. In particular, this work builds upon [16] by adding models of the RSOFC system and its associated Randles circuit. In this section, simulations and results are discussed in three grid connected conditions: stiff grid, weak grid and microgrid at the appearance of unbalance or with harmonic on voltages at the point of common coupling (PCC). Figure 5.10 simply shows the topology applied in this section. The RSOFC system and Randles circuit models in Figure 5.10 have already been discussed in Chapter 3.

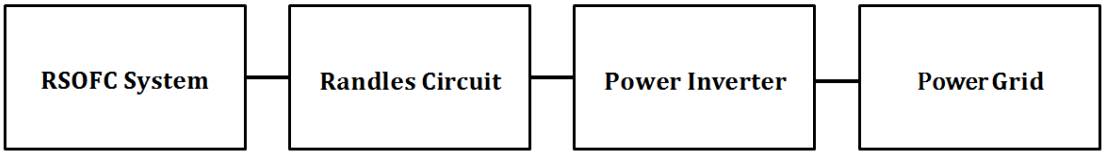

Figure 5.10 Block diagram of the SOFC integrated AC power system

5.3.2.2 Development of the RSOFC Integrated Power System

All the results generated during this study consider a 3-wire grid-connected inverter using a standard 6-switch IGBT bridge. The bridge is controlled using SV-PWM (Space Vector Pulse Width Modulation), at 5kHz switching frequency. This frequency is a compromise between lower switching losses on the one hand, and high-bandwidth controllability and low switching harmonics on the other. However in the electrical simulation the switching bridge is simulated in an "averaged" fashion using controllable voltage sources rather than switched elements. Because the high frequency current ripple introduced by the inverter switching frequency rarely affects to fuel cells and can be filtered easily, the PWM (pulse-width modulation) waveforms do not need to be simulated in detail, which in turn increases the simulation speed.

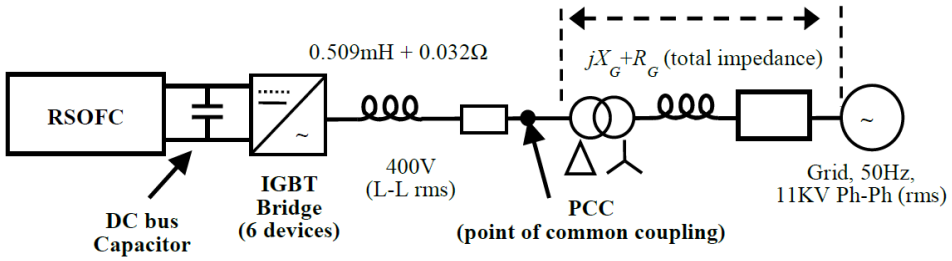

Figure 5.11 Grid connected 100kVA RSOFC power system

A simplified diagram of the inverter represented by the IGBT bridge is shown in Figure 5.11. The link inductor on 100 kVA base has values as X_L=0.10 pu, R_L=0.02 pu. This resistance of the link inductor also includes the resistance of the switching devices. The grid impedance is represented by $(jX_g + R_g)$ in Figure 5.11. In the Matlab/Simulink model the grid impedance is defined within the transformer at PCC in Figure 5.11 in the following case studies and simulations, the specifications of these grid scenarios are catalogued in **Error! Reference source not found.**:

Table 5.1 Grid conditions and impedance applied in the case studies

Settings/Scenarios	Stiff Grid	Weak Grid	Microgrid
Base Apparent Power (kVA)	1000	100	100
Grid Reactance (pu)	0.0046	0.128	0.032
Grid Resistance (pu)	0.0005	0.02	0.003

The applied unbalance and harmonic voltages are enabled by using programmable three-phase voltage sources from Simulink/SimPower package, which represents the infinite bus as well. In addition, the block of RSOFC system in Figure 5.11 represents a group of four fuel cell stacks connected in parallel operation to match the requirement of 100kVA rated power output of inverter bridges. The proposed RSOFC stack has been described in Chapter 4, and in this case study the number of cells in series is increased to 450. The stack has 2 branches of cells and gives 900 cells in total, this is to provide DC terminal with higher voltage level than what is mostly proposed in papers like [31][33], therefore no DC-DC push-pull/boost converters are required or modeled. The proposed system of four stacks is also designed to be connected in parallel in the purpose to share 1/8 of DC bridge current for each cell. In this way it is possible to reduce the resistive losses than connecting stacks in series (refer to the V-I and P-I curve in Chapter 4), so the cell terminal voltage can be higher.

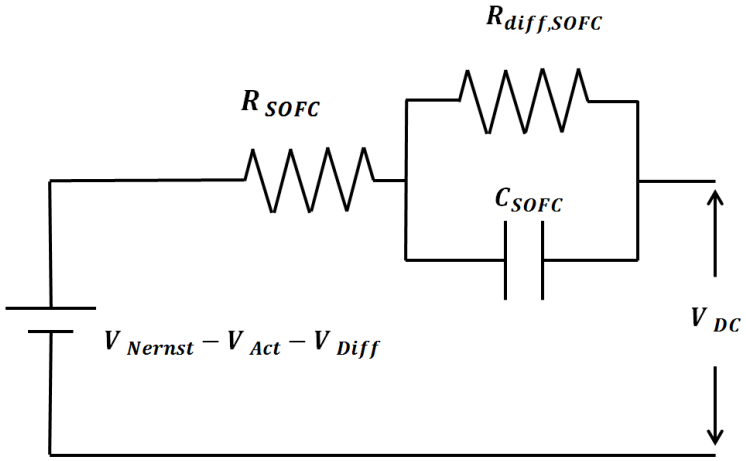

Figure 5.12 Diagram of the simplified 4-stack RSOFC system connected to power grid

It is assumed here that the fuel cell stacks are identical to each other and perform parallel exactly the same. Therefore a simplified version of the RSOFC system can be obtained by using controllable DC voltage source and other electric components provided in SimPower® from Matlab® as shown in Figure 5.12. The fuel cell model described in Chapter 3 is in charge of calculating the value of the voltage ($V_{Nernst} - V_{Act} - V_{Diff}$) for an integrated Randles circuit which is represented by R_{SOFC}, (0.004 pu) $R_{diff,SOFC}$ (1.6281× 10^{-4} pu) and C_{SOFC} (0.0042 pu) as the impedance values and count for the four-stack fuel cell system. Finally it is the V_{DC} connecting to the DC bus and representing the terminal voltage of the whole fuel cell system.

5.3.2.3 Control Time Lags due to Switching Frequency

There are inevitable time lags in control software because the finite switching frequency defines the sample rate and this brings challenges for all inverter control algorithms and their stability. These can be contributed by: (a) 50μs of analogue filter delay [16], (b) the effective time between the reading of the ADC channels, accounting for de-skewing [34] [35] and the beginning of the computational frame is. 37μs, (c) The computed SV-PWM drive timings are output to the switches. They appear as (on average) voltages which are effectively lagged by half a frame, or

125μs [16].

The control frame time applied to the control algorithms and simulations needs to be accounted for because it is the inverse of the sample rate [10] [36] [37]. The total time lag between actual measurements and the effective control of bridge voltage is approximately 1.8 frames. This lag time can be accounted by an addition of phase rotation of $\psi = 2\pi f \times 1.8T$ to the drive voltages during the inverse Park transformation, and f is the measured frequency from the PLL. Within the simulation environment, all these loop delays are carefully simulated. However the feed-forward term V_{dq}^{p} in Equation (2.1) is directly affected by this 1.8 frame delay. It causes constraints for the high-bandwidth controllers, which in this case are both power-flow ripple minimization and sinusoidal-current modes. For both high-bandwidth control modes, the remaining feed-forward terms and PID controllers also have to contend with the round-trip delay and this can reduce the performance. In the simulations, although all loop delays are carefully simulated as previously described, there are other effects that are not simulated. These include component tolerances, variable core losses, measurement noise, and EMC (electromagnetic coupling) issues.

5.3.2.4 Simulation Results

The scenarios in Figure 5.13 - Figure 5.15 are all under the condition of: power factor = 1, P = 0.5 pu, and the y-axis shows the ripple ratio versus the rated fuel cell current. The DC bus capacitor is not included in the simulations to avoid the filtering influences on ripples. This helps to determine the effects mainly caused by varying the voltage unbalance and THD (both magnitude and harmonic order).

As can be seen an increase in the THD as well as the unbalance of the AC voltage increases the distortion in the output ac current due to the increase in the magnitude of the harmonic components. This distortion in the AC current also introduces distortion in the current drawn from the RSOFC stack for in control modes as shown in Figure 5.13 - Figure 5.15, and this can be explained by the equations in Appendix H. The results show that the Ripple Minimization does the best job in lowering the ripple, however the Voltage Drive introduces much higher current ripple than others

modes and this can be significant at the grid condition with 3% of unbalance and 5% of THD, which is not acceptable according to the specification in Figure 5.2 [11].

Considering the worst condition of induced current ripple for all the three control modes which happens at 3% of unbalance and 5% of THD according to Figure 5.13 - Figure 5.15, then this scenario is adapted to the simulations in Figure 5.16 to demonstrate the influences can be brought by DC bus capacitor and power factor on fuel cell current ripple. Because of the non-unity power factor of the load, the ripples in the stack current increase according to the analysis in Appendix I. Figure 5.16 also shows the filtering capability of the capacitance connected across the DC bus, which plays an essential role especially for the Voltage Drive control.

It can be seen that to keep the current ripple within the required range two effective methods are concluded here. Firstly, power ripple can be minimized by using input current control—as the Ripple Minimization control does. Second is the simple and effective DC bus capacitor. A minimum DC bus capacitor of 10mF is suggested according to the results from Figure 5.16 for the ripple reduction. The ripple ratio can be decreased from 35% to ~ 4.6% for the worst scenario to satisfy the specification in Figure 5.2. However a higher value capacitance definitely makes ripple much smoother as indicated as well with the implications of more cost penalty and power loss. Finally the “type” of grid also plays a role in affecting the ripple ratio, especially for the Ripple Minimization and Voltage Drive where better ripple reduction can be provided at the weak grid than at stiff and microgrid.

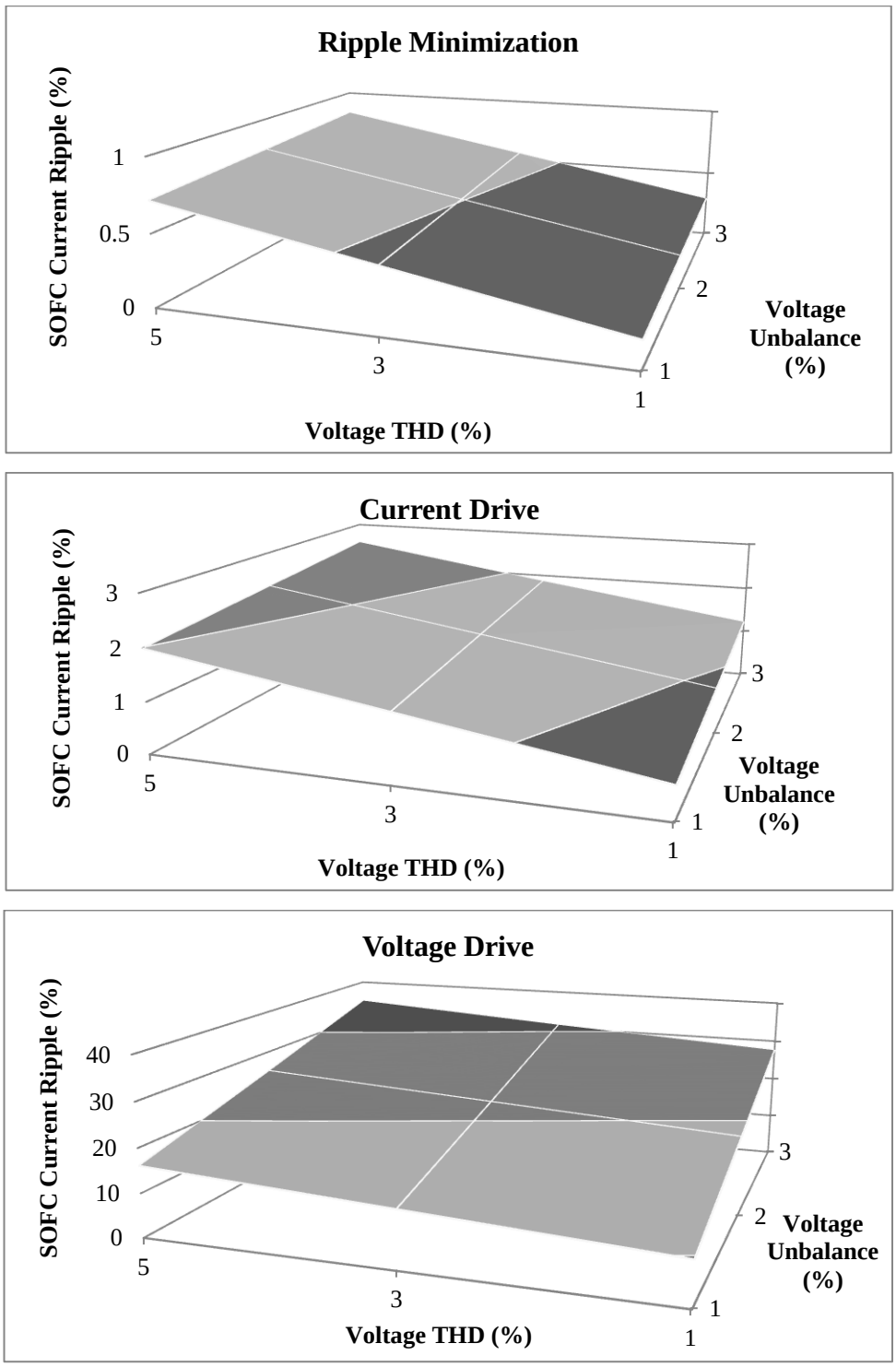

Figure 5.13 Current ripple induced at stiff grid by three control modes at varying voltage unbalance and THD (5^{th} harmonic) (pf=1, P=0.5pu)

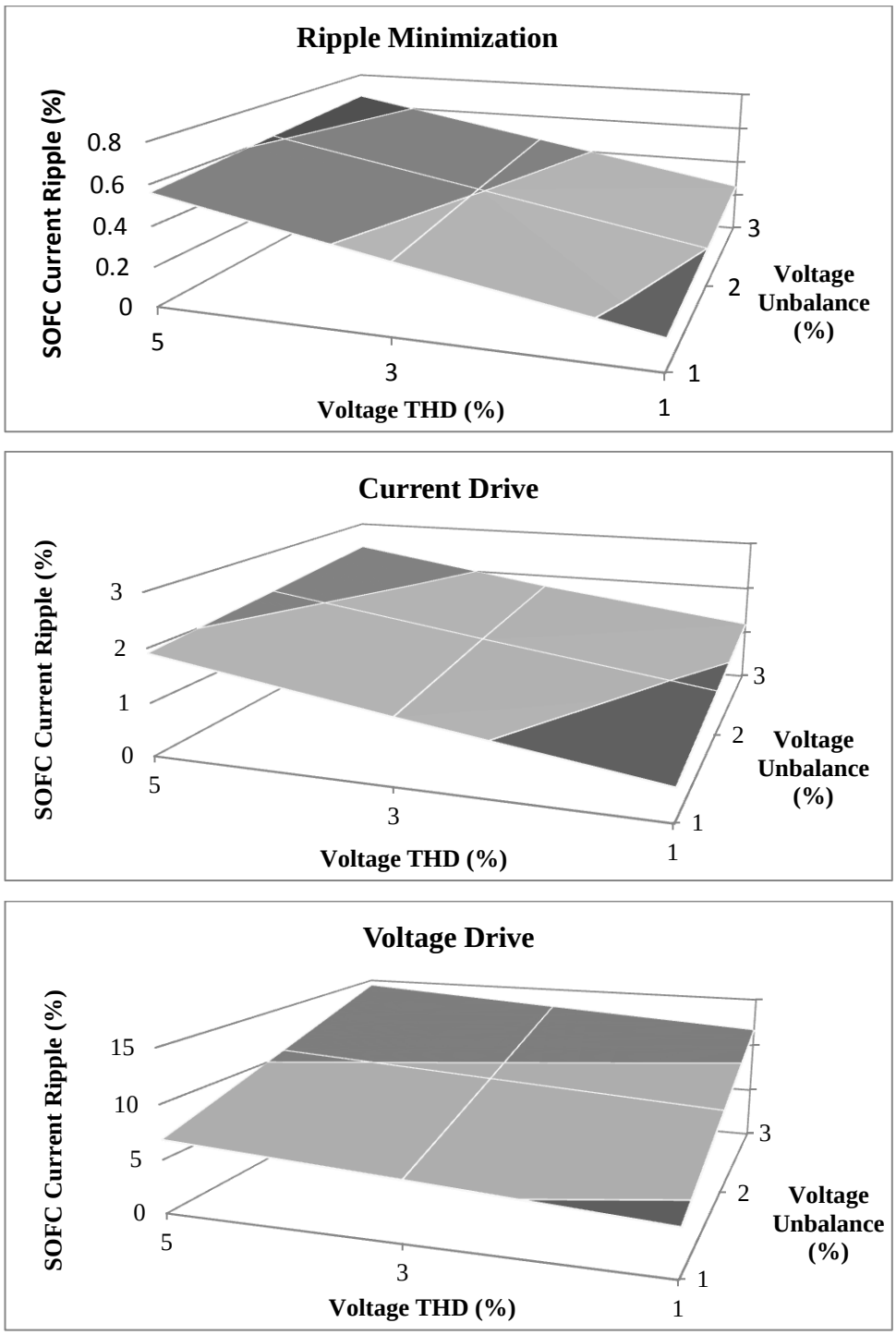

Figure 5.14 Current ripple induced at weak grid by three control modes at varying voltage unbalance and THD (pf=1, P=0.5pu)

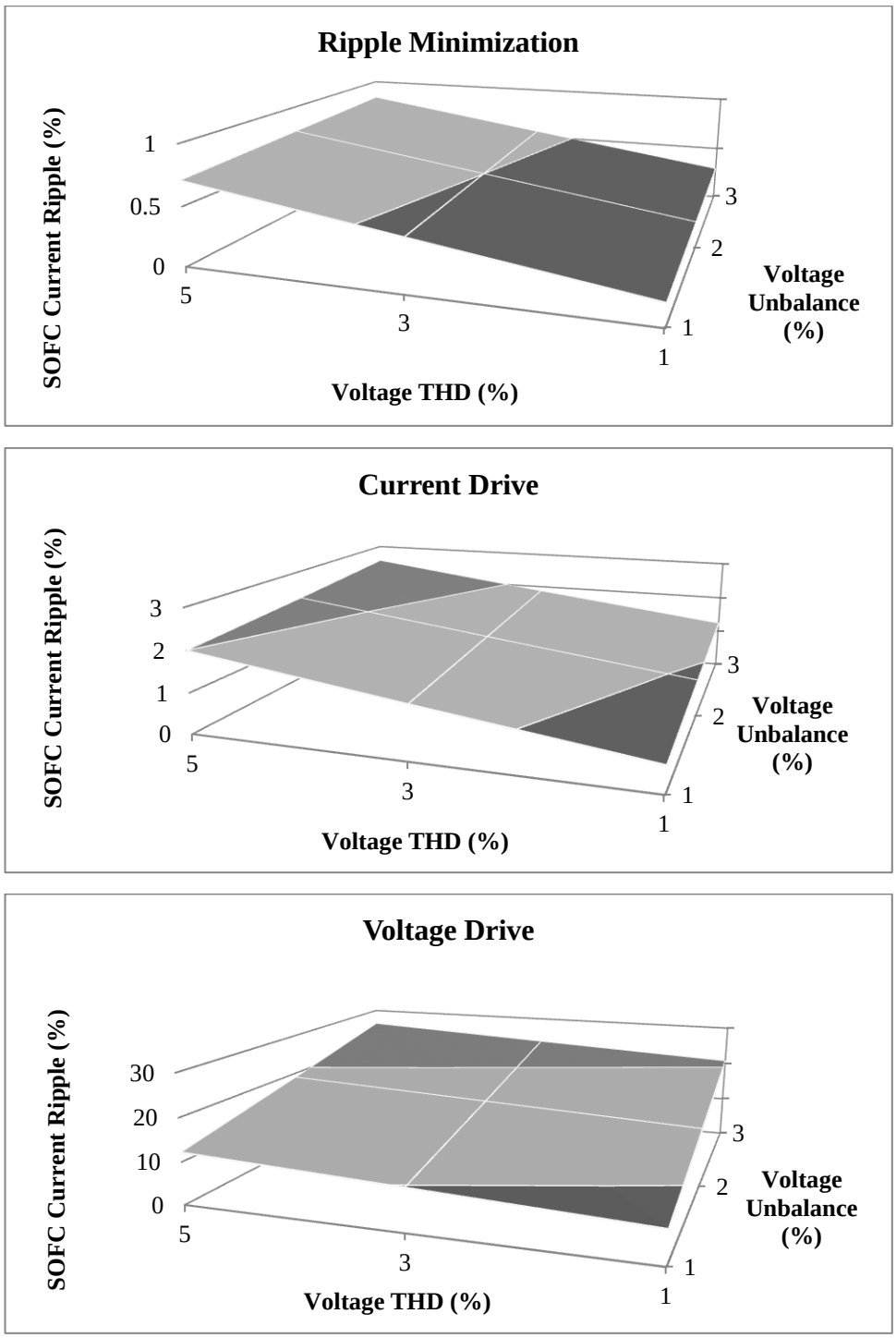

Figure 5.15 Current ripple induced at microgrid by three control modes at varying voltage unbalance and THD (pf=1, P=0.5pu)

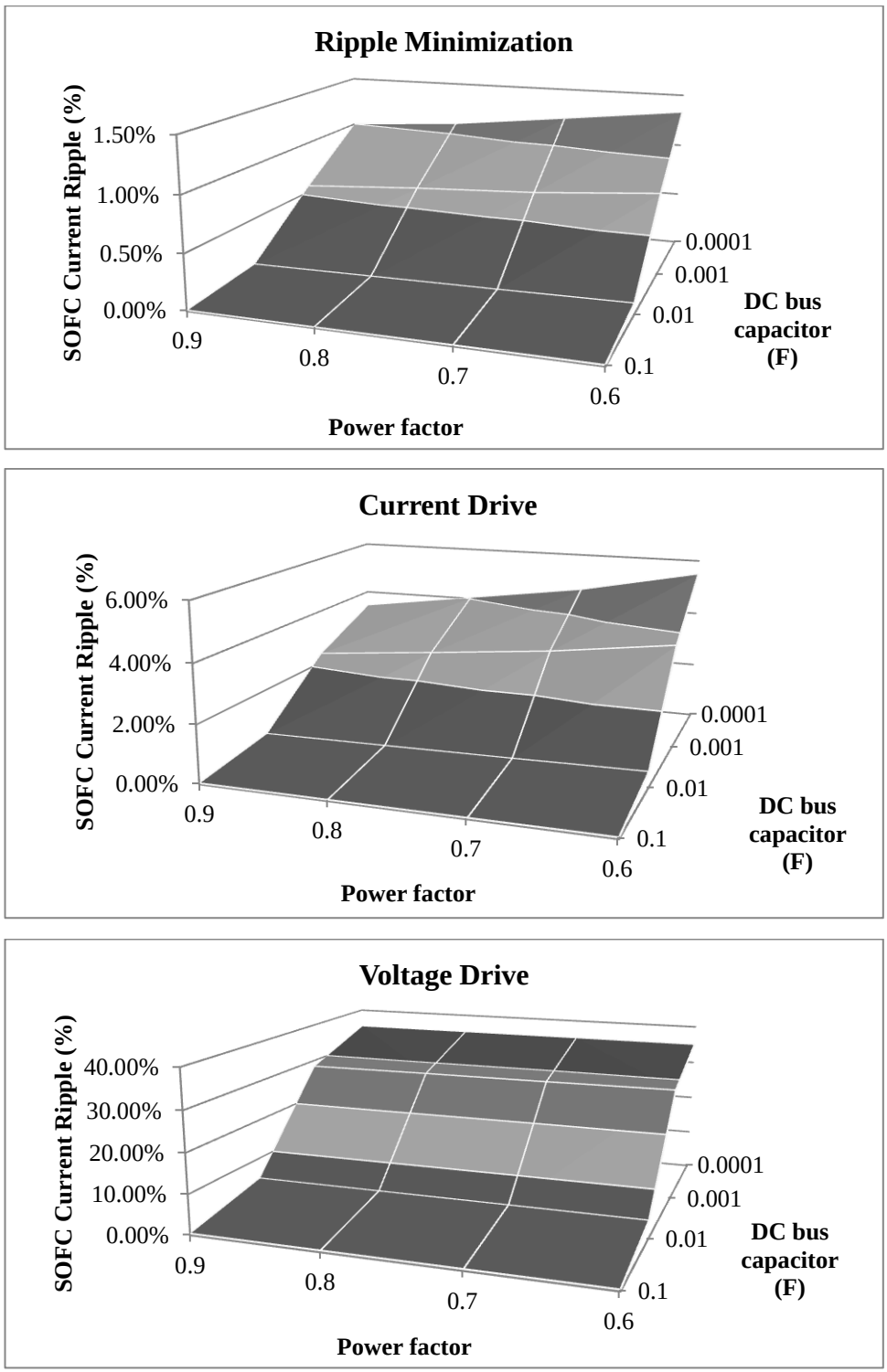

Figure 5.16 Effects of DC bus capacitor and power factor on SOFC current ripple at stiff grid (3% unbalance and 5% 5th harmonic at PCC)

5.3.2.5 Current Ripple Frequency Spectrum Analysis

The simulation results in Figure 5.13 - Figure 5.16 are determining the peak values of fuel cell current ripple. In this section the FFT analysis is applied to investigate the ripple frequencies in stiff grid only. The suggestion drawn from the previous section is followed, so that 10 mF of DC bus capacitor is used at the scenario of 3% of voltage unbalance at selected values of THD at the grid.

Figure 5.17 shows the ripple ratio (to rated current) versus power output. All controls induce greater ripples at higher power output because of the additional PI power controller, but for the Ripple Minimization the ripple is extremely small. In the Voltage Drive control mode, the ripple ratio is increased by 0.76% from 0.1 pu to 0.5 pu of targeted active power, which is the highest change observed. It is interesting to know that the magnitude of 300Hz ripple at the Current Drive and Voltage Drive is less than 100Hz ripple, but at the Ripple Minimization this is opposite. This is due in part to the finite controller bandwidth, which means that the control loops struggle to respond to a 5th harmonic voltage by sourcing additional harmonic currents. In addition, the sourced harmonics excite further voltage harmonics at the PCC. These in turn produce secondary current harmonics at other frequencies. Figure 5.18 shows the relationship between ripples and the harmonic orders. Close results are found between the 5^{th} and 7^{th} harmonic (5% of each applied in simulation), while the 3^{rd} harmonic normally does not appear at a three-phase AC system.

Referring to the introduction of this chapter that low frequency ripples (which are often regarded as the ones below 400Hz) affect the fuel cell most, with the trend that the lower frequencies give the severest contributions. Figure 5.17 and Figure 5.18 both show that the Ripple Minimization contributes the lowest 100Hz ripple which again earns its title as the friendliest control for fuel cell. However in the Current Drive and Voltage Drive the 100Hz ripple domains. Finally it also can be seen that a DC bus capacitor of 10mF is enough to give an effective filtering for all three controls, when power demand or harmonic order vary.

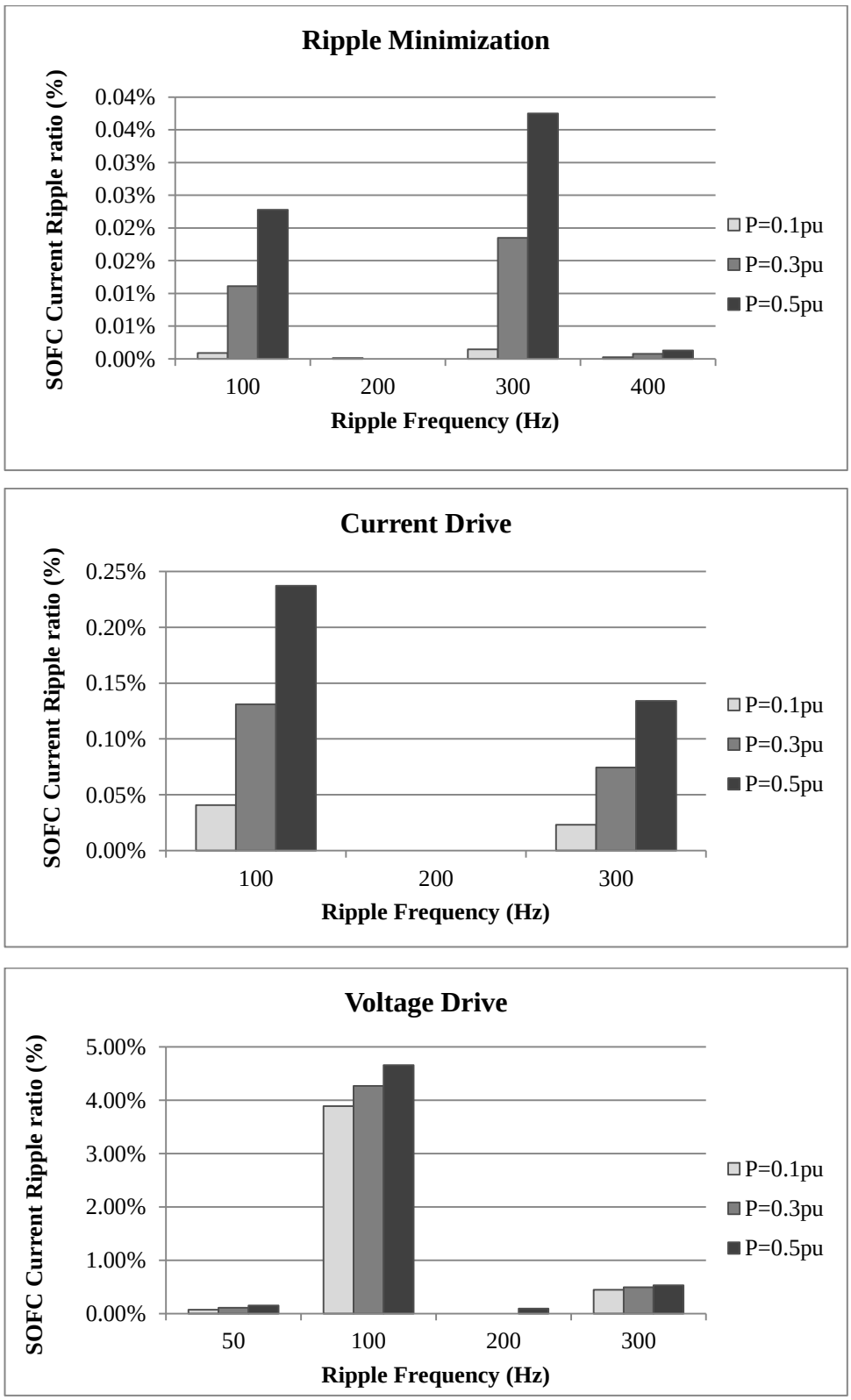

Figure 5.17 Ripple ratio versus power output (3% unbalance and 5% 5th harmonic)

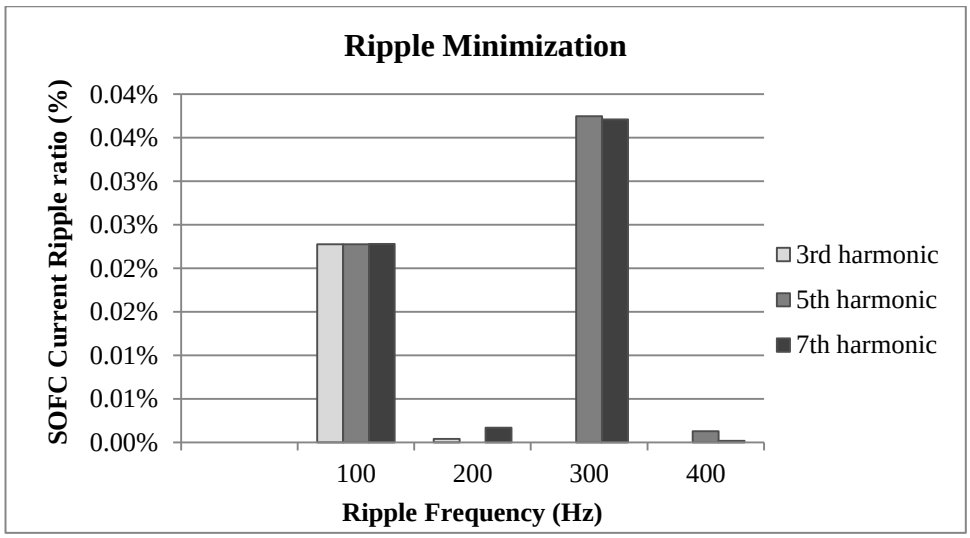

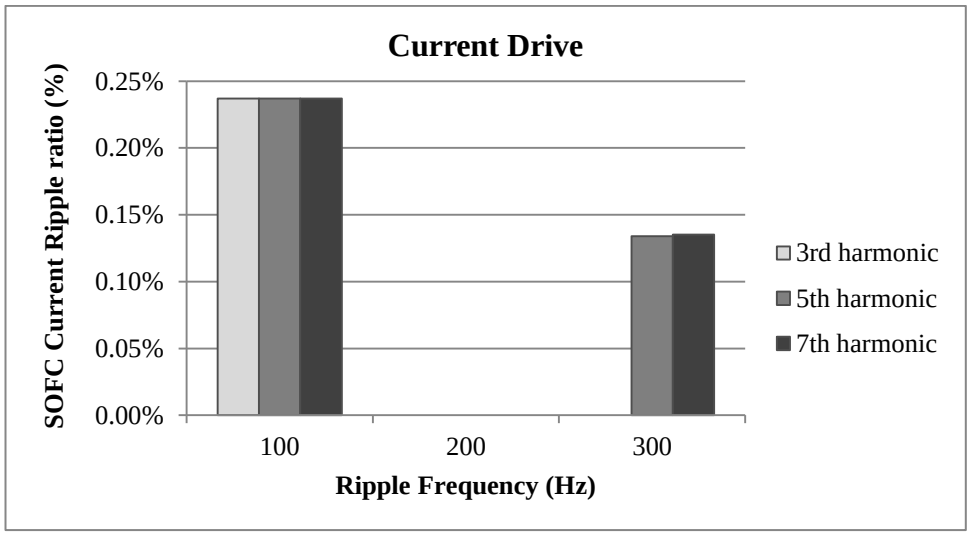

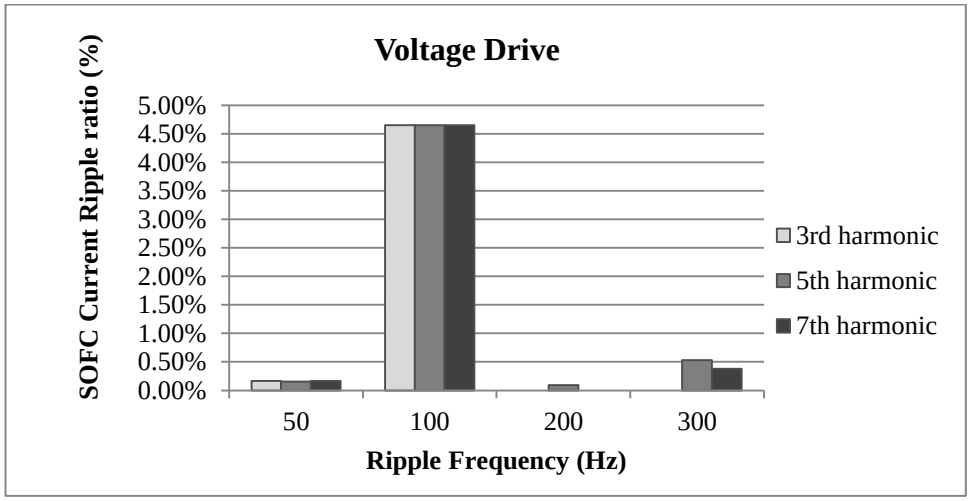

Figure 5.18 Ripple ratio versus harmonic orders (3% unbalance and 5% THD with selected order)

5.4 Case Studies and Simulations of SOFC Integrated Power System

In this section the simulations and investigations are extended to examine the inverter control related trade-offs at certain cases. Three grid conditions are applied again with control modes at different scenarios. The simulations examine AC power qualities and fuel cell efficiency as well as the power loss contributed by ripple, etc. Most literature as Ref. [33] exams the effects on the fuel utilization (FU) ratio induced by inverters, however in this research the fuel (H_2) consumption/production rate is more concerning because there is more interest in understanding how the control modes affect the discharge/recharge process during a cycle operation. The DC bus capacitance with values of 1 mF and 10 mF are chosen in simulations to present the comparisons in affecting the fuel cell performance.

These cases are the RSOFC system connected to stiff, weak and microgrid with three control modes, at 3% unbalance voltage, 5th harmonic with amplitude of 5%, 0.5 pu active power and 0.3 pu reactive power target, to investigate the overall performance on AC power quality and the fuel cell at challenging conditions. The simulation results are all presented in steady state. The fuel cell systems are initialized with 90% SOC with a fixed 1283K of temperature (at which the bronze-tin heat store starts to melt and stabilizes the system temperature). The figures below are showing the results in 1.5 cycle simulation time. The ripple current drawn by the inverter contributes to a loss which can be interpreted as a reduction in the available output power from the fuel cell [39]. The proportion of the power loss due to DC bus ripple twice the fundamental frequency on the Randles circuit is also calculated by Equation (5.18) in Table (5.2) – (5.4) as a percentage of the total power loss on the Randles circuit impedance. The tables also show the actual fuel cell power output (pu), fuel consumption rate (mole/s) and its efficiency.

$$P_{loss} = I^2_{ripple\ 100Hz} \times R_{100Hz} \qquad (5.18)$$

Finally as mentioned before, the following simulations are using the altered Ripple Minimization and Current Drive with power PID controller, the original two controls from [16] are discussed in Appendix E.

5.4.1 Stiff Grid: 3% unbalance and 5% 5th harmonic P=0.5 pu, Q=0.3 pu

Error! Reference source not found. shows that at the presence of both voltage unbalance and THD, the Ripple Minimization control mode successfully provides the best minimization of power-flow ripple however by sourcing currents with relative high THD (the predicted level can be calculated by equations in Appendix J). This also explains that the finite controller bandwidth sources additional harmonic current and excites further voltage THD at the PCC when responds to the 5th harmonic voltage. The Voltage Drive mode provides slightly better voltage quality than others, at the expense of highest current THD and significant 49.7% of unbalance. Hence this is the worst effect from this control which brings higher power ripple than the other controls as observed. It can be seen that the Voltage Drive also contributes more power loss and demands more power output from the fuel cell system. As a result, the fuel cell system will consume the fuel gas faster at lower efficiency, although the difference is small. A suspicious is that this is partly due to the non-unity of power factor and can be conducted with the simulations in Figure 5.19 which shows the requested power from fuel cell by inverter versus the varying power factor (at a constant active power *P*). The trends show that the Voltage Drive is keener in demanding higher power output at lower power factor, while Ripple Minimization and Current Drive behave similarly but less effectively. The results from Figure 5.19 can be related with the results from Figure 5.16, as both simulations show that lower power factor causes higher power demand for all control modes with greater power-flow ripples, which leads to increased fuel cell current ripples. It can be concluded that only within a specific range must the RSOFC system be used as a VAR compensator such as in the STATCOM system due to the increased current ripple drawn from too much reactive power.

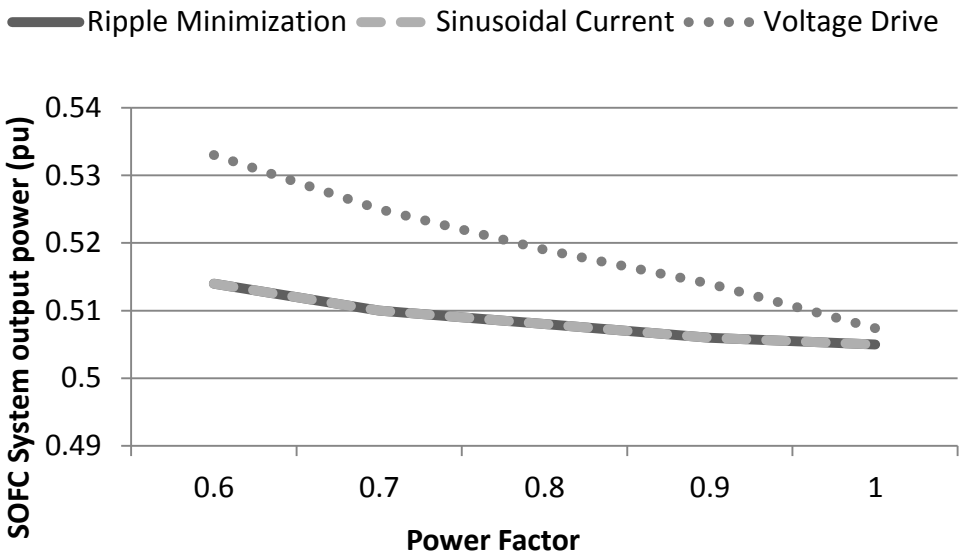

Figure 5.19 SOFC system output power versus power factor (Stiff grid, P=0.5pu)

For the Current Drive control, the effects on AC power qualities are between the Ripple Minimization and the Voltage Drive, and it provides the best result on current THD. In Ripple Minimization the actual currents tracks the reference I_{dq}^{ref} with unfiltered positive sequence voltage feedforward term V_{dq}. However in the presence of unbalanced voltages, V_{dq} moves in a circular trajectory at twice the fundamental frequency according to Appendix J which leads to the current reference with a second harmonic component. The utilization of filtered measurement of V_{dq} in positive and negative sequence leads to a nearly constant reference current I_{dq}^{ref}, so the current THD here is lower than in Ripple Minimization. However in this way the disturbance in V_{dq} at PCC will increase the active power ripples at the same frequency, as observed in **Error! Reference source not found.**.

Error! Reference source not found. shows both Ripple Minimization and Current Drive work similarly to fuel cell in terms of efficiency and fuel consumption rate. Higher frequency of ripple than 100Hz can be observed from Figure 5.20 due to the presence of the 5th harmonic. It is found during the simulation that when the inverter operates under Voltage Drive control the resultant DC bus ripple can be much larger than the other modes and the burden is heavy even for 1 mF of DC bus capacitance.

Simulations and Figure 5.20 (c-e) prove that in terms of ripple filtering and fuel cell system efficiency, the DC bus capacitor of 10 mF is suggested as a required choice with reasonable cost as well, as the previous case simulations agree with the same.

Because of the PID power controllers of the power inverter the ROSFC system is drove to generate slightly more power than requested at PCC to cover the power losses in inverter bridges and filter impedance, and also the part wasted in ripples especially when the inverter is operating in Voltage Drive mode, as shown in **Error! Reference source not found.**. In Chapter 4 it has been observed that higher power output from fuel cell means higher current being drawn, which in turn increasing the power loss on fuel cell internal impedance into heat as well. Therefore in the following case studies it can be always observed that the control mode which draws less power from fuel cell and DC bus ripple provides higher efficiency.

It can be concluded in this case study that both Ripple Minimization and Current Drive provide acceptable performance and effects on RSOFC system. These two control modes are considered being much beneficial to fuel cells than the Voltage Drive. In regards of the voltage quality at PCC, the Voltage Drive only provides slight improvements and the RSOFC system is less efficient. Also the current quality is much worse in Voltage Drive than others as both shown in**Error! Reference source not found.** and Figure 5.20. Therefore it is not worthy to apply the Voltage Drive control in stiff grids, even at relatively high level of voltage unbalance and THD.

Table 5.2 Power control, at Stiff Grid X_G = 0.0046, R_G = 0.0005, 3% Unbalance and 5% 5th Harmonic, P^* = 0.5 pu, Q^* = 0.3 pu

Measurements /Drives	Ripple Minimization	Current Drive	Voltage Drive
Fuel cell power flows (fundamental) (pu)	0.507	0.507	0.5165
Power ripple deviation from average (Pk-average pu)	0.009	0.045	0.407
I_d tracking errors (Pk-target) (pu)	0.025	0.018	1.2
I_q tracking errors (Pk-target) (pu)	0.05	0.036	0.26
V_{PCC} unbalance (%)	2.99	2.99	2.98
V_{PCC} THD (%)	5.11	5.11	5.08
I_{PCC} unbalance (%)	0.025	0.025	49.7
I_{PCC} THD (%)	5.8	0.21	19.9
V_{dc} ripple (Pk-average %) (1 mF)	0.236	1.26	13.58
V_{dc} ripple (Pk-average%) (10 mF)	0.031	0.214	2.4
Proportion of power ripple on Randle circuit (%) (1 mF)	0.005	0.137	16.8
Proportion of power ripple on Randle circuit (%) (10 mF)	1×10^{-4}	4.1×10^{-3}	0.92
Fuel (H_2) consumption rate (mole/s) (1 mF)	0.0669	0.0670	0.0718
Fuel (H_2) consumption rate (mole/s) (10 mF)	0.0669	0.0670	0.0686
SOFC stack average efficiency (%) (1 mF)	75.93	75.93	74.95
SOFC stack average efficiency (%) (10 mF)	75.93	75.93	75.6

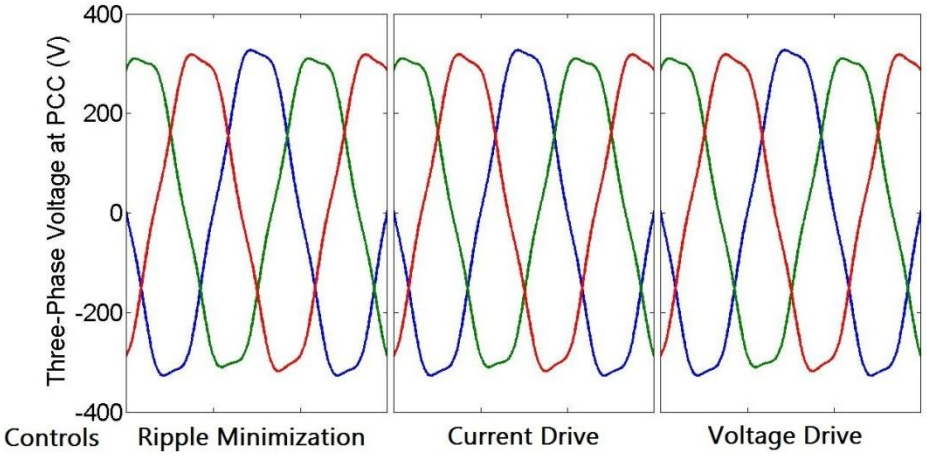
Three-Phase Voltage at PCC (V)
400
200
0
-200
-400
Controls
Ripple Minimization
Current Drive
Voltage Drive

(a)

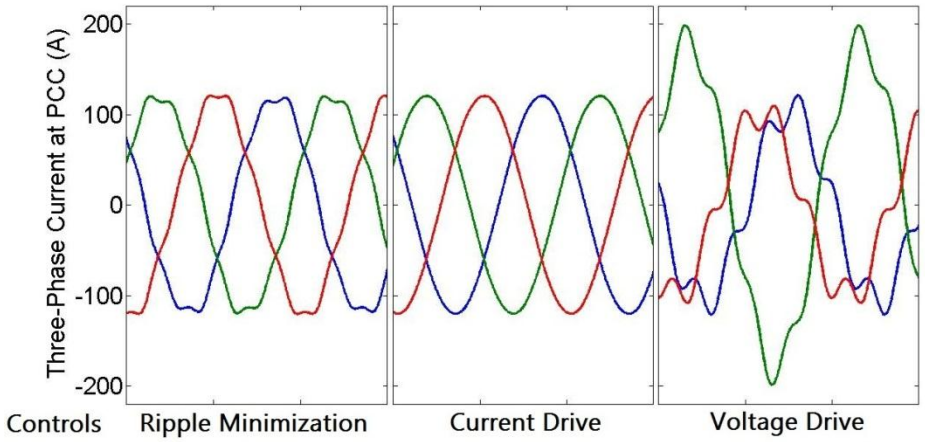
Three-Phase Current at PCC (A)
200
100
0
-100
-200
Controls
Ripple Minimization
Current Drive
Voltage Drive

(b)

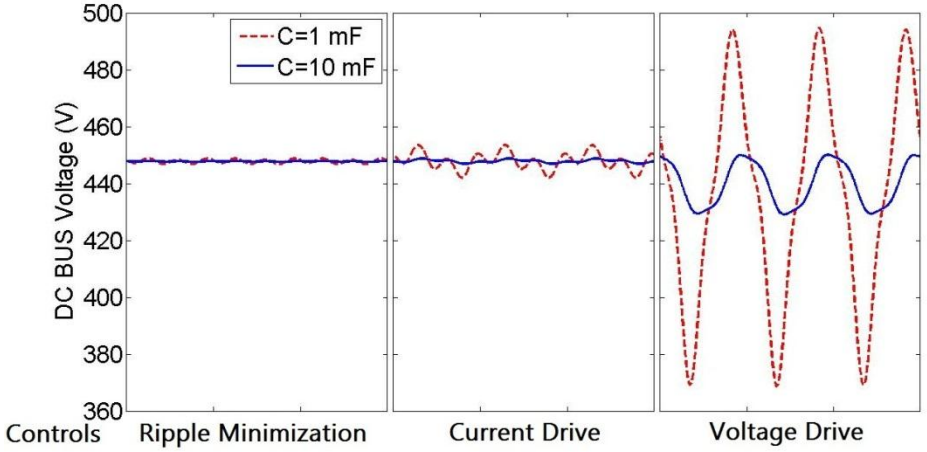
DC BUS Voltage (V)
500
480
460
440
420
400
380
360
C=1 mF
C=10 mF
Controls
Ripple Minimization
Current Drive
Voltage Drive

(c)

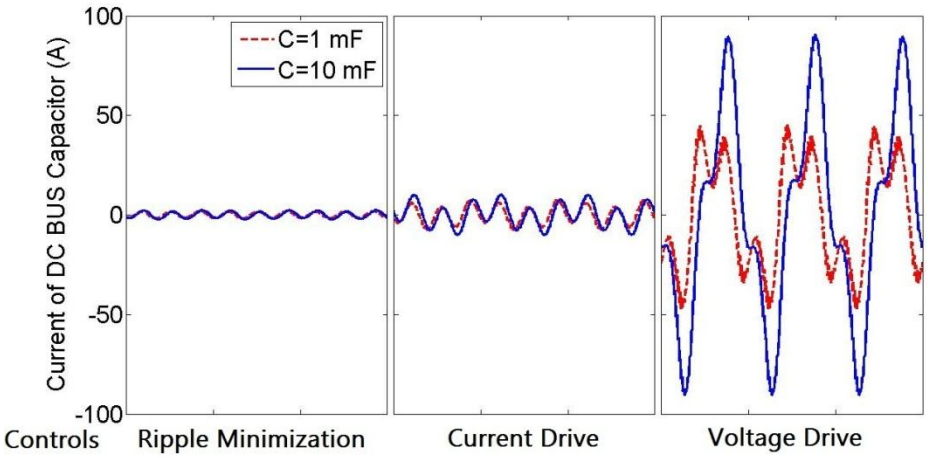

(d)

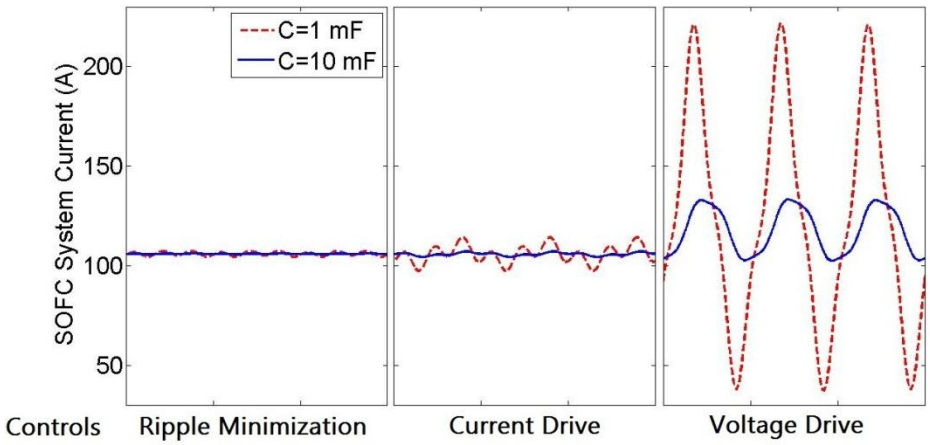

(e)

Figure 5.20 Power control at Stiff Grid, 3% Unbalance and 5% 5th Harmonic, P^* = 0.5 pu, Q^* = 0.3 pu, a,b) Three-phase voltage and current at the PCC, c) DC bus voltage, d) Current through DC bus capacitor, e) RSOFC system Current

5.4.2 Weak Grid: 3% unbalance and 5% 5th harmonic P=0.5 pu, Q=0.3 pu

Such a scenario might arise where an inverter is installed via a transformer of marginally 1pu rating, and/or at the end of a long overhead MV transmission line. Equally, the situation might arise where many small inverters with similar control algorithms are connected together so their output is aggregated.

In this case the Ripple Minimization and Current Drive controls again provide similar effects on power-flow ripple compared to in stiff grid, with slight improvement on voltage unbalance. The Voltage Drive provides much better effects on lowering both the power as listed in **Error! Reference source not found.** and DC bus ripples as shown in Figure 5.21 (e). Therefore it also draws less power from the RSOFC system to cover the losses due to ripple. **Error! Reference source not found.** also shows that the Voltage Drive provides much better reduction in voltage unbalance and THD in weak grid, which is also illustrated in Figure 5.21 (a). To explain this, it is possible to consider the infinite bus presents zero impedance to unbalance and harmonics. Without the presence of the inverter, the resulting unbalanced and harmonic voltages at the PCC could be estimated by a $V = ZI$ approach, accounting for the grid impedance at each harmonic frequency. The inverter in Voltage Drive control which synthesizes a balanced sinusoidal voltage source also presents a zero impedance to ground for both unbalanced and harmonic currents. Therefore, in the Voltage Drive control the effective impedance to ground for the unbalanced and harmonic currents, from the PCC, is the grid impedance in parallel with the inverter inductor impedance. Thus it is clear from **Error! Reference source not found.** that the Voltage Drive mode is successful in significantly reducing voltage both unbalance and THD at the PCC to ~1.27% and to 2.1% respectively. A reduction in either inductor impedance or grid impedance will further improve the power quality in this scenario. The AC power-quality improvements achieved by the voltage drive mode in this scenario are again obtained at the expense of high current unbalance and THD as shown in Figure 5.21 (b), and also with higher power-flow ripple than the scenarios with no injected harmonics.

In terms of fuel cell efficiency, all controls perform in the same trends as before, Ripple Minimization and Current Drive provide similar results as seen with the stiff grid. However the Voltage Drive makes the fuel cell system generating less additional power than in stiff grid, this effect and lower DC bus ripple lead to higher fuel cell efficiency in this mode. Suggestions in conclusion are that in cases of the AC voltage quality at PCC is being the priority when implementing the RSOFC system in weak grids, then the Voltage Drive is suggested to be applied with at least 10 mF of DC bus capacitance, even under certain high disturbance circumstances. And the major drawback in this situation is the slightly low fuel cell efficiency compared to the Ripple Minimization and Current Drive.

Table 5.3 Power control, at Weak Grid X_G = 0.128, R_G = 0.02, 3% Unbalance and 5% 5th Harmonic at Weak Grid, P^* = 0.5 pu, Q^* = 0 3 pu

Measurements /Drives	Ripple minimization	Current drive	Voltage drive
Fuel cell power flows (fundamental) (pu)	0.5074	0.5066	0.5134
Power ripple deviation from average (Pk-average pu)	0.008	0.041	0.184
I_d tracking errors (Pk-target) (pu)	0.028	0.017	1.04
I_q tracking errors (Pk-target) (pu)	0.05	0.035	0.12
V_{PCC} unbalance (%)	2.85	2.87	1.27
V_{PCC} THD (%)	5.15	4.72	2.1
I_{PCC} unbalance (%)	0.516	0.025	22.86
I_{PCC} THD (%)	5.84	0.20	8.61
V_{dc} ripple (Pk-average %) (1 mF)	0.2	1.175	6.15
V_{dc} ripple (Pk-average%) (10 mF)	0.028	0.204	1.08
Proportion of power ripple on Randle circuit (%) (1 mF)	0.004	0.122	4.19
Proportion of power ripple on Randle circuit (%) (10 mF)	7.5×10^{-5}	3.75×10^{-3}	0.197
Fuel (H_2) consumption rate (mole/s) (1 mF)	0.0670	0.0669	0.0686
Fuel (H_2) consumption rate (mole/s) (10 mF)	0.0670	0.0669	0.0680
SOFC stack average efficiency (%) (1 mF)	75.93	75.94	75.60
SOFC stack average efficiency (%) (10 mF)	75.93	75.95	75.72

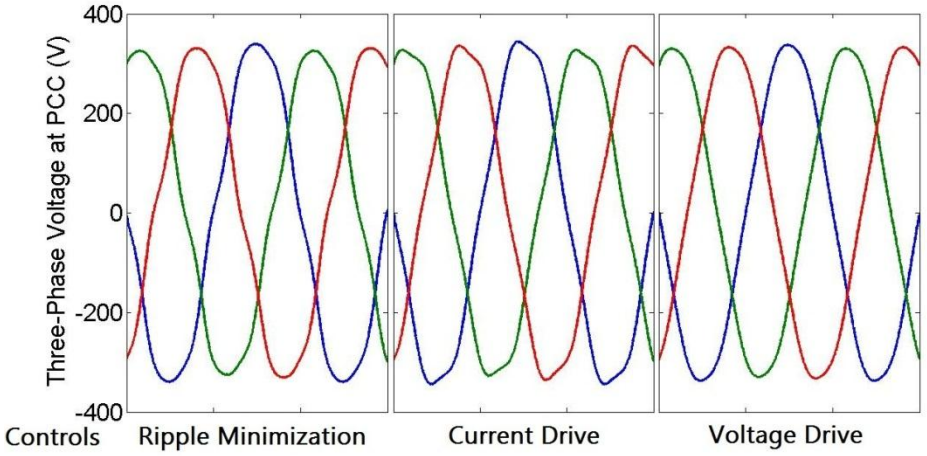
Three-Phase Voltage at PCC (V)
400
200
0
-200
-400
Controls
Ripple Minimization
Current Drive
Voltage Drive

(a)

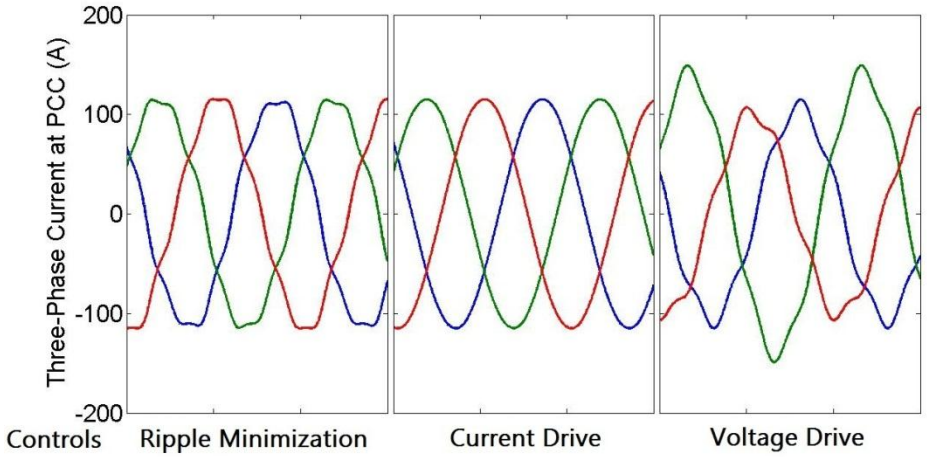
Three-Phase Current at PCC (A)
200
100
0
-100
-200
Controls
Ripple Minimization
Current Drive
Voltage Drive

(b)

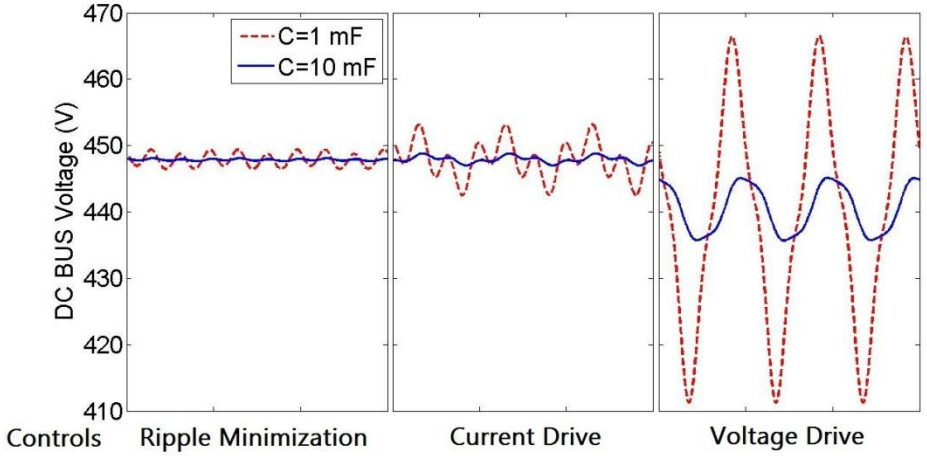
DC BUS Voltage (V)
470
460
450
440
430
420
410
C=1 mF
C=10 mF
Controls
Ripple Minimization
Current Drive
Voltage Drive

(c)

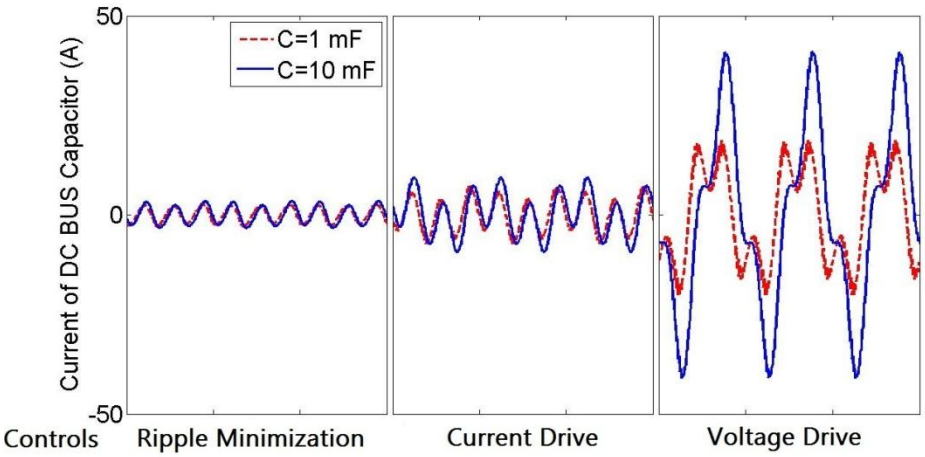

(d)

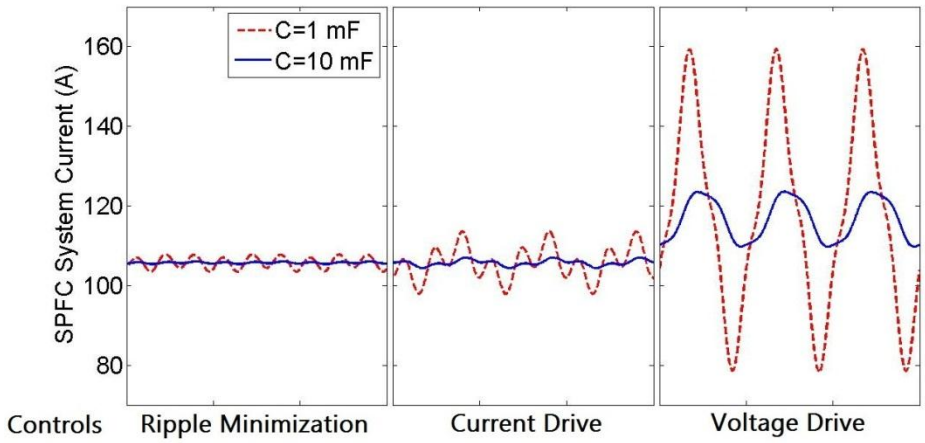

(e)

Figure 5.21 Power control at Weak Grid, 3% Unbalance and 5% 5th Harmonic, P^* = 0.5 pu, Q^* = 0.3 pu, a,b) Three-phase voltage and current at the PCC, c) DC bus voltage, d) Current through DC bus capacitor, e) RSOFC system Current

5.4.3 Microgrid: 3% unbalance and 5% 5th harmonic, P=0.5 pu, Q=0.3 pu

The overall simulation results of the Current Drive and Voltage Drive controls in microgrid are quite similar to their performances in stiff grid. However the Ripple Minimization mode provides poorer voltage THD and current unbalance in microgrid than in stiff grid, this is because the increased impedance of microgrid leads to higher proportions of secondary harmonics at PCC, as described previously. As the grid impedance applied in the simulation for microgrid is "between" stiff and weak grid, the Voltage Drive control also likely to provide effects in all aspects between the previous two cases, with considerably better voltage THD reduction as shown in **Error! Reference source not found.** and Figure 5.22. However, like in weak grid, only if the requirement of voltage quality at PCC is more strictly limited then will the Voltage Drive be applied in microgrids.

Table 5.4 Power control, at Microgrid X_G = 0.032, R_G = 0.003, 3% Unbalance and 5% 5th Harmonic, P^* = 0.5 pu, Q^* = 0.3 pu

Measurements /Drives	Ripple minimization	Current drive	Voltage drive
Fuel cell power flows (fundamental) (pu)	0.5071	0.5070	0.5147
Power ripple deviation from average (Pk-average pu)	0.007	0.044	0.312
I_d tracking errors (Pk-target) (pu)	0.025	0.018	1.17
I_q tracking errors (Pk-target) (pu)	0.052	0.036	0.21
V_{PCC} unbalance (%)	2.97	2.97	2.25
V_{PCC} THD (%)	5.08	5.07	3.8
I_{PCC} unbalance (%)	0.089	0.025	38.48
I_{PCC} THD (%)	5.82	0.211	15.4
V_{dc} ripple (Pk-average %) (1 mF)	0.19	1.25	10.44
V_{dc} ripple (Pk-average%) (10 mF)	0.025	0.214	1.84
Proportion of power ripple on Randle circuit (%) (1 mF)	0.003	0.136	10.9
Proportion of power ripple on Randle circuit (%) (10 mF)	6.5×10^{-5}	4.1×10^{-3}	0.56
Fuel (H_2) consumption rate (mole/s) (1 mF)	0.0670	0.0670	0.0701
Fuel (H_2) consumption rate (mole/s) (10 mF)	0.0670	0.0669	0.0682
SOFC stack average efficiency (%) (1 mF)	75.93	75.93	75.30
SOFC stack average efficiency (%) (10 mF)	75.93	75.93	75.67

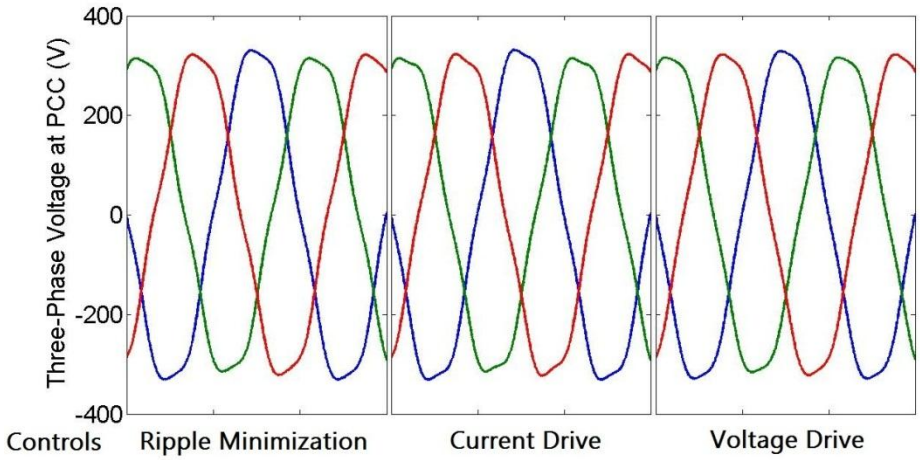
Three-Phase Voltage at PCC (V)
400
200
0
-200
-400
Controls
Ripple Minimization
Current Drive
Voltage Drive

(a)

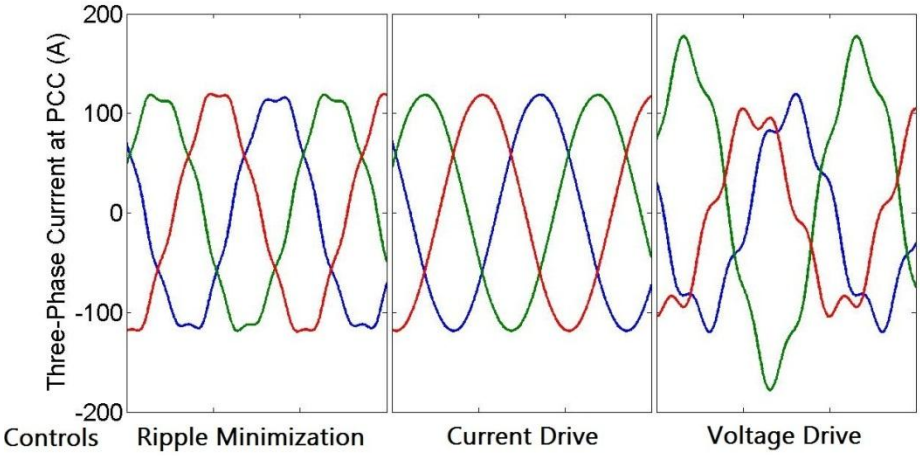
Three-Phase Currrent at PCC (A)
200
100
0
-100
-200
Controls
Ripple Minimization
Current Drive
Voltage Drive

(b)

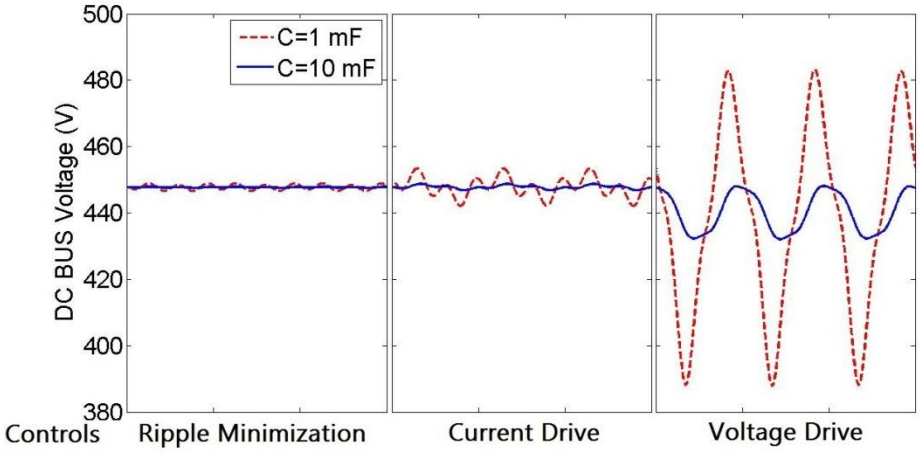
DC BUS Voltage (V)
500
480
460
440
420
400
380
C=1 mF
C=10 mF
Controls
Ripple Minimization
Current Drive
Voltage Drive

(c)

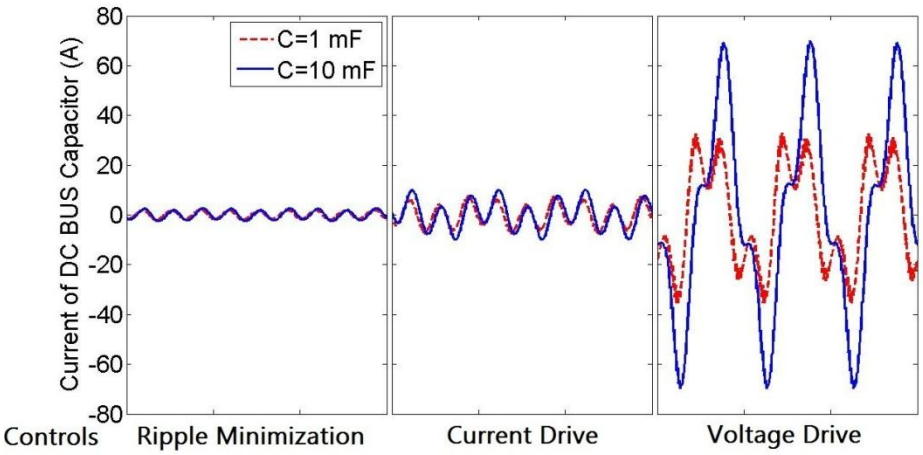

(d)

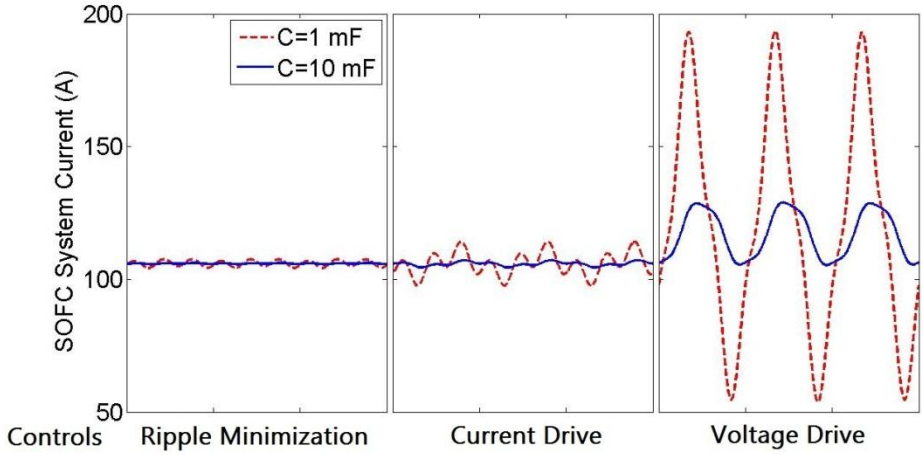

(e)

Figure 5.22 Power control at Microgrid 3% Unbalance and 5% 5th Harmonic, P^* = 0.5 pu, Q^* = 0.3 pu, a,b) Three-phase voltage and current at the PCC, c) DC bus voltage, d) Current through DC bus capacitor, e) SOFC stack Current

5.4.4 RSOFC System Recharging at Stiff Grid

In this section the operation of the RSOFC system is switched to the electrolysis mode which features a recharging process. The performances of Ripple Minimization and Current Drive on AC power quality and DC bus ripple are alike as in Section 5.4.1 of stiff grid scenarios. However the Voltage Drive control is introducing even higher current unbalance and THD in the recharging process. And in this case the target Q is set to zero when the fuel cell is recharging. It has been described in Chapter 3 that the fuel cell terminal voltage in electrolysis (recharging) mode is higher than in fuel cell (discharging) mode due to the fact that it is the Nernst voltage adding all the voltage polarisations (activation, diffusion polarisation and resistance voltage drop). This means that at a same power rating during the recharging process, the current drawn by the fuel cell system is actually lower than in discharge mode. According to Section 3.3 in Chapter 3 that the fuel (H_2) consumption and production rate is naturally characterized by the current flow within the fuel cell (whenever in fuel cell mode or electrolysis mode), therefore this finally leads to the fact that fuel cell recharges slower than it discharges with the same power input/output. **Error! Reference source not found.** also shows that the efficiency can be exceeded to more than 100%, this is due to the definition which is introduced in Section 3.6 Chapter 3 and Section 4.2 in Chapter 4. The Ripple Minimisation control is finally suggested to be used in electrolysis mode/recharging operation for the RSOFC system.

Table 5.5 Power control at Stiff Grid X_G = 0.0046, R_G = 0.0005, 3% Unbalance and 5% 5th Harmonic, P^* = 0.5 pu, Q^* = 0 pu

Measurements /Drive	Ripple minimization	Current drive	Voltage drive
Power ripple deviation from average (Pk) (pu)	0.026	0.035	0.37
V_{PCC} unbalance (%)	3	3	2.87
V_{PCC} THD (%)	5.08	5.08	4.85
I_{PCC} unbalance (%)	0.05	0.07	56.08
I_{PCC} THD (%)	5.52	0.57	29.5
V_{dc} ripple (Pk) (%) (1 mF)	0.34	0.5	5.8
V_{dc} ripple (Pk) (%) (10 mF)	0.045	0.11	1.23
Fuel (H_2) production rate (mole/s) (1 mF)	0.0498	0.0495	0.0491
Fuel (H_2) production rate (mole/s) (10 mF)	0.0498	0.0495	0.0496
SOFC stack average efficiency (%) (1 mF)	100.56	100.64	100.83
SOFC stack average efficiency (%) (10 mF)	100.56	100.63	100.61

5.5 Conclusions

In this Chapter the research focuses on the dynamic behaviors of the reversible solid oxide fuel cell (RSOFC) model utilized within AC power grids, with three competing inverter control algorithm applied at different scenarios. It is inevitable that low frequency current ripples occur when implementing power electronic converters/inverters for fuel cells. The ripple currents can be serious to fuel cell performance and life span if they are not limited. This chapter first examined the influences on state of charge, fuel consumption rate and system temperature due to the existence of ripples, and then the simulation and investigation are extended to scenarios at different grid conditions and AC qualities. Finally the parametric analysis and case studies of the effects of electrical feedbacks on fuel cell stack current ripple, including the effects contributed by voltage unbalance and THD, power factor, and DC bus capacitor at different grid scenarios are discussed.

The simulation results show that current ripple ratio at 50% (to rated current) leads to 6.5 ℃ more in temperature increase per hour and 1.28% faster in fuel consumption at current density of 5000 A/m^2 for the RSOFC system. However these effects are relatively small and can be reduced if ripples are properly filtered by a DC bus capacitor. The simulations of current ripple versus power factor conclude that all control modes tend to demand 0.01 ~ 0.015 pu more active power from the fuel cell when higher reactive power is requested from the power inverter, this would lead to an increase in current ripple at the range of 0.3% ~ 2.1%, as shown in Figure 5.16. Therefore it is suggested that if the RSOFC system is being used as a VAR compensator such as a part of STATCOM then a specific range of reactive power is required to be verified due to the increased current ripple.

During the analysis of the influences caused by state of charge, it is found that more concerns in both efficiency and safety operation can be drawn by low level of SOC, than high level of ripples. The significant decline in efficiency caused by low SOC is found to be a more negative impact than the current ripple in this research. An improved recommendation of the updated safety limit for SOC range is to be 20% to 95% rather than the original proposed range of 5% - 95% by the University of St.

Andrews. This is also for preventing of drawing more power which may cause over-current damage when the RSOFC system is operating at a low SOC and rated power.

It can be concluded that both Ripple Minimization and Current Drive provide acceptable performance and effects on RSOFC system in all grid conditions, they are considered much better than what Voltage Drive delivers especially in stiff grids. And it is concluded that the Ripple Minimization control mode is the friendliest control for the fuel cell in terms of providing low current ripple (normally < 1.4%), higher efficiency and lower power loss, compared to the other two modes. However this control mode tends to introduce a much higher current THD (5.8%) than Current Drive at PCC. From point of view of current quality, Current Drive does the best job in lowering the current unbalance (normally < 0.25%) and THD (normally < 0.03%) and meanwhile providing relatively good reduction in fuel cell current ripple (normally < 6%). The Current Drive and Ripple Minimization have similar fuel cell efficiencies at different grid conditions. The challenge is that the Voltage Drive can be harmful on fuel cell because in certain cases the ripple ratio (35% as maximum) and current THD (22.86% as maximum as shown in Table 5.3) can be significant. In addition, although the fuel cell current ripple can be out of the specification in Voltage Drive control under certain cases, simulations proved that a DC bus capacitor of at least 10 mF (for 100 kVA RSOFC rating with 450V at DC bus) can be enough to satisfy the ripple specifications. This helps Voltage Drive to be applicable by reducing the ripple ratio from 35% to 4.6% in stiff grid as the worst case (shown in Figure 5.16).

However from the point of view of the voltage quality at PCC, the Voltage Drive only provides slight improvements in stiff grids. The RSOFC system is also less efficient and the current quality is much worse in Voltage Drive than others. Therefore it is not worth applying the Voltage Drive control in stiff grids, especially at relative high level of voltage unbalance and THD. If the major concern is on current ripple related performance of RSOFC system then both Ripple Minimization and Current Drive are recommended in any grid condition, especially at high voltage unbalance and THD in stiff grids. However the Voltage Drive is providing great improvements on the voltage quality at PCC (1.27% of unbalance and 2.1% of THD as minimum as shown in **Error! Reference source not found.**Table 5.3) in weak

grids. Therefore in cases that the AC voltage quality at PCC is being the priority then the Voltage Drive is suggested to be applied with at least 10 mF of DC bus capacitance, especially under certain high disturbance circumstances.

5.6 References for Chapter 5

[1] W. Choi, Jo.W. P. Enjeti, “Development of an equivalent circuit model of a fuel cell to evaluate the effects of inverter ripple current,” , J. *Power Sources*, vol. 158, pp. 1324–1332, 2006

[2] EG&G Technical Services, Inc. *Fuel Cell Handbook (Seventh Edition)*, U.S. Department of Energy Office of Fossil Energy National Energy Technology Laboratory November 2004

[3] C. Liu, J.Lai, “Low Frequency Current Ripple Reduction Technique With Active Control in a Fuel Cell Power System With Inverter Load”, *IEEE Trans. Power Electronics*, pp. 1429 - 14362007

[4] F. K. Kyushu Univ, Fukuoka “Input Current-Ripple Consideration for the Pulse-link DC-AC Converter for Fuel Cells by Small Series LC Circuit,” in *Applied Power Electronics Conference and Exposition 2009.* APEC 2009. Twenty-Fourth Annual IEEE, pp. 447- 451 , Feb. 2009

[5] G Fontes , "Interactions between fuel cells and power converters influence of current harmonics on a fuel cell stack", in Power Electronics Specialists Conference, 2004. PESC 04. 2004 IEEE 35th Annual, 4729- 4735 Vol.6, June 2004

[6] R. S. Gemmen, “Analysis for the effect of inverter ripple current on fuel cell operating condition,” *J. Fluids Eng.*, vol. 125, no. 3, pp. 576–585, 2003.

[7] R.S. Gemmen, “Analysis for the effect of the ripple current on fuel cell operating condition,”*J. ASME,* vol. 369 (4), pp. 279–289, 2001.

[8] B. Wahdame, "Impact of power converter current ripple on the durability of a fuel cell stack", in *Industrial Electronics, 2008*. ISIE 2008. IEEE International Symposium on, 1495- 1500, 2008

[9] L. Palma, "An active power filter for low frequency ripple current reduction in fuel cell applications", in *Power Electronics Electrical Drives Automation and Motion (SPEEDAM)*, 2010 International Symposium on, 1308- 1313 , 2010

[10] B. Ozpineci, *Trade Study on Aggregation of Multiple 10-KW solid-oxide Fuel Cell Power*, Oak Ridge National Laboratory, ORNL/TM-2004/248

[11] A.M. Tuckey. “A low-cost inverter for domestic fuel cell applications,” in *Power Electronics Specialists Conference, 2002*. pesc 02. 2002 IEEE 33rd Annual, vol.1, pp. 339- 346, 2002.

[12] D. Chen and L. Li, “Novel Static Inverters With High Frequency Pulse DC Link,” *IEEE Trans. PE*, vol. 19, No. 4, pp. 971-978, Jul. 2004.

[13] K. Fukushima, T. Ninomiya, M. Shoyama, I. Norigoe, Y. Harada and K. Tsukakoshi, “Consideration for Input Current-Ripple of Pulse-link DCAC Converter for Fuel Cells,” *in Proc. of EPE-PEMC 2008*, pp. 148-153, Sep. 2008.

[14] O. Perego, P. Mora, S. Guastella, and C. Tornelli. (2010). DER-lab Round Robin testing on photovoltaic single phase inverters: DERlab, 2010 [Online]. Available:http://www.pv-tech.org/technical_papers/_a/derlab_round-robin_testing_of_photovoltaic_single-phase_inverters/, accessed June 2010.

[15] DERLab. (2009). Network of DER Laboratories and Pre-Standardisation: DER inverter white book [Online]. Available: http://derlab.eu/public/index.php, accessed June 2010.

[16] A.J Roscoe, S.J Finney, G.M Burt, “Trade-offs Between AC Power Quality and DC Bus Ripple for 3-Phase 3-Wire Inverter-Connected Devices Within Microgrids," *IEEE Trans. Power Electronics.* vol: 26, Issue: 3 pp. 674 – 688, March 2011.

[17] G Allen, 2002, ‘‘Equipment Design and Interface Specifications for 10 kW Inverter,’’ inverter specification data provided by Fuel Cell Technologies, Ltd. for the Future Energy Inverter Competition

[18] R. S. Gemmen, “Analysis for the effect of inverter ripple current on fuel cell operating condition,” *J. Fluids Eng.*, vol. 125, no. 3, pp. 576–585, 2003.

[19] Ballard Nexa® Power Module User’s manual.

[20] S.S. Penner, *Report of the DOE Advanced Fuel-Cell Commercialization Working Group*, , DOE Advanced Fuel Cell Working Group (AFC2WG) DOE/ER/0643, No. DEFG03-93ER30213, March 1995.

[21] P. Sanjaya.”Effects of electrical feedbacks on planar solid oxide fuel cell,” *J. Fuel Cell Science & Technology*, vol. 4, no2, pp. 154-166, 2007. ISSN 1550-624X

[22] R. Gemmen, “Analysis for the Effect of Inverter Ripple Current on Fuel Cell Operating Condition,” *Power Electronics for Fuel Cells Workshop*, Irvine, California, August 8–9, 2002.

[23] G Fontes, "Interactions between fuel cells and power converters influence of

current harmonics on a fuel cell stack", in Power Electronics Specialists Conference, 2004. PESC 04. 2004 IEEE 35th Annual, 4729- 4735 Vol.6, June 2004

[24] T Jacobsen, "Hysteresis in the solid oxide fuel cell cathode reaction," *J. Electrochimica Acta*, vol. 46, Issue 7, pp. 1019–1024, January 2001

[25] N. Pogaku and T. C. Green, "Harmonic mitigation throughout a distribution system: A distributed-generator-based solution," *IEE Proc.-Gener. Transmiss. Distrib*, vol. 153, no. 3, pp. 350–358, May 2006.

[26] S. V. Iyer, M. N. Belur, and M. C. Chandorkar, "A generalized computational method to determine stability of a multi-inverter microgrid," *IEEE Trans. Power Electron*., vol. 25, no. 9, pp. 2420–2432, 2010.

[27] G. Ramtharan, A. Arulampalam, J. B. Ekanayake, F. M. Hughes, and N. Jenkins, "Fault ride through of fully rated converter wind turbines with AC and DC transmission systems," *IET Renewable Power Gener*., vol. 3, no. 4, pp. 426–438, Dec. 2009.

[28] V. Mueller. ; Luu Hong Viet, "High Dynamic Control a PWM Rectifier under Unbalanced Voltage Supply with Deadbeat Current Controllers,", in *Power Electronics and Applications, 2005 European Conference*, Dresden Univ. of Technol., P. 1 – 11, 2005.

[29] S Buso, P Mattavelli *Digital Control in Power Electronics*, 2006 by Morgan & Claypool, ISBN-10: 1598291122

[30] H Akagi, E H Watanabe, and M Aredes, *Instantaneous Power Theory and Applications to Power Conditioning*, April 2007, Wiley-IEEE Press, ISBN: 978-0-470-10761-4

[31] R.Gopinath, S. Kim "Development of a Low Cost Fuel Cell Inverter System with DSP Control," IEEE Trans. Power Electronics.,vol. 19, Issue: 5, 2004

[32] A.M. Tuckey, N.T. Darwin, "A Low-Cost Inverter for Domestic Fuel Cell Applications", in *Power Electronics Specialists Conference, 2002*. vol. 1, pp. 339 – 346, 2002.

[33] R. S. Gemmen, "Analysis for the Effect of Inverter Ripple Current on Fuel Cell Operating Condition", J. Fluids Eng. May 2003 Volume 125, Issue 3, 576 (10 pages)

[34] A. J. Roscoe, A. Mackay, G. M. Burt, and J. R. McDonald, "Architecture of a

network-in-the-loop environment for characterizing AC power system behavior," IEEE Transactions on Industrial Electronics, vol. 57, pp. 1245-1253, 2010

[35] A. J. Roscoe, G. M. Burt, and J. R. McDonald, "Frequency and fundamental signal measurement algorithms for distributed control and protection applications," *IET Generation, Transmission & Distribution* vol. 3, pp. 485-495, May 2009

[36] K. H. Ahmed, A. M. Massoud, S. J. Finney, and B. W. Williams, "Sensorless Current Control of Three-Phase Inverter-Based Distributed Generation," *IEEE Trans. Power Delivery*, vol. 24, pp. 919-929, Apr 2009

[37] K. H. Ahmed, A. M. Massoud, S. J. Finney, and B. W. Williams, "Autonomous adaptive sensorless controller of inverter-based islanded-distributed generation system," *IET Power Electronics*, vol. 2, pp. 256-266, May 2009

[38] W. Choi, Jo.W. P. Enjeti, "Development of an equivalent circuit model of a fuel cell to evaluate the effects of inverter ripple current," , J. *Power Sources*, vol. 158, pp. 1324–1332, 2006

[39] C. Liu, J. Lai, "Low Frequency Current Ripple Reduction Technique With Active Control in a Fuel Cell Power System With Inverter Load", *IEEE Trans. Power Electronics*, pp. 1429 - 14362007

6 Conclusions and Future Works

6.1 Conclusions

A reversible solid oxide fuel cell (RSOFC) system has a high potential as a candidate of an energy storage device for buffering intermittent renewable energies. Such a RSOFC system is under development at the University of St. Andrews. This thesis proposes significant comprehensive models developed in University of Strathclyde who is a collaborative partner of this research. Associated simulations of the performance of RSOFC system are studied and discussed to identify the shortcomings of the original design, and to provide feedbacks for optimization, in turn, improving the fuel cell stack with an enhanced practical capability and realistic performance. In order to investigate the performance and stability analysis of the RSOFC system to be used within AC power system, the equivalent Randles-cell circuit representing the RSOFC is derived and implemented for both impedance spectroscopy (IS) and integrated power system simulations. The investigation and analysis of interactions between RSOFC and AC power systems under different scenarios are discussed, giving suggestions for enabling the operation of RSOFC system under certain control scheme and grid condition.

The generalized design of fuel cell systems involve controlled fuel/gas inlet and this is different from the RSOFC system proposed in this research. The RSOFC system applies a pressurised vessel and stores fuel gas (hydrogen) within the sealed stack without any fuel inlet or exhaust. Therefore a unique model is required to represent the performances of the Nernst voltage and cell polarisations which are highly variant to this specific stack geometry and the relative operating conditions, e.g. thermal dynamics, species partial pressures and the state of charge (SOC). Therefore it was decided to create a new complete polarisation model as part of the research rather than applying a generalized SOFC model.

A heat store device is proven to be required for the RSOFC system from this thesis. In the original design the stack temperature could rise rapidly especially at high

density of power outputs which led to an issue of overheating (irreversible mechanical damage may be caused to cells). However this is hard to avoid due to this specific design of a sealed vessel, so that the heat exchange between gas fluids and the external environment is not possible. To overcome this issue an innovative application of a copper-tin based internal heat storage system is proposed and proven to be able to prevent overheating by storing heat energy in phase change. The significant detailed heat store model features three physical stages as solid, partly molten and liquid with associated heat capacities. When the heat store is designed with mass of 500kg, it increases the fuel cell operation time by a factor of 7.5 times without overheating (from 1/2 hour to 3 and 3/4 hours) at rated power output, for a stack consisting 800 cells with cubed shape and size of 4 m^3 at 70 bar of system pressure. During the operation this has to be carefully monitored and controlled because the system temperature will go up again if the copper-tin compound is completely molten.

It can be difficult to allocate an optimised amount of heat store because it needs to be determined by both the operating power level and the fuel storage capability. The RSOFC system in this research is proposed to buffer the imbalances between the demand and power generation (especially for the intermittent renewable energies) within the power system. Therefore the ROSFC system is not required to be fully discharged or recharged in all operations but frequently operated in cycles without approaching the SOC limits. It is found during the case studies that multiple cycles can be achieved at half rated fuel cell current without overheating or cooling the system with at least 200kg of heat store, as long as the operation periods in both fuel cell mode and electrolysis mode are equal. However at the rated current the heat store melts 7.9 times faster in fuel cell mode than it cools into solid in electrolysis mode, so the overall molten heat store is highly possible to gradually increase in the long term. Therefore the concern of overheating remains at cycle operations at high rated power. Two steps can be considered. First of all the amount of heat store has to be designed large enough according to the length and numbers of cycle operations required. Secondly, the system can be effectively cooled down during the electrolysis operation and the most efficient condition is found to be at -20 A of fuel cell current. Therefore the RSOFC system operates at -20 A in electrolysis mode is recommended with no operation periods for further cooling effect.

The novel application of the heat store proposed in this research provides an enhancement on the cycle efficiency by minimizing the net heat loss during a cycle operation. The heat store with amount of 500kg could reserve up to 31.3% more heat energy to be used in electrolysis mode, so at the rated power the cycle efficiency can be increased by 1.1% compared to the case without the heat store (at 1010 ℃). However at half rated power operation only 0.2% of cycle efficiency can be boosted. It is because this boost depends on the power level, which means lower power rating leads to less heat energy being reserved for the electrolysis mode. However this benefit can also be compromised when the cell is operated towards the higher end of its current rating as more heat is produced through losses than can be usefully utilised to generate electrical energy, which leads to a greater drop in cycle efficiency than can be boosted.

Another proposal resulting from this research is to increase the system volume and pressure level within the optimized stack design. The increased pressurisation provides a major cell performance improvement. When the system is pressurized from 1 bar to 70 bar, the Nernst voltage increases 11.5 % from 0.924 V to 1.035 V (at 50% state of charge, 900 ℃), and the diffusion polarisation significantly decreases by more than 50%, leading to a significant ~18.6% boost in cell terminal voltage. Higher volume and pressure also greatly increase the heat capability of the gases. It is found in the simulations that steam, hydrogen and oxygen under 70 bar of pressure contribute a heat capacity equivalent to ~18% of the 500 kg heat store, which partly compensate the overheating issue as well. Also it is proved that the hydrogen/energy storage capability of the system is significantly increased by 28 times more than the original design with 2 m^3 of volume.

Employing the detailed and comprehensive model in simulations, it is found that the electro-transfer coefficient β cannot be simply assumed with the generic value as used by most literature, but needs to be derived for this specific fuel cell design. This coefficient is shown to be critical in simulations of activation polarisation. It is used to check whether the polarisation is in low or high condition, so β has to be found with an appropriate value, otherwise the simulations will be highly unstable. It is also realized that β is related to the involved electro-chemical reactions. In this thesis an

entirely new derivation methodology of β for simulations of activation polarisation is proposed, with a value of 0.3465 for this specific fuel cell. However the justification of the theoretically method proposed in this research is indeed necessary in the future work. It is possible to empirically measure the performance of real fuel cell to compare with simulation results to determine the value of β.

For the first time, this thesis has conducted investigations and simulation analyses of the combined system effects of AC power system parameters, grid perturbation and different inverter controls on the performance of the RSOFC system. In this thesis, three control algorithms published by researchers at the University of Strathclyde for power electronic inverters are used, named as Ripple Minimization, Current Drive and Voltage Drive. The fuel cell current ripple induced by the utilization of power electronic inverter and the related controls are analysed. The case studies focus on the differences in the performance of the three control modes, and their effects on the RSOFC system at grid conditions with the variant target P & Q, unbalance and harmonic voltages at point of common coupling (PCC). Different simulations were carried out to provide insight and understanding of the impacts on the RSOFC system when being implemented as an energy storage device within AC power system.

The study of the influences brought from stack current ripple to RSOFC system revealed that current ripple ratio at 50% (to rated current) can result temperature to increase with an acceleration of 6.5 ℃ per hour and 1.28% faster in fuel consumption. However these influences are relatively small and can be reduced or mitigated if ripples are well filtered properly by a DC bus capacitance. The simulations of current ripple versus power factor conclude that all control modes tend to demand 0.01 ~ 0.015 pu more active power from the fuel cell when higher reactive power is requested from the power inverter, this would lead to an increase in current ripple at the range of 0.3% ~ 2.1%.

Case studies of interactions between the RSOFC and AC power systems were carried out using power system conditions containing up to 3% voltage unbalance and 5% THD at the point of common coupling.

The case studies conclude that the Ripple Minimization control mode is the friendliest control for the fuel cell in terms of providing low current ripple (< 1.4%), higher efficiency and lower power loss, compared to other two modes. From the point of view of current quality, the Current Drive control mode does the best job in lowering the current unbalance (< 0.25%) and THD (< 0.03%), meanwhile providing relatively good reduction in fuel cell current ripples (< 6%). The Voltage Drive control mode can be harmful to fuel cell because in certain cases the ripple ratio (35% as maximum) and current unbalance (19.9% as maximum) can be significant. However, simulations proved that a DC bus capacitance of at least 10 mF (for 100 kVA RSOFC rating with 450V at DC bus) can be enough to satisfy the ripple specifications. This helps Voltage Drive control to be applicable by reducing the ripple ratio from 35% to 4.6% in the worst case.

It can be concluded that both Ripple Minimization and Current Drive are acceptable to the RSOFC system in all grid conditions, especially in stiff grids with the presence of high voltage unbalance and THD at PCC. The Voltage Drive is not worthy in stiff grids because in regards of the voltage quality at PCC, the Voltage Drive only provides slight improvements and the RSOFC system is less efficient. However in cases of weak grids where the AC voltage quality at PCC is considered as the priority while implementing the RSOFC system, the Voltage Drive control is therefore suggested since the voltage can be greatly improved (1.27% of unbalance and 2.1% of THD). Under such condition, the RSOFC system with 10 mF of DC bus capacitance is only 0.23% less efficient with 1.06% increase of DC bus ripple, compared to the Ripple Minimization at the circumstance of high disturbance at PCC.

During the research a significant decline in efficiency caused by low SOC is found to have a much more negative impact than the current ripple. The efficiency of the RSOFC system in fuel cell mode can be reduced by 26% when the SOC drops from 90% to 10%, whereas the efficiency drop induced by ripple ratio increasing from zero to 20% is less than 0.25%. In addition, the voltage of a single fuel cell can be reduced by 0.25 V when the SOC drops from 90% to 10%, which leads to a maximum power reduction as well. Therefore, in fact it is found that low SOCs lead to greater concerns in both efficiency and safety of operation than the magnitude of the current ripple. An improved recommendation of the safety limits for the SOC is

20% to 95% rather than the original proposed range of 5% - 95% by the University of St. Andrews. This updated safety range is also useful for avoiding damages cause by over-current which may be caused by drawing full power when the RSOFC system is operating at a low SOC with a correspondingly low terminal voltage.

6.2 Future works

There are several improvements that can be made in the future. A commercial computational fluid dynamics (CFD) model would give a more accurate representation of the RSOFC system behavior, by modelling heat transfer via radiation, convection and conduction, and mass flows through the electrode and electrolyte, as well as the enhanced impedance spectroscopy tests, due to conditions of various levels of ripple current. With such information, improved fuel cell technology will be possible, thereby enabling the necessary stack lifetimes for achieving commercial success. Protection schemes specified for this RSOFC system can be another of the future work. The most obvious protection would be a fuel cell controller trips under instantaneous over-current condition, and this has to be coordinated with the protection devices/relays from AC power network.

Whilst this research focussed on cell stacks directly connected to a power electronic converter, future work might analyse the drawbacks and advantages of inserting a DC-DC buck-boost converter which resolves some issues of variable terminal voltage (voltage regulation) at different SOCs and operating conditions. As an alternative to a DC-DC converter (with certain levels of loss), a lower-loss competing strategy might be to use banks of cell stacks which can be reconfigured in real-time from series to parallel operation and vice-versa using simple switches, providing an approximately constant DC voltage to the inverter at all times. This is interesting because every individual fuel cell has the same SOC due to the common fuel supply, unlike batteries. However, ageing within the stacks or unequal gas/heat diffusion/flow might need to be carefully monitored or understood to avoid recirculating currents for paralleled connection.

Finally if the RSOFC prototype can be available and accessible then a long term degradation test is highly recommended. Such long term tests would enable the work

developed in this thesis to be verified and compared, with the aims of increasing the efficiency and decreases the cost of RSOFC storage devices.

Appendices

Appendix A: Three Phase Voltage/Current Transformations

Clarke Transformation

It is very common to use the Clarke transformation or named *αβ0* transformation in the converter/inverter control for derivations of the reference voltage/current. It represents a very powerful tool for the analysis and modelling of three-phase electrical systems. It is used to map instantaneous three-phase voltages V_a, V_b and V_c on the *αβ0* axes as V_α, V_β and V_0. The Clarke transformation and its inverse transformation of three-phase generic voltages are given by

$$\begin{bmatrix} V_0 \\ V_\alpha \\ V_\beta \end{bmatrix} = \sqrt{\frac{2}{3}} \begin{bmatrix} \frac{1}{\sqrt{2}} & \frac{1}{\sqrt{2}} & \frac{1}{\sqrt{2}} \\ 1 & -\frac{1}{2} & -\frac{1}{2} \\ 0 & \frac{\sqrt{3}}{2} & -\frac{\sqrt{3}}{2} \end{bmatrix} \begin{bmatrix} V_a \\ V_b \\ V_c \end{bmatrix} \qquad \text{(A.1)}$$

$$\begin{bmatrix} V_a \\ V_b \\ V_c \end{bmatrix} = \sqrt{\frac{2}{3}} \begin{bmatrix} \frac{1}{\sqrt{2}} & 1 & 0 \\ \frac{1}{\sqrt{2}} & -\frac{1}{2} & \frac{\sqrt{3}}{2} \\ \frac{1}{\sqrt{2}} & -\frac{1}{2} & -\frac{\sqrt{3}}{2} \end{bmatrix} \begin{bmatrix} V_0 \\ V_\alpha \\ V_\beta \end{bmatrix} \qquad \text{(A.2)}$$

Similarly, three-phase generic instantaneous line currents, I_a, I_b and I_c, can be transformed on the *αβ0* axis in the same way. Supposing that it is physically meaningful to reduce the order of the mathematical model from three to two dimensions, the *αβ* transformation represents the most commonly used relation to perform the reduction of order. Another advantage of applying the *αβ0* transformation is to separate zero-sequence components from the three phase components because of α and β axes make no contribution to zero-sequence

components,, so that V_0 can be eliminated from the above equations, thus resulting in simplification. The graphical representation of $\alpha\beta$ axis is shown in Figure A 1.

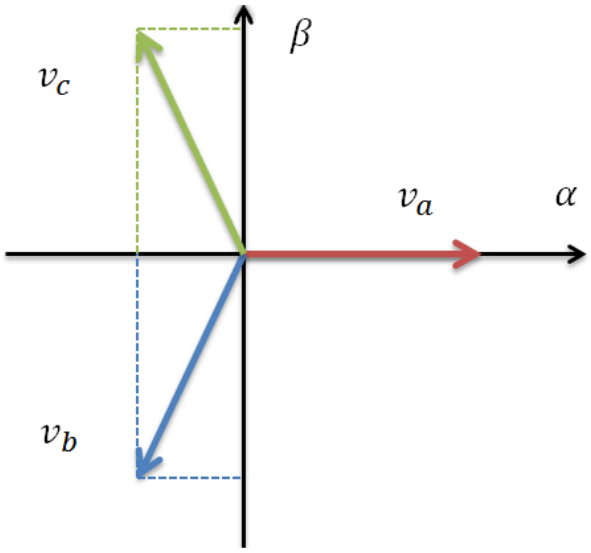

Figure A 1 Graphical representation of $\alpha\beta$ axis

Considering balanced three-phase voltages as:

$$\begin{aligned} V_a &= |V|\sin(\omega t) \\ V_b &= |V|\sin(\omega t - \frac{2\pi}{3}) \\ V_c &= |V|\sin(\omega t + \frac{2\pi}{3}) \end{aligned} \tag{A.3}$$

then it is easy to verify that

$$V_\alpha = \sqrt{\frac{3}{2}}|V|\sin(\omega t) \tag{A.4}$$

$$V_\beta = -\sqrt{\frac{3}{2}}|V|\cos(\omega t) \tag{A.5}$$

While neglecting V_0 in $\alpha\beta 0$ axis, an instantaneous voltage vector can be defined in α and β reference frame without loss of information. The vector $V_{\alpha\beta}$ can be interpreted as a rotating vector with amplitude of $\sqrt{\frac{3}{2}}|V|$, the angular rotation speed being equal to ω. The real axis is α while β representing the imaginary axis, as in Equation (A.6).

$$V_{\alpha\beta} = V_\alpha + jV_\beta \tag{A.6}$$

It should be noted that the vector defined above is a function of time, therefore, it should not be misinterpreted as a phasor. It is conventionally representing $V_{\alpha\beta}$ by using a factor with three phase voltage/current components. Where a $= e^{j\frac{2}{3}\pi}$. From Equation (A.1) it can be derived that

$$V_\alpha = V_a e^{j0} + \text{Real}\left[e^{j\frac{2}{3}\pi}\right]V_b + \text{Real}\left[e^{j\frac{4}{3}\pi}\right]V_c \tag{A.7}$$

$$V_\beta = 0 + \text{Img}\left[e^{j\frac{2}{3}\pi}\right]V_b + \text{Img}\left[e^{j\frac{4}{3}\pi}\right]V_c \tag{A.8}$$

Hence

$$V_{\alpha\beta} = V_a + aV_b + a^2V_c \tag{A.9}$$

Park's Transformation

Once the three-phase inverter has been proved to be completely equivalent to a couple of independent single-phase inverters, questions arise that whether the mapping of the system in the $\alpha\beta$ reference frame could be exploited to improve the current controller dynamic performance. The answer leads to Park's transformation (a rotating reference frame) which allows enhancement in tracking capabilities of the PI regulator. Instead of mapping the three-phase electrical system onto fixed (stationary) reference fame, Park's transformation maps onto a two-axis synchronous rotating reference frame (SRF). The SRF defines a new set of reference axes called d and q, which rotate around the static $\alpha\beta$ reference frame at a constant angular frequency ω. The symbol θ in Figure A 2 represents ωt.

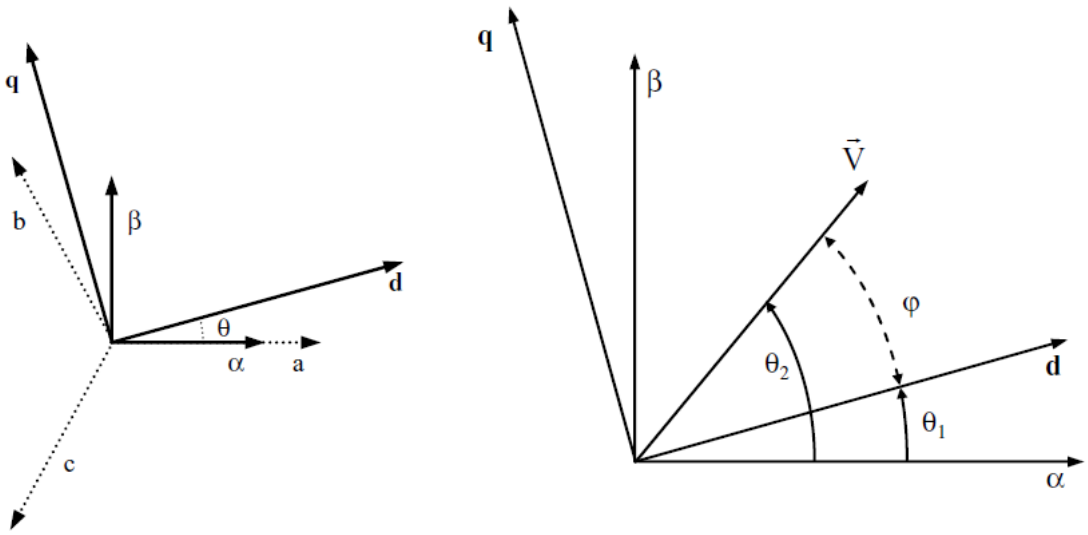

Figure A 2 Vector diagrams for Park's transformation derived from Clarke transformation

Park's transformation is widely used in the study of synchronous machine and the angular speed ω depends on the mechanism of the machine. However in the field of power electronic control the rotating vector angular speed is defined to equal the angular frequency of the original voltage which can be considered as the fundamental frequency of the system. One advantage is that the resultant vector

refers to dq reference frame V_{dq} is not moving at all. From Figure A 2 it implies that angles θ_1 and θ_2 will both increase with angular frequency ω, while angle φ will be constant and so will be the lengths of vector $\vec{V}$ projections on the d and q axes. Therefore the sinusoidal voltage/current signals with angular frequency ω will be seen as constant signals in the dq reference frame. Considering the figure above, the transformation matrix from $\alpha\beta$ to dq reference frame is showing as Equation (A.10).

$$\begin{bmatrix} V_d \\ V_q \end{bmatrix} = \begin{bmatrix} cos\theta & sin\theta \\ -sin\theta & cos\theta \end{bmatrix} \begin{bmatrix} V_\alpha \\ V_\beta \end{bmatrix} \tag{A.10}$$

and this can be simply expressed to vector V_{dq} as

$$\begin{aligned} V_{dq} = V_d + jV_q &= \left(V_\alpha + jV_\beta\right)(cos\theta - jsin\theta) \\ &= V_{\alpha\beta} e^{-j\theta} \end{aligned} \tag{A.11}$$

So it is possible to realize the vector V_{dq} as the vector $V_{\alpha\beta}$ rotating in clockwise with angular speed ωt in a balanced three-phase system. Meanwhile V_{dq} is directly derived from three-phase as shown in Equation (A.12). The transformation is the same for the case of a three-phase current (in positive sequence).

$$\begin{bmatrix} V_d \\ V_q \end{bmatrix} = \frac{2}{3} \begin{bmatrix} \cos(\omega t) & \cos(\omega t - \frac{2\pi}{3}) & \cos(\omega t + \frac{2\pi}{3}) \\ -\sin(\omega t) & -\sin(\omega t - \frac{2\pi}{3}) & -\sin(\omega t + \frac{2\pi}{3}) \end{bmatrix} \begin{bmatrix} V_a \\ V_b \\ V_c \end{bmatrix} \tag{A.12}$$

$$\begin{aligned} V_{dq} = V_d + jV_q &= \frac{2}{3}\left[e^{j(-\omega t)} V_a + e^{j\left(-\omega t + \frac{2\pi}{3}\right)} V_b + e^{j\left(-\omega t - \frac{2\pi}{3}\right)} V_b\right] \\ &= \frac{2}{3} e^{-j\omega t}\left[V_a + e^{j\frac{2\pi}{3}} V_b + e^{-j\frac{2\pi}{3}} V_b\right] \end{aligned} \tag{A.13}$$

However it is important to mention that the definition of Park's transformation, which can be referred as the classic definition is not used in this work. An alternative transformation in Matlab/Simulink modelling environment is defined differently as Equation (A.14).

$$\begin{bmatrix} V_d^p \\ V_q^p \end{bmatrix} = \frac{2}{3}\begin{bmatrix} \sin(\omega t) & \sin(\omega t - \frac{2\pi}{3}) & \sin(\omega t + \frac{2\pi}{3}) \\ \cos(\omega t) & \cos(\omega t - \frac{2\pi}{3}) & \cos(\omega t + \frac{2\pi}{3}) \end{bmatrix}\begin{bmatrix} V_a \\ V_b \\ V_c \end{bmatrix} \quad \text{(A.14)}$$

Equation (A.14) defines the *dq* components in positive sequence and can be decomposed as further:

$$\begin{aligned} V_{dq}^p &= V_d^p + jV_q^p \\ &= \frac{2}{3}\left[e^{j\left(\frac{\pi}{2}-\omega t\right)}V_a + e^{j\left(\frac{\pi}{2}-\omega t+\frac{2\pi}{3}\right)}V_b \right. \\ &\left. + e^{j\left(\frac{\pi}{2}-\omega t-\frac{2\pi}{3}\right)}V_b\right] \\ &= \frac{2}{3}je^{-j\omega t}\left[V_a + e^{j\frac{2\pi}{3}}V_b + e^{-j\frac{2\pi}{3}}V_b\right] \end{aligned} \quad \text{(A.15)}$$

It can be seen that the matlab/Simulink and classic version of Park's transformations to *dq* are linked by a rotation by 90 degrees, and with $\omega t = 0$ then both classic and Matlab/Simulink version of Park's transformation give identical result. Same conclusions can be found for negative sequence of both versions as well. And as long as V_{abc} is being converted via inverse Park's transformation from *dq* components through the same protocol after being controlled by the PI regulator therefore both resultants would no longer differ.

Appendix B: Concentrations of Gas Species on Bulk and Reaction Sites

To calculate the concentrations of the hydrogen and steam at the reactive surface, the following process is used. Equation (A.16) the Fick's law is the basis for these calculations, but is not used directly in the RSOFC model. It may be used to calculate the flux of hydrogen to the fuel electrode, where J_{H_2} is the flux of hydrogen to the fuel electrode, in mol$m^{-2}s^{-1}$, D is the mass diffusion coefficient (m^2s^{-1}), r is the radius of the cell (m), and J_{tot} is the sum of the hydrogen and steam flux, which always equals zero, as one molecule of steam is created for every molecule of hydrogen consumed.

$$J_{H_2} = -\frac{P_{an}D}{RT}\frac{dX_{H_2}}{dr} + X_{H_2}J_{tot} \qquad \text{(A.16)}$$

The diffusion coefficients of hydrogen and steam must be calculated before the concentrations at the bulk and the reactive surface can be determined. The ordinary diffusion coefficient of hydrogen $D_{H_2,m}$ in a steam-hydrogen mixture can be calculated using Equation (A.17), where D_{H_2,H_2O} is the mutual diffusion coefficient of hydrogen and steam, and X_{H_2} is the mole fraction of hydrogen in the system.

$$D_{H_2,m} = \frac{1 - X_{H_2}}{D_{H_2,H_2O}} \qquad \text{(A.17)}$$

The ordinary diffusion coefficient of steam $D_{H_2O,m}$ in a steam-hydrogen mixture can also be calculated, using Equation (A.18).

$$D_{H_2O,m} = \frac{1 - X_{H_2O}}{D_{H_2O,H_2}} \qquad \text{(A.18)}$$

The mutual diffusion coefficient of hydrogen and steam D_{H_2,H_2O} is calculated from a modified Fuller Equation (A.19), where P_{an} (bar) is the anode gas pressure (the fuel electrode in fuel cell mode) and v_i is the diffusion volume of species i (cm^3mol^{-1}).

The diffusion volume of hydrogen gas is 7.07 $cm^3 mol^{-1}$ and steam 12.7 $cm^3 mol^{-1}$. $M_{H_2H_2O}$ can be calculated from Equation (A.20), where M_{H_2} is 2 $g mol^{-1}$ and M_{H_2O} is 18 $g mol^{-1}$, and will be the same for hydrogen and steam. This mutual diffusion coefficient applies both to electrolysis and fuel cell mode.

$$D_{H_2,H_2O} = \frac{0.00143T^{1.75}}{P_{an} M_{H_2H_2O}^{1/2} \left[v_{H_2}^{1/3} + v_{H_2O}^{1/3}\right]^2} \quad \text{(A.19)}$$

$$M_{H_2,H_2O} = 2\left[\frac{1}{M_{H_2}} + \frac{1}{M_{H_2O}}\right]^{-1} \quad \text{(A.20)}$$

When Equation (A.16) is integrated, the following assumptions are made: that the hydrogen flux is equal and opposite to the steam flux, so the overall flux is zero as in Equation (A.21), and that the flux of hydrogen is directly proportional to the current, as in Equation (A.22).

$$J_{H_2} + J_{H_2O} = 0 \quad \text{(A.21)}$$

$$J_{H_2} = \frac{i}{2F} \quad \text{(A.22)}$$

When Equation (A.16) is integrated as in Equation (A.23), the limits taken are *l*, which is the outer surface of the fuel electrode, and *b* which is the point above the fuel electrode at which the concentration of hydrogen reaches the value of the bulk concentration, which is assumed to be $5 \times 10^3 m$. This gives Equation (A.24), where $L_{b,l}$ is the thickness of the diffusion layer between the concentration of gas in the bulk, and the outer surface of the fuel electrode, which gives the molar concentration of hydrogen at the fuel electrode outer surface, where P_{an} is the total gas pressure at the anode side in Pa. When the same process is carried out for steam, it gives Equation (A.25).

$$\int_{X_{H_2}^b}^{X_{H_2}^l} dX_{H_2} = \int_0^{L_{b,l}} -\frac{iRTL_{b,l}}{2FP_{an}D_{H_2,m}} dr \quad \text{(A.23)}$$

$$X_{H_2}^l = X_{H_2}^b - \frac{iRTL_{b,l}}{2FP_{an}D_{H_2,m}} \quad \text{(A.24)}$$

$$X_{H_2O}^l = X_{H_2O}^b + \frac{iRTL_{b,l}}{2FP_{an}D_{H_2O,m}} \quad \text{(A.25)}$$

For electrolysis mode, the equivalent integral is Equation (A.26), which is evaluated to Equation (A.27) for hydrogen. Note that the sign of the second term has changed, because $X_{H_2}^l$ is now the sum of the bulk concentration of hydrogen, and the hydrogen produced at the fuel electrode during electrolysis operation. It therefore follows that for electrolysis mode, the equations will be the same, but have opposite signs, as hydrogen is being produced, and steam consumed. Therefore the equation for steam diffusion will be Equation (A.28).

$$\int_{X_{H_2O}^b}^{X_{H_2O}^l} dX_{H_2O} = \int_0^{L_{bl}} -\frac{iRTL_{b,l}}{2FP_{an}D_{H_2O,m}} dr \quad \text{(A.26)}$$

$$X_{H_2}^l = X_{H_2}^b + \frac{iRTL_{b,l}}{2FP_{an}D_{H_2,m}} \quad \text{(A.27)}$$

$$X_{H_2O}^l = X_{H_2O}^b - \frac{iRTL_{b,l}}{2FP_{an}D_{H_2O,m}} \quad \text{(A.28)}$$

Diffusion of gas through the electrode microstructure may be modeled, if the diffusion mechanism is known. Two possible mechanisms are Knudsen diffusion, or molecular (Fickian) diffusion. Knudsen diffusion relies on the assumption that the gas molecule mean free path length is greater than the electrode pore diameter, and so molecules of hydrogen or steam are more likely to hit the pore walls than each other, whereas molecular diffusion assumes the opposite. The most appropriate mechanism for this model is molecular diffusion - the same type that occurs above the fuel electrode surface. Therefore, the diffusion coefficient of the gases through

the fuel electrode pores may be determined by scaling the mutual diffusion coefficients $D_{H_2,m}$ and $D_{H_2O,m}$ by the porosity ϵ (40%) and tortuosity τ (3.0) of the electrode, according to Equation (A.29) for fuel cell mode and Equation (A.30) for electrolysis mode.

$$D_{H_2,p} = D_{H_2,m}\left(\frac{\epsilon}{\tau}\right) \tag{A.29}$$

$$D_{H_2O,p} = D_{H_2O,m}\left(\frac{\epsilon}{\tau}\right) \tag{A.30}$$

If Equation (A.16), and a similar equation in which steam flux replaces hydrogen flux, are integrated along the anode length (thickness) L_{an} (fuel electrode in fuel cell mode), which is $2 \times 10^{-5} m$, and the hydrogen and steam molar fractions at the fuel electrode reactive surface may be calculated, for the fuel cell mode, according to Equation (A.31) and (A.32) respectively. For electrolysis, again the equations take the same form except the sign of the second term is positive, as $X^r_{H_2O} < X^l_{H_2O}$, that is, the mole fraction of steam at the fuel electrode surface *l* is greater than the mole fraction of steam at the fuel electrode reaction site *r*. The hydrogen concentration at the reactive surface is given by Equation (A.33) and the steam concentration at the electrode surface is given by Equation (A.34).

$$X^r_{H_2} = X^l_{H_2} - \frac{iRTL_{an}}{2FP_{an}D_{H_2,p}} \tag{A.31}$$

$$X^r_{H_2O} = X^l_{H_2O} + \frac{iRTL_{an}}{2FP_{an}D_{H_2O,p}} \tag{A.32}$$

$$X^r_{H_2} = X^l_{H_2} + \frac{iRTL_{an}}{2FP_{an}D_{H_2,p}} \tag{A.33}$$

$$X^r_{H_2O} = X^l_{H_2O} - \frac{iRTL_{an}}{2FP_{an}D_{H_2O,p}} \tag{A.34}$$

The total diffusion polarisation at the anode (fuel electrode in fuel cell mode) can then be calculated by Equation (A.35).

$$V_{diff,an} = \frac{RT}{2F} ln\left(\frac{X_{H_2}^b X_{H_2O}^r}{X_{H_2O}^b X_{H_2}^r}\right) \quad \text{(A.35)}$$

Appendix C: Randles Circuit State-space Functions:

$$V_{out} = V_{R_{cell}} + V_{C_{cell}} \quad \text{(A.36)}$$

$$I_{diff,cell} = -\frac{V_{C_{cell}}}{R_{diff,cell}} \quad \text{(A.37)}$$

$$I_{C_{cell}} = I - I_{R_{diff,cell}} \quad \text{(A.38)}$$

$$I_{C_{cell}} = -C\frac{dV_{C_{cell}}}{dt} \quad \text{(A.39)}$$

$$V_{R_{cell}} = V_{nernst} - I \times R_{cell} \quad \text{(A.40)}$$

Appendix D: Modelling the Heat Store Characteristic in Simulink

To accomplish bronze molten status of three thermal stages in model, several logic designs are developed in the Simulink block as shown in Figure A 3, Figure A 4 and Figure A 5. Figure A 3 shows the total heat capacities of the system. Figure A 4 is to determine which stage it is by monitoring temperature and the proportion of molten bronze. Figure A 5 calculates and integrates the changing rate of temperature corresponding to the state detected by Figure A 4. The integrators in Figure A 5 have the function of reset so the model of heat store can reverse its states from molten to solid as releasing the heat to endothermic reaction in electrolysis mode.

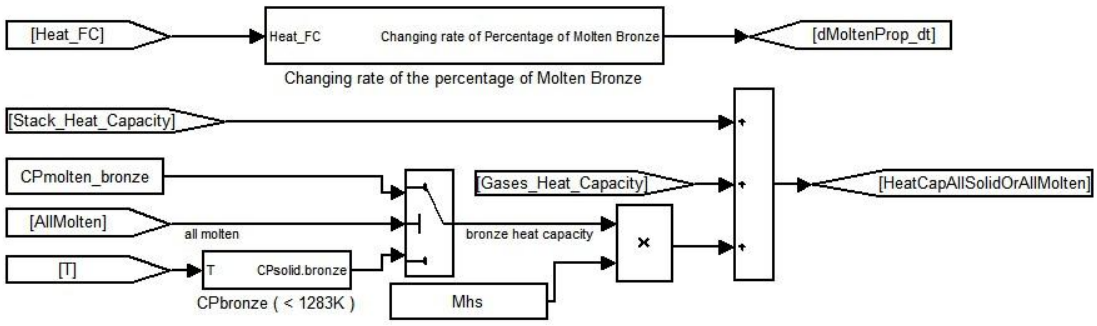

Figure A 3 Heat store model 1

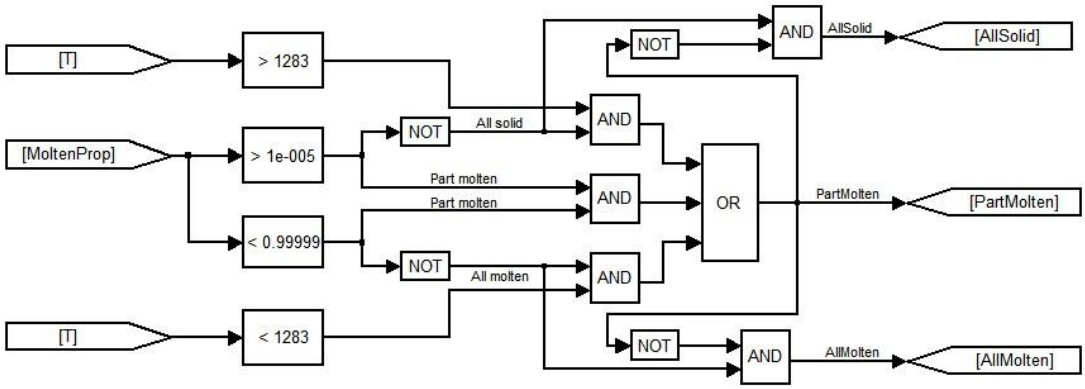

Figure A 4 Heat store model 2

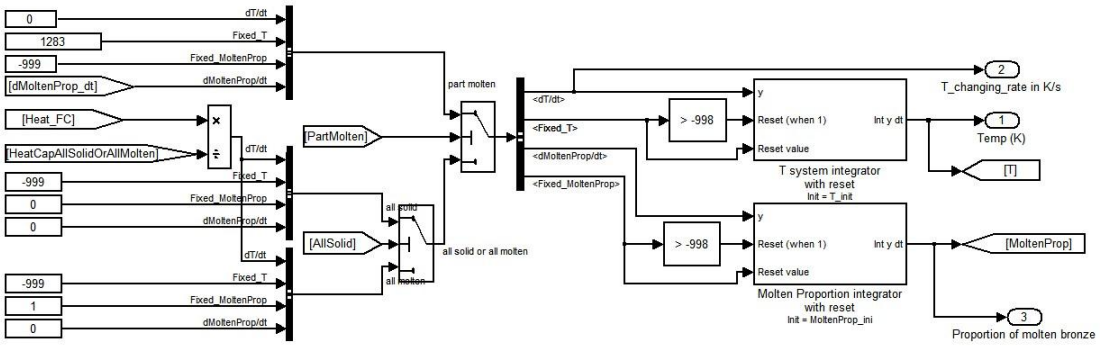

Figure A 5 Heat store model 3

Appendix E: Diagrams of original control schemes developed in University of Strathclyde

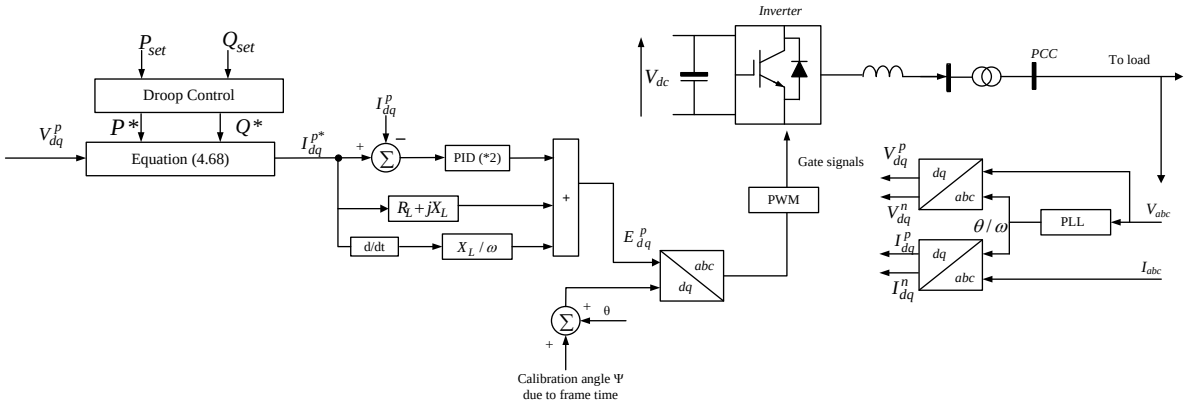

Figure A 6 Control diagram for high-bandwidth powerflow ripple minimization

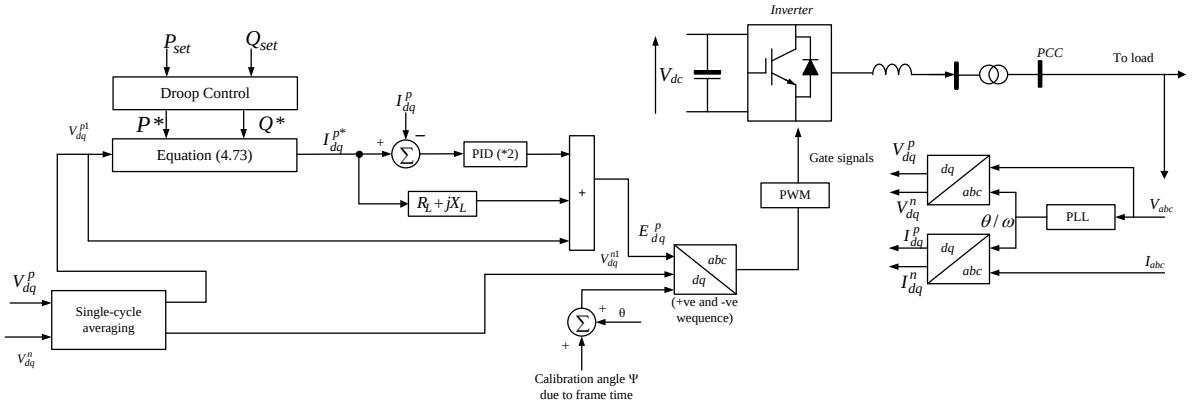

Figure A 7 Control diagram for high-bandwidth sinusoidal balanced currents

Appendix F: Three-phase Instantaneous Power in terms of Clarke Components.

The three-phase instantaneous active power can be calculated in terms of the $\alpha\beta 0$ components to replace the *abc* variables in Equation (A.41).

$$
\begin{aligned}
p_{3\phi}(t) &= v_a(t)i_a(t) + v_b(t)i_b(t) + v_c(t)i_c(t) \\
&= \sqrt{\frac{2}{3}}\left(\frac{1}{\sqrt{2}}v_0 + v_\alpha\right)\sqrt{\frac{2}{3}}\left(\frac{1}{\sqrt{2}}i_0 + i_\alpha\right) \\
&+ \sqrt{\frac{2}{3}}\left(\frac{1}{\sqrt{2}}v_0 - \frac{1}{2}v_\alpha + \frac{\sqrt{3}}{2}v_\beta\right)\sqrt{\frac{2}{3}}\left(\frac{1}{\sqrt{2}}i_0 - \frac{1}{2}i_\alpha + \frac{\sqrt{3}}{2}i_\beta\right) \\
&+ \sqrt{\frac{2}{3}}\left(\frac{1}{\sqrt{2}}v_0 - \frac{1}{2}v_\alpha - \frac{\sqrt{3}}{2}v_\beta\right)\sqrt{\frac{2}{3}}\left(\frac{1}{\sqrt{2}}i_0 - \frac{1}{2}i_\alpha - \frac{\sqrt{3}}{2}i_\beta\right) \\
&= \frac{2}{3}\left\{\left(\frac{1}{2}v_0 i_0 + \frac{1}{\sqrt{2}}v_0 i_\alpha + \frac{1}{\sqrt{2}}v_\alpha i_0 + v_\alpha i_\alpha\right)\right. \\
&+ \left(\frac{1}{2}v_0 i_0 - \frac{1}{2\sqrt{2}}v_0 i_\alpha + \frac{\sqrt{3}}{2\sqrt{2}}v_0 i_\beta - \frac{1}{2\sqrt{2}}v_\alpha i_0 + \frac{1}{4}v_\alpha i_\alpha - \frac{\sqrt{3}}{4}v_\alpha i_\beta\right. \\
&\left. + \frac{\sqrt{3}}{2\sqrt{2}}v_\beta i_0 - \frac{\sqrt{3}}{4}v_\beta i_\alpha + \frac{3}{4}v_\beta i_\beta\right) \\
&+ \left(\frac{1}{2}v_0 i_0 - \frac{1}{2\sqrt{2}}v_0 i_\alpha - \frac{\sqrt{3}}{2\sqrt{2}}v_0 i_\beta - \frac{1}{2\sqrt{2}}v_\alpha i_0 + \frac{1}{4}v_\alpha i_\alpha + \frac{\sqrt{3}}{4}v_\alpha i_\beta\right. \\
&\left.\left. - \frac{\sqrt{3}}{2\sqrt{2}}v_\beta i_0 + \frac{\sqrt{3}}{4}v_\beta i_\alpha + \frac{3}{4}v_\beta i_\beta\right)\right\} = v_\alpha i_\alpha + v_\beta i_\beta + v_0 i_0
\end{aligned}
\tag{A.41}
$$

There are no zero-sequence current components in three-phase, three-wire systems, that is, $i_0 = 0$. In this case, only the instantaneous powers defined on the $\alpha\beta$ axes exist. Refer to the conventional concept of the complex power defined using a voltage phasor and the conjugate of a current phasor, it is also valid for the instantaneous complex power under $\alpha\beta$ frames and vectors of $v_{\alpha\beta}$ and $i_{\alpha\beta}$.

$$S = p + jq = v_{\alpha\beta} i^*_{\alpha\beta} = \left(v_\alpha i_\alpha + v_\beta i_\beta\right) + j(v_\beta i_\alpha - v_\alpha i_\beta) \qquad (A.42)$$

Since instantaneous voltages and current ($v_{\alpha\beta}$ and $i_{\alpha\beta}$) are used, there are no restrictions in complex power S, and it can be applied during steady states or during transients. And the well-known *p* and *q* definition is

$$\begin{bmatrix} p \\ q \end{bmatrix} = \begin{bmatrix} v_\alpha & v_\beta \\ v_\beta & -v_\alpha \end{bmatrix} \begin{bmatrix} i_\alpha \\ i_\beta \end{bmatrix} \qquad (A.43)$$

Similar to Equation (A.41), if the $\alpha\beta$ variables of the instantaneous imaginary power *q* as defined in Equation (A.42) are replaced by the equivalent expression referred to the *abc* axes then the following relation can be found:

$$q = v_\beta i_\alpha - v_\alpha i_\beta = \frac{1}{\sqrt{3}}[(v_a - v_b)i_c + (v_b - v_c)i_a + (v_c - v_a)i_b] \qquad (A.44)$$

The imaginary power *q*, while calculated directly from the *abc* phases that results from the sum of products of line voltages and line currents in different phases. Hence, the reactive power *q* in three-phase system does not contribute to the total energy flow between the source and the load, or vice-versa. It is proportional to the quantity of energy that is being exchanged between the phases of the system. This understanding is very important in the following analysis of inverter controls under generalized unbalanced system. Finally to note that, the instantaneous *pq* theory is valid to synchronous reference frame (Park's transformation) as well.

$$\begin{bmatrix} V_d \\ V_q \end{bmatrix} = \begin{bmatrix} cos\theta & sin\theta \\ -sin\theta & cos\theta \end{bmatrix} \begin{bmatrix} V_\alpha \\ V_\beta \end{bmatrix} \qquad (A.45)$$

Appendix G: Derivation of the Conventional Electrical Equations in SRF

Derivation of the conventional electrical equations on the ac side of the PWM dc/ac inverter in synchronous rotating reference frame (SRF) is discussed as follow.

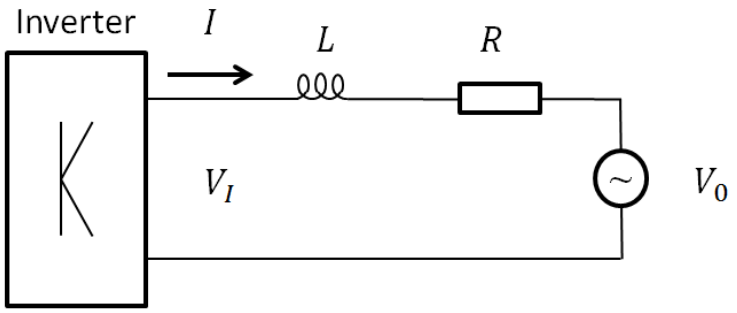

Figure A 8 Conventional layout of inverter with inductor

$$V_0 = V_I + L\frac{dI}{dt} + RI \tag{A.46}$$

And this is valid in *dq* frame too as

$$V_{0dq} = V_{Idq} + L\frac{dI_{dq}}{dt} + RI_{dq} \tag{A.47}$$

and

$$\frac{dI_d}{dt} = \frac{2}{3}\left[\frac{dI_a}{dt}\cos(\omega t) - \omega I_a \sin(\omega t) + \frac{dI_b}{dt}\cos\left(\omega t - \frac{2\pi}{3}\right) - \omega I_b \sin\left(\omega t - \frac{2\pi}{3}\right) + \frac{dI_c}{dt}\cos\left(\omega t + \frac{2\pi}{3}\right) - \omega I_c \sin\left(\omega t + -\frac{2\pi}{3}\right)\right] \tag{A.48}$$

from Equation (A.46) we know $\frac{dI_a}{dt} = \frac{V_{0a} - V_{Ia} - RI_a}{L}$, therefore

$$\frac{dI_d}{dt} =$$

$$\frac{2}{3L}\left[(V_{0a} - V_{Ia} - RI_a)\,cos(\omega t) + (V_{0b} - V_{Ib} - RI_b)\,cos\left(\omega t - \frac{2\pi}{3}\right)\right.$$
$$\left. + (V_{0c} - V_{Ic} - RI_c)\,cos\left(\omega t + -\frac{2\pi}{3}\right)\right]$$
$$+ \omega\left[-I_a\,sin(\omega t) - I_b\,sin\left(\omega t - \frac{2\pi}{3}\right) - I_c\,sin\left(\omega t + \frac{2\pi}{3}\right)\right] \quad \text{(A.49)}$$

Applying the Park's transformation then it gives that

$$L\frac{dI_d}{dt} = V_{0d} - V_{Id} - RI_d + \omega LI_q \quad \text{(A.50)}$$

The derivation of the Equation (A.50) then can be applied to $L\frac{dI_q}{dt}$, and the duel sequence I_{dq}^p and I_{dq}^n as well. They are shown as:

$$V_{0d}^p = V_{Id}^p + L\frac{dI_d^p}{dt} + RI_d^p - \omega LI_d^p$$

$$V_{0q}^p = V_{Iq}^p + L\frac{dI_q^p}{dt} + RI_q^p + \omega LI_q^p \quad \text{(A.51)}$$

$$V_{0d}^n = V_{Id}^n + L\frac{dI_d^n}{dt} + RI_d^n + \omega LI_d^n$$

$$V_{0q}^n = V_{Iq}^n + L\frac{dI_q^n}{dt} + RI_q^n - \omega LI_q^n$$

Appendix H: Analysis of the Effect of Load Harmonic Distortion on the Stack Current Ripple

The current drawn by the inverter from the output of the RSOFC system, as shown in Figure 5.12, can be written using small signal analysis as

$$i_{bus} = \left(i_{load} + C_f \frac{dv_f}{dt}\right) d_{vsi} \tag{A.52}$$

where d_{vsi} is the duty ratio of the inverter switches assuming small signal approximation and can be defined as $d_{vsi} = d_m sin\omega t$, ω is the frequency of the reference voltage for the inverter. Assuming no phase delay of the output voltage of the inverter with respect to the reference voltage, v_f can be written as $V_m sin\omega t$. Then assuming stiff bus voltage, Equation (A.52) becomes

$$i_{bus} = \left(i_{load} + \omega C_f V_m cos\omega t\right) d_m sin\omega t \tag{A.53}$$

Let us consider that the load current contains higher order harmonics (odd order specifically since AC current), then the load current can be explained as

$$i_{h,load}(t) = \sum_{k=1,3,5\ldots} I_{mk} sin(k\omega t + \phi_k) \tag{A.54}$$

Using Equation (A.53), the current drawn by the inverter can be written as

$$\begin{aligned} i_{bus}(t) = \frac{d_m}{2} \sum_{k=1,3,5\ldots} & I_{mk}\{cos[(k-1)\omega t + \phi_k] \\ & - cos[(k+1)\omega t + \phi_k]\} + \omega C_f V_m \sin(2\omega t) \end{aligned} \tag{A.55}$$

The filter capacitance being very small, the second term in Equation (A.55) is negligible as compared to the first term for finite load current. Assuming the real

power drawn by the harmonic load to be the same as that of a resistive load drawing current with amplitude I_m then $I_m = I_{m1}cos\phi_1$. Equation (A.55) in terms of the fundamental current, I_{m1}

$$
\begin{aligned}
i_{bus}(t) &= \frac{I_{m1}d_m}{2}\sum_{k=1,3,5\ldots} c_k\{cos[(k-1)\omega t+\phi_k] - cos[(k+1)\omega t+\phi_k]\} \\
&= \frac{I_{m1}d_m}{2}\Bigg\{cos\phi_1 - (cos(2\omega t+\phi_1) \\
&\quad - \sum_{k=3,5\ldots} c_k[\cos((k-1)\omega t+\phi_k) - \cos((k+1)\omega t+\phi_k)]\Bigg\} \\
&= \frac{I_m d_m}{2}\sum_{k=3,5\ldots}\Bigg\{1 \\
&\quad - \frac{1}{cos\phi_1}\Bigg[cos(2\omega t+\phi_1) \\
&\quad - \sum_{k=3,5\ldots} c_k[\cos((k-1)\omega t+\phi_k) - \cos((k+1)\omega t+\phi_k)]\Bigg]\Bigg\}
\end{aligned}
$$

(A.56)

where $c_k = \frac{I_{mk}}{I_{m1}}$, and ϕ_k is described by

$$\phi_k = cos^{-1}\left(\frac{cos\phi_1}{\sqrt{k^2(1+cos^2\phi_1) - cos^2\phi_1}}\right) \qquad \text{(A.57)}$$

Simplifying Equation (A.56),

$$
\begin{aligned}
i_{bus}(t) = \frac{I_m d_m}{2}\Bigg\{ & 1 \\
& - A \sum_{j=2,4,6\ldots} \left[c_{j-1}\cos\left(j\omega t + \phi_{j-1}\right)\right. \\
& \left. - c_{j+1}\cos\left(j\omega t + \phi_{j+1}\right)\right]\Bigg\} \\
& = \frac{I_{m1} d_m}{2}\left\{1 - A \sum_{j=2,4,6\ldots} \alpha_j\left[\cos\left(j\omega t + \psi_j\right)\right]\right\}
\end{aligned}
\tag{A.58}
$$

Where $A = \frac{1}{cos\phi_1}$, α_j and ψ_j are given as

$$\alpha_j = \sqrt{c_{j-1}^2 + c_{j+1}^2 - 2c_{j-1}c_{j+1}\cos(\phi_{j+1} - \phi_{j-1})} \tag{A.59}$$

$$\psi_j = tan^{-1}\left(\frac{c_{j-1}sin\phi_{j-1} - c_{j+1}sin\phi_{j+1}}{c_{j-1}cos\phi_{j-1} - c_{j+1}cos\phi_{j+1}}\right) \tag{A.60}$$

Assuming a fraction of the ripple in the bus current is absorbed in the bus capacitor *C*

$$i_c(t) = \frac{I_m d_m A}{2} \sum_{j=2,4,\ldots} (1 - \delta_j)\alpha_j\left[\cos\left(j\omega t + \psi_j\right)\right] \tag{A.61}$$

where $\delta_j = \frac{2\delta}{j}$ for j=2,4,6,…

Assuming the size of the capacitance should be chosen such that, the ripple in the bus voltage is smaller 5%. That is,

$$|\Delta v_{bus}(t)| = \left|\frac{1}{C}\frac{I_m d_m A}{2}\sum_{j=2,4,\ldots}(1-\delta_j)\int \cos(j\omega t+\psi_j)\,dt\right|$$
$$= \left|\frac{1}{C}\frac{I_m d_m A}{2}\sum_{j=2,4,\ldots}\frac{1-\delta_j}{j}\alpha_j\cos(j\omega t+\psi_j)\right| \quad \text{(A.62)}$$
$$< 0.05\frac{V_m}{d_m}$$

So

$$(1-D)i_{FC}(t) = \frac{I_m d_m}{2}\left[1 - A\sum_{j=2,4,\ldots}\delta_j\alpha_j\cos(j\omega t+\psi_j)\right] \quad \text{(A.63)}$$

$$i_{FC}(t) = \frac{I_m d_m}{2(1-D)}\left[1 - 2A\delta\sum_{j=2,4,\ldots}\frac{\alpha_j}{j}\cos(j\omega t+\psi_j)\right] \quad \text{(A.64)}$$

Since, $i_{FC}(t) = I_{FC} + \hat{\imath}_{FC}(t)$, where I_{FC} is the mean stack current and $\hat{\imath}_{FC}(t)$ is the ripple component of the stack current. Now the fraction of the ripple in the stack current is given by

$$\frac{\hat{\imath}_{FC}(t)}{I_{FC}} = \frac{\delta}{cos\phi_1}\sum_{j=2,4,\ldots}a_j\cos(j\omega t+\psi_j) \quad \text{(A.65)}$$

Where $a_j = \frac{2\alpha_j}{j}$, j=2,4,6,…

Equation (A.65) states that the amplitude of the ripple in the stack current increases with an increase in $|\phi_1|$. Again this ripple is dependent on α_j and ψ_j (Equation (A.61)), which depend on the fraction of the harmonic components c_j and their frequencies, $j\omega$. Now let us consider the harmonic current consists of only third and fifth harmonics.

Case I. Let us assume, c_3=0.2, c_5=0.11, and ϕ_1=0.4. Then, ϕ_3=0.903 and ϕ_5=1.13 radians and THD=0.228. From Equation (A.60), α_2 =0.8304, ψ_2=0.284, α_4=0.096,

ψ_4=0.642, α_6=0.11, and ψ_6=1.13. Using the following values, the fraction of the ripple in the bus current is found to be 0.995 to that of the mean bus current. With δ =0.2, and the ripple in stack current is 0.193.

Case II. Let us assume, c_3=0.5, c_5=0.24, and ϕ_1=0.4. Then ϕ_3=0.903 and ϕ_5=1.13 radians and THD=0.554. Equation (A.60) α_2 =0.611, ψ_2 =−0.005, α_4 =0.272, ψ_4=0.703, α_6=0.24, and ψ_6 =1.13. Using these values, with δ = 0.2 and using Equation (A.65), the fraction of the ripple in the stack current is 0.188.

From above two cases, we observe the ripple in the stack current decreases with an increase in the THD for a particular power factor of the fundamental current $\cos\phi_1$.

Appendix I: Analysis of the Effect of Load Power Factor on the Stack Current Ripple

For a resistive load, $i_{load} = I_m sin\omega t$, and Equation (A.53) becomes:

$$\begin{aligned} i_{bus} &= \left(I_m sin\omega t + \omega C_f V_m cos\omega t\right) d_m sin\omega t \\ &= \frac{I_m d_m}{2}[1 - \cos(2\omega t)] + \frac{\omega C_f V_m d_m}{2}\sin(2\omega t) \end{aligned} \quad \text{(A.66)}$$

The filter capacitance being very small, the second term in Equation (A.66) is negligible as compared to the first term. The approximate expression for the bus current becomes:

$$i_{bus} = \frac{I_m d_m}{2}[1 - \cos(2\omega t)] \quad \text{(A.67)}$$

For a reactive load with power factor, *p.f.*= $\cos\phi$, $i_{load} = I_m^{'}\sin(\omega t + \phi)$. Now for same active power as before,

$$\frac{V_m I_m}{2} = \frac{V_m I_m^{'}}{2}\cos\phi \;\rightarrow I_m^{'} = \frac{I_m}{\cos\phi} \quad \text{(A.68)}$$

Now Equation (A.53) becomes

$$\begin{aligned} i_{bus}(t) &= \left(\frac{I_m}{\cos\phi}\sin(\omega t + \phi) + \omega C_f V_m cos\omega t\right) d_m sin\omega t \\ &= \frac{I_m d_m}{2}\left[1 - \frac{\cos(2\omega t + \phi)}{\cos\phi}\right] \\ &+ \frac{\omega C_f V_m d_m}{2}\sin(2\omega t) \end{aligned} \quad \text{(A.69)}$$

Using the same approximation as Equation (A.67), the expression for the bus current becomes

$$i_{bus}(t) = \frac{I_m d_m}{2}[1 - A\cos(2\omega t + \phi)] \quad \text{(A.70)}$$

Where $A = {}^{1}/_{\cos\phi} > 1$ for all $\phi \neq 0$. At the output of the boost converter, assuming constant duty ratio *D* of the boost converter in the steady state

$$i_{bus}(t) = (1 - D)i_{FC}(t) - i_C(t) \tag{A.71}$$

Assuming a fraction δ of the ripple in the bus current flows in the bus capacitor *C*,

$$i_C(t) = \frac{I_m d_m}{2}(1 - \delta)A\cos(2\omega t + \phi) \tag{A.72}$$

Assuming the size of the capacitance should be chosen such that, the ripple in the bus voltage is smaller 5%. That is,

$$\begin{aligned} |\Delta v_{bus}(t)| &= \left|\frac{1}{C}\frac{I_m d_m(1-\delta)A}{2}\int \cos(2\omega t \right. \\ &\left. + \phi)dt\right| = \left|\frac{I_m d_m(1-\delta)A}{4\omega C}\right| \\ &< 0.05\frac{V_m}{d_m} \end{aligned} \tag{A.73}$$

Now,

$$(1 - D)i_{FC}(t) = \frac{I_m d_m}{2}[1 - \delta A\cos(2\omega t + \phi)] \tag{A.74}$$

$$i_{FC}(t) = \frac{I_m d_m}{2(1 - D)}[1 - \delta A\cos(2\omega t + \phi - k_1)] \tag{A.75}$$

Since, $i_{FC}(t) = I_{FC} + \hat{\imath}_{FC}(t)$, where I_{FC} is the mean stack current and $\hat{\imath}_{FC}(t)$ is the ripple component of the stack current. Now the fraction of the ripple in the stack current is given by

$$\frac{\hat{\imath}_{FC}(t)}{I_{FC}} = \frac{\delta}{cos\phi_1}\cos(2\omega t + \phi - k_1) \tag{A.76}$$

Equation (A.74) states that the amplitude of the ripple in the stack current increases with an increase in $|\phi|$. Hence, the ripple current increases with decrease in the load power factor.

Appendix J: Disturbance on *dq* Components of Ripple Minimization Control

Due to the measurements of V_{dq}^{p} is unfiltered therefore the desired I_{dq}^{p*} tracks well corresponding to the P^* and Q^* set points then results a significant decrease in output power ripple at the point of common connection (PCC). However as long as the information describing unbalance and harmonics present in V_{dq}^{p} then as a result it leads to an I_{dq}^{p*} trajectory contains a second harmonic component due to the exists of a circular trajectory at twice the fundamental frequency in V_{dq}^{p}. Thus, although only a positive-sequence controller is used, its bandwidth is high enough to also capture and control negative sequence and harmonic effects.

According to that the generalized trajectories of V_{dq}^{p} under situations of unbalance and harmonics, the $\alpha e^{j(N\omega t+\phi)}$, can be realized. Therefore V_d^p and V_q^p can be replaced by $1+\alpha cos(N\omega t+\phi)$ and $\alpha sin(N\omega t+\phi)$ which representing a circular oscillating component from the nominal point (*1+j0*) of vector V_{dq}^{p}. Hence:

$$\begin{bmatrix} I_d^{P*} \\ I_q^{P*} \end{bmatrix} = \frac{1}{[(1+\alpha\cos(N\omega t+\phi))^2+(\alpha\sin(N\omega t+\phi))^2]} \begin{bmatrix} 1+\alpha cos(N\omega t+\phi) & \alpha sin(N\omega t+\phi) \\ \alpha sin(N\omega t+\phi) & -(1+\alpha cos(N\omega t+\phi)) \end{bmatrix} \begin{bmatrix} P^* \\ Q^* \end{bmatrix} \tag{A.77}$$

$$\begin{bmatrix} I_d^{P*} \\ I_q^{P*} \end{bmatrix} = \begin{bmatrix} \dfrac{P^*(1+\alpha cos(N\omega t+\phi))+Q^*\alpha sin(N\omega t+\phi)}{1+\alpha^2+2\alpha cos(N\omega t+\phi)} \\ \dfrac{P^*\alpha sin(N\omega t+\phi)-Q^*(1+\alpha cos(N\omega t+\phi))}{1+\alpha^2+2\alpha cos(N\omega t+\phi)} \end{bmatrix} \tag{A.78}$$

This shows that I_d^{P*} and I_q^{P*}current harmonics will (predominantly) have the same order as the V_{dq}^{P} perturbations. Note that there is a slight non-linear effect, caused by

the denominators in Equation (A.78). This means that there will also be reduced contributions at 0x, 2x, 3x the frequency of the V_{dq}^{P} perturbations, particularly if α, the size of the perturbation becomes any significant proportion of the unity (per-unit) value. Applying the inverse Park's transformation and further mathematical analysis required of help of trigonometric function and the implementation of Fourier analysis in Matlab/Simulink, the desired three-phase current I_{abc} can then be obtained in Equation (A.79).

$$\begin{bmatrix} I_a \\ I_b \\ I_c \end{bmatrix} = P^* \begin{bmatrix} \left(sin(\omega t) - \sum_{k=1}^{\infty} (-\alpha)^k \, sin\big((kN-1)\omega t + k\phi\big) \right) \\ \left(sin\left(\omega t - \frac{2\pi}{3}\right) - \sum_{k=1}^{\infty} (-\alpha)^k \, sin\left((kN-1)\omega t + \frac{2\pi}{3} + k\phi\right) \right) \\ \left(sin\left(\omega t + \frac{2\pi}{3}\right) - \sum_{k=1}^{\infty} (-\alpha)^k \, sin\left((kN-1)\omega t - \frac{2\pi}{3} + k\phi\right) \right) \end{bmatrix} - Q^* \begin{bmatrix} \left(cos(\omega t) - \sum_{k=1}^{\infty} (-\alpha)^k \, cos\big((kN-1)\omega t + k\phi\big) \right) \\ \left(cos\left(\omega t - \frac{2\pi}{3}\right) - \sum_{k=1}^{\infty} (-\alpha)^k \, cos\left((kN-1)\omega t + \frac{2\pi}{3} + k\phi\right) \right) \\ \left(cos\left(\omega t + \frac{2\pi}{3}\right) - \sum_{k=1}^{\infty} (-\alpha)^k \, cos\left((kN-1)\omega t - \frac{2\pi}{3} + k\phi\right) \right) \end{bmatrix} \quad \text{(A.79)}$$

Equation (A.79) indicates that the fundamental component of the current is always balanced with an infinite sequence of harmonics at order of $(kN-1)$. And the amplitudes of the harmonics are decreasing with increasing *k*. When the measurements of voltage contain balanced fundamentals and harmonics the currents derived from Equation (A.79) will be balanced. Further analysis also indicates that in this case the triple order of harmonics do not exist, although either "positive sequence" or "negative sequence" harmonics content may be significant. For

unbalanced voltage fundamentals or harmonics, it shows that $\mathrm{mod}(N, 3) \neq 0$, the triple order of harmonics will not disappear. Equation (A 104) also shows that in this case the harmonic content of the current waveforms will be unbalanced. The clearest example is that unbalanced fundamental voltages will lead to $N = -2$ and unbalanced 3rd harmonic currents, giving different wave-shapes on the three phases. By Table I and Equation (A.79), the primary response to any voltage harmonic of order N_H will primarily be current harmonics of order $(N_H - 2)$ and/or $(N_H + 2)$, while the primary response to unbalance is unbalanced 3rd harmonics. However, harmonic responses on currents will tend to induce further voltage harmonics at the PCC at these new frequencies, and in turn results in further secondary current harmonics. In a weak grid scenario, this can make the control mode highly undesirable.

Appendix K: Standard sin & cos Trigonometric Identities

$$sin(A \pm B) = sinA \cdot cosB \pm cosA \cdot sinB \quad \text{(A.80)}$$

$$cos(A \pm B) = sinA \cdot cosB \mp cosA \cdot sinB \quad \text{(A.81)}$$

$$sinA + sinB = 2sin\left(\frac{A+B}{2}\right)cos\left(\frac{A-B}{2}\right) \quad \text{(A.82)}$$

$$sinA - sinB = 2cos\left(\frac{A+B}{2}\right)sin\left(\frac{A-B}{2}\right) \quad \text{(A.83)}$$

$$cosA + cosB = 2cos\left(\frac{A+B}{2}\right)cos\left(\frac{A-B}{2}\right) \quad \text{(A.84)}$$

$$cosA - cosB = -2sin\left(\frac{A+B}{2}\right)sin\left(\frac{A-B}{2}\right) \quad \text{(A.85)}$$

$$sinA \cdot sinB = \frac{cos(A-B) - cos(A+B)}{2} \quad \text{(A.86)}$$

$$sinA \cdot cosB = \frac{sin(A+B) + sin(A-B)}{2} \quad \text{(A.87)}$$

$$cosA \cdot cosB = \frac{cos(A+B) + cos(A-B)}{2} \quad \text{(A.88)}$$

Appendix L: Analysis of the Perturbations due to Voltage Unbalance and Harmonics

In the controllers for power electronic inverters the rotating vector angular speed in *dq* frame is defined to equal the fundamental frequency of the system. This is achieved by using the Phase Lock Loop (PLL) to lock to the voltage frequency at point of common connection (PCC), which aims to keep the resultant vector with V_q equalling zero. Equation (A.14) can be decomposed as further into positive V_{dq}^{p} and negetive sequences V_{dq}^{n} of *dq* components:

$$\begin{aligned} V_{dq}^{p} = V_d^{p} + jV_q^{p} &= \frac{2}{3}\left[e^{j\left(\frac{\pi}{2}-\omega t\right)}V_a + e^{j\left(\frac{\pi}{2}-\omega t+\frac{2\pi}{3}\right)}V_b + e^{j\left(\frac{\pi}{2}-\omega t-\frac{2\pi}{3}\right)}V_b\right] \\ &= \frac{2}{3}je^{-j\omega t}\left[V_a + e^{j\frac{2\pi}{3}}V_b + e^{-j\frac{2\pi}{3}}V_b\right] \end{aligned} \tag{A.89}$$

$$V_{dq}^{n} = V_d^{n} + jV_q^{n} = \frac{2}{3}je^{-j\omega t}\left[V_a + e^{-j\frac{2\pi}{3}}V_b + e^{j\frac{2\pi}{3}}V_b\right] \tag{A.90}$$

Synchronous Reference Frame *dq* component under the presence of unbalance

Considering a voltage unbalance with magnitude M_U and phase ϕ_U relative to the positive sequence and implement it into Matlab/Simulink version of Park's transformation yields the following equation: (assuming a three-wire system that the zero sequence is ignored):

$$\begin{bmatrix} V_d \\ V_q \end{bmatrix} = \frac{2}{3}\begin{bmatrix} \sin(\omega t) & \sin(\omega t-\frac{2\pi}{3}) & \sin(\omega t+\frac{2\pi}{3}) \\ \cos(\omega t) & \cos(\omega t-\frac{2\pi}{3}) & \cos(\omega t+\frac{2\pi}{3}) \end{bmatrix}\begin{bmatrix} M_F\sin(\omega t)+M_U\sin(\omega t+\phi_U) \\ M_F\sin\left(\omega t-\frac{2\pi}{3}\right)+M_U\sin(\omega t+\frac{2\pi}{3}+\phi_U) \\ M_F\sin\left(\omega t+\frac{2\pi}{3}\right)+M_U\sin(\omega t-\frac{2\pi}{3}+\phi_U) \end{bmatrix} \tag{A.91}$$

$$\begin{bmatrix} V_d \\ V_q \end{bmatrix} = \begin{bmatrix} M_F - M_U \cos(2\omega t + \phi_U) \\ M_U \left(2sin\phi_U \left(\frac{1 + cos(2\omega t)}{2} \right) + 2cos\phi_U \frac{sin(2\omega t)}{2} - sin\phi_U \right) \end{bmatrix} \tag{A.92}$$

where M_F is the fundamental magnitude. Apply the trigonometric function (A.86) in Appendix C yields:

$$\begin{bmatrix} V_d \\ V_q \end{bmatrix} = \begin{bmatrix} M_F - M_U \cos(-2\omega t - \pi - \phi_U) \\ M_U \sin(-2\omega t - \pi - \phi_U) \end{bmatrix} \tag{A.93}$$

It is obvious that under the presence of unbalanced voltage there is an oscillation performed as a circular superposition at twice the fundamental frequency in V_{dq} at PCC.

Generic balanced harmonics in synchronous reference frame (*dq* component)

Voltage with harmonic only at PCC (considering order N, $\phi_H \neq 0$ on all three phases (i.e. the waveforms are the same distorted shapes)) can be represented in synchronous reference frame as Equation (A.94)

$$\begin{bmatrix} V_d \\ V_q \end{bmatrix} = \frac{2}{3}\begin{bmatrix} \sin(\omega t) & \sin(\omega t - \frac{2\pi}{3}) & \sin(\omega t + \frac{2\pi}{3}) \\ \cos(\omega t) & \cos(\omega t - \frac{2\pi}{3}) & \cos(\omega t + \frac{2\pi}{3}) \end{bmatrix}\begin{bmatrix} M_H \sin(N\omega t + \phi_H) \\ M_H \sin(N\left(\omega t - \frac{2\pi}{3}\right) + \phi_H) \\ M_H \sin(N\left(\omega t + \frac{2\pi}{3}\right) + \phi_H) \end{bmatrix}$$

(A.94)

Appling the trigonometric function (A.86) (A.87) in Appendix C yields:

$$V_d = \frac{M_H}{3}\begin{pmatrix} cos\big((N-1)\omega t + \phi_H\big) - cos\big((N+1)\omega t + \phi_H\big) \\ +cos\left((N-1)\left(\omega t + \frac{2\pi}{3}\right) + \phi_H\right) - cos\left((N+1)\left(\omega t + \frac{2\pi}{3}\right) + \phi_H\right) \\ +cos\left((N-1)\left(\omega t - \frac{2\pi}{3}\right) + \phi_H\right) - cos\left((N+1)\left(\omega t - \frac{2\pi}{3}\right) + \phi_H\right) \end{pmatrix}$$

(A.95)

$$V_q = \frac{M_H}{3}\begin{pmatrix} sin\big((N-1)\omega t + \phi_H\big) + sin\big((N+1)\omega t + \phi_H\big) \\ +sin\left((N-1)\left(\omega t + \frac{2\pi}{3}\right) + \phi_H\right) + sin\left((N+1)\left(\omega t + \frac{2\pi}{3}\right) + \phi_H\right) \\ +sin\left((N-1)\left(\omega t - \frac{2\pi}{3}\right) + \phi_H\right) - sin\left((N+1)\left(\omega t - \frac{2\pi}{3}\right) + \phi_H\right) \end{pmatrix}$$

(A.96)

Cases of positive, negative and zero sequence harmonics are distinguished as follow

Zero sequence harmonics (3rd, 6th, 9th etc.) in synchronous reference frame

From Equation (A.95) and (A.96), but with harmonic order as a triple-N harmonic, and by setting:

$$a = (N-1)\omega t + \phi_H \tag{A.97}$$

$$b = (N+1)\omega t + \phi_H \tag{A.98}$$

then

$$\begin{bmatrix} V_d \\ V_q \end{bmatrix}$$

$$= \frac{M_H}{3}\begin{bmatrix} cosa - cosb + cos\left(a - \frac{2\pi}{3}\right) - cos\left(b + \frac{2\pi}{3}\right) + cos\left(a + \frac{2\pi}{3}\right) - cos\left(b - \frac{2\pi}{3}\right) \\ sina + sinb + sin\left(a - \frac{2\pi}{3}\right) + sin\left(b + \frac{2\pi}{3}\right) + sin\left(a + \frac{2\pi}{3}\right) + sin\left(b - \frac{2\pi}{3}\right) \end{bmatrix} \tag{A.99}$$

And by applying Equation (A.82) and (A.84)

$$\begin{bmatrix} V_d \\ V_q \end{bmatrix}$$

$$= \frac{M_H}{3}\begin{bmatrix} cosa + 2cos\left(\frac{a+a}{2}\right)cos\left(\frac{-\frac{2\pi}{3}-\frac{2\pi}{3}}{2}\right) - cosb - 2cos\left(\frac{b+b}{2}\right)cos\left(\frac{-\frac{2\pi}{3}-\frac{2\pi}{3}}{2}\right) \\ sina + 2sin\left(\frac{a+a}{2}\right)cos\left(\frac{-\frac{2\pi}{3}-\frac{2\pi}{3}}{2}\right) + sinb + 2sin\left(\frac{b+b}{2}\right)cos\left(\frac{-\frac{2\pi}{3}-\frac{2\pi}{3}}{2}\right) \end{bmatrix} \tag{A.100}$$

$$\begin{bmatrix} V_d \\ V_q \end{bmatrix}$$

$$= \frac{M_H}{3}\begin{bmatrix} cosa + 2cosa\left(\frac{-1}{2}\right) - cosb - 2cosb\left(\frac{-1}{2}\right) \\ sina + 2cosa\left(\frac{-1}{2}\right) + sinb + 2sinb\left(\frac{-1}{2}\right) \end{bmatrix} \tag{A.101}$$

$$\begin{bmatrix} V_d \\ V_q \end{bmatrix} = M_H \begin{bmatrix} cos\big((N-1)\omega t + \phi_H\big) \\ sin\big((N-1)\omega t + \phi_H\big) \end{bmatrix} \tag{A.102}$$

Positive sequence harmonics (4th, 7th, 10th etc.) in synchronous reference frame

From Equation (A.95) and (A.96), but with harmonic order as a positive sequence, and by settings of Equation (A.97) and (A.98):

$$\begin{bmatrix} V_d \\ V_q \end{bmatrix} = \frac{M_H}{3}\begin{bmatrix} cosa - cosb + cos(a) - cos\left(b - \frac{2\pi}{3}\right) + cos(a) - cos\left(b + \frac{2\pi}{3}\right) \\ sina + sinb + sin(a) + sin\left(b - \frac{2\pi}{3}\right) + sin(a) + sin\left(b + \frac{2\pi}{3}\right) \end{bmatrix} \tag{A.103}$$

And by applying Equation (A.82) and (A.84)

$$\begin{bmatrix} V_d \\ V_q \end{bmatrix} = \frac{M_H}{3}\begin{bmatrix} 3cosa - cosb - 2cos\left(\frac{b+b}{2}\right)cos\left(\frac{-\frac{2\pi}{3} - \frac{2\pi}{3}}{2}\right) \\ 3sina + sinb - 2sin\left(\frac{b+b}{2}\right)cos\left(\frac{-\frac{2\pi}{3} - \frac{2\pi}{3}}{2}\right) \end{bmatrix} \tag{A.104}$$

$$\begin{bmatrix} V_d \\ V_q \end{bmatrix} = \frac{M_H}{3}\begin{bmatrix} 3cos(a) \\ 3sin(a) \end{bmatrix} \tag{A.105}$$

$$\begin{bmatrix} V_d \\ V_q \end{bmatrix} = M_H\begin{bmatrix} cos\big((N-1)\omega t + \phi_H\big) \\ sin\big((N-1)\omega t + \phi_H\big) \end{bmatrix} \tag{A.106}$$

Thus, the positive-sequence harmonics produce V_{dq} perturbations at a frequency of $(N-1)\omega t$.

Negative sequence harmonics (2nd, 5th, 8th etc.) in synchronous reference frame

From Equation (A.95) and (A.96), but with harmonic order as a positive sequence, and by settings of Equation (A.97) and (A.98):

$$\begin{bmatrix} V_d \\ V_q \end{bmatrix} = \frac{M_H}{3}\begin{bmatrix} cosa - cosb + cos\left(a + \frac{2\pi}{3}\right) - cos(b) + cos\left(a - \frac{2\pi}{3}\right) - cos(b) \\ sina + sinb + sin\left(a + \frac{2\pi}{3}\right) + sin(b) + sin\left(a - \frac{2\pi}{3}\right) + sin(b) \end{bmatrix} \quad \text{(A.107)}$$

And by applying Equation (A.82) and (A.84)

$$\begin{bmatrix} V_d \\ V_q \end{bmatrix} = \frac{M_H}{3}\begin{bmatrix} cosa + 2cos\left(\frac{a+a}{2}\right)cos\left(\frac{\frac{2\pi}{3} - \frac{2\pi}{3}}{2}\right) - 3cosb \\ sina + 2sin\left(\frac{a+a}{2}\right)cos\left(\frac{\frac{2\pi}{3} - \frac{2\pi}{3}}{2}\right) + 3sinb \end{bmatrix} \quad \text{(A.108)}$$

$$\begin{bmatrix} V_d \\ V_q \end{bmatrix} = \frac{M_H}{3}\begin{bmatrix} -3cos(b) \\ 3sin(b) \end{bmatrix} \quad \text{(A.109)}$$

$$\begin{bmatrix} V_d \\ V_q \end{bmatrix} = M_H \begin{bmatrix} cos(-(N+1)\omega t - \phi_H + \pi) \\ sin(-(N+1)\omega t - \phi_H + \pi) \end{bmatrix} \quad \text{(A.110)}$$

Thus, the positive-sequence harmonics produce V_{dq} perturbations at a frequency of $-(N+1)\omega t$.